6-25-2024

Pressure and Rate Transient Analyses for Plume Characterization and Storage Capacity Estimation of CO2 Storage Projects

Mohamed Elnoby Mokhtar Abdelaal
Louisiana State University and Agricultural and Mechanical College

PRESSURE AND RATE TRANSIENT ANALYSES FOR PLUME CHARACTERIZATION AND STORAGE CAPACITY ESTIMATION OF CO_2 STORAGE PROJECTS

A Dissertation

Submitted to the Graduate Faculty of the
Louisiana State University and
Agriculture and Mechanical College
in partial fulfillment of the
requirements for the degree of
Doctor of Philosophy

in

The Craft and Hawkins Department of Petroleum Engineering

by
Mohamed Elnoby Mokhtar Abdelaal
B.S., Suez University, 2014
M.S., Suez University, 2018
August 2024

Praise and thanks to Allah for giving me the potential to achieve this work

To the soul of my father, to my mother, thank you for raising me. Your prayers backed me during hardships. Without you, I would not have achieved any goal in my life

To my wife, Amaal, thank you for your love, support, and believing in me since we first met, and thank you for taking care of our children when I was not there to help. This achievement is ours

To my children, Yaseen and Nourseen, thank you for being a part of my life. You are the source of joy and happiness to our family

Acknowledgments

I would like to thank my advisor, Dr. Mehdi Zeidouni, for his mentorship and support throughout my PhD. His guidance was fundamental in approaching and tackling tough problems in depth and with persistence.

I am thankful to all my committee members, Dr. Susan Hovorka, Dr. Karsten Thompson, and Dr. Eurico D'Sa, for devoting their time, and for providing invaluable feedback and suggestions. Their encouragement has been crucial in achieving this milestone.

I would like to thank the Craft and Hawkins Department of Petroleum Engineering for providing the technical/educational support, the good research environment, and the softwares necessary for my research.

I would like to thank the US Department of Energy for funding this research. Also, I want to thank LSU's Institute for Energy Innovation for funding part of this work.

Table of Contents

List of Tables

List of Figures

Abstract

Reservoir characterization is a key factor for effective management of commercial-scale Geologic CO_2 Storage (GCS) projects. Pressure/rate transient analyses (PTA/RTA) have evolved as reliable tools for assessing hydrocarbon and GCS reservoirs. Injection rate and pressure data are routinely measured as a part of GCS projects' surveillance, or during transient well testing. The data contain valuable information about the subsurface that can be extracted. The extracted information enables the operator to evaluate the effectiveness of injection operations, and to make remedial/corrective interventions. In this current work, different analytical and numerical techniques are presented to characterize, assess, and maximize the economic and volumetric value of the target formations devoted for CO_2 storage.

The objectives of this study are achieved through developing novel analytical models that describe the evolution of bottomhole pressure during or after CO_2 injection at a constant-rate. The analytical models are derived through solving the governing equations that describe CO_2-brine flow in the reservoir. The models are solved using rigorous mathematical techniques considering simplifying assumptions about rock and fluid properties. Based on the developed analytical models, graphical interpretation methodologies are introduced to analyze injection rate and pressure data using PTA and RTA techniques. The analytical models and the interpretation methodologies are validated against numerical simulations and real field datasets to demonstrate their robustness and practical application. The simulations are conducted on representative geological models using commercial reservoir simulation tools.

Results indicate that the interpretation methodologies can be reliably utilized to (1) infer the fluid mobilities and radial extent of the CO_2 dry-out zone to assess CO_2 injectivity, (2) monitor the spatial-temporal evolution of CO_2 plume to constrain CO_2 in the designated storage area, and (3) predict the ultimate storage capacity of a target formation to assess the feasibility of the GCS project to accommodate the large supply of CO_2. Then, to maximize the economic and volumetric value of a given fixed pore space, simulations studies are performed to investigate the factors that affect CO_2 injectivity and subsequent storage capacity. This includes investigating the injection well operating conditions, and physical processes controlling CO_2 distribution around the injection well.

Chapter 1. Introduction

1.1. Background and Motivation

Geologic CO_2 Storage (GCS) has become a prominent proposal to mitigate climate change through making deep cuts in the anthropogenic CO_2 emissions to the atmosphere. Technical and economic feasibility of commercial-scale GCS projects requires injecting CO_2 at high rates to accommodate the envisioned large supply of CO_2. CO_2 injectivity is dramatically enhanced with the expansion of the less-viscous highly-mobile CO_2 especially within the dry-out zone. On the other hand, it is negatively affected by the salt drying out due to brine vaporization in the vicinity of the wellbore. Assessing the injectivity of a GCS project requires accurate estimation of the radial extents and phase mobilities of the CO_2 dry-out zone and plume. In addition, monitoring the temporal-spatial evolution of the injected CO_2 is required to ensure containment within the target formation. Pressure-transient analysis (PTA) theory can be employed to characterize the dry-out zone and the plume. PTA is the process of obtaining information about a reservoir through analyzing pressure transients induced by injection or production at a constant rate over a short period of time. PTA techniques utilize analytical solutions that represent fluid flow in porous formations considering simplifying assumptions about fluid and rock properties. PTA techniques have been long used to characterize the subsurface in hydrocarbon production operations. Conventionally, PTA has many well testing analysis applications including inferring: (1) the absolute permeability of the reservoir and skin factor, (2) the initial/average reservoir pressure, and (3) the movement of fluid banks in enhanced oil recovery operations (e.g., in water and steam flooding). In the context of GCS, PTA has been revolving as an effective tool for reservoir characterization (e.g., to infer the permeability of the reservoir, and to track the CO_2 plume). In this work, PTA theory will be utilized to assess the injectivity of CO_2 by inferring the spatial extents and fluid mobilities of the dry-out zone and CO_2 plume. Specifically, the pressure falloff testing analysis will be used to interpret the behavior of the bottomhole pressure recorded during a pause during storage operations.

Reliable estimation of the storage capacity is necessary to assess the potential of a target formation to store the anticipated volumes of CO_2. Storage capacity estimation is straightforward for depleted oil and gas reservoirs given their production history and recoverable reserves. Nevertheless, it is complicated for saline aquifers due to the complexities related to data acquisition and trapping mechanisms. Rate-transient analysis (RTA) theory can be utilized to estimate the storage capacity of a closed target saline formation. In the context of hydrocarbon production, RTA has been long deployed to infer the initial hydrocarbon in-place and the ultimate recovery of a closed drainage area. RTA utilizes the production rate, pressure, and cumulative data routinely measured during production operations. This is unlike PTA theory which employs transient pressure data induced by a constant rate of production over a short period of time. Nevertheless, methods of RTA are very similar to those used for PTA. Specifically, the theory of RTA has evolved by looking at the reservoir production as a very long pressure-transient period during which production rates and pressures are likely variable. The key concept that has been introduced to allow for the extension of PTA theory to RTA (referred to as production data analysis) is the material balance time. Using material balance time, wells operating at variable pressure/rate conditions during the boundary-dominated flow (BDF) period will behave as if they were operating at a constant rate of production. This renders the methods of PTA theory applicable and provides the theoretical basis for RTA. In this work, we will extend the theory of RTA to estimate the ultimate storage capacity of a closed

saline formation through analyzing the available injection pressure and rate data. The attempts of this work are analogous to the developments in the petroleum reservoir engineering which translated the PTA theory to RTA. The proposed approach is foreseen to be very useful especially during early years of CO_2 storage projects. It should help the operators to constrain the anticipated CO_2 volume using dynamic data analysis.

Maximizing the volumetric value of a given pore space is essential for the technical and economic feasibility of GCS projects. The storage capacity of a potential formation is a function of the static formation characteristics (e.g., porosity and thickness). However, it can be enhanced/deteriorated by the injectivity variations caused by the dynamic practices adopted during storage operations. Preferred target formations should offer reasonable injectivity to accommodate CO_2 at high rates. Injectivity is quantified by the injectivity index which has been defined as the ratio of the injection rate per unit difference between the bottomhole pressure and the average reservoir pressure. The interplay between the injection rate and the pressure difference translates to injectivity variations. This variation is primarily controlled by the flow capacity, relative permeability, fluid mobilities, salt dry-out, formation damage/stimulation, and the adopted injection strategies. In this work, the effect of different well operating conditions on the injectivity variations and subsequent storage capacity will be investigated. The goal is to determine the optimum injection scheme to maximize the volumetric and economic value of the given pore space.

Distribution of CO_2 along the injection interval of a storage formation has significant effect on the injectivity and subsequent storage capacity. The distribution of CO_2 is affected by the degree of vertical heterogeneity of the flow capacity along the injection interval, and the difference in the hydrostatic pressure gradients between the wellbore and the aquifer. Also, CO_2 would be unevenly distributed along the injection interval due to gravity override driven by the density difference between CO_2 and brine. This "gravity override" is quantified by the dimensionless group of gravity number. A lower gravity number is preferred as it expresses a more uniform CO_2 displacement, which positively impacts the injectivity and storage capacity. In this work, the interplay between different physical processes and reservoir parameters affecting CO_2 distribution along the injection interval are investigated. The complex wellbore physics associated with heat transfer, CO_2 phase change, and interactions with the reservoir rock and fluid will be honored via utilizing coupled wellbore-reservoir simulation modeling.

One of the limiting factors to maximizing the ultimate storage capacity of a target formation is the bottomhole pressure buildup caused by CO_2 injection. The magnitude of overpressure should not exceed the regulatory maximum injection pressure to protect the geomechanical integrity of the formation and caprock. In addition, pressure buildup affects the injectivity variation according to the definition of injectivity index. Gravity override affects the bottomhole pressure buildup, and as a result, the injectivity and the ultimate storage capacity. Therefore, reliable estimation of the bottomhole pressure while considering strong gravity forces is essential. In this work, an analytical approach will be presented to predict the bottomhole pressure behavior during CO_2 injection via a vertical well centered in the middle of a high-gravity storage saline formation. The proposed analytical model will account for strong gravity forces which play an important role in controlling the distribution of fluids and pressures in high-gravity storage formations.

1.2. Problem Statement

The goals of this current work is to develop novel analytical models and interpretation techniques to characterize GCS saline reservoirs using PTA and RTA methods commonly used in petroleum reservoir engineering. The purpose is to assess the CO_2 injectivity, the temporal-spatial plume evolution, and the storage capacity via analyzing the available pressure and rate data. Additionally, we will conduct simulation studies to investigate the different factors that would maximize the technical, volumetric, and economic values of a given fixed pore space. Specifically, the problems that will be addressed in this research are:

1. To develop a graphical interpretation technique able to infer the fluids' mobilities and the radial extents of the dry-out zone and CO_2 plume through interpreting pressure falloff tests conducted during a pause during CO_2 injection. First, a forward three-zone analytical model is developed to represent the pressure profile during a pause during CO_2 injection into a single-layer infinite-acting aquifer. The model is derived through solving the diffusivity equations governing the pressure distribution in the reservoir during the falloff period. The solution at the wellbore is validated against data generated using a numerical reservoir simulator. Then, a graphical interpretation technique is derived through approximating the analytical solution by asymptotic solutions in real-time domain. The graphical technique should be able to analyze the falloff pressure data to infer the fluid mobilities and radial extents of the dry-out zone and CO_2 plume. The potential application of the interpretation technique is next tested through analyzing pressure falloff tests conducted considering a single-layer infinite-acting aquifer. The effects of gravity/buoyancy, closed aquifer's outer boundaries, formation dip angle, horizontal permeability anisotropy, variable injection rate prior to the test, linear/channeled reservoirs, and long/short injection are investigated. The technique is validated against real field datasets obtained from GCS projects.

2. To develop of a two-step graphical interpretation technique able to infer the pore volume, and to estimate the ultimate storage capacity of closed GCS reservoirs. This is achieved via analyzing the available injection pressure and rate data using RTA methods. First, a mathematical expression is introduced to infer the pore volume of a closed saline formation. This is accomplished by extending the pseudo-steady state solution - which predicts the overpressure in closed systems in response to injection at a constant rate – to interpret data of variable schedule. Then, the analytical expression is manipulated to estimate the ultimate storage capacity based on material balance techniques. The reliability of the methodology is next substantiated through application to synthetic data representing wells operating at variable pressure and rate schedule. The practical potential of the technique is tested against real field data obtained from commercial-scale GCS projects.

3. To investigate the effects of the injection well operating conditions on the CO_2 injectivity variations and subsequent storage capacity of closed storage formations. The purpose is to articulate the optimum injection scheme that maximizes the volumetric and economic value of a given fixed pore volume devoted for CO_2. To achieve this objective, a simulation study is conducted using a black-oil numerical reservoir simulator. First, continuous/intermittent injection at constant terminal pressure/rate conditions is studied to articulate the optimum injection strategy. Then, a simple net-present value (NPV) is conducted to identify the most

economically feasible injection scheme. Next, different injection schemes are applied to a synthetic GCS project with an injection history to identify their implications. Finally, a sensitivity analysis is performed to investigate the impact of varying the injection rate, vertical permeability, outer boundary conditions, well penetration and formation dip angle.

4. To investigate the interplay between different reservoir parameters and physical processes that control the CO_2 flow rate distribution along the injection interval of storage saline formation. Coupled wellbore-reservoir modeling is used to achieve this goal. First, the effect of CO_2/brine interface movement within the wellbore, vertical heterogeneity of flow capacity, change in the average fluid mobility within layers, and the pressure difference between the wellbore and the reservoir is investigated. Implications of brine backflow into the wellbore on wellbore refilling with brine, and hence, rate distribution are also addressed. A sensitivity analysis is performed next to study the impact of varying the injection rate on the flow rate profile. The effects of decoupled modeling (sink well injection), presence of permeable formations overlying/underlying the target zone, and intermittent injection and the associated salt dry-out are also investigated.

5. To develop an analytical solution to predict the evolution of bottomhole pressure during CO_2 injection. The solution accounts for the buoyancy forces which have significant effect of the evolution of the overpressure. The solution is developed while considering vertical equilibrium of pressure with a sharp interface separating CO_2 and brine. First, a closed-form solution is developed to estimate the evolution of CO_2/brine interface. The interface solution extends the semi-analytical/iterative expressions derived in the literature to predict the evolution of the plume. Then, the pressure solution is obtained by coupling the interface solution with the governing equation of the corresponding pressure field. Next, the pressure solution is validated against synthetic data generated numerically using a black-oil numerical reservoir simulator. The pressure solution is also validated against real field data obtained from GCS project to confirm its reliability and practical application.

1.3. Research Methodology

Two modeling approaches are adopted to achieve the objectives of this study, which are analytical and numerical modeling. A brief introduction on the adopted modeling approaches is highlighted in this section:

1.3.1. Analytical Modeling

Analytical modeling is a commonly used approach for solving complex physical problems using mathematical techniques. It provides explicit solutions of physical problems approximated through postulating simplifying assumptions about reservoir rock and fluid properties. Analytical modeling is relatively fast and cheap as compared to numerical modeling which requires extensive spatial-temporal discretization of the governing flow equations for a more rigorous solution. Analytical modeling is extremely valuable because it enables the explicit relationship between the pressure behavior and the reservoir characteristics. Therefore, analytical modeling represents the basis of the pressure-based reservoir characterization which is main goal of this current study. In this work, analytical modeling is used to achieve the 1^{st}, 2^{nd}, and 5^{th} objectives. The governing flow equations

and the initial/boundary conditions are solved using commonly used mathematical methods (e.g., Laplace transformation and ODE solution techniques). Necessary assumptions are postulated to enable explicit mathematical solution of the governing equations without significantly affecting the accuracy of the results. The rationale behind the simplifying assumptions, their shortcomings, and the effects on the results are addressed. The solutions are manipulated afterwards to develop analytical graphical interpretation techniques to analyze rate and pressure data using PTA/RTA techniques.

1.3.2. Numerical Modeling

Numerical simulation is a commonly used reliable approach to rigorously solve complex physical problems without being constrained by the restrictive assumptions required in analytical modeling. Numerical simulation solves for the primary unknown (e.g., pressure and saturation) by finding a numerical approximation of the governing flow equations and initial and boundary conditions in space and time. Numerical simulators use discretization approaches (e.g., finite-difference and finite element methods) to transform the governing flow equations, initial and boundary conditions of the problem into algebraic equations. The algebraic equations are then solved numerically using advanced numerical solvers. Specifically, the model domain is discretized into smaller cells that can be numerically solved to time steps for the desired unknown variables. The higher the degree of discretization, the more representative is the model and accurate are the simulation results. Fine discretization is very valuable in improving the results especially for non-linear problems (e.g., CO_2/brine displacement). However, this increases the computational cost of the simulation model that a compromise is always necessary. In this current research, numerical simulation is utilized to achieve the 3rd and 4th objectives. Also, we will use numerical simulation to validate the analytical models developed as a part of the 1st, 2nd, and 5th objectives of this work.

Accurate modeling of fluid properties is required for accurate simulation of the multi-phase flow displacement in CO_2/brine systems. These properties are rigorously predicted using sophisticated equation-of-states (EoSs) which evidently increase the computational overburden and execution times of simulations. The computational overburden can be significantly reduced by converting the compositional properties of CO_2 and brine into black-oil pressure/volume/temperature (PVT) data. In black-oil modeling, CO_2 dissolution into the aqueous phase and brine vaporization into the gaseous phase are accounted for using the solution gas/oil ratio and vaporized oil/gas ratio, respectively. In this work, a black-oil reservoir simulator (CMG-IMEX) is used to achieve the 3rd objective. It is, also, used to validate the analytical models of the 1st, 2nd, and 5th objectives. On the other hand, CMG-STARS is used to achieve the 4th objective of this work. CMG-STARS is a non-isothermal compositional reservoir simulator capable of modeling the complex wellbore physics associated with the non-isothermal injection of CO_2 which cannot be modeled using black-oil simulation. CMG-STARS does not use EoS to establish the phase equilibrium or to model mutual solubility. Instead, it uses gas-oil K-values to model phase change of CO_2, and oil-water K-values to model the mutual solubility. A flexible wellbore model is coupled with the reservoir model to simulate the phase change of CO_2, complex physics within the wellbore, and between the wellbore and the reservoir. Overall, CMG-IMEX and CMG-STARS numerically solves the governing flow equations for the spatio-temporal profiles of the desired variable unknowns (e.g., saturation, pressure, temperature, and phase flow rates) after specifying the initial and boundary conditions specified to the problem.

1.4. Overview of Chapters

In this section, an overview of the subsequent chapters of the dissertation is introduced.

Chapter 2 introduces a review of the current state of the research topics addressed in the subsequent chapters. This includes presenting a comprehensive literature review on PTA/RTA applications to assess and characterize the GCS saline reservoirs. It also includes a review on the studies that were devoted to investigate the effect of dynamic practices and physical processes on the CO_2 injectivity and subsequent storage capacity. Additionally, a literature review is presented on the analytical models that attempted to predict the evolution of the bottomhole pressure caused by CO_2 injection.

Chapter 3 introduces a novel analytical model to describe the bottomhole pressure behavior during a pause in CO_2 injection via a vertical well into single-layer infinite-acting aquifer. The developed model allows for predicting the pressure falloff down the injection well during a shut-in period following CO_2 injection at a constant rate. The analytical model is validated against synthetic data generated using a numerical reservoir simulator. A graphical interpretation technique is developed to analyze the pressure falloff behavior based on the analytical model. The potential application of the technique is also investigated through analyzing synthetic and real field data.

Chapter 4 introduces a novel graphical interpretation technique to assess the storage potential of a closed storage saline formation through interpreting the injection rate, pressure, and cumulative volume data. The technique is extended to estimate the ultimate storage capacity of the formation based on material balance methods. The graphical interpretation technique is validated against synthetic data as well as real field data obtained from a demonstration-scale GCS project.

Chapter 5 shows the effects of adopting different well operation conditions on the CO_2 injectivity and subsequent storage capacity. The study articulates the most economically and technically appealing injection scheme that should be adopted to maximize the volumetric and economic value of a given fixed pore space. The chapter is concluded by a sensitivity analysis that addresses the impact of varying the injection rate, vertical permeability, outer boundary conditions, well penetration and formation dip angle on the storage capacity considering different injection schemes.

Chapter 6 investigates the interplay and net effect of the physical processes controlling the CO_2 distribution along the injection interval of a thick saline reservoir. This includes investigating the effect of movement of CO_2/brine interface within the wellbore, individual layer flow capacities, gravity override, and pressure difference between the wellbore the aquifer. Implications of brine backflow into the wellbore on wellbore refilling with brine, and consequently, rate distribution are addressed. In addition, a sensitivity analysis to investigate the impact of varying the injection rate on the flow rate distribution is performed. The effects of using a decoupled model, wellbore shut-ins and associated salt dry-out, and presence of permeable formations overlying/underlying the target zone are also addressed.

Chapter 7 introduces a novel analytical solution to predict the bottomhole pressure response during CO_2 injection in infinite-acting deep saline formations. While accounting for strong gravity forces, the solution is developed assuming vertical equilibrium of pressure with a sharp interface between

CO_2 and brine. The pressure solution is validated against synthetic data generated using numerical simulation. The robustness of the pressure solution is substantiated through validation against real field bottomhole pressure data obtained from a GCS pilot project.

Chapter 8 presents the conclusions of the research introduced throughout the dissertation, followed by recommendations for future work.

Chapter 2. Literature Review

2.1. Application of PTA to Characterize CO_2 Plume and Dry-Out Zone in Deep Saline Aquifers

With CO_2 injection in brine-saturated formations, a saturation profile is formed in the reservoir soon after the start of injection due to the discrepancies between the properties of the dry CO_2 and the in-situ brine. Neglecting the capillary and gravity forces, the system can be approximated by three zones of saturation separated by two radial discontinuities extending the Buckley and Leverett (1942) displacement theory (Burton et al., 2008; Noh et al., 2007; Zeidouni et al., 2009). The injected CO_2 evaporates/displaces the brine around the wellbore, forming a zone referred to as the CO_2 dry-out zone where CO_2 occupies approximately 100 % of the pore space. The dry-out zone is surrounded by a two-phase zone where CO_2 and brine flow in equilibrium, and it extends to the boundaries of CO_2 plume. The plume is constrained by a third zone which is the in-situ single-phase brine zone.

Effective management of commercial-scale GCS projects necessitates accurate estimation of the spatial-temporal evolution of CO_2 plume. The undesired CO_2 exposure near potential leakage pathways (e.g. abandoned wells, faults, etc.) should be detected and managed by monitoring the CO_2 plume evolution. Time-lapse seismic surveys have been utilized to provide information about CO_2 distribution especially in locations where no monitoring wells exist. 3-D and 4-D time-lapse seismic surveys are widely used to track the CO_2 plume size (Alfi et al., 2015; Arts et al., 2004; Arts et al., 2003; Chadwick et al., 2006a; Chadwick et al., 2006b; Chadwick et al., 2010; Chadwick et al., 2005; Chadwick and Noy, 2010; Chadwick et al., 2009; Chadwick and Noy, 2015). On the other hand, several studies have been devoted to determine the extent of the plume using PTA theory (Hu et al., 2015; Mishra et al., 2013; Tran and Zeidouni, 2018; Tran and Zeidouni, 2017). Pressure arrival time, in response to pulse rate perturbations at an active well, has been investigated to predict the CO_2 plume evolution. Tran and Zeidouni (2017) proposed a graphical interpretation technique that uses pressure arrival times to estimate the average CO_2 saturation between well pairs within the injection domain. The technique is based on plotting the coefficient of mixed-phase diffusivity versus the CO_2 saturation. Hu et al. (2015) reconstructed the CO_2 distribution in a vertical plane between a closely spaced vertical well pair using pressure arrival times received at multiple points in the observation well. CO_2 saturation distribution can be reconstructed by inverting the mixed-phase diffusivity coefficient based on single-phase proxy of the diffusivity coefficient. The time evolution of CO_2 plume is then tracked by comparing the diffusivity tomograms. Mishra et al. (2013) utilized pressure falloff response at a monitoring well to estimate the intrinsic permeability of the reservoir using the two-zone composite analytical model (Ambastha, 1989; Ramey, 1970). The authors demonstrated that a log-log derivative of falloff data at late time converges to a value that is proportional to single-phase brine mobility. The authors, also, emphasized that the CO_2 front can be tracked based on estimating the effective total compressibility through history matching of injection-falloff responses. Instead of using well pairs, Tran and Zeidouni (2018) proposed a method to determine CO_2 plume extent using a single well located outside the plume. The method is based on monitoring the pressure behavior at that well in response to injection/production at a constant rate for short period. The plume boundary is characterized by a deviation in the pressure derivative diagnostic plot. The deviation is due to the significant discrepancy between CO_2 and brine properties. Shchipanov et al. (2019) studied the

application of PTA to monitor the reservoir flow barriers (e.g., faults) through utilizing real-time pressure data. The authors employed time-lapse analysis of sequential falloff responses to track the growth of CO_2 plume.

Estimation of the radial extent of the dry-out zone, and the fluid mobilities in the dry-out zone and the two-phase zone is required to assess the injectivity of CO_2. These unknowns significantly impact the injectivity (Burton et al., 2008; Pruess and Müller, 2009; Zeidouni et al., 2009). As we mentioned, CO_2 occupies approximately 100 % of the pore space within the dry-out zone. With CO_2 injection, the injectivity increases due to expanding the low viscosity and high mobility dry-out zone (Ehlig-Economides et al., 2010). Nevertheless, evaporation of brine causes salt to precipitate over time which negatively affects the porosity and permeability in the vicinity of the wellbore, and hence, the mobility and injectivity. Zeidouni et al. (2009) presented an analytical model to estimate the amount of salt dry-out around the wellbore as a function of time and space. The model is extended to evaluate the effect of salt dry-out on the permeability using a time-dependent skin that is a function of the radial extent of dry-out zone. Experiments conducted by Zuluaga (2005) suggest that the absolute permeability reduction caused by salt precipitation has typical values of 15 to 30 %. Also, CO_2 injectivity is dependent on the fluid mobility in the two-phase zone which is a function of relative permeability (Burton et al., 2008). Using a practical range of relative permeability data, Mathias et al. (2013) performed a sensitivity study on the effect of the relative permeability on injectivity. The authors concluded that injectivity can change by +/- 57 % for open aquifers, and the change is not significant for closed aquifers where the effect of system compressibility is dominant. Burton et al. (2008) showed that uncertainty in the relative permeability information can alter CO_2 injectivity in open aquifers by four folds for the range of data studied therein. Application of PTA theory to assess CO_2 injectivity is not new. Ehlig-Economides et al. (2010) presented a simulation study to address the significance of successive pressure falloff testing in estimating the fluid mobilities, and in monitoring the advancement of the dry-out zone. The authors concluded that regular planning of falloff tests for commercial scale GCS projects can provide good estimations of fluid mobilities. In their study, a three-region composite reservoir model with constant pressure outer boundary was used to infer the mobility by analyzing the simulated falloff data. In a recent study, Mishra et al. (2021) extended the PTA theory to infer the injectivity or productivity index by analyzing the pressure, rate and cumulative data from a depleted pinnacle reef oil field complex. The authors demonstrated that a Cartesian plot of the rate-normalized pressure change versus the material balance time should exhibit a straight line behavior during the boundary-dominated flow period. The *y*-intercept of the straight line is equal to the inverse of the injectivity/productivity index. The shortcoming of the aforementioned PTA techniques to characterize the dry-out zone and the plume is attributed to their dependence on the composite reservoir models and/or assuming single-phase proxy of the two-phase diffusivity.

2.2. Application of PTA/RTA to Estimate the Ultimate Storage Capacity of CO_2 in Deep Saline Aquifers

Storage capacity of a formation is the fraction of the pore space available to host the injected CO_2. Reliable estimation of the ultimate storage capacity is necessary to assess the potential of a target formation, and the ability of a GCS project to store the anticipated large volumes of CO_2. Storage capacity estimation is straightforward for depleted oil and gas reservoirs given their production

history and recoverable reserves. Nevertheless, it is complicated for deep saline aquifers due to the complexities related to data acquisition and trapping mechanisms that act at different rates and time scales. Bachu et al. (2007) stated that reliable estimates of storage capacity in saline aquifers are practical only over local scales given the required high resolution input data which may not be available over global scale. Kopp et al. (2009) provided a review on the challenges associated with storage capacity estimation in saline formations. The challenges include the adopted injection strategies, lack of data relevant to the subsurface, and the trapping mechanisms that contribute differently to the total storage. Bradshaw et al. (2007) showed that unreliable, and sometimes contradictory, assessments of storage capacity arise because of the limitations in knowledge, data, and time. Several other works presented comprehensive reviews on the storage capacity estimation methods in deep saline aquifers, depleted oil and gas reservoirs, and unminable coal seams (Aminu et al., 2017; Bachu, 2015; Cantucci et al., 2016).

Reliable estimation of the storage capacity and storage efficiency can be obtained using numerical reservoir simulation tools. Based on numerous simulations that consider a wide range of geological conditions, NETL (2007) reported that storage efficiency in saline formations has typical values of 1.0-4.0 % of the formation bulk volume. However, simulation is complex and requires detailed geological models to accurately represent the subsurface which may not be available in practice due to lack of data. Therefore, parallel analytical modeling efforts were introduced to estimate the storage capacity of target saline aquifers (Bachu et al., 2007; Doughty et al., 2001; Ehlig-Economides and Economides, 2010). The models are based on refining the formation's theoretical capacity through introducing a multiplier/coefficient. The coefficient theoretically ranges from 0 to 1 based on the geologic conditions. Doughty et al. (2001) proposed that the effective capacity is given by multiplying the average porosity of the formation by a coefficient that honors multi-phase flow, formation geometry, and geological heterogeneity. Bachu et al. (2007) proposed that the effective storage volume is equal to the theoretical capacity times a storage coefficient. The theoretical capacity is the entire pore volume minus the irreducible liquid saturation. The storage coefficient, which ranges from 0 to 1, honors the effects of permeability heterogeneity, buoyancy, and sweep efficiency. For closed storage saline systems, the results of the parametric study of Ehlig-Economides and Economides (2010) showed that the total volume of CO_2 cannot exceed 1.0 % of the formation pore volume. For such systems, the pressure-limited storage capacity can be estimated using analytical models that predict the overpressure caused by CO_2 injection (Azizi and Cinar, 2013a, b; De Simone and Krevor, 2021; Mathias et al., 2011a; Mathias et al., 2011b). According to these models, the ultimate storage capacity corresponds to the maximum allowable injection pressure that can be reached over the injection period. Ganjdanesh and Hosseini (2018) developed a MATLAB simulation tool that employs the analytical models (Azizi and Cinar, 2013a, b; Hosseini et al., 2014; Mathias et al., 2011b) to estimate the storage capacity for open and closed saline aquifers. De Simone and Krevor (2021) developed an analytical model to estimate the dynamic storage capacity for a multi-well storage system. The model considers various scenarios of well numbers and interwell spacing. The authors implemented their model into a simulation tool that optimizes the injection site's design for the number of wells and interwell spacing. One limitation of the aforementioned analytical models is their tendency to generalize local inputs over global scales due to lack of data. This means that the heterogeneous nature of the geological conditions, injection schemes, and reservoir performance may not be honored. This would greatly impact the reliability of the storage capacity estimates. Fortunately, this practical variability is, evidently, reflected into the dynamic behavior of the injection pressure and rate data. PTA/RTA

theory can be applied to estimate the ultimate storage capacity through analyzing the available injection data, routinely recorded as a part of GCS's surveillance.

PTA/RTA techniques have been utilized to estimate the storage capacity of depleted oil and gas reservoirs using injection pressure and rate data analysis (Chen et al., 2015; Edwards et al., 2015; Shchipanov et al., 2019; Xiao et al., 2016). Neglecting capillarity and gravity forces, Chen et al. (2015) presented an analytical model to estimate the CO_2 storage capacity in depleted shale reservoirs. The model is based on PTA considering CO_2 is continuously injected at a constant rate. By utilizing PTA/RTA, Xiao et al. (2016) developed semi-analytical approaches to estimate the abandonment pressure and the storage capacity for CO_2 injection in depleted shale gas reservoirs. For continuous injection at a constant pressure, Edwards et al. (2015) presented a solution that evaluates CO_2 storage capacity in depleted shale gas reservoirs via history matching gas production data. They applied their model to estimate CO_2 storage capacity in Barnett shale. In the context of hydrocarbon recovery, PTA/RTA has been long used to estimate the initial hydrocarbon in place and the ultimate hydrocarbon recovery from bounded reservoir using production data analysis. Blasingame and Lee (1986) introduced a general solution that describes the behavior of bottomhole pressure for a well producing at variable rate in a bounded reservoir. The solution, which is based on the principle of superposition, accounts for the effect of rate and pressure changes when interpreting production data. For gently varying rates, a plot of the "rate-normalized pressure drop" versus the superposition time function, referred to as material balance time, would exhibit a straight line on a Cartesian scale. Drainage area and shape factor can be obtained from its slope and intercept respectively. The work was then extended to interpret and analyze production data exhibiting variable rate/pressure changes for gas wells (Blasingame and Lee, 1988). Using pressure drop-normalized rate and material balance time, Palacio and Blasingame (1993) showed that single-phase gas and oil wells, producing under the BDF conditions at any pressure and rate schedule, will act as if they were producing at constant terminal rate. Their work along with parallel developments by others (Agarwal et al., 1999; Fraim, 1987; Mattar and Anderson, 2005) extended the pressure drawdown analysis theory to that of production data analysis which is the basis of RTA theory used for production data analysis. Extension of the RTA technique, to estimate the pore volume and the ultimate storage capacity of storage saline aquifers, is addressed in this study. Our attempts in this work are analogous to the abovementioned achievements presented to estimate the initial hydrocarbon in place and the ultimate recovery through extending the PTA theory to RTA theory.

2.3. Dynamic Practices to Maximize the Injectivity and Ultimate Storage Capacity of CO_2 in Deep Saline Aquifers

Preferred target formations should offer not only adequate pore space, but also, reasonable injectivity to accommodate the anticipated large volumes of CO_2 at the desired high rates. Injectivity is measured by the injectivity index which has been defined as the ratio of the injection rate per unit difference between the bottomhole injection pressure and the average reservoir pressure. This definition is analogous to the productivity index definition that is widely used in hydrocarbon well production evaluation. Practically, the injectivity index can be estimated with reasonable degree of accuracy using well testing techniques, core and log measurements, and simple analytical models (Pooladi-Darvish et al., 2011). CO_2 injectivity in a saline formation is primarily controlled by the formation flow capacity (permeability × thickness). In general, the higher the flow capacity, the higher the injectivity. Additionally, the injectivity is affected by other factors including relative permeability,

phase mobilities, CO_2 dry-out zone/plume extents, degree of salt precipitation, as well as the stress dependency of permeability (Azizi and Cinar, 2013a; Mathias et al., 2013; Pooladi-Darvish et al., 2011). The injectivity increases with the expansion of the lower viscosity and the higher mobility CO_2 dry-out zone (Ehlig-Economides et al., 2010). However, salt precipitation causes reduction in the porosity and absolute permeability near the wellbore (Pruess and Müller, 2009; Zeidouni et al., 2009) which, in turn, inversely impacts the injectivity. Some studies have been devoted in the literature to investigate the effect of relative permeability on the injectivity (Burton et al., 2008; Mathias et al., 2013). Mathias et al. (2013) performed a sensitivity analysis of the effect of relative permeability on injectivity variations. The authors concluded that the injectivity change is dramatic for open and low permeability closed aquifers. On the other hand, the change is not significant for high permeability closed aquifers where the aquifer compressibility plays a more important role. Burton et al. (2008) found that the relative permeability can change the injectivity in open aquifers up to a factor of four for the practical ranges of relative permeability presented in their study.

In addition, the technical and economic feasibility of GCS projects require maximizing the amount of CO_2 injected per well per unit pore volume. The ultimate storage capacity of a potential storage formation is evidently a function of the static formation characteristics (e.g., formation porosity and thickness). However, it can be dramatically enhanced/deteriorated by the injectivity variations caused by the dynamic practices adopted during injection of CO_2. Several studies have been presented in the literature to investigate the dynamic practices that can be adopted to enhance the injectivity and subsequent storage capacity of saline formations. Ozah et al. (2005) demonstrated that injection of CO_2 through horizontal wells improves CO_2 injectivity as compared to vertical wells. This would allow for more volumes of CO_2 to be stored especially into formations with high vertical-to-horizontal permeability ratios. For a fixed pore volume, Okwen et al. (2011a) studied the effect of well orientation on the storage capacity achieved before reaching the maximum allowable pressure. The authors concluded that horizontal wells provide higher storage capacity for isotropic conditions. However, for strongly anisotropic conditions, vertical wells would be more effective. Jikich et al. (2003) studied the impact of horizontal well lateral length, and depth in storage formation on CO_2 injection rate. The authors reported that the injection rate increases linearly with the well lateral length. However, it decreases when the injector is not placed at the middle depth of the storage formation. Moreover, well stimulation can significantly improve CO_2 injectivity and, as a result, the storage capacity especially for low permeability aquifers. Ghaderi et al. (2009) studied the effect of hydraulic fracturing on the storage capacity of an aquifer with 15 % porosity and 1500 mD permeability. The results showed that – using a vertically fractured well and a horizontal well with four staggered hydraulic fractures in two separate cases - the capacity is improved in the range of 10 % to 35 %. Their study was then extended by Huerta et al. (2020) for horizontal wells with a series of hydraulically-induced fractures in low permeability aquifers. The authors showed that injection via multi-fractured horizontal wells improve both the injectivity and storage capacity – of a fixed pore volume - as compared to the non-fractured horizontal and vertical wells. For multi-well systems, Pooladi-Darvish et al. (2011) studied the effect of well placement, number of wells, and stimulation in individual wells on the injectivity. The authors proposed an analytical relation representing multi-well system by a single well equivalent skin. The relation is helpful in assessing different alternatives of well placement, number of wells, and individual well stimulation on CO_2 injectivity and subsequent storage capacity.

Despite the abovementioned attempts, the effect of the well operating conditions on the injectivity and the storage capacity of saline formations have not been addressed in the literature. Therefore,

investigating the effect of well operating conditions on injectivity/ultimate capacity for CO_2/brine systems is required, and it is addressed in this current research. Our investigations are analogous to those attempts devoted to optimize the productivity and subsequent economics of oil and gas wells. In the context of hydrocarbon production, numerical simulations have been used to investigate the effect of well operating conditions on the productivity and the economics of the primary hydrocarbon recovery. Connaughton and Crawford (1975) studied the effect of production rate on the ultimate recovery from solution gas drive oil reservoir. The authors found that the oil recovery is greater for the highest production rate case, and the recovery to a 100-psi abandonment pressure ranged from 17.6 % for the lowest rate case to 22.8 % for the highest rate case. At low rates, the liberated gas segregates at the top of the reservoir and is produced rapidly, which as a result, depletes the reservoir energy and decreases oil recovery. Raza et al. (2019) presented a simulation study to evaluate the dependency of hydrocarbon recovery on production rate for gas and oil reservoirs of different drive mechanisms. The authors reported that oil recovery decreases with the increase of production rate for most drive mechanisms. The decrease is significant for the weak water drive oil reservoir, while a slight decrease is observed for the solution-gas drive reservoir. The authors attributed this slight decrease to the fact that higher rates cause the reservoir pressure to drop below the bubble point faster allowing for the more mobile gas to be liberated and produced. On the other hand, for gas reservoirs, the recovery generally increases with increasing the production rate. The increase is dramatic for strong water drive reservoir.

2.4. Coupled Wellbore-Reservoir Modeling to Evaluate CO_2 Flow Rate Distribution and Subsequent Injectivity and Storage Capacity in Deep Saline Aquifers

The flow rate distribution along the injection interval of a storage formation would enhance/deteriorate the sweep efficiency, injectivity, and ultimate storage capacity of the formation. Uniform/cylindrical displacement of the injected CO_2 is preferable for efficient storage, especially at the early times of injection. Uniform displacement not only improves the sweep efficiency, but also, allows for more volumes of the aquifer brine to come in contact with the injected CO_2 which enhances CO_2 trapping by dissolution. Nevertheless, the flow of CO_2 from the wellbore into the aquifer is generally biased towards the top layers of the aquifer that the bottom perforations could be underutilized. For CO_2 injection through a fully-penetrating vertical well, a number of physical processes and reservoir parameters control/affect CO_2 flux distribution between the layers of the storage formation. This includes: (1) movement of CO_2/brine interface within the wellbore, (2) buoyancy/gravity override, (3) difference in the hydrostatic pressure gradient between the CO_2-filled wellbore and the brine-saturated aquifer, (4) individual layer flow capacities, (5) temporal change in the effective/average mobility of fluids within the layers, and (6) backflow of brine into the wellbore. An overview of these parameters is detailed in the following paragraphs.

Modeling of CO_2 injection in saline aquifers often assumes the wellbore to be initially filled with CO_2 to achieve better numerical convergence. However, in reality, the wellbore is initially filled with brine, and CO_2 needs to fully/partially displace the brine out of the wellbore to start flowing into the formation. This means that CO_2 will not start flowing through a certain perforation unless the CO_2/brine interface within the wellbore is moved below that perforation level. The timing of brine displacement can range from few minutes to very long time such that CO_2 may not reach the bottom of the injection interval over the entire injection period of the project (Ennis-King et al., 2018). Ennis-King et al. (2018) showed that for CO_2 to reach the bottom of the injection interval, the injection rate should be higher than a threshold value. If this rate is not achieved, one (or more)

of the bottom perforations could be underutilized which negatively affects the injectivity as well as the storage capacity.

Difference in the hydrostatic pressure gradient between the wellbore and the aquifer contributes to the uneven distribution of CO_2 along the injection interval (Kumar and Bryant, 2009). This is because CO_2 would fully/partially occupy the wellbore shortly after the start of injection while the brine resides in the aquifer. Due to the density difference between CO_2 and brine, the hydrostatic pressure gradient within the wellbore should be lower than that deep into the aquifer. According to Darcy's law, CO_2 flow from the wellbore into the aquifer is directly proportional to the pressure difference between the wellbore and the aquifer. Due to the discrepancy in the hydrostatic pressure gradients, this pressure difference should be higher at the top layers of the aquifer as compared to the bottom ones. Therefore, a higher fraction of the injected CO_2 is expected to flow into the top layers as compared to the bottom ones.

The uneven distribution of CO_2 has been also related to the gravity override driven by the density difference between CO_2 and brine (Arts et al., 2003; Okwen et al., 2011b; Torp and Dale, 2003), and more generally, to the relative dominance of the gravity and viscous forces (Kopp et al., 2009). Strong viscous forces favor a more uniform/cylindrical displacement while strong gravity forces promote CO_2 flow biasness towards the top layers of the aquifer. The relative importance between the gravity and viscous forces is measured by the dimensionless gravity number given by (Kopp et al., 2009):

$$\Gamma = \frac{2\pi\left(\rho_a - \rho_g\right) gkH^2}{\mu_g q}$$

where ρ_a and ρ_g are the densities of the aqueous and gaseous phases respectively, g is the constant of gravitational acceleration, k is the intrinsic permeability, H is the aquifer thickness, μ_g is the gaseous phase viscosity, and q is the CO_2 injection rate. Gravity forces should not be effective when $\Gamma < 0.5$ (Nordbotten et al., 2005b; Okwen et al., 2010). Note that gravity number is a strong function of aquifer thickness (proportional to H^2), indicating the importance of gravity override in thick aquifers.

The effect of absolute permeability heterogeneity on the evolution of CO_2 plume was investigated by several studies (Gershenzon et al., 2017a; Gershenzon et al., 2017b; Gershenzon et al., 2014; Han et al., 2010; Singh and Bromhal, 2019; Wen and Benson, 2019). Wen and Benson (2019) conducted systematic simulations to study the plume migration in infinite-acting layered reservoirs with a wide range of permeability contrast. The authors demonstrated that higher contrasts in permeability reduce plume footprint, and improve dissolution rates. For open aquifers, Singh and Bromhal (2019) concluded that the areal extent of the plume is controlled by heterogeneities along the vertical direction. They showed that the presence of thin streaks of low permeability reduces the area of the plume. Through a series of simulations, Han et al. (2010) showed that lower vertical-to-horizontal permeability ratios suppresses the buoyancy-driven CO_2 migration and maximizes residual trapping. Through a series of simulations conducted on highly heterogeneous fluvial-type reservoirs, the works of Gershenzon and co-authors showed that contrasts in permeability between formation rocks improves capillary and residual trapping of CO_2.

CO_2 flux distribution among layers can change in response to the variations in the time-dependent average mobility within those layers. The average mobility is a function of the radial extents of the dry-out and two-phase zones. With continuous CO_2 injection, the dry-out and two-phase zones extend over time, improving the average mobility as well as the injectivity (Burton et al., 2009). Therefore, the CO_2 flux within the layers that take higher cumulative volume of CO_2 (e.g. top layers) would be further enhanced over time. This is because of the improved average mobility as compared to the layers that take less volumes of CO_2 (e.g. bottom layers). This simply means that layers that admit more CO_2 become capable of admitting more CO_2 because of the enhanced mobility. In addition, when large proportion of the injected CO_2 is taken by the top layers of the aquifer due to one (or more) of the abovementioned parameters, one (or more) of the bottom perforations may no longer contribute to injection, and brine backflow to the wellbore can be initiated. In this situation, the advancing CO_2 at the top of the formation will push the aquifer's in-situ brine back into the wellbore. This causes the CO_2/brine interface to rise within the wellbore which can impact the injection performance. The effect of backflow on salt precipitation within the dry-out zone has been identified by several publications (Giorgis et al., 2007; Miri and Hellevang, 2016; Norouzi et al., 2021; Ott et al., 2011; Pruess and Müller, 2009), but its effect on CO_2 flux distribution has not been investigated. The parameters/processes controlling the CO_2 distribution over the injection interval have been described above. Some studies have addressed the effect of these parameters on CO_2/brine displacement, plume evolution, and storage capacity. However, the interplay between them and their net effect on the CO_2 flux distribution over the injection interval remains a gap to be addressed in this work.

2.5. Evolution of Overpressure in High-Gravity Storage Saline Aquifers

As mentioned before, potential storage formations should provide reasonable injectivity to store CO_2 at the desired rates (Bachu et al., 2007). Injectivity is primarily controlled by the flow capacity of the formation (Burton et al., 2008). However, it can be constrained by the bottomhole pressure that accompany CO_2 injection (EPA, 2008a; IEAGHG, 2010). Additionally, gravity override affects the bottomhole pressure behavior, and thus, the injectivity and storage capacity. Therefore, accurate estimation of the overpressure, while accounting for gravity effects, is needed to optimize the potential of a given pore space.

Several analytical models have been presented in the literature to predict the bottomhole pressure buildup during constant-rate injection of CO_2 (Azizi and Cinar, 2013a; Burton et al., 2008; Celia et al., 2011; Ehlig-Economides and Economides, 2010; Hosseini et al., 2014; Mathias et al., 2011c; Mathias et al., 2009). For steady-state flow conditions, Burton et al. (2008) presented an analytical model to estimate the bottomhole pressure buildup using Darcy's law. According to the solution, the pressure variation at the wellbore is given by the combined pressure buildups across the three zones of the reservoir. For different outer boundary systems, Azizi and Cinar (2013a) introduced similar analytical models to estimate the bottomhole pressure variations during CO_2 injection in single-layer reservoirs. After applying the boundary conditions, the solutions are obtained through simultaneously solving linearized pressure diffusivity equations representing the pressure behavior within different zones. Using the principle of superposition, Hosseini et al. (2014) extended Azizi and Cinar (2013a)'s solution to multi-well injection into single-layer reservoirs. For closed systems, Ehlig-Economides and Economides (2010) derived an analytical model to predict the overpressure during the boundary-dominated flow period. To derive their solution, the authors

extended Burton et al. (2008)'s solution considering the relationship between the steady-state and pseudo-steady state flow equations. Moreover, Mathias et al. (2009) developed an analytical solution to determine the bottomhole pressure response during CO_2 injection into an infinite-acting CO_2/brine system. The solution neglects the capillary and gravity forces, and it considers vertical equilibrium of the pressure distribution with a sharp interface separating CO_2 and brine. The solution was derived based on Nordbotten and Celia (2006)'s similarity solution that has been developed to determine the evolution of the interface. The solution was then extended to predict the bottomhole pressure buildup during CO_2 injection in closed boundary systems (Mathias et al., 2011c).

In reality, CO_2/brine displacement is not only governed by viscous forces caused by injection, but also by gravity forces. Few works have been devoted to develop analytical and/or semi-analytical solutions to determine the overpressure while accounting for gravity forces (Celia et al., 2011; Nordbotten and Celia, 2006; Nordbotten et al., 2009). For strong gravity forces and assuming vertical equilibrium of pressure, Nordbotten and Celia (2006) developed coupled semi-analytical solutions to determine the evolution of CO_2/brine interface and pressure field within the injection domain. The solutions are represented by non-linear ordinary differential equations (ODEs) which can be solved numerically. In 2009, Nordbotten et al. (2009) provided a semi-analytical solution for the Nordbotten and Celia (2006)'s ODE of the pressure field considering weak gravity forces. Then, Celia et al. (2011) provided a closed-form analytical form of Nordbotten et al. (2009)'s semi-analytical solution. One limitation of the aforementioned models is either the necessity for numerical solution or the need to assume weak/negligible gravity to enable analytical solution. A summary of the literature analytical models and the proposed solution herein is displayed in Table 2.1 below. The table compares the models according to their pros and cons based on the postulated assumptions.

Table 2.1. Comparison between the available analytical/semi-analytical models

Model	Gravity effect	Capillary effect	Pressure equilibration	Mutual solubility	Modeling approach
Nordbotten and Celia (2006)	Yes	No	Yes	Yes	Semi-analytical
Nordbotten et al. (2009)	Yes	No	Yes	No	Semi-analytical
Mathias et al. (2009)	No	No	Yes	No	Analytical
Celia et al. (2011)	Weak	No	Yes	No	Analytical
Azizi and Cinar (2013a)	No	No	No	Yes	Analytical
This study	Yes	No	Yes	No	Analytical

Chapter 3. Pressure Falloff Testing to Characterize CO_2 Plume and Dry-Out Zone during CO_2 Injection in Deep Saline Formations

In this chapter, the application of PTA to infer the fluid mobilities and the radial extents of the dry-out zone and CO_2 plume is presented. First, a forward three-zone analytical model is developed to describe the pressure behavior during a pause during CO_2 injection into single-layer infinite-acting aquifer. A graphical interpretation technique is then presented to analyze the falloff pressure data through adopting the analytical model. The pressure solution at the wellbore is next validated against synthetic data generated using a numerical reservoir simulator. The potential application of the technique is investigated through analyzing synthetic and real field data. The limitations of the interpretation technique are finally addressed through investigating the effects of buoyancy, formation outer boundaries, dip angle, horizontal permeability anisotropy, and variable injection rate during the period that precedes the test.

3.1. Problem Description and Analytical Model Derivation

Consider the physical model shown in Fig. 3.1. CO_2 is injected at a constant rate through a fully penetrating vertical well into a homogeneous and isotropic reservoir with uniform porosity and thickness. While neglecting the gravitational and capillary forces, the system can be approximated by three zones of different saturations and pressures following the modified Buckley and Leverett (1942) theory. In the vicinity of the wellbore, the dry-out zone exists where in-situ brine has been vaporized/displaced by the dry CO_2. The dry-out zone is surrounded by the two-phase zone where CO_2 and brine flow simultaneously in equilibrium. The CO_2 plume is bounded by the single-phase brine zone. The three zones are separated by two radial discontinuities with an infinite-acting outer boundary. The pressure profile in each zone is related to the fluid mobility within the zone. The diffusivity equation in terms of pressure can be used to describe the behavior within each zone. The behavior of pressure during shut-in can be obtained by analytically solving the governing equations upon linearization. The linearization is achieved by adopting the following assumptions: (1) the two-phase zone has a constant saturation and it is given by the arithmetic average of the gas saturations at the interfaces, and (2) the fluids viscosities and compressibilities are constant.

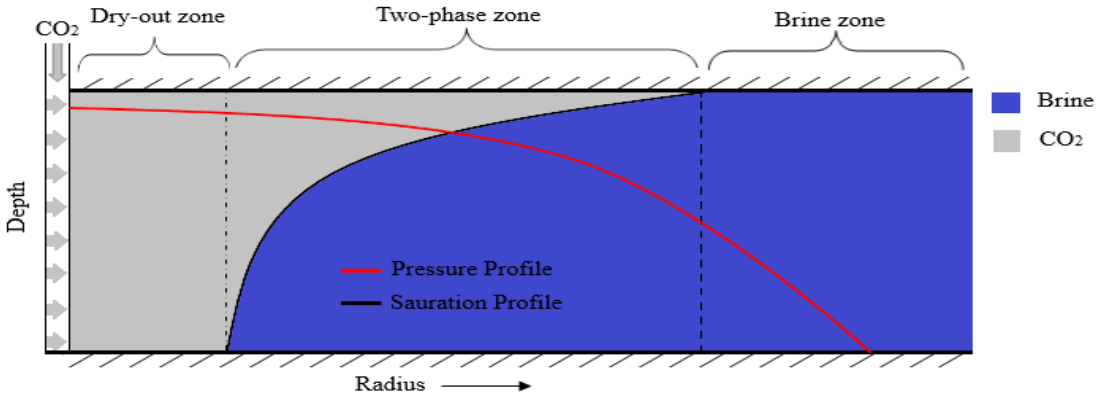

Figure 3.1. A schematic illustration of a typical CO_2/brine system showing saturation profile near the wellbore

In dimensionless form and for a sink well injection, the governing equations for the dry-out, two-phase, and brine zones are, respectively, given by Eqs. 1 through 3:

$$\frac{1}{r_D}\frac{\partial}{\partial r_D}\left(r_D\frac{\partial p_{D1}}{\partial r_D}\right)=\frac{\partial p_{D1}}{\partial \Delta t_D} \qquad 0\le r_D\le r_{Ddry} \tag{3.1}$$

$$\frac{1}{r_D}\frac{\partial}{\partial r_D}\left(r_D\frac{\partial p_{D2}}{\partial r_D}\right)=\frac{1}{F_{\lambda g}\eta_{D2}}\frac{\partial p_{D2}}{\partial \Delta t_D} \qquad r_{Ddry}\le r_D\le r_{DBL} \tag{3.2}$$

$$\frac{1}{r_D}\frac{\partial}{\partial r_D}\left(r_D\frac{\partial p_{D3}}{\partial r_D}\right)=\frac{1}{\eta_{D3}}\frac{\partial p_{D3}}{\partial \Delta t_D} \qquad r_D\ge r_{DBL} \tag{3.3}$$

where the dimensionless radius, shut-in time and pressure, respectively, are given by:

$$r_D=\frac{r}{r_w} \tag{3.4}$$

$$\Delta t_D=\frac{k\overline{k_{rg}}\Delta t}{\phi\mu_g c_{tg} r_w^2} \tag{3.5}$$

$$p_D=\frac{2\pi hk\overline{k_{rg}}\left(p-p_i\right)}{q\mu_g} \tag{3.6}$$

In Eqs. 3.1 through 3.6, r is the radius from the well, r_w is the wellbore radius, Δt is the shut-in time, k is the absolute permeability, $\overline{k_{rg}}$ is the gas relative permeability in the dry-out zone, ϕ is the formation porosity, μ_g is the gas viscosity, c_{tg} is the total compressibility of the dry-out zone, h is the formation thickness, q is the total injection rate at the reservoir conditions, p_i is the initial reservoir pressure, r_{Ddry} and r_{DBL} are the dimensionless radii of the dry-out and two-phase zones respectively (*BL* stands for Buckley-Leverett solution which gives the front velocity in immiscible displacement (Azizi and Cinar, 2013a). η_{D2}, η_{D3} and $F_{\lambda g}$ are the diffusivity and the mobility ratios given by:

$$\eta_{D2}=\frac{c_{tg}}{c_t} \tag{3.7}$$

$$\eta_{D3}=\frac{c_{tg}}{c_{tw}}\frac{\overline{\lambda_w}}{\overline{\lambda_g}} \tag{3.8}$$

$$F_{\lambda g}=\frac{\lambda_{ave}}{\overline{\lambda_g}} \tag{3.9}$$

where: $\overline{\lambda_g}=\dfrac{k\overline{k_{rg}}}{\mu_g}$, $\overline{\lambda_w}=\dfrac{k}{\mu_w}$, $c_{tg}=c_g+c_r$, $c_{tw}=c_w+c_r$

$c_t=c_gS_{g,ave}+c_w\left(1-S_{g,ave}\right)+c_r$ and $S_{g,ave}=0.5\left(S_{gdry}+S_{gBL}\right)$

The average/effective mobility in the two-phase zone is given by the formula derived by Oruganti and Mishra (2013) as follows:

$$\lambda_{ave}=k\times\left\{\frac{1}{\lambda_{2\phi,dry+}}+\left[\frac{1}{\lambda_{2\phi,BL-}}-\frac{1}{\lambda_{2\phi,dry+}}\right]\times\left[\frac{1}{\ln\left(r_{BL}/r_{dry}\right)}-\frac{1}{\left(r_{BL}/r_{dry}\right)-1}\right]\right\}^{-1} \tag{3.10}$$

In Eqs. 3.7 through 3.10, c_t and c_{tw} are the total compressibilities of the two-phase and the single-phase brine zones respectively, $\overline{\lambda_w}$ is the brine mobility, $\overline{\lambda_g}$ is the mobility in the dry zone, λ_{ave} and $S_{g,ave}$ are the total mobility and the average gas saturation in the two-phase zone, S_{gdry} and S_{gBL} are gaseous phase saturations at r_{dry} and r_{BL} respectively, c_w, c_r and c_g are the compressibilities of brine, rock, and gas, respectively, $\lambda_{2\varphi,dry+}$ is the mobility in the two-phase zone immediately downstream r_{dry}, and $\lambda_{2\varphi,BL-}$ is the mobility in the two-phase zone immediately upstream r_{BL}.

Eqs. 3.1 through 3.3 are subject to the following initial and boundary conditions:

$$p_{D1} = g_1(r_D), \quad \Delta t_D = 0 \tag{3.11}$$

$$p_{D2} = g_2(r_D), \quad \Delta t_D = 0 \tag{3.12}$$

$$p_{D3} = g_3(r_D), \quad \Delta t_D = 0 \tag{3.13}$$

$$r_D \frac{\partial p_{D1}}{\partial r_D} = 0, \quad r_D \to 0 \tag{3.14}$$

$$p_{D1} = p_{D2}, \quad r_D = r_{Ddry} \tag{3.15}$$

$$\frac{\partial p_{D1}}{\partial r_D} = F_{\lambda g} \frac{\partial p_{D2}}{\partial r_D}, \quad r_D = r_{Ddry} \tag{3.16}$$

$$p_{D2} = p_{D3}, \quad r_D = r_{DBL} \tag{3.17}$$

$$\frac{\partial p_{D3}}{\partial r_D} = F_{\lambda w} \frac{\partial p_{D2}}{\partial r_D}, \quad r_D = r_{DBL} \tag{3.18}$$

$$p_{D3} = 0, \quad r_D \to \infty \tag{3.19}$$

where: $$F_{\lambda w} = \frac{\lambda_g + \lambda_w\big|_{Sg,ave}}{\overline{\lambda_w}} = \frac{\lambda_{ave}}{\overline{\lambda_w}}$$

The terms g_1, g_2, and g_3 are the pressure distributions in the three zones respectively at the time of shut-in. Eq. 3.14 represents a no-flow condition at the wellbore during the falloff period. Eqs 3.15 and 3.17 state that there is pressure continuity at the interfaces r_{Ddry} and r_{DBL}. Eqs 3.16 and 3.18 indicate that the flow is continuous at the interfaces, and Eq. 3.19 represents the infinite-acting nature of the system. Azizi and Cinar (2013a) derived exact solutions that describe the pressure distribution during injection in three-zone system of moving interfaces. The solutions - obtained using Laplace transformation - have the following dimensionless form:

$$\begin{aligned} g_1(r_D) = &-\frac{1}{2} Ei\left(-\frac{r_D^2}{4t_{iD}}\right) + \frac{1}{2} Ei\left(-\zeta_{Ddry}\right) - \frac{1}{2F_{\lambda g}} Ei\left(-\frac{\zeta_{Ddry}}{F_{\lambda g}\eta_{D2}}\right) \\ &+ \frac{1}{2F_{\lambda g}} Ei\left(-\frac{\zeta_{DBL}}{F_{\lambda g}\eta_{D2}}\right) - \frac{1}{2}\frac{\overline{\lambda_g}}{\overline{\lambda_w}} Ei\left(-\frac{\zeta_{DBL}}{\eta_{D3}}\right), \quad t_D \geq \frac{r_D^2}{4\zeta_{Ddry}} \end{aligned} \tag{3.20}$$

$$g_2(r_D) = -\frac{1}{2F_{\lambda g}} Ei\left(-\frac{r_D^2}{4F_{\lambda g}\eta_{D2}t_{iD}}\right) + \frac{1}{2F_{\lambda g}} Ei\left(-\frac{\zeta_{DBL}}{F_{\lambda g}\eta_{D2}}\right) - \frac{1}{2}\frac{\overline{\lambda_g}}{\overline{\lambda_w}} Ei\left(-\frac{\zeta_{DBL}}{\eta_{D3}}\right), \quad \frac{r_D^2}{4\zeta_{DBL}} \le t_D \le \frac{r_D^2}{4\zeta_{Ddry}} \tag{3.21}$$

$$g_3(r_D) = -\frac{1}{2}\frac{\overline{\lambda_g}}{\overline{\lambda_w}} Ei\left(-\frac{r_D^2}{4\eta_{D3}t_{iD}}\right), \quad t_D \le \frac{r_D^2}{4\zeta_{DBL}} \tag{3.22}$$

where: $\zeta_{Ddry} = \dfrac{r_{Ddry}^2}{4t_{iD}}$ and $\zeta_{DBL} = \dfrac{r_{DBL}^2}{4t_{iD}}$

In Eqs. 3.20 through 3.22, t_{iD} is dimensionless injection time, ζ_{Ddry} and ζ_{DBL} are dimensionless velocities of the interfaces r_{Ddry} and r_{DBL}, respectively, and *Ei* is the exponential integral function. The exact falloff solutions are derived by applying Laplace transformation technique. The detailed derivation is given Appendix A. The dimensionless pressure distribution during the falloff period in the three zones is given by Eqs. 3.23 through 3.25 respectively as follows.

$$p_{D1} = \frac{1}{2\Delta t_D}\int_0^{rDdry} x g_1(x)\exp\left(-\frac{r_D^2+x^2}{4\Delta t_D}\right) I_o\left(\frac{x r_D}{2\Delta t_D}\right) dx + \mathcal{L}^{-1}\left[AI_o\left(r_D\sqrt{z}\right)\right], \ 0 \le r_D \le r_{Ddry} \tag{3.23}$$

$$p_{D2} = \frac{1}{2F_{\lambda g}\eta_{D2}\Delta t_D}\int_{rDdry}^{rDBL} x g_2(x)\exp\left(-\frac{x^2+r_D{}^2}{4F_{\lambda g}\eta_{D2}\Delta t_D}\right) I_o\left(\frac{x r_D}{2F_{\lambda g}\eta_{D2}\Delta t_D}\right) dx + \mathcal{L}^{-1}\left[CI_o\left(r_D\sqrt{\frac{z}{F_{\lambda g}\eta_{D2}}}\right)\right] + \mathcal{L}^{-1}\left[DK_o\left(r_D\sqrt{\frac{z}{F_{\lambda g}\eta_{D2}}}\right)\right], \ r_{Ddry} \le r_D \le r_{DBL} \tag{3.24}$$

$$p_{D3} = \frac{1}{2\eta_{D3}\Delta t_D}\int_{rDBL}^{\infty} x g_3(x)\exp\left(-\frac{r_D{}^2+x^2}{4\eta_{D3}\Delta t_D}\right) I_o\left(\frac{x r_D}{2\eta_{D3}\Delta t_D}\right) dx + \mathcal{L}^{-1}\left[FK_o\left(r_D\sqrt{\frac{z}{\eta_{D3}}}\right)\right], \ r_D \ge r_{DBL} \tag{3.25}$$

where *z* is the Laplace transform variable, *x* is an arbitrary integration variable, I_o, K_o are the modified Bessel functions of first and second kinds of zero order respectively, and the coefficients *A*, *C*, *D* and *F* are given in Appendix A. The solution for the falloff pressure response at the wellbore in dimensionless form is obtained by setting $r_D = 1$ in Eq. 3.23 as follows:

$$p_{wD}(\Delta t_D) = \frac{1}{2\Delta t_D}\int_0^{rDdry} x g_1(x)\exp\left(-\frac{x^2+1}{4\Delta t_D}\right) I_o\left(\frac{x}{2\Delta t_D}\right) dx + \mathcal{L}^{-1}\left[AI_o\left(\sqrt{z}\right)\right] \tag{3.26}$$

The analytical solutions given by Eqs. 3.23 through 3.26 can be inverted into real-time domain using a numerical inversion algorithm (Stehfest, 1970). Nevertheless, to implement the analytical solution in interpreting pressure falloff data, approximate expressions in real-time domain are required. Therefore, the solution of Eq. 3.26 is reduced to three asymptotic approximate solutions corresponding to three time periods: (1) the early-time solution for flow dominated by the dry-out zone, (2) the intermediate-time solution for flow dominated by the two-phase zone, and (3) the late-time asymptotic solution for flow dominated by the single-phase brine zone. The approximate solutions are explained as follows.

3.1.1. Early-time Approximation

At early stages of a falloff test, the pressure perturbation is within the limits of the dry-out zone where the radial flow is dominated by single-phase gaseous phase only. The second term in Eq. 3.26 can be neglected and the solution reduces to:

$$p_{wD}\left(\Delta t_D\right)=\frac{1}{2\Delta t_D}\int_0^{rDdry} x g_1\left(x\right)\exp\left(-\frac{x^2+1}{4\Delta t_D}\right)I_o\left(\frac{x}{2\Delta t_D}\right)dx \tag{3.27}$$

Substituting for g_1 and performing the integration of Eq. 3.27, the early-time solution is:

$$\begin{aligned} p_{wD}=&\frac{1}{2}Ei\left(-\frac{1}{4\Delta t_D}\right)-\frac{1}{2}Ei\left(-\frac{1}{4t_{iD}}\right)+\frac{1}{2}Ei\left(-\zeta_{Ddry}\right)-\frac{1}{2F_{\lambda g}}Ei\left(-\frac{\zeta_{Ddry}}{F_{\lambda g}\eta_{D2}}\right)\\ &+\frac{1}{2F_{\lambda g}}Ei\left(-\frac{\zeta_{DBL}}{F_{\lambda g}\eta_{D2}}\right)-\frac{1}{2}\frac{\overline{\lambda_g}}{\overline{\lambda_w}}Ei\left(-\frac{\zeta_{DBL}}{\eta_{D3}}\right)\end{aligned} \tag{3.28}$$

The argument of the first *Ei* function in Eq. 3.28 includes Δt_D in the denominator, while remaining arguments are function of t_{iD} in the denominator. Δt_D and t_{iD} are large making the arguments small (< 0.01) so that the *Ei* terms can be approximated by $Ei(-x) = \ln(x) + \gamma$ where $\gamma = 0.577215$ is the Euler's constant. Therefore, the dimensionless bottomhole pressure during shut-in is given by:

$$p_{wD}=-\frac{1}{2}\ln\left(\Delta t_D\right)+\frac{1}{2}\ln\left(t_{iD}\right)+\frac{1}{2}\ln\left(\zeta_{Ddry}\right)+\frac{1}{2F_{\lambda g}}\ln\left(\frac{\zeta_{DBL}}{\zeta_{Ddry}}\right)-\frac{1}{2}\frac{\overline{\lambda_g}}{\overline{\lambda_w}}\ln\left(\frac{\zeta_{DBL}}{\eta_{D3}}\right)+\frac{1}{2}\gamma\left(1-\frac{\overline{\lambda_g}}{\overline{\lambda_w}}\right) \tag{3.29}$$

In dimensional form, this early-time solution becomes:

$$p_{ws}=-\frac{q}{4\pi\overline{\lambda_g}h}\ln\left(\Delta t\right)+p_i+\frac{q}{2\pi\overline{\lambda_g}h}\left[\begin{aligned}&\ln\left(r_{dry}\right)+\frac{\overline{\lambda_g}}{\lambda_{ave}}\ln\left(\frac{r_{BL}}{r_{dry}}\right)-\frac{\overline{\lambda_g}}{\overline{\lambda_w}}\ln\left(r_{BL}\right)+\frac{1}{2}\ln\left(\frac{\phi c_{tg}}{4\overline{\lambda_g}}\right)\\&-\frac{1}{2}\frac{\overline{\lambda_g}}{\overline{\lambda_w}}\ln\left(\frac{\phi c_{tw}}{4\overline{\lambda_w}t_i}\right)+\frac{1}{2}\gamma\left(1-\frac{\overline{\lambda_g}}{\overline{\lambda_w}}\right)\end{aligned}\right] \tag{3.30}$$

If there is additional damage or stimulation, we can add the physical skin factor (s). Then, the bottomhole pressure is given by:

$$p_{ws} = -\frac{q}{4\pi\overline{\overline{\lambda_g}}h}\ln(\Delta t) + p_i + \frac{q}{2\pi\overline{\overline{\lambda_g}}h}\left[\begin{array}{l}\ln(r_{dry}) + \dfrac{\overline{\lambda_g}}{\lambda_{ave}}\ln\left(\dfrac{r_{BL}}{r_{dry}}\right) - \dfrac{\overline{\lambda_g}}{\overline{\overline{\lambda_w}}}\ln(r_{BL}) + \dfrac{1}{2}\ln\left(\dfrac{\phi c_{tg}}{4\overline{\overline{\lambda_g}}}\right) \\ -\dfrac{1}{2}\dfrac{\overline{\lambda_g}}{\overline{\overline{\lambda_w}}}\ln\left(\dfrac{\phi c_{tw}}{4\overline{\overline{\lambda_w}}t_i}\right) + \dfrac{1}{2}\gamma\left(1 - \dfrac{\overline{\lambda_g}}{\overline{\overline{\lambda_w}}}\right) + s\end{array}\right] \tag{3.31}$$

Eq. 31 implies that:

i. At early time, the bottomhole pressure during shut-in (p_{ws}) drops linearly as a function of the natural logarithm of the shut-in time (Δt).

ii. The mobility in the dry-out zone can be inferred from the slope of the straight line fitted through the data points corresponding to the dry-out zone.

iii. The second and the third terms in the right-hand side (RHS) of Eq. 3.31 represent the y-intercept of the straight fitted line. This intercept is a function of the radial extents of the dry-out zone and the plume.

In addition, Eq. 3.29 can be written in terms of the apparent skin factor (s_a):

$$p_{wD} = -\frac{1}{2}\ln(\Delta t_D) + \frac{1}{2}\ln(t_{iD}) + s_a \tag{3.32}$$

where:

$$s_a = \frac{1}{2}\ln(\zeta_{Ddry}) + \frac{1}{2F_{\lambda g}}\ln\left(\frac{\zeta_{DBL}}{\zeta_{Ddry}}\right) - \frac{1}{2}\frac{\overline{\lambda_g}}{\overline{\overline{\lambda_w}}}\ln\left(\frac{\zeta_{DBL}}{\eta_{D3}}\right) + \frac{1}{2}\gamma\left(1 - \frac{\overline{\lambda_g}}{\overline{\overline{\lambda_w}}}\right) + s \tag{3.33}$$

Substituting for ζ_{Ddry}, ζ_{DBL} and η_{D3} in Eq. 3.32, s_a can be expressed as follows:

$$s_a = \ln(r_{dry}) + \frac{\overline{\lambda_g}}{\lambda_{ave}}\ln\left(\frac{r_{BL}}{r_{dry}}\right) - \frac{\overline{\lambda_g}}{\overline{\overline{\lambda_w}}}\ln(r_{BL}) + \frac{1}{2}\ln\left(\frac{\phi c_{tg}}{4\overline{\overline{\lambda_g}}t_i}\right) - \frac{1}{2}\frac{\overline{\lambda_g}}{\overline{\overline{\lambda_w}}}\ln\left(\frac{\phi c_{tw}}{4\overline{\overline{\lambda_w}}t_i}\right) + \frac{1}{2}\gamma\left(1 - \frac{\overline{\lambda_g}}{\overline{\overline{\lambda_w}}}\right) + s \tag{3.34}$$

3.1.2. Intermediate-time Approximation

Once the pressure perturbation passes the dry-out zone and the flow becomes dominated by the two-phase zone, the bottomhole pressure response can be obtained by approximating the exact solution corresponding to this intermediate time. Comparing Eq. 3.28 to Eq. 3.20 and following the same procedure, the bottomhole pressure response in dimensionless form is given by:

$$p_{wD} = \frac{1}{2F_{\lambda g}} Ei\left(-\frac{1}{4F_{\lambda g}\eta_{D2}\Delta t_D}\right) - \frac{1}{2F_{\lambda g}} Ei\left(-\frac{1}{4F_{\lambda g}\eta_{D2} t_{iD}}\right) + \frac{1}{2F_{\lambda g}} Ei\left(-\frac{\zeta_{DBL}}{F_{\lambda g}\eta_{D2}}\right) - \frac{1}{2}\frac{\overline{\lambda_g}}{\overline{\overline{\lambda_w}}} Ei\left(-\frac{\zeta_{DBL}}{\eta_{D3}}\right) \quad (3.35)$$

For long times, Eq. 3.35 approximates to:

$$p_{wD} = -\frac{1}{2F_{\lambda g}} \ln\left(\Delta t_D\right) + \frac{1}{2F_{\lambda g}} \ln\left(t_{iD}\right) + \frac{1}{2F_{\lambda g}} \ln\left(\frac{\zeta_{DBL}}{F_{\lambda g}\eta_{D2}}\right) - \frac{1}{2}\frac{\overline{\lambda_g}}{\overline{\overline{\lambda_w}}} \ln\left(\frac{\zeta_{DBL}}{\eta_{D3}}\right) + \frac{1}{2}\gamma\left(\frac{1}{F_{\lambda g}} - \frac{\overline{\lambda_g}}{\overline{\overline{\lambda_w}}}\right) \quad (3.36)$$

In dimensional form and accounting for skin factor, the intermediate-time solution is given by the following equation:

$$p_{ws} = -\frac{q}{4\pi\lambda_{ave}h} \ln\left(\Delta t\right) + p_i + \frac{q}{2\pi\overline{\lambda_g}h}\left[\begin{array}{l} \frac{1}{2}\frac{\overline{\lambda_g}}{\lambda_{ave}} \ln\left(\frac{\phi c_t r_{BL}^2}{4\lambda_{ave}}\right) - \frac{1}{2}\frac{\overline{\lambda_g}}{\overline{\overline{\lambda_w}}} \ln\left(\frac{c_{tw}}{\overline{\overline{\lambda_w}}}\frac{\phi r_{BL}^2}{4t_i}\right) \\ + \frac{1}{2}\gamma\left(\frac{\overline{\lambda_g}}{\lambda_{ave}} - \frac{\overline{\lambda_g}}{\overline{\overline{\lambda_w}}}\right) + s \end{array}\right] \quad (3.37)$$

The following can be implied from Eq. 3.37:

i. p_{ws} declines linearly with $\ln(\Delta t)$.

ii. The average mobility in the two-phase zone can be inferred from the slope of the straight line fitted through the data points corresponding to the two-phase zone.

iii. The 2nd and the 3rd terms in the RHS of Eq. 3.37 represent the intercept of the fitted line which depends on the extent of the plume.

3.1.3. Late-time Approximation

Once the pressure perturbation passes the two-phase zone and the flow becomes dominated by the single-phase brine zone, the dimensionless pressure response at the wellbore can be determined using the following asymptotic solution (the approximation details are provided in Appendix B):

$$p_{wD} = \frac{1}{2}\frac{\overline{\lambda_g}}{\overline{\overline{\lambda_w}}} \ln\left(\frac{\Delta t_D + t_{iD}}{\Delta t_D}\right) \quad (3.38)$$

The late-time asymptotic solution is the same as the solution derived by Mishra et al. (2013) for pressure behavior at late-times. In dimensionless form, the late-time solution is given by:

$$p_{ws} = p_i + \frac{q}{4\pi\overline{\overline{\lambda_w}}h} \ln\left(\frac{\Delta t + t_i}{\Delta t}\right) \quad (3.39)$$

where the argument inside the natural log is the Horner time ratio (HTR) (Horner, 1951).

The following can be implied from Eq. 3.39:

i. Unlike the early-time and the intermediate time solution, p_{ws} is no longer a linear function of ln(Δt). Instead, it is a linear function of ln(HTR).

ii. If the single-phase brine zone is to be sensed by the falloff test, the mobility in the brine zone can be inferred from the slope of the straight line fitted through the data points corresponding to the zone.

iii. The intercept of the fitted straight line at HTR = 1 represents the initial reservoir pressure.

3.2. Description of the Falloff Interpretation Technique

A graphical interpretation technique of falloff pressure data is presented based on Eqs. 3.31, 3.37, and 3.39. The reservoir parameters including the mobilities of the fluids in the first two zones, the extents of the interfaces, and the apparent skin factor are obtained using the following procedure:

1. Based on Eq. 3.31, a semi-log plot of p_{ws} versus Δt, corresponding to the dry-out zone, should exhibit a straight-line behavior with slope m_1 and intercept b_1 given by:

$$m_1 = -\frac{q}{4\pi\overline{\lambda_g}h} \tag{3.40}$$

$$b_1 = p_i + \frac{q}{2\pi\overline{\lambda_g}h}\left[\begin{array}{l}\ln\left(r_{dry}\right) + \dfrac{\overline{\lambda_g}}{\lambda_{ave}}\ln\left(\dfrac{r_{BL}}{r_{dry}}\right) - \dfrac{\overline{\lambda_g}}{\overline{\lambda_w}}\ln\left(r_{BL}\right) + \dfrac{1}{2}\ln\left(\dfrac{\phi c_{tg}}{4\overline{\lambda_g}}\right) \\ -\dfrac{1}{2}\dfrac{\overline{\lambda_g}}{\overline{\lambda_w}}\ln\left(\dfrac{\phi c_{tw}}{4\overline{\lambda_w}t_i}\right) + \dfrac{1}{2}\gamma\left(1-\dfrac{\overline{\lambda_g}}{\overline{\lambda_w}}\right) + s\end{array}\right] \tag{3.41}$$

Therefore, the mobility in the dry-out zone is given by:

$$\overline{\lambda_g} = \frac{q}{4\pi|m_1|h} \tag{3.42}$$

During the infinite-acting radial flow (IARF) corresponding to dry-out zone, the logarithmic derivative should fall on a horizontal line with a constant value on the log-log diagnostic plot given by:

$$\frac{d\left(p_i - p_{ws}\right)}{d\ln\left(\Delta t\right)} = \Delta t\frac{d\Delta p_{ws}}{d\Delta t} = \frac{q}{4\pi\overline{\lambda_g}h} = \text{Constant} \tag{3.43}$$

2. Based on Eq. 3.37, a semi-log plot of p_{ws} versus Δt corresponding to two-phase zone, should exhibit a straight-line behavior with slope m_2 and intercept b_2 given by:

$$m_2 = -\frac{q}{4\pi\lambda_{ave}h} \tag{3.44}$$

$$b_2 = p_i + \frac{q}{2\pi\overline{\lambda_g}h}\left[\begin{array}{l}\frac{1}{2}\frac{\overline{\lambda_g}}{\lambda_{ave}}\ln\left(\frac{\phi c_t r_{BL}^2}{4\lambda_{ave}}\right) - \frac{1}{2}\frac{\overline{\lambda_g}}{\overline{\lambda_w}}\ln\left(\frac{c_{tw}}{\overline{\lambda_w}}\frac{\phi r_{BL}^2}{4t_i}\right) \\ +\frac{1}{2}\gamma\left(\frac{\overline{\lambda_g}}{\lambda_{ave}} - \frac{\overline{\lambda_g}}{\overline{\lambda_w}}\right) + s\end{array}\right] \tag{3.45}$$

Therefore, the average mobility in the two-phase zone is given by:

$$\lambda_{ave} = \frac{q}{4\pi|m_2|h} \tag{3.46}$$

During the IARF corresponding to two-phase zone, the derivative should fall on a horizontal line with a value of $\frac{q}{4\pi\lambda_{ave}h}$ on log-log scale.

3. Based on Eq. 3.39, a semi-log plot of p_{ws} versus HTR, corresponding to the single-phase brine zone, should exhibit a straight-line behavior with a slope proportional to the mobility in the brine zone. Nevertheless, the brine zone may be too far to be sensed by a falloff test. In such case, we assume that the mobility in the brine zone is known through a test conducted prior to CO_2 injection and is given by:

$$\overline{\lambda_w} = \frac{k}{\mu_w} \tag{3.47}$$

4. Given the early-time and intermediate-time solutions are identical at the interface between the dry-out and the two-phase zones. Then, the extent of the dry-out zone is given by equalizing Eqs. 3.37 and 3.39 at the intersection time Δt_x:

$$r_{dry} = \exp\left\{\left(1-\frac{\overline{\lambda_g}}{\lambda_{ave}}\right)^{-1}\left[\begin{array}{l}\frac{1}{2}\left(1-\frac{\overline{\lambda_g}}{\lambda_{ave}}\right)\left(\ln(\Delta t_x)-\gamma\right) \\ -\frac{1}{2}\ln\left(\frac{\phi c_{tg}}{4\overline{\lambda_g}}\right)+\frac{1}{2}\frac{\overline{\lambda_g}}{\lambda_{ave}}\ln\left(\frac{\phi c_t}{4\lambda_{ave}}\right)\end{array}\right]\right\} \tag{3.48}$$

A note that the intermediate-time approximate solution may not match the actual/simulated data points corresponding to the two-phase zone. Instead, it presents a straight line of constant slope parallel to, but not overlapping, the actual data points exhibiting the same slope on semi-log plot. This mismatch is expected since a constant saturation in two-phase zone was assumed in deriving the analytical solution. However, in reality, there is a gradual decrease in the gas saturation over the two-phase zone towards the plume edge. Consequently, the intermediate-time approximate solution should be parallel to, but slightly shifted below the straight line fitted through the actual/simulated data points exhibiting the same slope and average mobility.

Therefore, the observed intercept value b_2 will be higher than the intercept value given by Eq. 3.37. Using the observed value in the interpretation results in overestimated intersection time, and hence, in overestimated extent of the dry-out zone according to Eq. 3.48. According to the boundary condition of Eq. 3.15, there is pressure continuity at the interface between the early-time and intermediate-time solutions. Therefore, b_2 could have been corrected by shifting the fitted line downwards so that it passes through the interface point. However, this point cannot be exactly identified, and thus, it cannot be deterministically used for correction. Despite the difficulty to correct b_2, we found that the effect of the observed overestimated b_2 can be offset by substituting for the total compressibility of the two-phase zone (c_t) with the compressibility of dry-out zone (c_{tg}). This substitution yields improved estimates of the extent of the dry-out zone. This assumption is generally acceptable since CO_2 compressibility is very high compared to brine compressibility that c_t should be slightly lower than c_{tg}, by definition.

5. Given that the physical skin factor and mobility in the brine zone are known, the extent of the plume is obtained by rearranging Eq. 3.41 as follows:

$$r_{BL} = \exp\left\{\left(\frac{\overline{\lambda_g}}{\lambda_{ave}} - \frac{\overline{\lambda_g}}{\overline{\overline{\lambda_w}}}\right)^{-1}\left[\begin{array}{l}\dfrac{2\pi\overline{\lambda_g}h}{q}\left(b_1 - p_i\right) - \left(1 - \dfrac{\overline{\lambda_g}}{\lambda_{ave}}\right)\ln\left(r_{dry}\right) - \dfrac{1}{2}\ln\left(\dfrac{\phi c_{tg}}{4\overline{\lambda_g}}\right) \\ + \dfrac{1}{2}\dfrac{\overline{\lambda_g}}{\overline{\overline{\lambda_w}}}\ln\left(\dfrac{\phi c_{tw}}{4\overline{\lambda_w}t_i}\right) - \dfrac{1}{2}\gamma\left(1 - \dfrac{\overline{\lambda_g}}{\overline{\overline{\lambda_w}}}\right) - s\end{array}\right]\right\} \tag{3.49}$$

Alternatively, the extent of the plume can be obtained by implementing Eq. 3.48 and using the observed value of b_2, while substituting for c_t with c_{tg} in Eq. 3.50:

$$r_{BL} = \exp\left\{\left(\frac{\overline{\lambda_g}}{\lambda_{ave}} - \frac{\overline{\lambda_g}}{\overline{\overline{\lambda_w}}}\right)^{-1}\left[\begin{array}{l}\dfrac{2\pi\overline{\lambda_g}h}{q}\left(b_2 - p_i\right) + \dfrac{1}{2}\dfrac{\overline{\lambda_g}}{\overline{\overline{\lambda_w}}}\ln\left(\dfrac{\phi c_{tw}}{4t_i\overline{\lambda_w}}\right) - \dfrac{1}{2}\dfrac{\overline{\lambda_g}}{\lambda_{ave}}\ln\left(\dfrac{\phi c_t}{4\lambda_{ave}}\right) \\ - \dfrac{1}{2}\gamma\left(\dfrac{\overline{\lambda_g}}{\lambda_{ave}} - \dfrac{\overline{\lambda_g}}{\overline{\overline{\lambda_w}}}\right) - s\end{array}\right]\right\} \tag{3.50}$$

6. The apparent skin factor is then obtained using Eq. 3.34.

3.3. Validation of the Analytical Model

The analytical solution given by Eq. 3.26 is validated against synthetic data generated using CMG-IMEX (CMG-IMEX, 2020). The fluid PVT properties are estimated using Hassanzadeh et al. (2008) algorithm which converts the compositional CO_2/brine properties into black-oil PVT data. The relative permeability data is generated using Corey's model (Corey, 1954b) given by:

$$k_{rc} = k_{rc}^{\,o}\left[\frac{S_c}{1 - S_{wr}}\right]^n \tag{3.51}$$

$$k_{rw} = k_{rw}^{\,o}\left[1-\left(\frac{S_g}{1-S_{wr}}\right)\right]^m \tag{3.52}$$

where $k_{rc}^{\,o}$ and $k_{rw}^{\,o}$ are the endpoint relative permeabilities to CO_2 and brine, respectively, n and m are the saturation exponents of CO_2 and brine, respectively, and S_{wr} is the residual brine saturation. In this work, we consider the saturation exponents are 2.0 and the residual saturation of brine is 0.3. The endpoint relative permeability values of CO_2 and brine are assigned 0.33 and 1.0, respectively.

Table 3.1. Input data for the validation and application cases (empty cells indicate same values as left column)

	Case 1	Case 2	Case 3	Case 4	Case 5	Case 6
Number of layers	1	80				
Number of grids	1*500	80*500	300*300*1			
Initial reservoir pressure (MPa)	20.1					
Injection rate (tons/year)	10^6					variable
Total injection time (day)	1000					
Shut-in time for validation (day)	1000					
Shut-in time for application (day)	20					
Depth to top (m)	2000					
Porosity (fraction)	0.2					
Reservoir temperature (^{o}C)	100					
Injection well radius (m)	0.1					
Permeability in *x*-direction (mD)	50					
Permeability in *y*-direction (mD)	50		250			
Vertical permeability (mD)	5					
Capillary pressure	included					
Dip angle (^{o})	0			2		
Rock compressibility (1/kPa)	5e-7					
Reservoir external radius (m)	50000				15000	
Layer thickness (m)	1*50	80*0.625				
Density of CO_2 (kg/m^3)	477.064					
Viscosity of CO_2 (cp)	0.03693					
Compressibility of CO_2 (1/kPa)	5.02e-5					
Viscosity of brine (cp)	0.28717					
Compressibility of brine (1/kPa)	4.77e-7					
Residual saturation of brine	0.30					
Gas relative permeability in dry zone	0.8					
CO_2 endpoint relative permeability	0.33					
Gas relative permeability exponent	2					
Brine relative permeability exponent	2					

The reduction of the absolute permeability because of salt precipitation in the near wellbore region is considered. CMG is currently unable to model the precipitation of solid salt associated with vaporization of the brine by dry CO_2. However, experiments of Zuluaga (2005) suggest that assigning values in the range of 0.7 to 0.85, for the relative permeability to gas in the dry-out zone, would be representative of the absolute permeability reduction due to salt precipitation around the wellbore. Therefore, we reduced the relative permeability to CO_2 in the dry-out zone to 0.8 to artificially account for the absolute permeability reduction due to salt precipitation. In addition, the capillary pressure curve is generated using van Genuchten (1980) formulation given by:

$$p_c\left(S_w\right) = -p_{th}\left(\left[S^*\right]^{-1/m} - 1\right)^{1-m} \tag{3.53}$$

$$\text{where:} \quad S^* = \frac{S_w - S_{wr}}{1 - S_{wr}}$$

where p_c and p_{th} are the capillary and threshold pressures, respectively. In this work, we consider the threshold pressure is equal to 20 kPa and the pore-size distribution parameter is 0.8. The input data used in the validation is given in Table 3.1. Two cases are presented to validate the model which are:

3.3.1. Single-Layer (Base) Case

For the base case, CO_2 is injected for 1000 days at a constant injection rate of 1.0 million tons per year into a 50-meter thick layer through a fully penetrating vertical well in the center of a circular single-layer reservoir. This rate corresponds to the standard rate of CO_2 produced by a medium-sized coal fired power plant. For the analytical model calculations, the gas viscosity and density are evaluated at the bottomhole pressure achieved at the end of injection period while the brine viscosity and compressibility are evaluated at the initial formation pressure (Oruganti and Mishra, 2013). In addition, the gas compressibility should be evaluated at the initial formation pressure for good match with simulation results. The validation results are displayed in Fig 3.2. The primary *y*-axis of Fig. 3.2 illustrates the comparison of the analytically and the numerically calculated bottomhole shut-in pressure data, and the secondary *y*-axis shows the comparison of the log-log diagnostic plot in terms of the pressure derivative calculated with respect to shut-in time. The comparisons illustrate a good agreement between analytical and numerical results.

3.3.2. Multi-Layer Case

For the buoyant forces to be effective and dominant, the vertical section of the aquifer is refined through discretizing it into 80 layers each of 0.625-m thickness. All other properties are identical to the base case as shown in Table 3.1 (case 2). The comparison of the analytical and the numerical bottomhole shut-in pressures is shown on the primary *y*-axis of Fig. 3.3, while the comparison of the log-log diagnostic plots is shown on the secondary *y*-axis. Despite the close match between the analytical and the numerical solutions, the deviation is noticeable due to the effect of buoyancy, as expected.

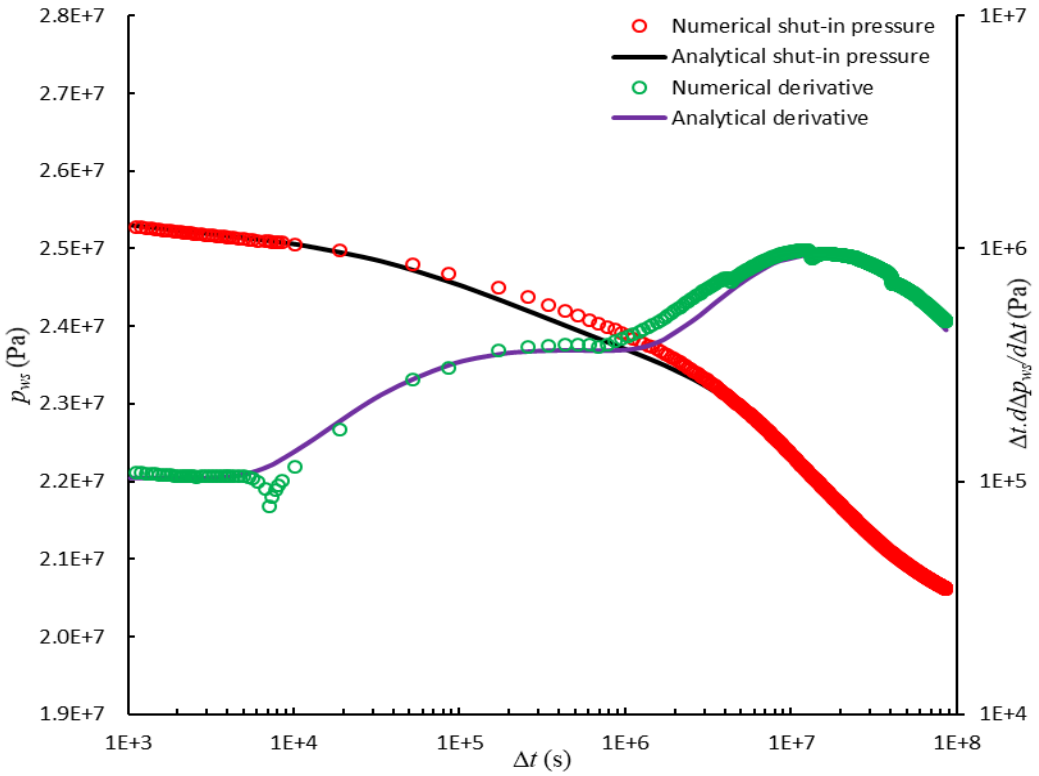

Figure 3.2. Comparison of the analytical and the numerical values of shut-in pressure (on the primary *y*-axis) and derivative (on the secondary *y*-axis) for the single-layer base case

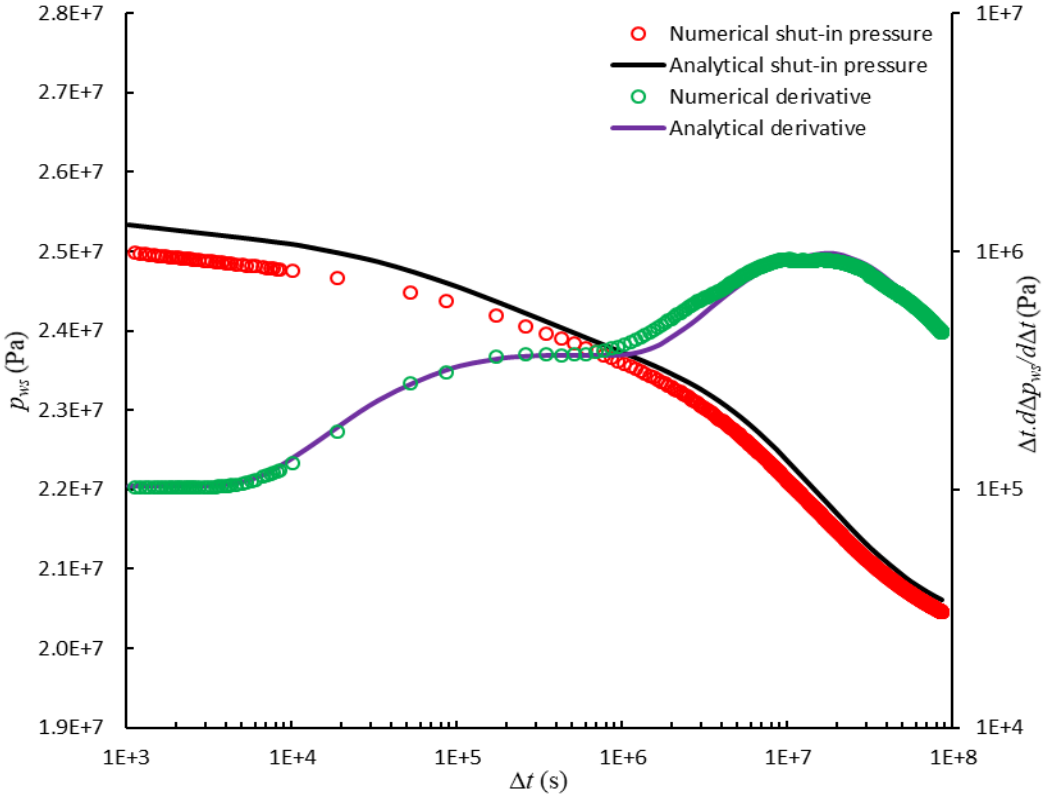

Figure 3.3. Comparison of the analytical and the numerical values of shut-in pressure (on the primary *y*-axis) and derivative (on the secondary *y*-axis) for the multi-layer case (case 2)

3.4. Application of the Interpretation Technique

In this section, the interpretation technique is applied to the synthetic data of the validation cases. In addition, new cases are presented to further investigate the potential application of the technique. The cases consider horizontal permeability anisotropy, formation dip angle, boundary-dominated flow, and variable-rate prior to shut-in (Table 3.1). Analysis in the validation section indicates that the first two zones are well observed at relatively short time (before 2 hr for the dry-out zone and between 72 and 300 hr for the two-phase zone). Therefore, the falloff period can be significantly shortened. Thus, in the section, the well is shut-in for 20 days following 1000 days of continuous injection at a constant rate.

3.4.1. Base Case

As shown on the diagnostic plot (Fig. 3.4), a deviation from the horizontal line corresponding to the dry-out zone is observed at Δt = 1.68 hr, and the IARF corresponding to the two-phase zone is observed at 120 hr < Δt < 192 hr. Then, the data points corresponding to these intervals are line fitted (Fig. 3.4). The fitted line corresponding to the dry-out zone has slope m_1 = -1.03×10^5 Pa/log-cycle and intercept b_1 = 2.60×10^7 Pa, and the fitted line corresponding to the two-phase zone has slope m_2 = -3.57×10^5 Pa/log-cycle and intercept b_2 = 2.88×10^7 Pa. The two fitted lines intersect at ~ 19.3 hr. The gas viscosity and density, evaluated at the bottomhole flowing pressure at the end of injection period, are equal to 0.0476 cp and 589.0 kg/m^3 respectively. Therefore, the volumetric injection rate at the subsurface conditions can be given by:

$$q = \frac{1 \text{ Mt/year}}{589 \text{ kg/m}^3} = \frac{10^9}{365 \times 86400 \times 589} = 0.053837 \text{ m}^3/\text{s}$$

The mobility in the dry-out zone is calculated using Eq. 3.42 as follows:

$$\overline{\lambda_g} = \frac{q}{4\pi |m_1| h} = \frac{0.053837}{4\pi \left|-1.03\times10^5\right| (50)} = 8.3388\times10^{-10} \quad \text{m}^2/\text{Pa.s} = 844.9 \text{ mD/cp}$$

The effective permeability in the dry-out zone is calculated as follows:

$$k_g = \overline{k_{rg}} k = \overline{\lambda_g} \mu_g = \frac{q}{4\pi |m_1| h} \mu_g = 844.9 \times 0.0476 = 40.2 \text{ mD}$$

The average mobility in the two-phase zone is calculated using Eq. 3.46 as follows:

$$\lambda_{ave} = \frac{q}{4\pi |m_2| h} = \frac{0.053837}{4\pi \left|-3.57\times10^5\right| (50)} = 2.4045\times10^{-10} \quad \text{m}^2/\text{Pa.s} = 243.6 \text{ mD/cp}$$

Given the absolute permeability (k = 50 mD) assumed known from a single-phase well test prior to CO_2 injection, the mobility in the brine zone is calculated using Eq. 3.47 as follows:

$$\overline{\lambda_w} = \frac{k}{\mu_w} = \frac{0.05 \times 9.869 \times 10^{-13}}{2.87 \times 10^{-4}} = 1.7194 \times 10^{-10} \quad \text{m}^2/\text{Pa.s} = 174.2 \text{ mD/cp}$$

Assuming $c_t = c_{tg}$ where $c_{tg} = c_g + c_r = 5.07 \times 10^{-8}$ Pa^{-1}, the extent of the dry-out zone is calculated using Eq. 3.48 as follows:

$$r_{dry} = \exp\left\{\left(1 - \frac{\overline{\lambda_g}}{\lambda_{ave}}\right)^{-1}\left[\frac{1}{2}\left(1 - \frac{\overline{\lambda_g}}{\lambda_{ave}}\right)\left(\ln\left(\Delta t_x\right) - \gamma\right) - \frac{1}{2}\ln\left(\frac{\phi c_{tg}}{4\overline{\overline{\lambda_g}}}\right) + \frac{1}{2}\frac{\overline{\lambda_g}}{\lambda_{ave}}\ln\left(\frac{\phi c_t}{4\lambda_{ave}}\right)\right]\right\}$$

$$r_{dry} = \exp\left\{\left(1 - \frac{8.3388 \times 10^{-10}}{2.4045 \times 10^{-10}}\right)^{-1} \times \left[\begin{array}{l} \frac{1}{2} \times \left(1 - \frac{8.3388 \times 10^{-10}}{2.4045 \times 10^{-10}}\right) \times \left(\ln\left(19.3 \times 3600\right) - 0.577215\right) \\ -\frac{1}{2} \times \ln\left(\frac{0.2 \times 5.07 \times 10^{-8}}{4 \times 8.3388 \times 10^{-10}}\right) \\ +\frac{1}{2} \times \left(\frac{8.3388 \times 10^{-10}}{2.4045 \times 10^{-10}}\right) \times \ln\left(\frac{0.2 \times 5.07 \times 10^{-8}}{4 \times 2.4045 \times 10^{-10}}\right) \end{array}\right]\right\} = 47.3 \text{ m}$$

Given the physical skin factor ($s = 0$), the extent of the plume is calculated using Eq. 3.49:

$$r_{BL} = \exp\left\{\left(\frac{\overline{\lambda_g}}{\lambda_{ave}} - \frac{\overline{\lambda_g}}{\overline{\overline{\lambda_w}}}\right)^{-1}\left[\begin{array}{l} \frac{2\pi\overline{\lambda_g}h}{q}\left(b_1 - p_i\right) - \left(1 - \frac{\overline{\lambda_g}}{\lambda_{ave}}\right)\ln\left(r_{dry}\right) - \frac{1}{2}\ln\left(\frac{\phi c_{tg}}{4\overline{\overline{\lambda_g}}}\right) \\ +\frac{1}{2}\frac{\overline{\lambda_g}}{\overline{\overline{\lambda_w}}}\ln\left(\frac{\phi c_{tw}}{4\overline{\overline{\lambda_w}}t_i}\right) - \frac{1}{2}\gamma\left(1 - \frac{\overline{\lambda_g}}{\overline{\overline{\lambda_w}}}\right) - s \end{array}\right]\right\}$$

$$r_{BL} = \exp\left\{\left(\frac{8.3388 \times 10^{-10}}{2.4045 \times 10^{-10}} - \frac{8.3388 \times 10^{-10}}{1.7194 \times 10^{-10}}\right)^{-1} \times \left[\begin{array}{l} \left(\frac{2\pi \times 8.3388 \times 10^{-10} \times 50}{0.053837}\right) \times \left(2.60 \times 10^7 - 2.01 \times 10^7\right) \\ -\left(1 - \frac{8.3388 \times 10^{-10}}{2.4045 \times 10^{-10}}\right) \times \ln\left(47.3\right) - \frac{1}{2} \times \ln\left(\frac{0.2 \times 5.07 \times 10^{-8}}{4 \times 8.3388 \times 10^{-10}}\right) \\ +\frac{1}{2} \times \left(\frac{8.3388 \times 10^{-10}}{1.7194 \times 10^{-10}}\right) \times \ln\left(\frac{0.2 \times 9.775 \times 10^{-10}}{4 \times 1.7194 \times 10^{-10} \times 864 \times 10^5}\right) \\ -\frac{1}{2} \times 0.577215 \times \left(1 - \frac{8.3388 \times 10^{-10}}{1.7194 \times 10^{-10}}\right) - 0 \end{array}\right]\right\} = 507.9 \text{ m}$$

Also, the extent of the plume can be calculated in terms of b_2 using Eq. 3.50 and assuming $c_t = c_{tg}$:

$$r_{BL} = \exp\left\{\left(\frac{\overline{\lambda_g}}{\lambda_{ave}} - \frac{\overline{\lambda_g}}{\overline{\overline{\lambda_w}}}\right)^{-1}\left[\frac{2\pi\overline{\lambda_g}h}{q}\left(b_2 - p_i\right) + \frac{1}{2}\frac{\overline{\lambda_g}}{\overline{\overline{\lambda_w}}}\ln\left(\frac{\phi c_{tw}}{4t_i\overline{\overline{\lambda_w}}}\right) - \frac{1}{2}\frac{\overline{\lambda_g}}{\lambda_{ave}}\ln\left(\frac{\phi c_t}{4\lambda_{ave}}\right) - \frac{1}{2}\gamma\left(\frac{\overline{\lambda_g}}{\lambda_{ave}} - \frac{\overline{\lambda_g}}{\overline{\overline{\lambda_w}}}\right) - s\right]\right\}$$

$$r_{BL}=\exp\left\{\left(\frac{8.3388\times10^{-10}}{2.4045\times10^{-10}}-\frac{8.3388\times10^{-10}}{1.7194\times10^{-10}}\right)^{-1}\times\left[\begin{array}{l}\left(\frac{2\pi\times8.3388\times10^{-10}\times50}{0.053837}\right)\times\left(2.88\times10^{7}-2.01\times10^{7}\right)\\+\frac{1}{2}\times\left(\frac{8.3388\times10^{-10}}{1.7194\times10^{-10}}\right)\times\ln\left(\frac{0.2\times\ 9.775\times10^{-10}}{4\times864\times10^{5}\times1.7194\times10^{-10}}\right)\\-\frac{1}{2}\times\left(\frac{8.3388\times10^{-10}}{2.4045\times10^{-10}}\right)\times\ln\left(\frac{0.2\times5.07\times10^{-8}}{4\times2.4045\times10^{-10}}\right)\\-\frac{1}{2}\times0.577215\times\left(\frac{8.3388\times10^{-10}}{2.4045\times10^{-10}}-\frac{8.3388\times10^{-10}}{1.7194\times10^{-10}}\right)-0\end{array}\right]\right\}=507.9\ \ \text{m}$$

The apparent skin factor is calculated using Eq. 3.34 as follows:

$$s_a=\ln\left(r_{dry}\right)+\frac{\overline{\lambda_g}}{\lambda_{ave}}\ln\left(\frac{r_{BL}}{r_{dry}}\right)-\frac{\overline{\lambda_g}}{\lambda_w}\ln\left(r_{BL}\right)+\frac{1}{2}\ln\left(\frac{\phi c_{tg}}{4\overline{\lambda_g}t_i}\right)-\frac{1}{2}\frac{\overline{\lambda_g}}{\overline{\lambda_w}}\ln\left(\frac{\phi c_{tw}}{4\overline{\lambda_w}t_i}\right)+\frac{1}{2}\gamma\left(1-\frac{\overline{\lambda_g}}{\overline{\lambda_w}}\right)+s$$

$$s_a=\left\{\begin{array}{l}\ln\left(47.3\right)+\left(\frac{8.3388\times10^{-10}}{2.4045\times10^{-10}}\right)\times\ln\left(\frac{507.9}{47.3}\right)-\left(\frac{8.3388\times10^{-10}}{1.7194\times10^{-10}}\right)\times\ln\left(507.9\right)+\frac{1}{2}\times\ln\left(\frac{0.2\times5.07\times10^{-8}}{4\times8.3388\times10^{-10}\times864\times10^{5}}\right)\\-\frac{1}{2}\times\left(\frac{8.3388\times10^{-10}}{1.7194\times10^{-10}}\right)\times\ln\left(\frac{0.2\times9.775\times10^{-10}}{4\times1.7194\times10^{-10}\times864\times10^{5}}\right)+\frac{1}{2}\times0.577215\times\left(1-\frac{8.3388\times10^{-10}}{1.7194\times10^{-10}}\right)+0\end{array}\right\}=19.5$$

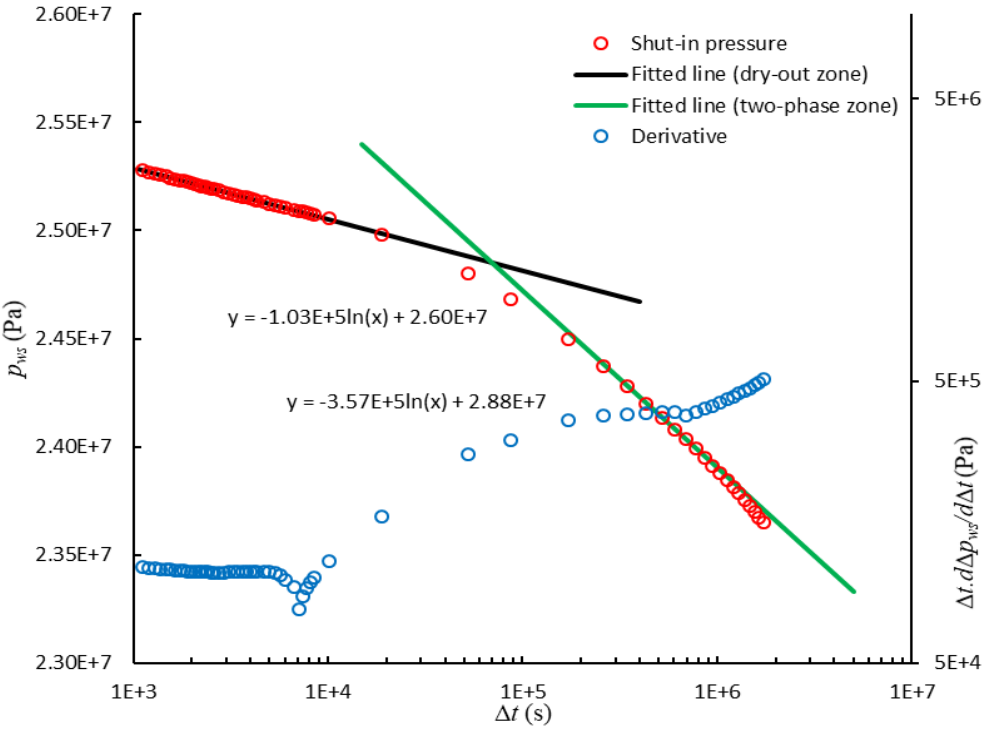

Figure 3.4. Application of the graphical technique to the numerical data for the single-layer base case (case 1)

As shown in Table 3.2, the interpretation results are in good agreement with the simulated values used/observed in generating the numerical data. The estimated mobility in the dry-out zone has absolute relative error (*ARE*) ~ 0.58 % compared to the actual value while the estimated average mobility in the two-phase zone has *ARE* ~ 1.50 % compared to the actual value. In addition the estimated extents of the dry-out zone and the plume have *AREs* ~ 3.67 % and ~ 12.84 % with the actual extents, respectively. A note that the actual/simulated average mobility is the volumetric average of the total mobility in each cell within the two-phase zone. Also, the actual extent of the dry-out zone is marked by the last grid cell having gas saturation equal to unity, and the actual extent of the plume is marked by the last grid cell having non-zero gas saturation.

3.4.2. Effect of Buoyancy

In this case, the effect of buoyancy is investigated through refining the vertical dimension of the reservoir into 80 layers (case 2 in Table 3.1). The dry-out zone is observed before 1.2 hr, and the two-phase zone is observed at 96 hr < Δt < 192 hr as shown in Fig. 3.5. The pressure points, corresponding to each zone, are line fitted and the interpretation technique is applied as shown in Fig. 3.5. The gas viscosity and density, evaluated at the bottomhole flowing pressure at the end of injection period, are equal to 0.0471 cp and 584.0 kg/m^3 respectively. The inferred parameters are in good agreement with the actual values as displayed in Table 3.2. The estimated mobility in the dry-out zone has *ARE* ~ 3.69 % with the actual mobility while the average mobility in the two-phase zone has *ARE* ~ 4.61 % with the actual value in the intermediate layer. The estimated extent of the dry-out zone deviates from the actual extent in the intermediate layer by ~ 11.61 %. However, the extent of the plume is overestimated.

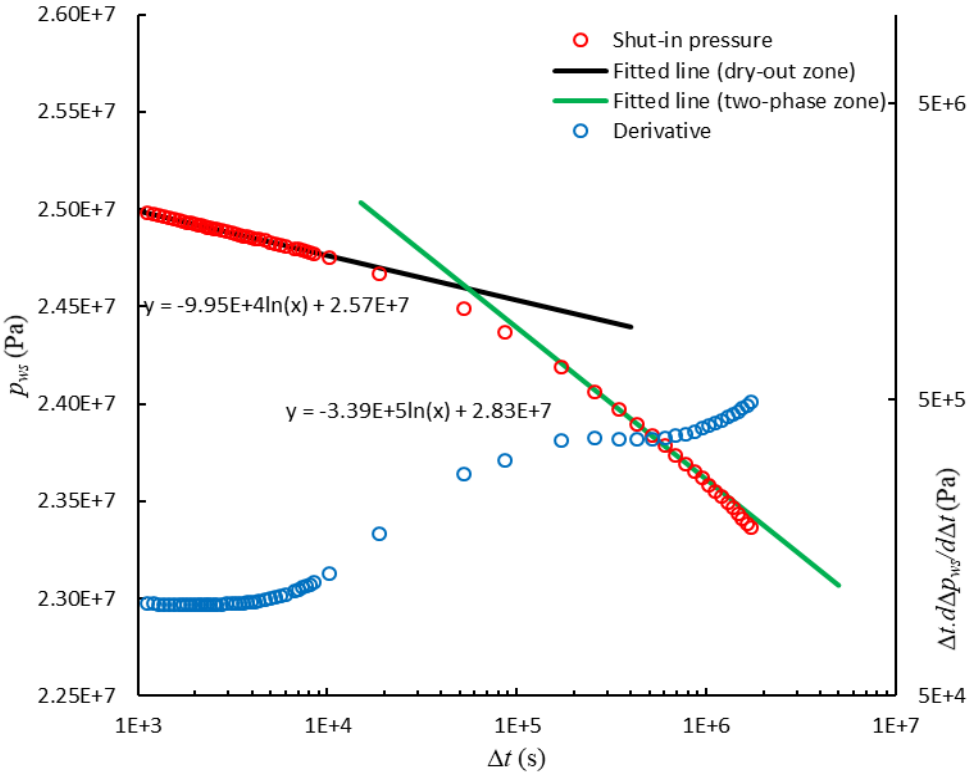

Figure 3.5. Application of the graphical technique to the numerical data for the multi-layer case (case 2)

Table 3.2. Results of the graphical interpretation technique for cases (1-2)

	Single-layer case (case-1)		Multi-layer case (case-2)	
	Estimated	Actual	Estimated	Actual
Mobility in dry-out zone (mD/cp)	844.9	840.0	880.4	849.1
Average mobility in two-phase zone (mD/cp)	243.6	240.0	258.8	330.2 (upper layer) 247.4(intermediate) 203.8 (lower)
Extent of dry-out zone (m)	47.3	49.1	43.4	50.7 (upper layer) 49.1 (intermediate) 49.1 (lower layer)
Extent of CO_2 plume (m)	507.9	582.7	1151.9	684.2 (upper layer) 549.2(intermediate) 418.7 (lower layer)
Apparent skin factor (-)	19.5	--	18.9	--

In addition, to better investigate the effect of buoyancy, we modified the 80-layer case through increasing the vertical permeability from 5 mD (k_v/k_h = 0.1) to 20 mD (k_v/k_h = 0.4) where k_v is the vertical permeability and k_h is the horizontal permeability. The interpretation results, displayed in Table 3.3, indicate that the estimated values of mobilities and the extent of the dry-out zone are in good agreement with the actual values. However, we notice that the degree of plume extent overestimation is more significant than in the low k_v multi-layer case. This deviation is attributed to the dominating buoyant force caused by increasing the vertical resolution of the aquifer and/or the high vertical permeability.

Table 3.3. Interpretation results for case 2 modified by increasing vertical permeability to 20 mD

	Estimated	Actual
Mobility in dry-out zone (mD/cp)	865.2	854.6
Average mobility in two-phase zone (mD/cp)	273.8	356.5 (upper) – 301.3 (intermediate) – 204.1 (lower)
Extent of dry-out zone (m)	42.3	49.1 (upper) – 49.1 (intermediate) – 47.6 (lower)
Extent of CO_2 plume (m)	1521.4	714.5 (upper) – 509.8 (intermediate) – 315.6 (lower)

3.4.3. Effect of Horizontal Permeability Anisotropy

In this case, the plume is allowed to extend further in *y*-direction as compared to *x*-direction. This is achieved through modifying the base case by setting the ratio of the absolute permeability in *y*-direction to that in *x*-direction as 0.2 (case 3 in Table 3.1). As shown on the diagnostic plot (Fig. 3.6), the dry-out zone is observed at 0.53 hr < Δt < 0.96 hr while the two-phase zone is observed at 72 hr < Δt < 144 hr. The gas viscosity and density, evaluated at the bottomhole flowing pressure

at the end of injection period, are equal to 0.0425 cp and 534.8 kg/m^3 respectively. The plume and the dry-out zone are no longer circular, but elliptic due to permeability anisotropy. Results indicate that the estimated mobilities are in close agreement with the actual values, and the extent of the dry-out zone and the plume approximately average the actual extents in both direction (see Table 3.1). This validates the potential application of the interpretation technique to anisotropic aquifers.

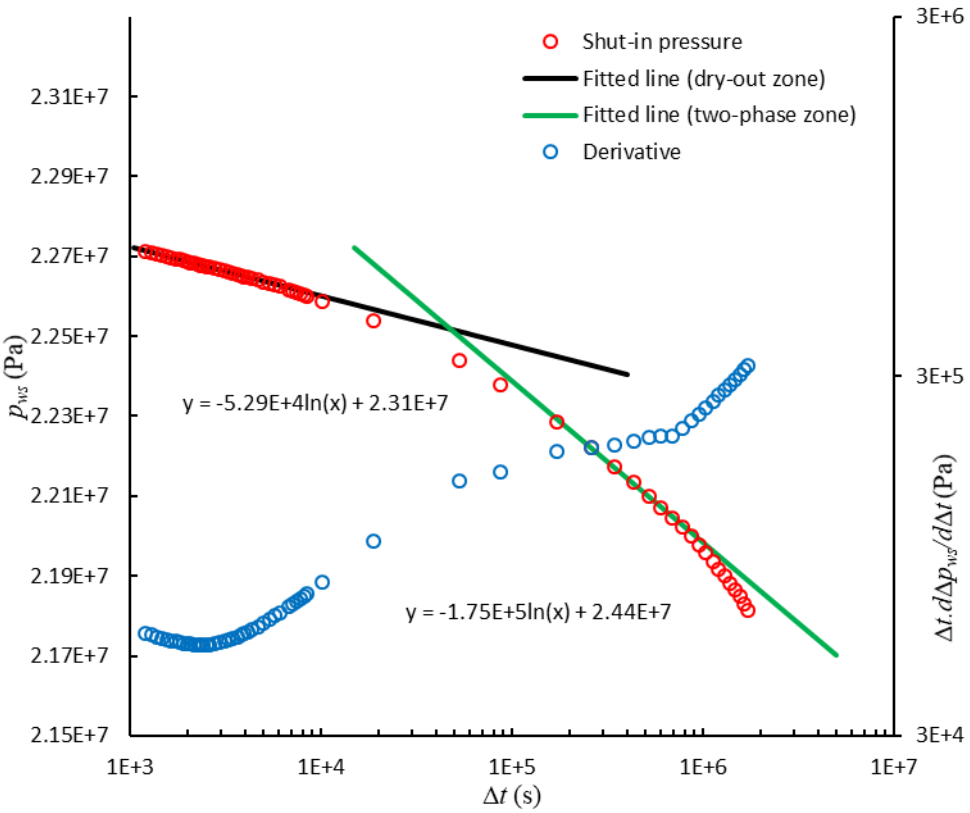

Figure 3.6. Application of the graphical technique to numerical shut-in pressures (primary *y*-axis) and derivative (secondary *y*-axis) for a single-layer aquifer with permeability anisotropy

3.4.4. Effect of Formation Dip Angle

In this case, the base case is modified by introducing a 2.0^o dip angle of the formation (case 4 in Table 3.1). As illustrated by the diagnostic plot (Fig. 3.7), the dry-out zone is observed before 1.68 hr and the two-phase zone is observed at 120 hr < Δt < 192 hr. The gas viscosity and density, evaluated at the bottomhole flowing pressure at the end of injection period, are equal to 0.0476 cp and 589.1 kg/m^3 respectively. Due to dip, the actual extent of the dry-out zone and the plume are no longer the same on both sides of the well. The extent up-dip is further than the extent down-dip, and the difference increases with higher dip and permeability values. The interpretation results are displayed in Table 3.4. The estimated mobility values are in good agreement with the actual values. The extent of the dry-out zone slightly underestimates the actual values on both sides of the well, and the estimated extent of the plume is consistent with the actual extent downdip. Therefore, the graphical interpretation technique is useful in interpreting falloff tests for slightly dipping aquifers.

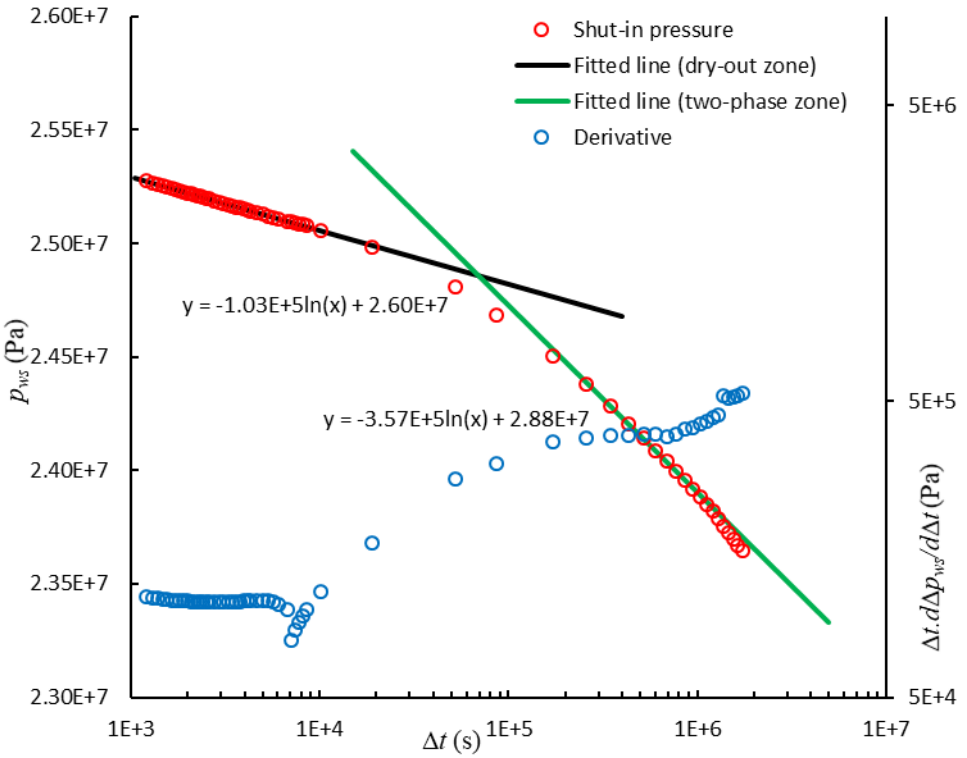

Figure 3.7. Application of the interpretation technique to numerical shut-in pressures (primary *y*-axis) along with the derivative (secondary *y*-axis) for a single-layer aquifer with 2° dip angle

Table 3.4. Results of the graphical interpretation technique for cases (3-4)

	Effect of permeability anisotropy (case-3)		Effect of formation dip angle (case-4)	
	Estimated	Actual	Estimated	Actual
Mobility in dry-out zone (mD/cp)	1807.2	2106.7	843.8	839.9
Average mobility in two-phase zone (mD/cp)	545.7	538.6 (*x*-direction) 554.1 (*y*-direction)	243.1	239.9 (down-dip) 240.5 (up-dip)
Extent of dry-out zone (m)	58.4	30 (*x*-direction) 75 (*y*-direction)	47.5	49.1 (down/up-dip)
Extent of CO_2 plume (m)	693.6	435 (*x*-direction) 930 (*y*-direction)	501.7	549.4 (down-dip) 609.1 (up-dip)
Apparent skin factor (-)	19.1	--	19.5	--

3.4.5. Bounded Reservoir

In this case, the base case is modified by reducing the reservoir's external radius by 70 % (case 5 in Table 3.1). The application of the graphical technique and the log-log diagnostic plot are shown in Fig. 3.8. The dry-out zone is observed before Δt = 1.2 hr and the two-phase zone is observed at 120 hr < Δt < 192 hr. Because of the aquifer's limited volume, the pseudo-steady state flow behavior is established 870 days before shut-in (after 130 days of injection). The gas viscosity and density, evaluated at the bottomhole flowing pressure at the end of injection period, are equal to 0.0477 cp and 589.6 kg/m^3 respectively. The interpretation results, shown in Table 3.5, indicate that estimated mobility values are in good match with the actual values. The extent of the dry-out zone is in close match with the actual value, while the extent of the plume underestimates the actual value. The displayed results validate the potential application of the interpretation technique to bounded aquifers where the BDF is established before conducting the falloff test.

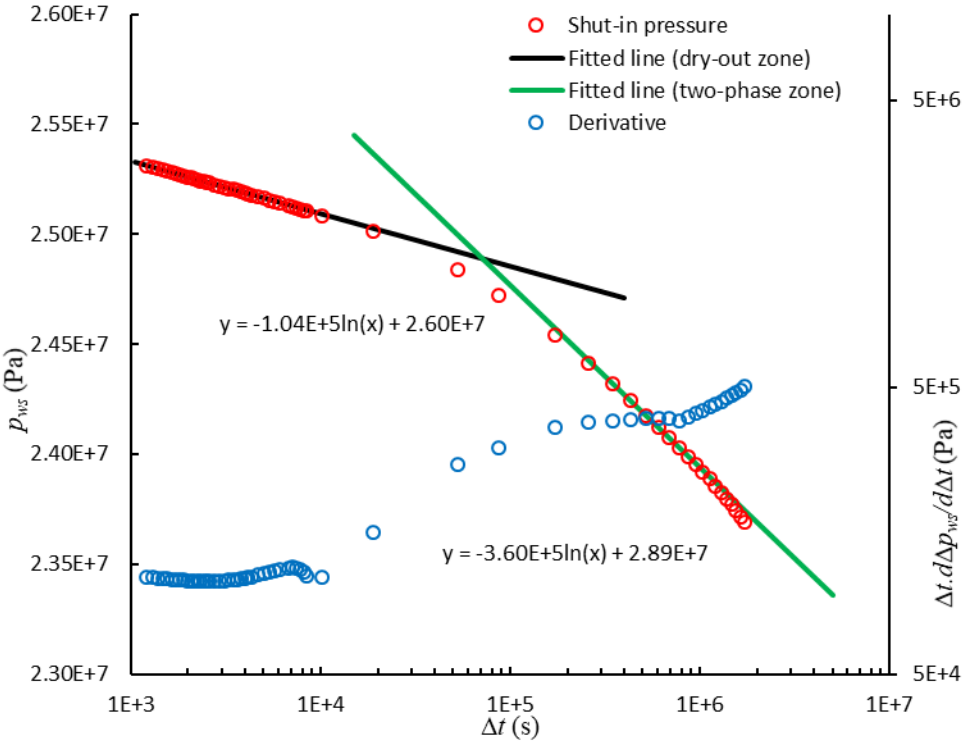

Figure 3.8. Application of the graphical technique to numerical shut-in pressures (on the primary *y*-axis) along with the derivative (on the secondary *y*-axis) for a single-layer bounded aquifer

3.4.6. Effect of Injection Rate Variation

In this case, the effect of variable injection rate history that precedes shut-in is investigated. The base case is modified by introducing injection rate history. The target injection rate of 1.0 Mt/year is established and kept constant over the last 200 days prior to the test. The injection rate history - at reservoir conditions - is shown in Fig. 3.9. Horner pseudo-producing time (*pseudo-injecting* time for our case) approximation method can be used to account for the injection rate history prior

to shut-in (Horner, 1951). The method honors the cumulative injection and the final injection rate prior to shut-in. The pseudo-injecting time is given by $t_{pi} = Q/q_{last}$ where Q is the cumulative injection and q_{last} is the last injection rate prior to shut-in. For this case, the calculated pseudo-injecting time is 935.5 days. Fig. 3.10 illustrates the diagnostic plot and the application of the interpretation technique. The dry-out zone is observed before Δt = 1.6 hr and the two-phase zone is observed at 120 hr < Δt < 192 hr. The gas viscosity and density, evaluated at the bottomhole flowing pressure at the end of injection period, are equal to 0.0476 cp and 589.2 kg/m^3 respectively. As shown in Table 3.5, the estimated mobility values are in good match with the actual values. The extent of the dry-out zone is in good agreement with the actual value while the extent of the plume slightly underestimates the actual values. Therefore, the interpretation technique is useful in interpreting falloff tests conducted on wells with variable injection rates prior to the falloff test.

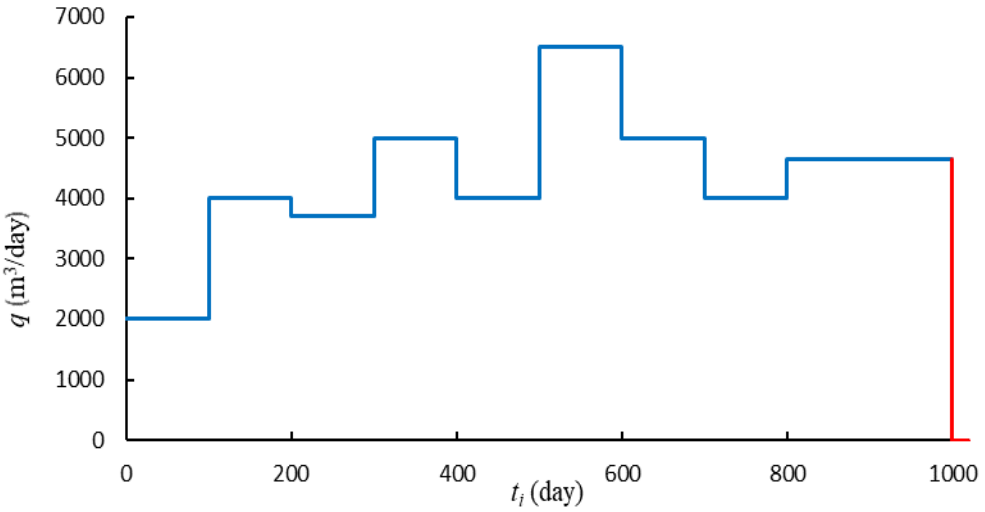

Figure 3.9. Injection rate history for the single-layer aquifer case with variable injection rates before shut-in

Table 3.5. Results of the graphical interpretation technique for cases (5-6)

	Bounded reservoir (case-5)		Injection rate variation (case-6)	
	Estimated	Actual	Estimated	Actual
Mobility in dry-out zone (mD/cp)	837.0	838.9	843.7	840.0
Average mobility in two-phase zone (mD/cp)	240.9	240.6	241.7	240.7
Extent of dry-out zone (m)	47.9	47.9	46.2	47.6
Extent of CO_2 plume (m)	453.9	579.8	500.4	557.4
Apparent skin factor (-)	19.5	--	19.5	--

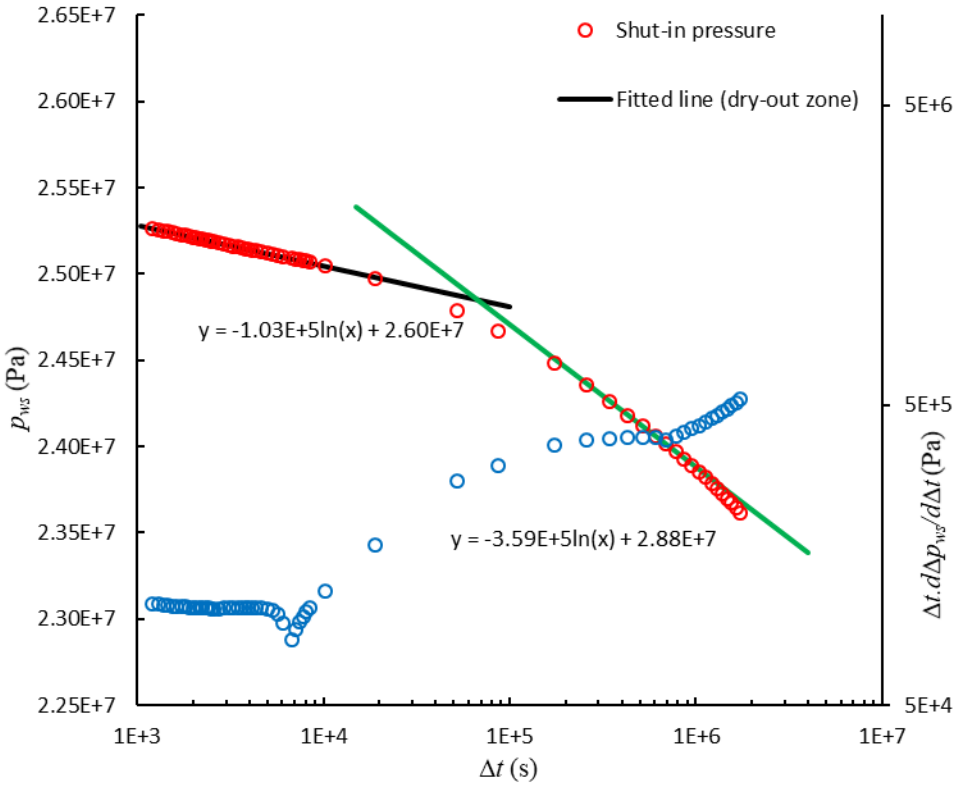

Figure 3.10. Application of the graphical technique to the numerical shut-in pressures (on primary *y*-axis) along with the derivative (on secondary *y*-axis) for a single-layer aquifer with variable injection rate history

A note that the Horner pseudoinjecting time method should only be used when the duration of the last injection period t_{last} is at least 10 times the duration of the falloff period Δt (Spivey and Lee, 2013). However, we investigated our interpretation method for cases where t_{last} is less than $10\Delta t$ and found that the fluid mobilities and the extent of the dry-out zone can be accurately estimated with the developed interpretation technique. However, the extent of the plume r_{BL} may be significantly overestimated with decreasing t_{last} far below $10\Delta t$. Interpretation results for t_{last} = 100 days ($t_{last} = 5\Delta t$) and t_{last} = 30 days ($t_{last} = 1.5\Delta t$) are displayed in Table 3.6 below.

Table 3.6. Effect of the last injection period on the interpretation results

	Variable-rate case (t_i=100 day)		Variable-rate case (t_i=30 day)	
	Estimated	Actual	Estimated	Actual
Mobility in dry-out zone (mD/cp)	860.1	854.1	865.6	866.5
Average mobility in two-phase zone (mD/cp)	258.1	243.7	278.3	245.9
Extent of dry-out zone (m)	43.0	46.0	41.7	44.5
Extent of CO_2 plume (m)	1719.5	541.1	3553.5	541.1

3.5. Additional Investigations

3.5.1. Effect of Short Injection Period relative to the Falloff Period

The interpretation technique is similar to the traditional MDH method (Miller et al., 1950) used to interpret single-phase shut-in tests using the principle of superposition in time. Nevertheless, our methodology is not restricted to the limitation imposed on the MDH method (Miller et al., 1950), used to interpret single-phase shut-in tests following constant-rate flow period, which is based on the principle of superposition in time. In MDH method, the duration of the injection period should be at least 10 times longer than the falloff duration. The limitation of the MDH method arises when the superposition equation is reduced to the MDH equation through neglecting the shut-in period relative to the flowing period (i.e. generally when $\Delta t/t_i \leq 0.1$). On the other hand, this assumption is not adopted in approximating our analytical solution. This is confirmed by the simulated falloff tests analyzed in the validation section where ($\Delta t/t_i = 1 >> 0.1$). In addition, we ran a case with short injection duration compared to the falloff. In this case, the base case is modified by operating the well for 300 days followed by 900 days shut-in. The application of the interpretation method along with the diagnostic plot is shown in Fig. 3.11 below. The pressure signal corresponding to the dry-out zone is observed before 0.5 hr, and the two-phase zone occurs between 48 hr and 96 hr. The interpretation results, displayed in Table 3.7, are in good agreement with the actual values validating the potential application of the proposed technique to cases of short injection times compared to falloff times.

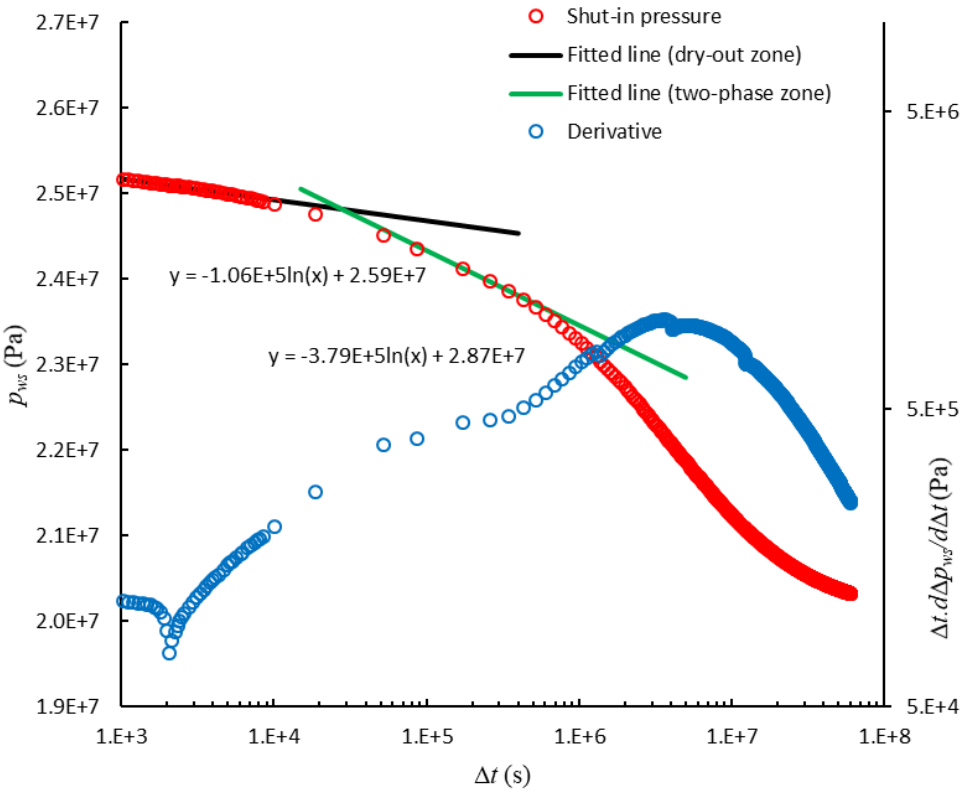

Figure 3.11. Application of the interpretation technique to a case with short injection time (300 day) compared to long falloff time (900 days)

A note that at late time the derivative plot, shown in Fig. 3.11, exhibits sharp decline, and one may not expect a horizontal line corresponding to the brine zone. This is due to the fact that the pressure derivative, here, is calculated with respect to the shut-in time. However, to achieve a horizontal line corresponding to the brine region, the derivative should be calculated with respect to HTR (i.e. not Δt) as we explained before.

Table 3.7. Results for case with short injection time (300 day) relative to falloff period (900 day)

	Estimated	Actual
Mobility in dry-out zone (mD/cp)	818.9	843.3
Average mobility in two-phase zone (mD/cp)	229.7	259.3
Extent of dry-out zone (m)	29.2	26.3
Extent of CO_2 plume (m)	349.2	364.1

Also, the results of this work indicate that the dry-out and the two-phase zones may be observed at relatively short time of shut-in (before 2 hr for the dry-out zone and between 72-192 hr for the two-phase zone in the cases presented herein) while the single-phase brine zone may be too far to be seen by the falloff test. However, if present, it should be analyzed using HTR rather than the shut-in time following the late-time asymptotic solution. The diagnostic plot of the validation cases (Figs. 3.2 and 3.3) shows that the two-phase zone's front indicated by a very long transition (hump) in the derivative plot is due to the significant variation in properties between CO_2 and brine at the edge of the plume. The upward shift of the hump is related to the storativity ratio and the mobility contrast between the two-phase zone and the single-phase brine zone while the horizontal levels are related to the mobility values in the corresponding zones. With the gradual decrease of CO_2 saturation accompanied by a gradual increase of brine saturation over the two-phase zone toward the edge of the plume, the mobility decreases significantly making the single-phase brine zone to partially act like a no-flow boundary with respect to the plume until the pressure drop between the two zones is sufficient for the pressure diffusion to occur within the single-phase zone. However, we cannot assume the brine zone to fully act like a no flow boundary unless the mobility ratio is equal to zero (Spivey and Lee, 2013) and the derivative plot shows a clear unit-slope line which is not the case herein. In situations where the unit-slope line is achieved and clearly observed, the pseudo-steady state method can be used to infer the upper bound of the CO_2 plume. The PSSF method is applied to infer the drainage volume from single-phase reservoir limits testing (Spivey and Lee, 2013), and it can be used to infer the location of the interface between regions for systems with radial discontinuities where the PSSF may establish during the transition from region to another. One example is the field application of PSSF method to in-situ combustion project that resembles a multi-bank system where the burned volume/steam-swept volume can be inferred by utilizing the falloff tests conducted to investigate the effectiveness of the project by monitoring the progress of the fire front (Kamal, 2009).

3.5.2. Effect of Long Injection (i.e., Matured Dry-Out Zone and CO_2 Plume)

In this case, we test the effect of long duration of the injection period on the interpretation results where dry-out zone and CO_2 plume are well-established. The base case is modified by operating

the well for 20 years instead of 1000 days ~ 2.7 years for the base case. To capture the pressure signals corresponding to dry-out and two-phase zones, the injection period is followed by 50 days shut-in instead of 20 days. The application of the interpretation method along with the diagnostic plot is displayed in Fig. 3.12. The pressure signal corresponding to the dry-out zone is observed before 2.4 hr, and the two-phase zone occurs between 240 hr and 1200 hr, as expected. The interpretation results, shown in Table 3.8, indicate that the inferred mobilities are in reasonable agreement with the actual values. Nevertheless, the extent of the dry-out zone is slightly underestimated with *ARE* ~ 18 % and the extent of the plume is highly underestimated with *ARE* ~ 38 %. Therefore, caution should be practiced when applying the interpretation methodology to GCS projects where CO_2 is being injected for a long time.

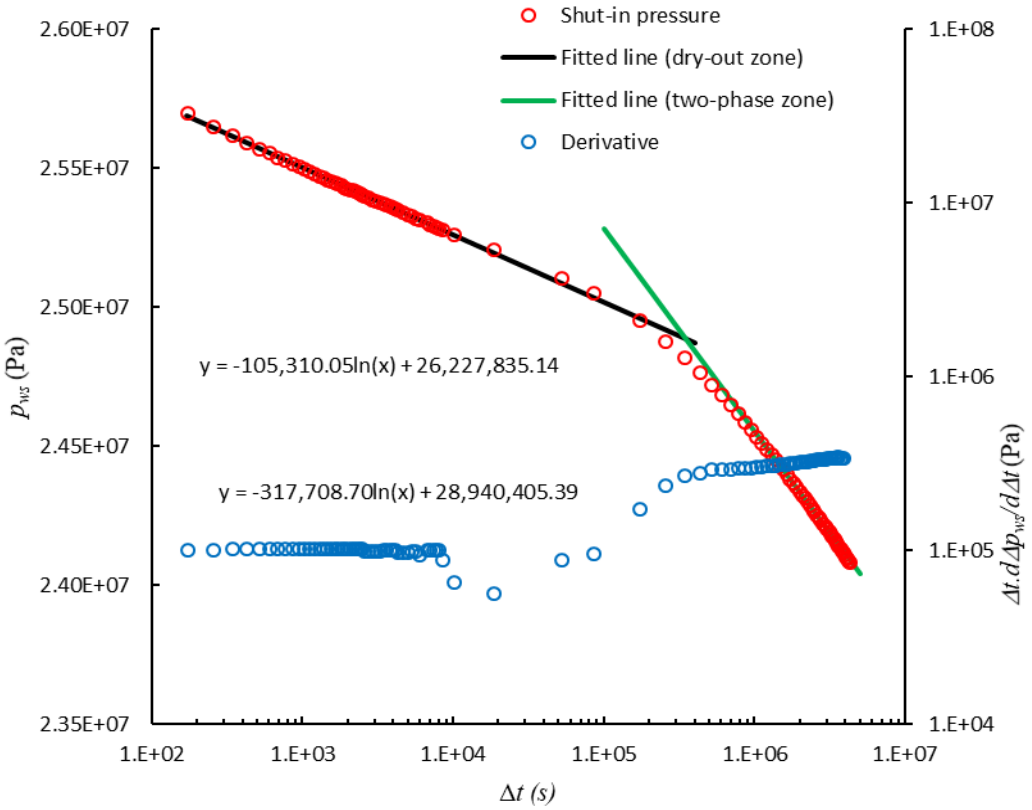

Figure 3.12. Application of the interpretation technique to a case with 20 years duration of the injection period

Table 3.8. Results for a case with 20 yeas duration of the injection period

	Estimated	Actual
Mobility in dry-out zone (mD/cp)	821.3	834.3
Average mobility in two-phase zone (mD/cp)	272.2	238.8
Extent of dry-out zone (m)	110.1	134.9
Extent of CO_2 plume (m)	960.9	1567.1

3.5.3. Unknown Initial Reservoir Pressure

Application of the proposed graphical interpretation technique to bounded aquifers has been shown before. However, our interpretation technique is based on the initial reservoir pressure which is assumed known from an earlier single-phase test. Alternatively, the interpretation can be based on the bottomhole flowing pressure at the time of shut-in p_{wf} rather than the initial reservoir pressure p_i. This could be the case for bounded aquifers where PSSF may have established early before the falloff test. p_{wf} is given by Azizi and Cinar (2013a)'s as follows:

$$p_{wf} = p_i + \frac{q}{2\pi h\overline{\overline{\lambda_g}}}\left[\begin{array}{l}\ln\left(r_{dry}\right)+\frac{1}{2}\ln\left(\frac{1}{r_w^2}\right)+\frac{\overline{\lambda_g}}{\lambda_{ave}}\ln\left(\frac{r_{BL}}{r_{dry}}\right)-\frac{\overline{\lambda_g}}{\overline{\overline{\lambda_w}}}\ln\left(r_{BL}\right)\\ -\frac{1}{2}\frac{\overline{\lambda_g}}{\overline{\overline{\lambda_w}}}\ln\left(\frac{c_{tw}\phi}{4t_i\overline{\overline{\lambda_w}}}\right)-\frac{1}{2}\frac{\overline{\lambda_g}}{\overline{\overline{\lambda_w}}}\gamma+s\end{array}\right] \tag{3.51}$$

In terms of p_{wf} the early-time and the intermediate-time solutions are obtained by subtracting Eq. 3.51 from Eqs. 3.31 and 3.37 respectively as follows:

$$p_{ws} = -\frac{q}{4\pi h\overline{\overline{\lambda_g}}}\ln\left(\Delta t\right)+p_{wf}+\frac{q}{4\pi h\overline{\overline{\lambda_g}}}\left[\ln\left(\frac{\phi c_{tg}r_w^2}{4\overline{\overline{\lambda_g}}}\right)+\gamma\right] \tag{3.52}$$

$$p_{ws} = -\frac{q}{4\pi h\lambda_{ave}}\ln\left(\Delta t\right)+p_{wf}+\frac{q}{2\pi h\overline{\overline{\lambda_g}}}\left[\begin{array}{l}\frac{1}{2}\frac{\overline{\lambda_g}}{\lambda_{ave}}\ln\left(c_t r_{dry}^2\right)-\frac{1}{2}\ln\left(r_{dry}^2\right)\\ +\ln\left(r_w\right)+\frac{1}{2}\frac{\overline{\lambda_g}}{\lambda_{ave}}\ln\left(\frac{\phi}{4\lambda_{ave}}\right)+\frac{1}{2}\frac{\overline{\lambda_g}}{\lambda_{ave}}\gamma\end{array}\right] \tag{3.53}$$

Based on Eqs. 3.52 and 3.53, a semi-log plot of p_{ws} versus Δt should yield straight lines corresponding to the dry-out zone and the two-phase zone with slopes m_1, m_2 and intercepts b_1, b_2 respectively. m_1 and m_2 are still expressed by Eqs 3.40 and 3.44 while b_1, b_2 can be expressed in terms of p_{wf} as follows:

$$b_1 = p_{wf}+\frac{q}{4\pi h\overline{\overline{\lambda_g}}}\left[\ln\left(\frac{\phi c_{tg}r_w^2}{4\overline{\overline{\lambda_g}}}\right)+\gamma\right] \tag{3.54}$$

$$b_2 = p_{wf}+\frac{q}{2\pi h\overline{\overline{\lambda_g}}}\left[\begin{array}{l}\frac{1}{2}\frac{\overline{\lambda_g}}{\lambda_{ave}}\ln\left(c_t r_{dry}^2\right)-\frac{1}{2}\ln\left(r_{dry}^2\right)+\ln\left(r_w\right)\\ +\frac{1}{2}\frac{\overline{\lambda_g}}{\lambda_{ave}}\ln\left(\frac{\phi}{4\lambda_{ave}}\right)+\frac{1}{2}\frac{\overline{\lambda_g}}{\lambda_{ave}}\gamma\end{array}\right] \tag{3.55}$$

Eqs 3.52 and 3.53 imply that the mobilities can be inferred using the same Eqs. 3.42 and 3.46. In addition to the intersection-time point method that has been used throughout the previous cases (Eq. 3.48), the extent of the dry-out zone can be inferred by rearranging Eq. 3.53 while substituting for c_t with c_{tg} to offset the effect of the overestimated intercept:

$$r_{dry} = \exp\left\{\left(\frac{\overline{\lambda_g}}{\lambda_{ave}} - 1\right)^{-1}\left[\begin{array}{l}\dfrac{2\pi h\overline{\lambda_g}}{q}\left(b_2 - p_{wf}\right) - \dfrac{1}{2}\dfrac{\overline{\lambda_g}}{\lambda_{ave}}\ln\left(c_t\right) - \ln\left(r_w\right) \\ -\dfrac{1}{2}\dfrac{\overline{\lambda_g}}{\lambda_{ave}}\ln\left(\dfrac{\phi}{4\lambda_{ave}}\right) - \dfrac{1}{2}\dfrac{\overline{\lambda_g}}{\lambda_{ave}}\gamma\end{array}\right]\right\} \tag{3.56}$$

As shown in Table 3.9, the close agreement between the estimated extents of the dry-out zone (using Eq. 3.54) and the values estimated using the intersection-time method (Eq. 3.48) with the actual extents assures the validity of Eq. 3.56.

Table 3.9. Comparison of the estimated extent of the dry-out zone using Eqs. 3.48 and 3.54 with the actual values

	p_{wf}, at shut-in, MPa	Extent of dry-out zone, m (Eq. 3.56)	Extent of dry-out zone, m (Eq. 3.48)	Actual extent of dry-out zone, m
Case 1	26.352	42.6	47.3	49.1
Case 2	26.025	38.9	43.4	50.7 (upper) 49.1 (intermediate) 49.1 (lower)
Case 3	23.200	82.1	58.4	30 (x-direction) 75 (y-direction)
Case 4	26.356	42.9	47.5	49.1
Case 5	26.393	43.8	47.9	49.7
Case 6	26.346	41.8	46.2	47.6

Unfortunately, Eqs. 3.52 and 3.53 are not function of r_{BL}. Therefore, we still have to use either Eq. 3.49 or Eq. 3.50 in terms of p_i to infer the extent of the plume. Generally, for better characterizing bounded CO_2/brine systems where the BDF is established before shut-in (and the average reservoir pressure p_{ave} far exceeds p_i due to continuous CO_2 injection in the limited aquifer volume), it may be better to revisit the exact solution presented in this work, and its real-time approximations. We should obtain solutions considering the pressure behavior during CO_2 injection into a bounded aquifer where a no-flow outer boundary condition is adopted in deriving the injection pressure.

3.5.4. Effect of Channeled/Linear Reservoirs

Application of the graphical interpretation technique to infinite-acting radial flow (IARF) where the CO_2 plume evolves symmetrically around the wellbore has been demonstrated through several cases. Also, the usefulness of the technique has been shown to a case which considers absolute

horizontal permeability anisotropy where the dry-out zone and the plume are no longer circular. The results of that case demonstrated that the interpretation technique can be utilized to accurately infer the average extent of the dry-out zone and the plume in both direction. However, in situations where the extent of the plume is significantly dissimilar in both directions, the IARF interpretation technique may be invalid due to distortion caused by linear flow. This situation is encountered in practice when the reservoir extension is limited in one of the direction due to presence of a sealing fault or a closed boundary relatively close to the wellbore (referred to as a channeled reservoir). Therefore, in this investigation, we check the potential application of the interpretation technique to analyze falloff data for a case representing channeled reservoir where linear flow can establish. In this case, we revisited the model dimensions and gridding scheme to enable linear evolution of the plume. We modified the discretization setup from the radial scheme to the Cartesian scheme considering 50 km in *x*-direction and 0.3 km in *y*-direction model extension. We discretized the model into a total of 40401 gridblocks with 201 gridblocks in each direction. The gridblock sizes in both directions are distributed logarithmically, with the finest (0.1 m) near the wellbore and the largest far from the wellbore. This allows for capturing the variation in pressure and saturation around the wellbore. The wellbore is centered in the middle of the aquifer. Due to the limited volume of the reservoir as compared to the base case, injecting at 1.0 Mt/year should cause a huge overpressure that can jeopardize the integrity of the formation. Therefore, we reduced the injection rate for this case to 0.25 Mt/year. The remaining fluid and rock properties are identical to the base case shown in Table 3.1. A 3-dimentional image of the model is shown in Fig. 3.13 below. Also, Fig. 3.14 shows a simulator-generated aerial view of the model illustrating the CO_2 saturation at end of the injection period. As is shown, the plume evolves linearly in *x*-direction due to the limited extension of the reservoir in *y*-direction.

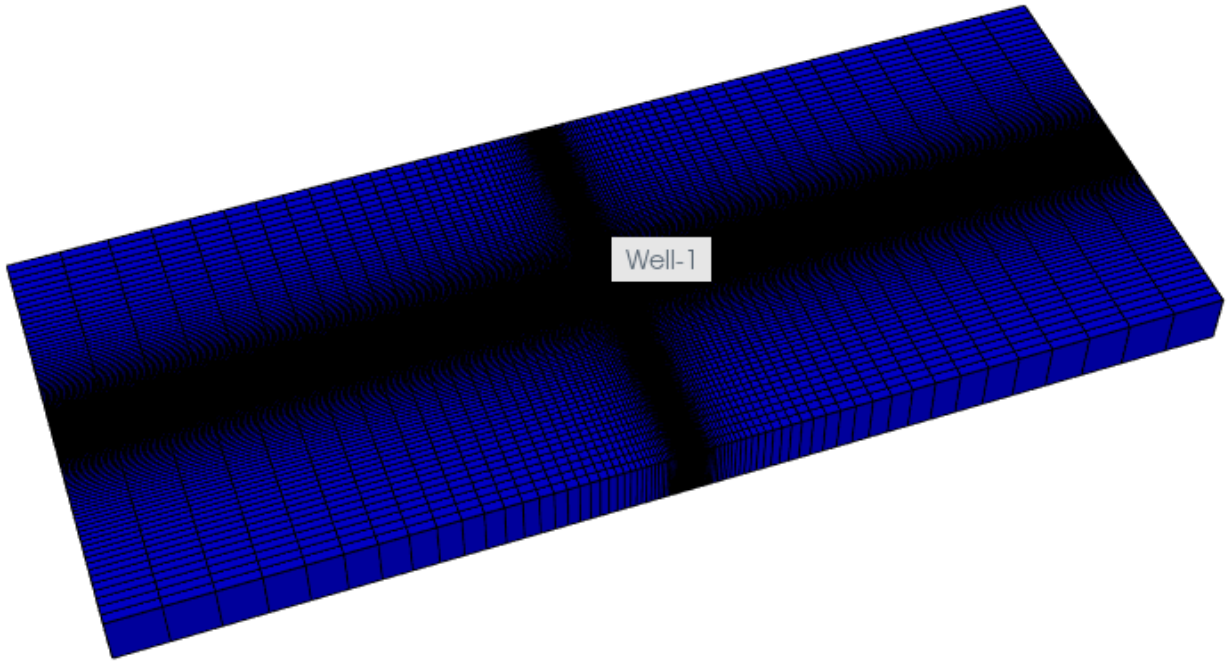

Figure 3.13. A simulator-generated image showing a 3-D view (not to scale) of the Cartesian model for an aquifer with restricted extension in *y*-direction

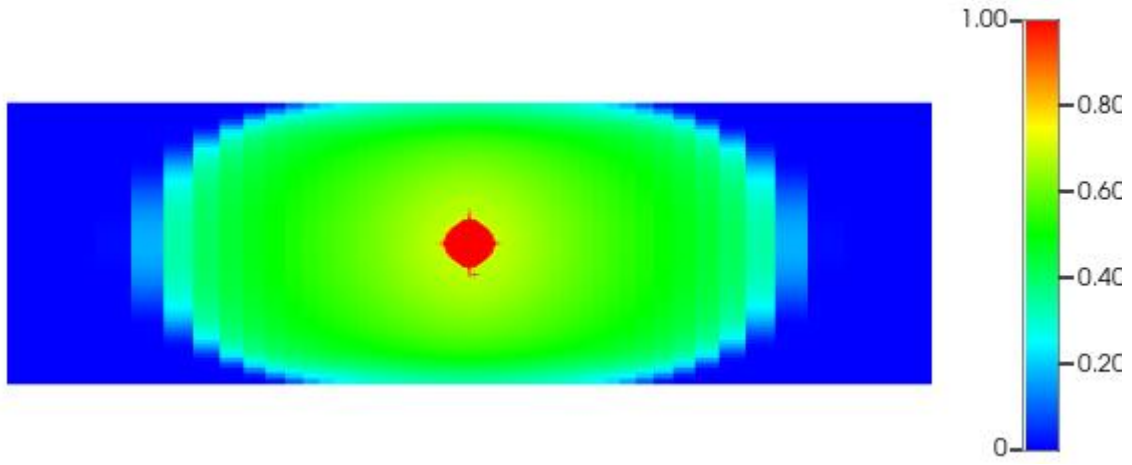

Figure 3.14. A simulator generated 2-D image showing the asymmetric evolution of the plume due to the restricted extension of the aquifer in y-direction

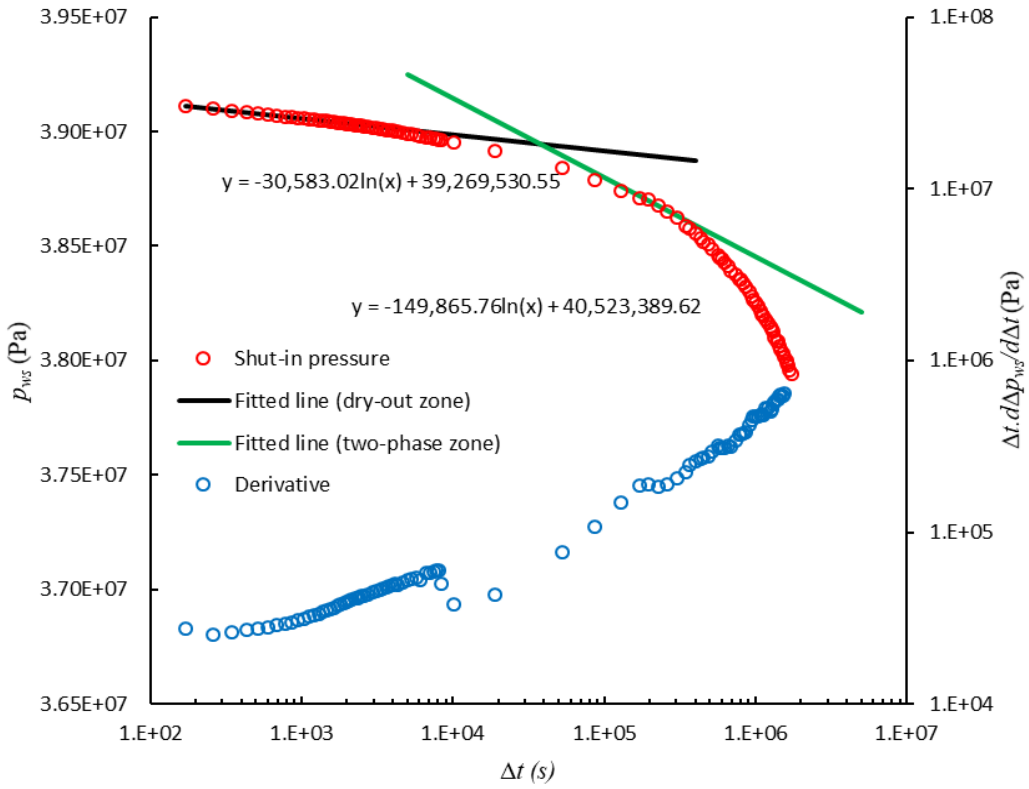

Figure 3.15. Application of the interpretation technique to channeled/linear reservoir

Fig. 3.15 illustrates the diagnostic plot and the application of the interpretation technique. As is shown, the IARF corresponding to the dry-out zone is observed before 0.17 hr. We notice that the IARF corresponding to the two-phase zone is slightly distorted due to the establishment of linear flow regime. This is indicated by the half-slope line observed after 168 hr. Nevertheless, we can notice a short zero-slope line at 48 hr < Δt < 96 hr. The interpretation results, shown in Table 3.10, indicate that the inferred mobilities are in reasonable match with the actual values. The extent

of the dry-out zone slightly underestimates the actual value, while the extent of the plume is highly overestimated. Therefore, in channeled reservoirs, the interpretation technique should not be used to infer the extent of the plume, ant it can be only applied when the IARF is not significantly distorted by the established linear flow due to reservoir channeling. In such situations where the linear flow is dominating (e.g. in hydraulically fractured reservoirs), we should observe clear half slope line behaviors corresponding to the dry-out and two-phase zones on the diagnostic plot. In this case, the whole analytical model and interpretation technique should be revisited. To show the effect of linear flow on the diagnostic plot, we re-ran the channeled reservoir case while reducing the number of gridblocks in *y*-direction from 201 to only 1 with the same linear extension (0.3 km). This would enable pure/dominating linear flow in *x*-direction. The log-log diagnostic plot shown in Fig. 3.16 indicate the half-slope lines corresponding to the dry-out zone and the two-phase zone, rendering the IARF interpretation technique inapplicable, and a whole revisit of the analytical model is required in this case.

Table 3.10. Results for the channeled/linear reservoir case

	Estimated	Actual
Mobility in dry-out zone (mD/cp)	569.1	611.5
Average mobility in two-phase zone (mD/cp)	170.1	117.0
Extent of dry-out zone (m)	27.9	25.1

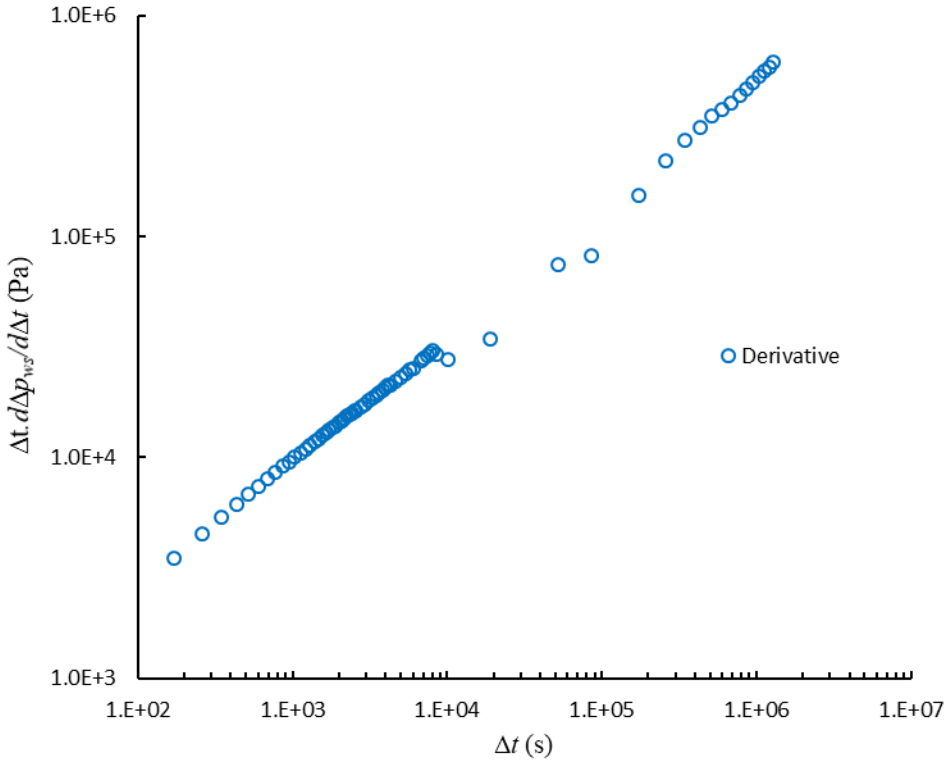

Figure 3.16. Log-log diagnostic plot of dominating linear flow behavior

3.6. Practical Considerations for Optimum Designing of the Falloff Tests

This study has implications for designing falloff tests in CO_2/brine systems. Therefore, and based on the abovementioned interpretation cases, we provide guidelines/considerations for designing falloff tests that should be adopted. Violating these considerations in actual falloff tests may lead to inability of the operator to apply the interpretation technique. The considerations can be detailed as follows:

3.6.1. Wellbore Storage

One challenge in testing CO_2/brine systems is the short duration of the dry-out zone that is mainly caused by the highly-mobile CO_2. As shown by the diagnostic plots of the interpretation cases, the pressure perturbation may pass the dry-out zone within a very short time after well shut-in. As a Consequence, the pressure transient signal corresponding to dry-out zone may be masked by the wellbore storage (WBS), making its characterization unfeasible. In practice, the WBS effect is identified by unit-slope linear behavior for both pressure and its log-derivative on the diagnostic plot. For a falloff test in hydrocarbon reservoirs, the WBS effect diminishes and the reservoir response begins beyond the dimensionless time $t_D > 50*C_D*\exp(0.15s)$ (Chen and Brigham, 1978) where s is the skin factor and C_D is the dimensionless WBS coefficient. On the other hand, identification of the WBS effect is more complex if the WBS coefficient is variable. In GCS operations, the WBS is likely variable given the experience from other injection operations. However, the end of WBS effect can be always identified based on the start of the zero-slope line corresponding to radial flow. The upper bound of the early-time response duration is marked by the dimensionless intersection time between the early-time solution and the intermediate-time solution given by:

$$\Delta t_D = 0.4453 r_{Ddry}^2 \left(\frac{\overline{\lambda_g} c_t}{\lambda_{ave} c_{tg}} \right)^{\frac{\overline{\lambda_g}}{\overline{\lambda_g} - \lambda_{ave}}} \tag{3.57}$$

Eq. 3.57 implies that the duration of the pressure response corresponding to the dry-out zone is a function of: (1) the mobility ratio and the storativity ratio between the dry-out and two-phase zones, and (2) the dimensionless extent of the dry-out zone which is function of the injection rate, injection time duration, formation thickness, and porosity. Specifically, the duration of the dry-out zone is inversely proportional to the diffusivity constant η and the aquifer thickness h which are characteristic properties of the rock and fluid system. Nevertheless, using smart completion for selective injection in certain layer(s) can minimize h which can elongate the duration of the dry-out zone. Also, longer injecting period and/or higher injection rates elongate the pressure signal representative of the dry-out zone. Alternatively, setting a downhole shut-in tool when conducting the test can eliminate the WBS effect that would otherwise obscure development of the early-time response required to characterize the dry-out zone. Also, the hump on the derivative plot marks the beginning of the brine-filled zone influence on the falloff pressure response. The upper bound of the intermediate-time response is given by the dimensionless intersection time between the intermediate-time and the late-time solutions as follows:

$$\left(\Delta t_D + t_{iD}\right)\left(\Delta t_D\right)^{\frac{\lambda_{ave}}{\overline{\lambda_w}}-1} = \left(\frac{r_{DBL}^2\,\overline{\lambda_g}\,c_t}{4\lambda_{ave}c_{tg}}\right)^{\frac{\overline{\lambda_w}}{\lambda_{ave}}}\left(\frac{4t_{iD}c_{tg}\,\overline{\lambda_w}}{r_{DBL}^2 c_{tw}\,\overline{\lambda_g}}\right)\exp\left(\gamma\left(\frac{\overline{\lambda_w}}{\lambda_{ave}}-1\right)\right) \tag{3.58}$$

Eqs. 3.58 implies that the duration of the clean period to observe the intermediate-time response is function of the following factors: (1) the dimensionless injection time, (2) the mobility ratios and the storativity ratios between the three zones, and (3) the dimensionless extent of the dry-out and two-phase zones which are functions of formation thickness, formation porosity, injection rate, and duration of injection period. This means that the duration required to detect different zones' interfaces can be estimated for the given system conditions, and hence, a test with proper duration can be conducted. Specifically, the duration of the upper bounds of the dry-out and two-phase zones can be estimated using the concept of radius of investigation. This method depends on: (1) estimating the extents of both zones, reached at the end of injection period, using the modified Buckley-Leverett equation, (2) using the total compressibility of the two-phase zone assuming the relative permeability is known. For the base case, we found that the upper bound duration of the dry-out zone is 2.88 hr, and that of the two-phase zone is 398 hr which are consistent with the durations observed in our falloff analysis.

3.6.2. Movement of CO_2/brine Interface

At the beginning of shut-in, the wellbore is filled with CO_2. However, over time, brine may re-enter the wellbore during a falloff test. The probable upward movement of the CO_2/brine interface between the perforations and the pressure gauge will cause a time-dependent pressure offset. Consequently, the recorded pressure will not represent the aquifer behavior induced by pressure falloff. Therefore, this phenomenon should be eliminated by setting the gauge as close as possible to the perforation and/or subtracting the pressure offset from the gauge data.

3.6.3. Rate Fluctuations and Shut-downs

As discussed before, the pseudoinjecting time method is used to approximate the variable rate history prior to shut-in. The method honors the last injection rate prior to shut-in since it has the most significant effect on the falloff response, and it satisfies material balance by considering the cumulative fluid that has been injected into the aquifer. The method should be used only when the duration of the last injection period is long enough (about 10 times the falloff period for perfect results) (Spivey and Lee, 2013). Nevertheless, for various reasons, the injection rate may vary throughout the period prior to shut-in, and as a result, the pseudoinjecting time method cannot be applied. The rate fluctuations, if not considered, can distort the falloff signal corresponding to the dry-out zone, the transition region, and may extend to the signal corresponding to the two-phase zone. This situation is common when the well is not equipped with permanent downhole gauge and well shut-in for lowering the gauge into the well is required. In such case, the following measures should be adopted: (1) the falloff pressure/shut-in time data should not be recorded directly after setting the gauge in place, (2) the well should be operated again at the same injection rate it was operating before lowering the gauge, and (3) the injection duration should hold long enough that the temporary shut-in and/or the rate fluctuations prior to shut-in no longer affect the falloff response.

A note that an injection rate of 1 Mt/year of CO_2 is often considered as a standard injection rate and has been used as the injection rate throughout this falloff pressure study. This rate represents the CO_2 produced by a medium-sized coal-fired power plant, but most of the time CO_2 will be injected through multiple wells to reduce the pressure perturbations caused to the aquifer to minimize leakage risks. While we used the 1 Mt/year CO_2 injection, it may not be practical to inject at this rate through a single well to ensure the geomechanical integrity of the formation rock.

3.7. Field Application

3.7.1. Illinois Basin Decatur Project

The Illinois Basin Decatur Project (IBDP) is a demonstration-scale GCS project funded by the US Department of Energy as one of the Regional Carbon Sequestration Partnership projects (Finley et al., 2013; Streibel et al., 2014). The storage reservoir is the Cambrian Mount (Mt.) Simon Sandstone occurring at a depth of 5545 ft. The reservoir is overlain by Eau-Claire shale formation acting as the seal (Couëslan et al., 2014). The lower Mt. Simon Sandstone is the principal target formation with an average porosity and absolute permeability of 20 % and 185 mD respectively. The initial pressure and temperature of the reservoir are 23.0 MPa and 60 ^{o}C, respectively. The corresponding bottomhole CO_2 density and viscosity, respectively, equal to 764 kg/m^3 and 0.066 cp, (Streibel et al., 2014). The reported injection rate prior to shut-in at reservoir conditions is 8632 bbl/day, and the tested injection interval is 55 ft. thick. The raw falloff data were obtained from the DOE/NETL Energy Data eXchange (EDX, 2018), and plotted in Fig. 3.17 that shows the injection/falloff pressure sequence used for inversion. As indicated, the analyzed falloff event lasts for 123 hr after an injection period of about 25 hr.

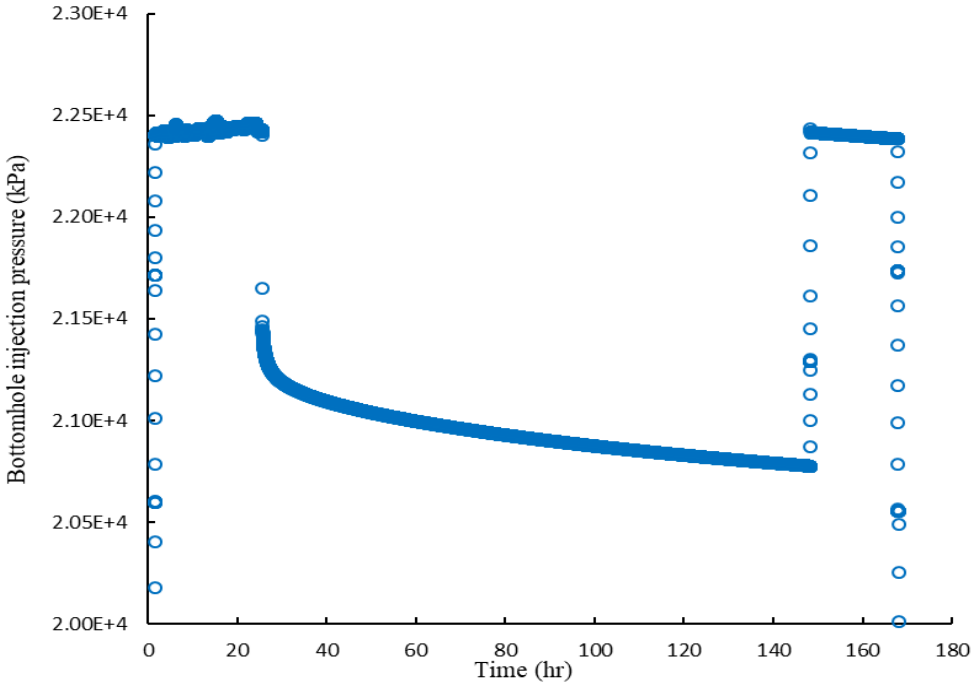

Figure 3.17. Injection/falloff pressure sequence from the test conducted in June 2013 at the IBDP GCS project

As shown on the diagnostic plot (Fig. 3.18), the unit-slope line - that indicates the WBS effect - is observed before 50 sec (0.01 hr). The IARF behavior – that corresponds to the dry-out and two-phase zones - is observed at 150 sec (0.04 hr) < Δt < 350 sec (0.1 hr), and that corresponds to the two-phase zone is observed at 5000 sec (1.39 hr) < Δt < 15000 sec (4.17 hr). The data points corresponding to these intervals are line fitted on semi-log scale shown in Fig. 3.19. The two fitted lines intersect at 1233 sec (0.34 hr). The interpretation results (Table 3.11) are obtained using the developed technique considering the following properties c_r = 5.0×10^{-7} 1/kPa, c_w = 4.02×10^{-7} 1/kPa, and c_g = 1.49×10^{-5} 1/kPa (evaluated at the bottomhole conditions). The fluid mobilities are inferred to be 2291.4 mD/cp (for the dry-out zone), and 1112 mD/cp (for the two-phase zone). With this, the absolute permeability is estimated 190 mD (based on 0.066 cp CO_2 viscosity, and assuming 20 % absolute permeability reduction due to salt dry-out in the near wellbore region). This estimation matches the reported average absolute permeability for the lower Mt. Simon Sandstone which is 185 mD. The inferred radial extent of the dry-out zone is 22.4 m, and it compares well with the value estimated using the modified Buckley-Leverette equation. Fig. 4 in Couëslan et al. (2014) show that approximately 52,000 metric tons cumulative amount of CO_2 were injected until before the falloff test in June 2013. Using the modified Buckley-Leverett equation, the extents of the dry-out and two-phase zones are calculated to be 23.3 m and 384.2 m respectively (knowing porosity = 20 % and interval thickness = 55 ft., and assuming relative permeability is matched using Corey's model with the saturation exponents of 3.0, residual brine saturation of 0.45, and the end-point relative permeabilities of 1.0 for brine and 0.33 for CO_2). However, the extent of two-phase zone is highly overstimated using the interpretation technique.

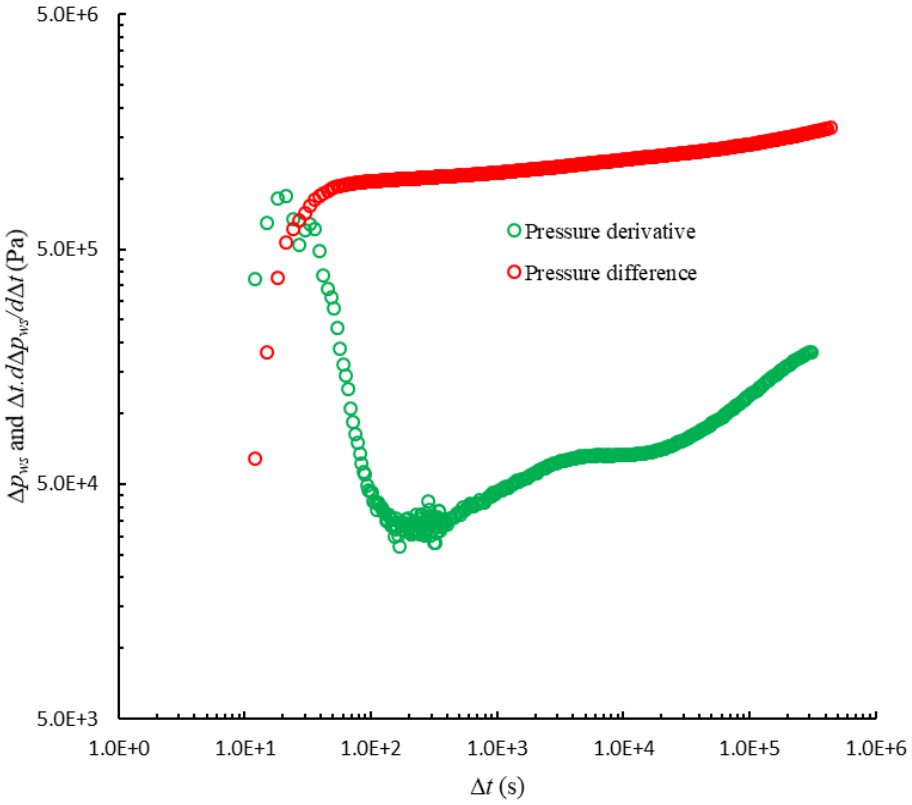

Figure 3.18. Log-log diagnostic plot of the falloff data from the test conducted in June 2013 at the IBDP GCS project

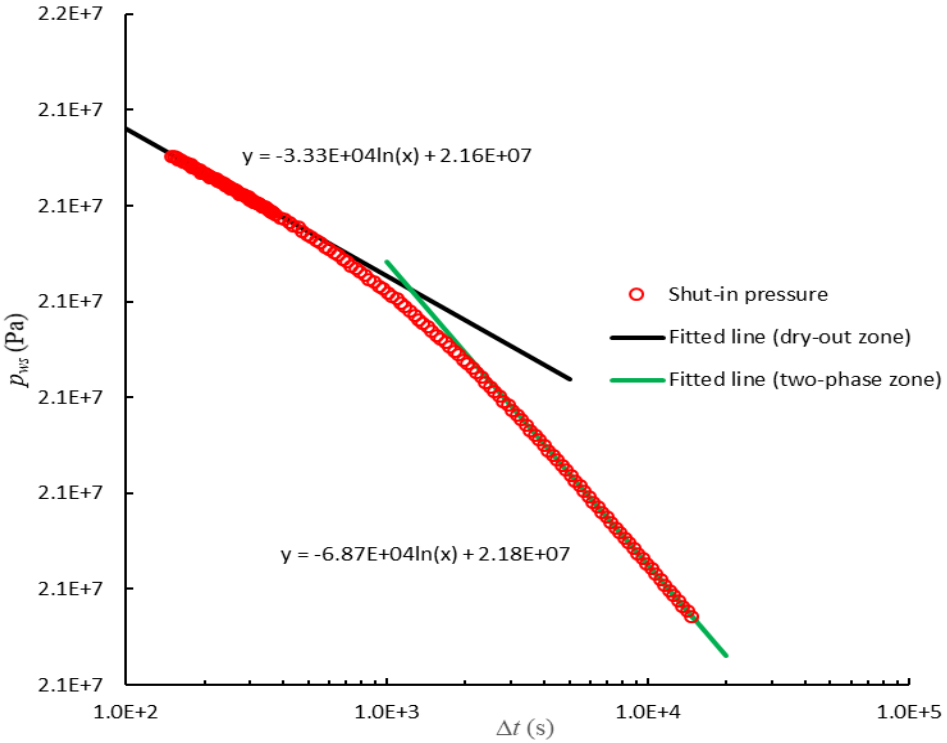

Figure 3.19. Application of the graphical technique to the falloff data from the test conducted in June 2013 at the IBDP GCS project

Table 3.11. Interpretation results for a falloff test at the IBDP GCS project

	Interpretation methodology	Using Buckley-Leverette equation
Mobility in dry-out zone (mD/cp)	2291.4	--
Average mobility in two-phase zone (mD/cp)	1112.0	--
Absolute permeability of the reservoir (mD)	190	185 (average from logs and core analysis)
Extent of dry-out zone (m)	22.4	23.3
Extent of two-phase zone (m)	--	384.2

3.7.2. MRCP's State-Charlton GCS Validation Test

Some practical falloff tests may not have considered one (or more) of the aforementioned design measures which caused masking of the early-time pressure responses. One example is falloff data from the State-Charlton test which is one of the validation tests conducted under Phase II of the Midwest Regional Carbon Sequestration Partnership's (MRCSP's) project. The State-Charlton CO_2 injection system consists of two wells; one is an injector well and the other is for monitoring. The project was initiated in 2008 where CO_2 was injected over two campaigns in the target saline formation. During the first campaign, 10241 tons were injected over 18 days where a falloff test was conducted. The data is obtained from DOE/NETL website (EDX, 2018), and plotted in Fig.

3.20. We investigated the falloff data using the diagnostic plots. The WBS effect obscures the early-time responses as indicated by the unit-slope line behavior of the pressure change and the derivative plots (Fig. 3.21). Thus, the developed interpretation technique cannot be used here.

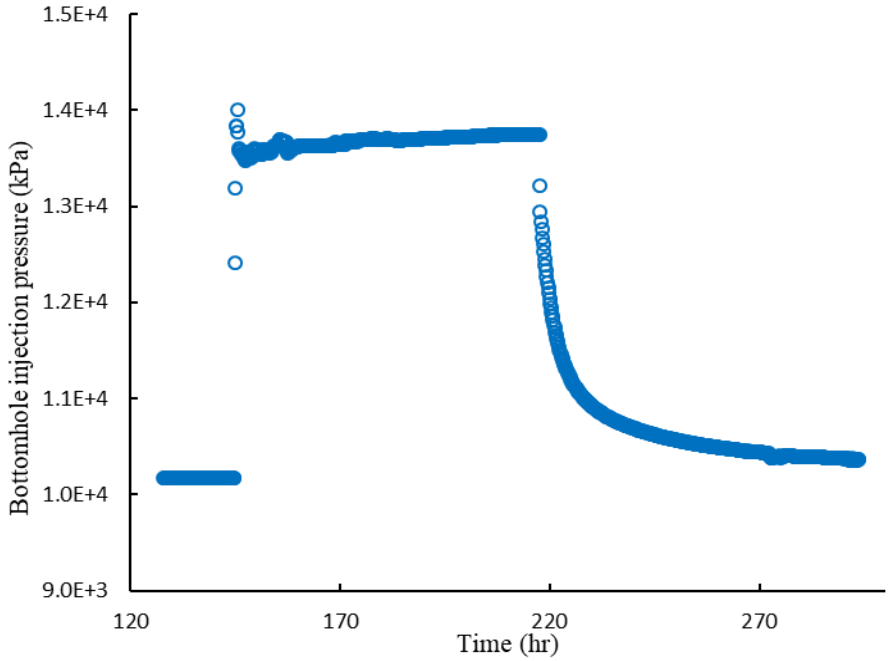

Figure 3.20. Bottomhole pressures from the State-Charlton validation test

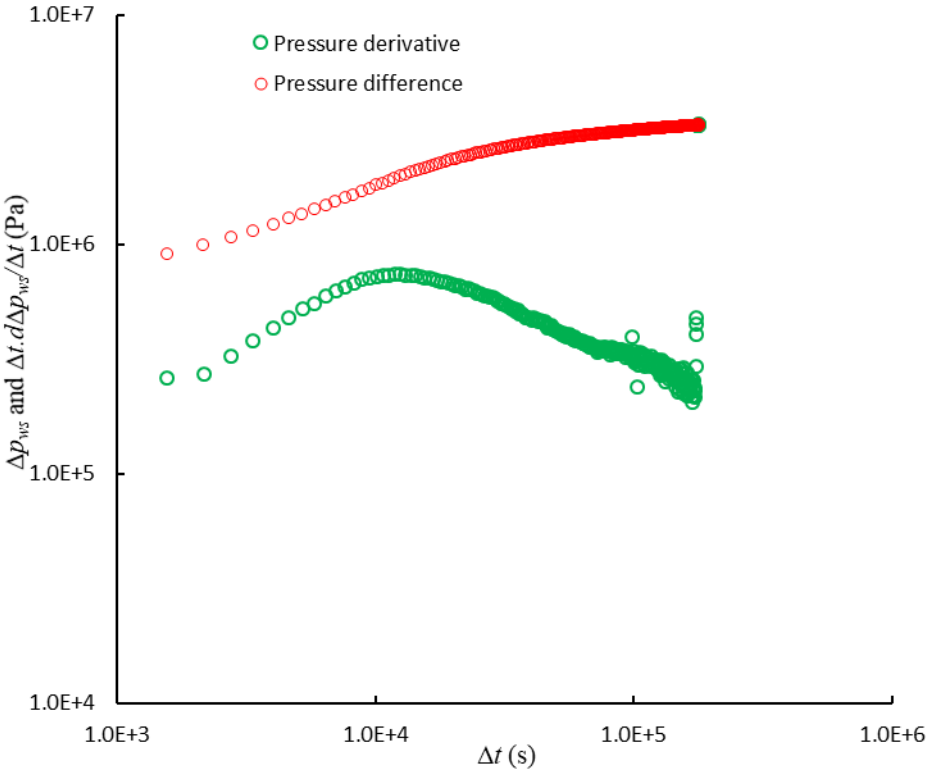

Figure 3.21. Log-log diagnostic plot of the falloff pressure difference and log-derivative

3.7.3. MRCP's State-Charlton GCS Validation Test

The Burger plant project is another validation test of the MRCSP Phase II. The primary objective is to test CO_2 storage potential in three saline formations in the Appalachian basin. During the test, around 3000 tons of CO_2 were injected over 4-6 weeks. We analyzed four pressure falloff events; two in Oriskany formation, one in Salina formation, and one in Clinton formation using the log-log diagnostic plot of the pressure difference and log-derivative. The bottomhole pressure data were obtained from DOE/NETL website (EDX, 2018) and plotted in Figs. 3.22, 3.25, and 3.27. For all cases, WBS obscures the early-time responses (as displayed in Figs. 3.23, 3.24, 3.26, and 3.28), rendering the technique inapplicable.

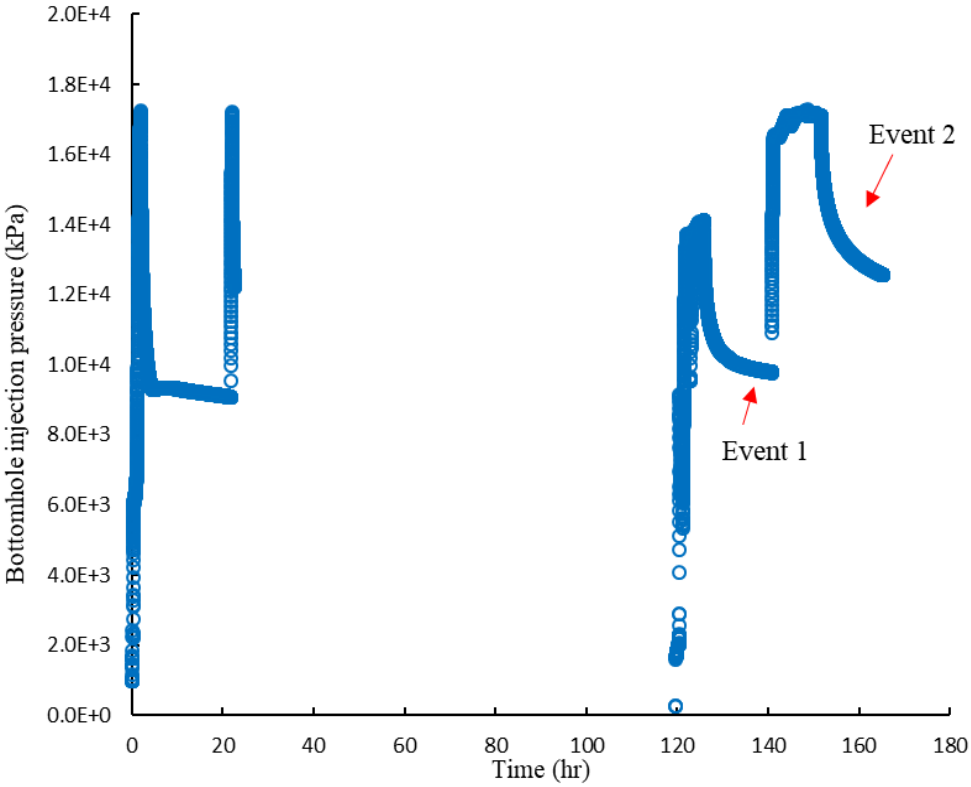

Figure 3.22. Bottomhole pressures from Oriskany formation of the Burger Plant validation test

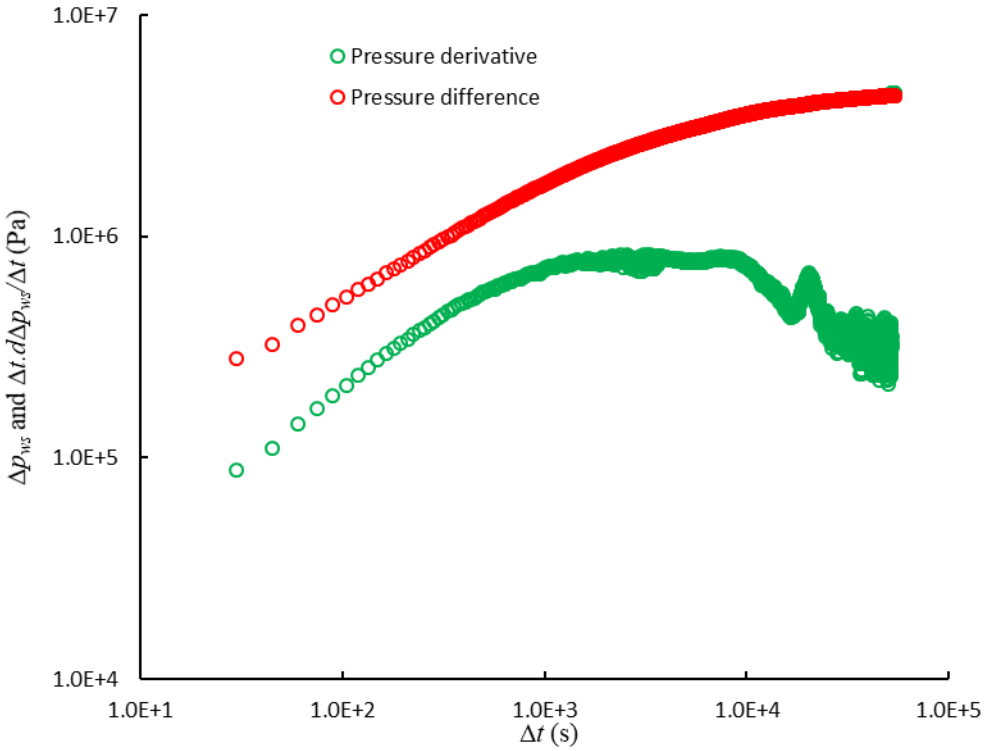

Figure 3.23. Log-log diagnostic plot of the falloff pressure difference and derivative of the falloff events in Oriskany formation for falloff event 1

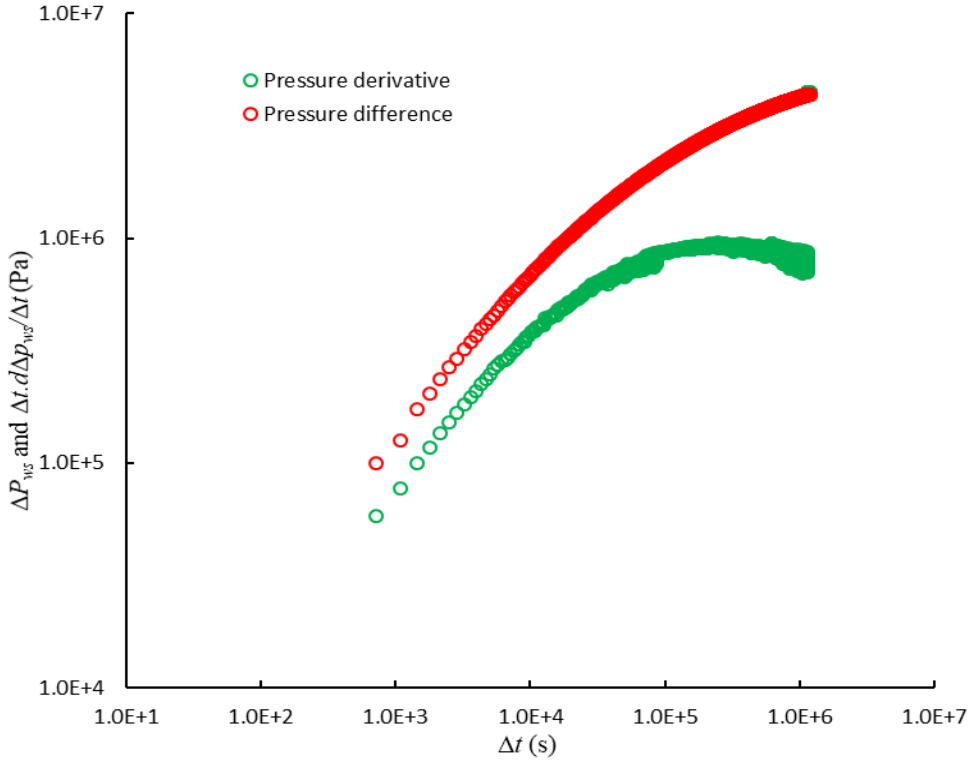

Figure 3.24. Log-log diagnostic plot of the falloff pressure difference and derivative of the falloff events in Oriskany formation for falloff event 2

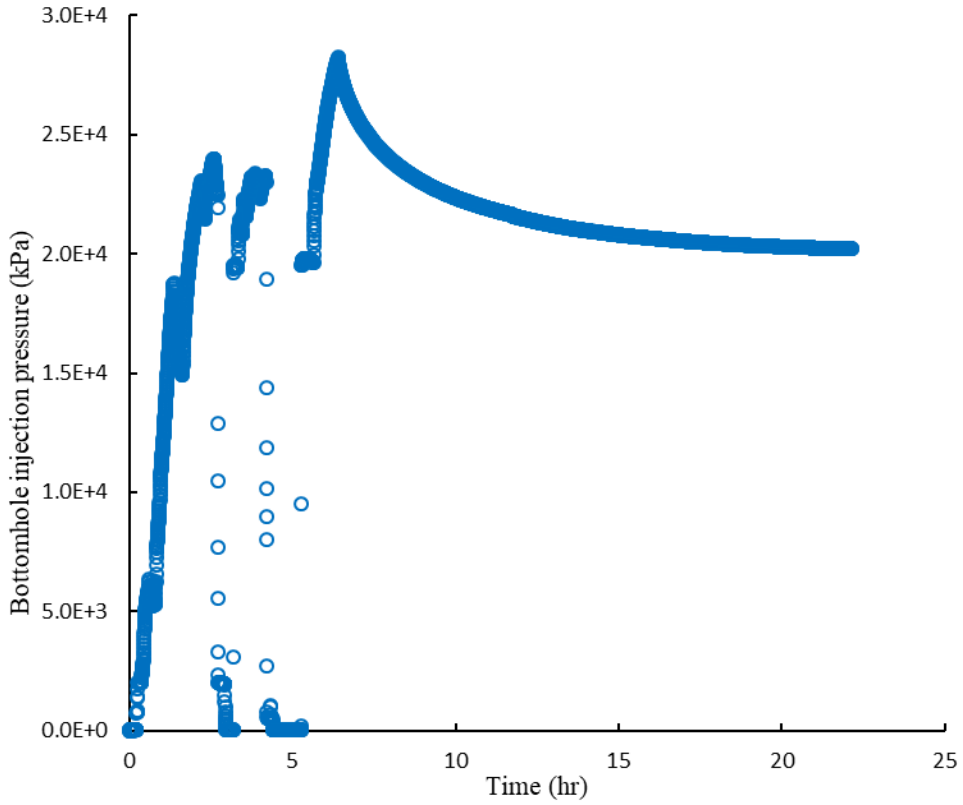

Figure 3.25. Bottomhole pressures from the Salina formation of the Burger Plant validation test

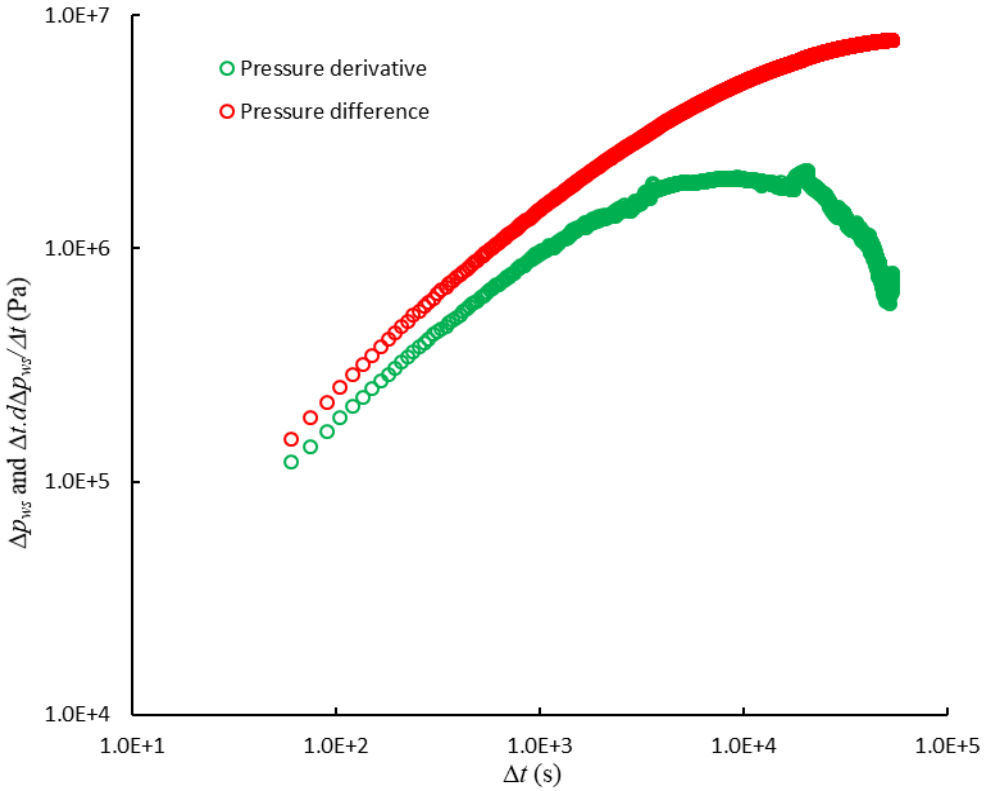

Figure 3.26. Log-log diagnostic plot of the falloff pressure difference and log-derivative of the falloff data from the Salina formation of the Burger Plant validation test

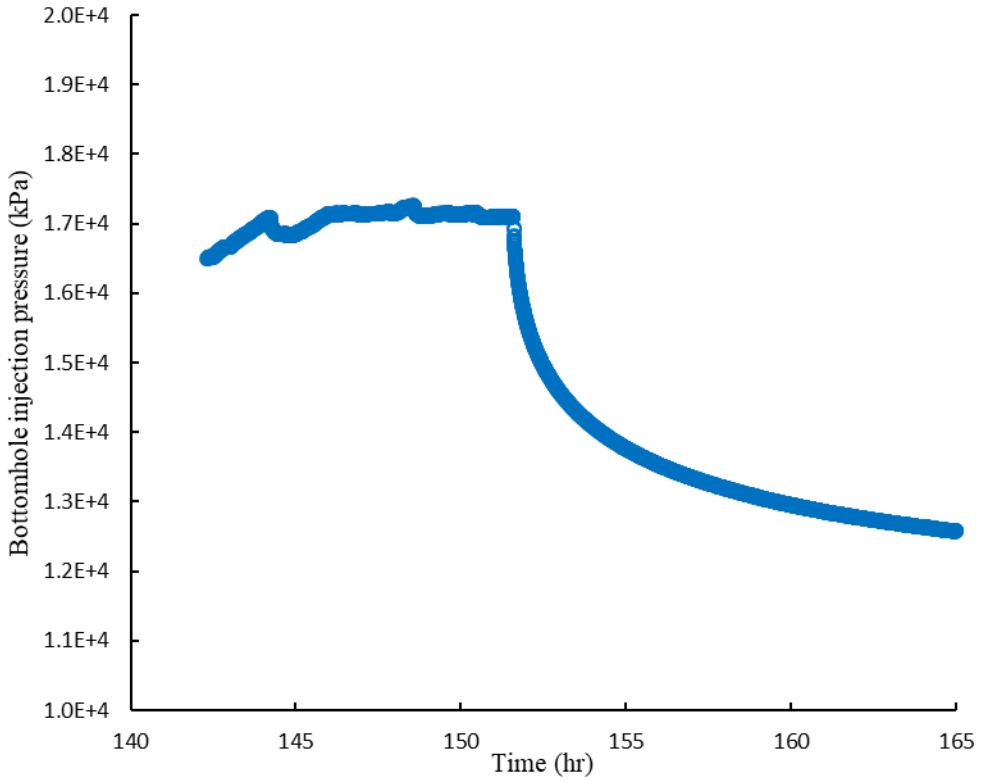

Figure 3.27. Bottomhole pressures from the Clinton formation of the Burger Plant validation test

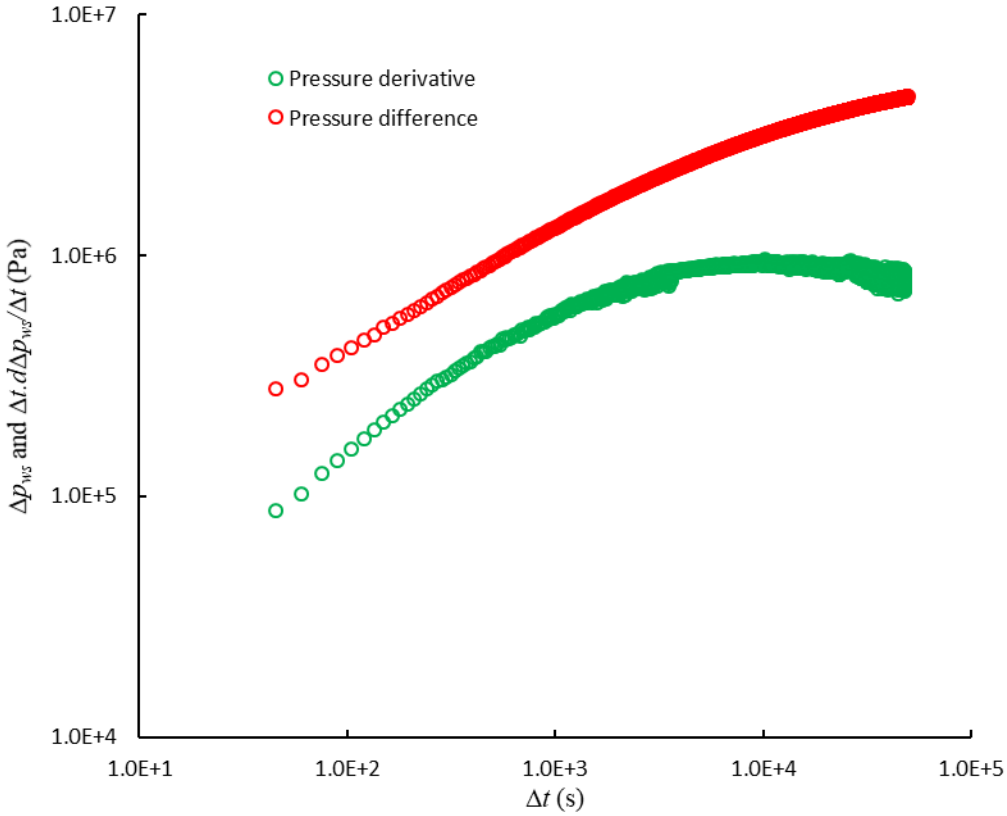

Figure 3.28. Log-log diagnostic plot of the falloff pressure difference and log-derivative of the falloff data from the Clinton formation of the Burger Plant validation test

Chapter 4. Injection Data Analysis to Estimate the Ultimate Storage Capacity of Deep Closed Saline Formations

In this chapter, the application of RTA to assess the storage potential of a closed storage saline formation is presented through developing a two-step graphical interpretation technique. First, a mathematical expression is introduced to infer the pore volume through interpreting the available data of injection rate, pressure, and cumulative volume. The expression extends the pseudo-steady state (PSSF) solution, which predicts the overpressure during CO_2 injection into closed systems, to account for variable pressure/rate conditions. The key concept that allows this extension is the material balance time where CO_2 injection data can be interpreted regardless of the pressure/rate history schedule. The utilization of material balance time to interpret CO_2 injection data of variable schedule is validated against synthetic data representing different well operating conditions. The technique is then extended to predict the storage capacity using material balance techniques. The developed graphical interpretation technique is next applied to synthetic data considering different well operating conditions to address its reliability. Finally, the practical potential of the technique is substantiated via application to real field dataset obtained from a large-scale GCS project.

4.1. Problem Description and Mathematical Model Derivation

Considering the closed CO_2/brine system shown in Fig. 4.1 (a). With CO_2 injection, a saturation profile is formed in the aquifer soon after the start of injection. As we mentioned before, the system can be approximated by three different zones of saturation separated by two radial discontinuities (Fig. 4.1 (b)) following the modified Buckley and Leverett (1942) theory.

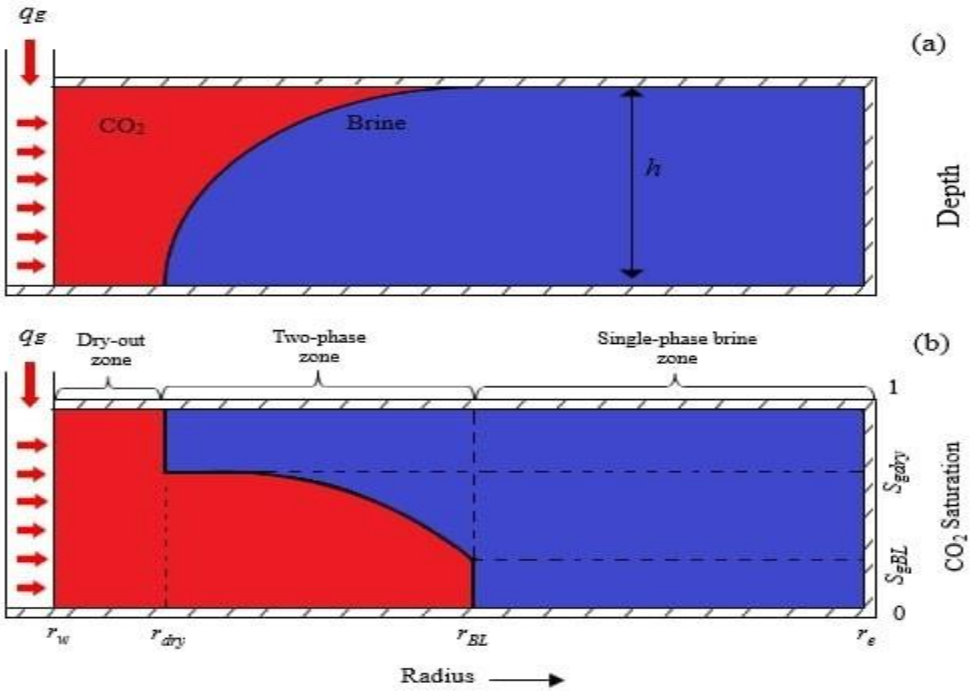

Figure 4.1. Schematic illustration (not to scale) of (a) the physical CO_2/brine system with sharp interface, and (b) three-zone approximation of the physical system based on the Buckley-Leverett displacement theory

Neglecting the gravitational forces and capillarity, Ehlig-Economides and Economides (2010) provided an analytical model to estimate the bottomhole pressure p_{wi} during CO_2 injection via a fully penetrating vertical well. The overpressure during the boundary-dominated flow period is:

$$p_{wi} - p_i = \frac{q_g B_g}{2\pi kh}\left[\frac{\mu_g}{\overline{k_{rg}}}\ln\left(\frac{r_{dry}}{r_w}\right) + \left(\frac{k_{rg}}{\mu_g} + \frac{k_{rw}}{\mu_w}\right)^{-1}_{S_{g,ave}} \ln\left(\frac{r_{BL}}{r_{dry}}\right) + \mu_w \ln\left(\frac{0.472 r_e}{r_{BL}}\right)\right] + \frac{Q_g B_g}{V_p c_t} \qquad (4.1)$$

where p_I is the initial reservoir pressure, q_g is CO_2 injection rate at surface conditions, B_g is the gas formation volume factor, k and h are the reservoir absolute permeability and thickness respectively, μ_g and μ_w are viscosities of CO_2 and brine respectively, r_{dry} and r_{BL} are the radii of the dry-out and two-phase zones respectively, r_w is the wellbore radius, r_e is the outer radius of the reservoir, $\overline{k_{rg}}$ is the gas relative permeability in the dry-out zone, k_{rg} and k_{rw} are the relative permeabilities of CO_2 and brine evaluated at the average gas saturation in the two-phase, Q_g is the total injected volume of CO_2 at standard conditions, V_p is the reservoir pore volume, and c_t is the total system compressibility. The radial extents of the dry-out and two-phase zones can be obtained using the modified Buckley-Leverett displacement theory (Burton et al., 2008; Noh et al., 2007; Zeidouni et al., 2009).

Ehlig-Economides and Economides (2010) did not derive Eq. 4.1 in their work, but they extended Burton et al. (2008)'s solution which was derived for steady-state flow (SSF) in 1D radial system considering the relationship between the SSF and PSSF equations. Burton et al. (2008) treated the reservoir as a homogeneous system of which the mobility can be assigned considering flow in series through the three-zone system. To accommodate this treatment, the mobility of each zone was assumed constant. Specifically, the gaseous phase saturation in the two-phase zone was assumed constant and approximated by the arithmetic average of the gaseous phase saturations at the interfaces. The relative permeabilities to the gaseous and the aquoues phases within the two-phase zone were considered fixed and evaluated at the arithmetic average gaseous phase saturation. Additionally, the fluids' viscosities were considered constant and evaluated at the initial reservoir pressure and temperature. In addition to the aformenetioned assumptions which were necessary to obtain the pressure reponse assuming a given saturation distribution, more assumptions have been implicitly made in obtaining the saturation distribution a priori. The assumptions made in deriving the three-zone saturation distribution solution are: 1D radial flow, homogenous and isotropic reservoir with uniform thickness, isothermal flow, and negligible gravity and capillary forces. Despite the aforementioned assumptions, the model has been reliably used to evaluate the pressure especially at the wellbore where viscous forces are dominant and given the generally small window over which the saturations may vary within the two-phase zone (Burton et al., 2008; Oruganti and Mishra, 2013).

Utilizing the concept of material balance time (t_{MB}), Eq. 4.1 can be rearranged - by dividing both sides by $q_g B_g$ - as follows:

$$\frac{p_{wi}-p_i}{q_g B_g}=\frac{1}{2\pi kh}\left[\frac{\mu_g}{k_{r,S_g=1}}\ln\left(\frac{r_{dry}}{r_w}\right)+\left(\frac{k_{rg}}{\mu_g}+\frac{k_{rw}}{\mu_w}\right)^{-1}_{S_{g,ave}}\ln\left(\frac{r_{BL}}{r_{dry}}\right)+\mu_w\ln\left(\frac{0.472r_e}{r_{BL}}\right)\right]+\frac{1}{V_p c_t}t_{MB} \qquad (4.2)$$

where: $t_{MB}=\frac{Q_g}{q_g}$

One characteristic of material balance time function is its rapid growth over time. As a result, the 1st term in the right-hand side of Eq. 4.2 can be neglected as compared to the 2nd term soon after the BDF is established. Therefore, Eq. 4.2 can be approximated by:

$$\frac{p_{wi}-p_i}{q_g B_g}=\frac{\Delta p}{q_g B_g}\approx\frac{1}{V_p c_t}t_{MB} \qquad (4.3)$$

Eq. 4.3 implies the following:

i. Using the material balance time, injection wells - operating at constant bottomhole pressure or operating at variable injection rate/pressure schedule - will act as if they were operating at constant injection rate under BDF conditions.

ii. A log-log plot of the rate-normalized pressure buildup ($\Delta p/q_g B_g$) versus material balance time (t_{MB}) should exhibit a unit-slope line behavior during the BDF period.

iii. A Cartesian plot of ($\Delta p/q_g B_g$) versus t_{MB} should exhibit a straight line behavior during the BDF period. The pore volume of the reservoir can be inferred from this slope.

A note that the assumption of negligible b_r here is only to show that BDF data would follow a unit-slope (or closed to unit-slope) behavior on the log-log diagnostic graph. This would help to identify the data which correspond to the BDF period. Nevertheless, it doesn't affect our analysis since b_r will not be neglected throughout the calculations as it is required to estimate the storage capacity.

4.2. Description of the Interpretation Technique

4.2.1. Inference of the Reservoir Pore Volume

Based on Eq. 4.3, the pore volume of a closed storage formation can be inferred as follows

i. Measure/estimate the bottomhole injection pressure, rate, and cumulative CO_2 volume.

ii. Calculate the rate-normalized pressure buildup $\Delta p/q_g B_g$ and material balance time t_{MB}.

iii. Plot $\Delta p/q_g B_g$ versus t_{MB} on log-log scale and identify the data points exhibiting unit-slope line which correspond to the BDF period.

iv. A Cartesian plot of $\Delta p/q_g B_g$ versus t_{MB}, corresponding to the BDF period, should show a straight line behavior with slope *m* given by:

$$m = \frac{1}{V_p c_t} \tag{4.4}$$

v. With known compressibilities of rock (c_r) and brine (c_r), the pore volume is given by:

$$V_p = \frac{1}{m c_t} = \frac{1}{m\left(c_r + c_w\right)} \tag{4.5}$$

4.2.2. Estimation of the Ultimate Storage Capacity – Rigorous Approach

With CO_2 injection in a closed system, and accounting for material balance, the average reservoir pressure will increase over time following Ehlig-Economides and Economides (2010):

$$\bar{p} = p_i + \frac{1}{V_p c_t} Q_g B_g \tag{4.6}$$

A plot of $\bar{p}$ versus $Q_g B_g$ on a Cartesian scale plot will follow a straight line behavior. The ultimate storage capacity is estimated by extrapolating the straight line to the maximum allowable injection pressure (p_{max}). Although, $\bar{p}$ may not available in practice, it can be estimated using the available pressure and rate data. Combining Eqs. 4.1 and 4.6, the average reservoir pressure $\bar{p}$ is given by (Ehlig-Economides and Economides, 2010):

$$\bar{p} = p_{wi} - q_g B_g b_r \tag{4.7}$$

where:

$$b_r = \frac{1}{2\pi kh}\left[\frac{\mu_g}{k_{rg}} \ln\left(\frac{r_{dry}}{r_w}\right) + \left(\frac{k_{rg}}{\mu_g} + \frac{k_{rw}}{\mu_w}\right)^{-1}_{S_{g,ave}} \ln\left(\frac{r_{BL}}{r_{dry}}\right) + \mu_w \ln\left(\frac{0.472 r_e}{r_{BL}}\right)\right] \tag{4.8}$$

Accordingly, the ultimate storage capacity can be estimated using the following procedure:

i. Given ϕ and *h* are known, calculate the external radius of the reservoir as follows:

$$r_e = \sqrt{\frac{V_p}{\pi \phi h}} \tag{4.9}$$

ii. Given the relative permeability information is known, calculate the radial extents of the dry-out and two-phase zones using the extended fractional flow curve (Burton et al., 2008) (see details in Appendix C):

$$r_{dry} = \sqrt{\frac{Q_g B_g}{\pi \phi h} \frac{df_g}{dS_g}\bigg|_{S_{gdry}}} \tag{4.10}$$

$$r_{BL} = \sqrt{\frac{Q_g B_g}{\pi \phi h} \frac{df_g}{dS_g}\bigg|_{S_{gBL}}} \tag{4.11}$$

Where f_{gdry} and f_{gBL} are the values of gas fractional flow at r_{dry} and r_{BL} respectively.

iii. With known absolute permeability and fluids viscosities, calculate b_r using Eq. 4.8.

iv. With b_r, and the injection data, calculate $\bar{p}$ using Eq. 4.7.

v. Plot $\bar{p}$ versus $Q_g B_g$ on a Cartesian scale and extrapolate the straight line to the p_{max}.

vi. Read the corresponding $Q_g B_g$ which represents the ultimate storage capacity the formation can accommodate without exceeding the pressure limit.

vii. Calculate the storage efficiency (E) by dividing the ultimate storage capacity by the reservoir pore volume.

4.2.3. Estimation of the Ultimate Storage Capacity – Approximate Approach

Estimation of the ultimate storage capacity - using the rigorous approach - requires some reservoir parameters (e.g. the relative permeability) to be known a priori (see Eq. 4.8). This may not be the case in practice. On the other hand, the term b_r – which is required to calculate $\bar{p}$ in the rigorous approach - reaches a quasi-stable value during the BDF period. This value can be approximated by the *y*-intercept of the straight line of the Cartesian plot of $\Delta p/q_g B_g$ versus t_{MB}. Therefore, we propose an approximate approach to estimate the storage capacity as follows:

i. In terms of b_r, Eq. 4.2 can be written as follows:

$$\frac{p_{wi} - p_i}{q_g B_g} = b_r + \frac{1}{V_p c_t} t_{MB} \tag{4.12}$$

ii. Plot $\Delta p/q_g B_g$ versus t_{MB} and line-fit the data points corresponding to the BDF period.

iii. Read the *y*-intercept of the straight line. This intercept approximates the quasi-stable value of b_r according to Eq. 4.12.

iv. Calculate $\bar{p}$ using Eq. 4.7. Then, estimate the ultimate storage capacity and the storage efficiency using the same steps of the rigorous appraoch.

Fig. 4.2 displays a flowchart which summarizes the steps of the two-step graphical interpretation

technique, and Fig. 4.3 shows the behavior of the time-dependent term b_r during the BDF period for different operating conditions of the injection well.

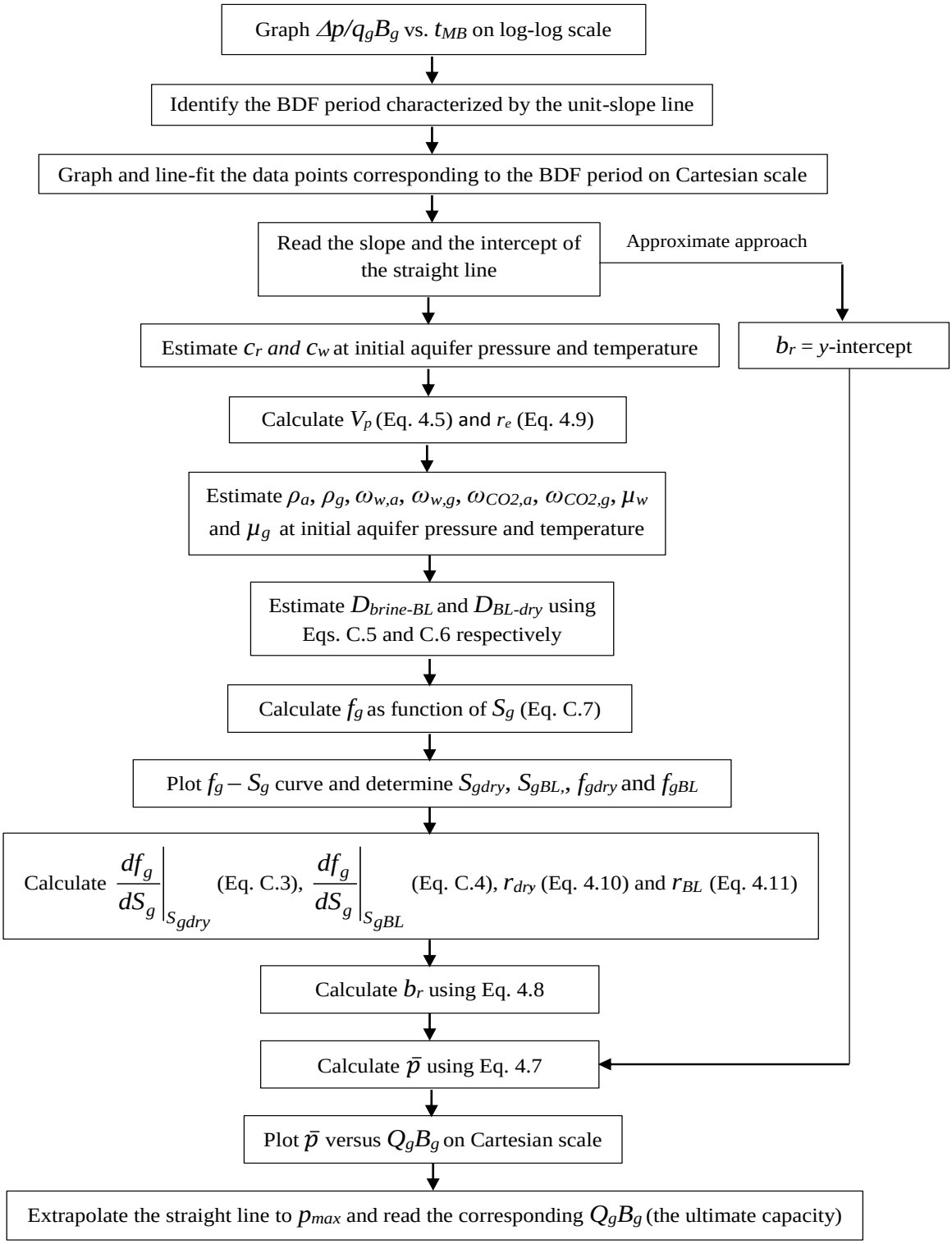

Figure 4.2. A flowchart of the developed two-step graphical interpretation technique

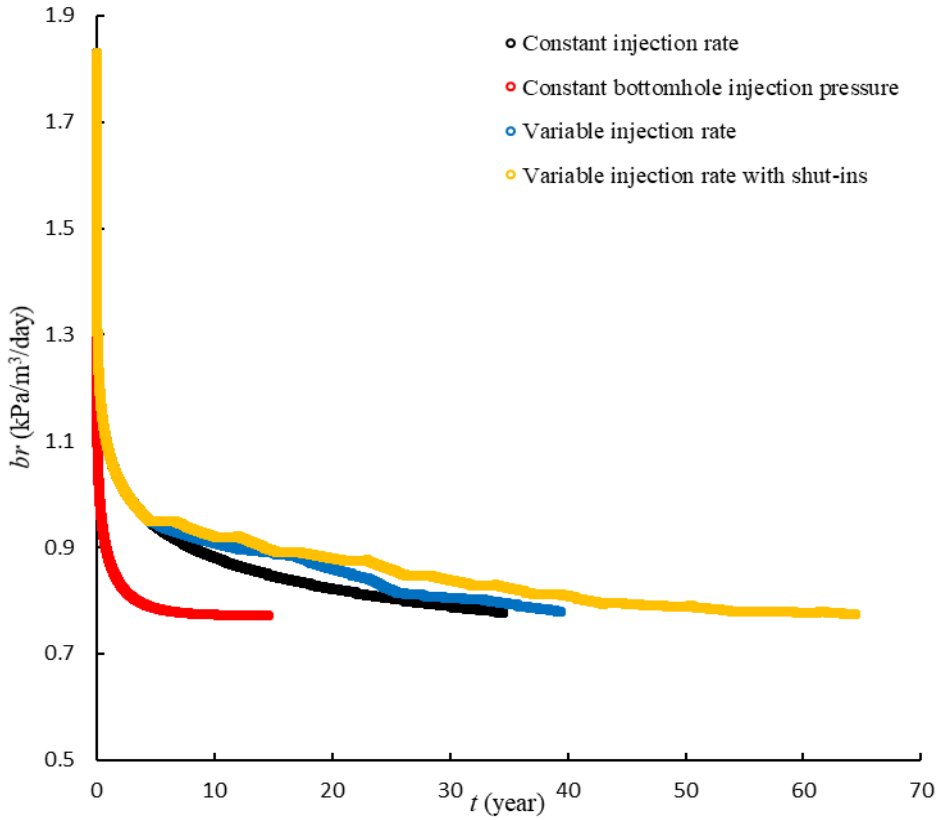

Figure 4.3. Behavior of the time-dependent term (b_r) - estimated using Eq. 4.8 - for synthetic cases representing different well operation conditions

4.3. Validation of the Applicability of Material Balance Time to Interpret CO_2 Injection Data of Variable Schedule

The potential application of the material balance time to CO_2 injection data is substantiated through four synthetic cases representing different operating conditions of the injection well. The synthetic pressure and rate data are generated using CMG-IMEX (2019). The PVT data are estimated using Hassanzadeh et al. (2008)'s algorithm which converts the compositional CO_2/brine properties into black oil PVT properties. The relative permeability data are generated using Corey's model (Corey, 1954b), and the relative permeability to gas in the dry-out zone is assigned 0.8 to model absolute permeability reduction caused by salt precipitation in the vicinity of the wellbore. The capillary pressure data is generated using van Genuchten (1980) formulation considering pore-size distribution parameter and threshold values of 0.8 and 20 kPa respectively. These values represent a coarse-grained high quality reservoir with a low capillary pressure curve (Alkan et al., 2010). The input data for simulation is detailed in Table 4.1. A constant injection rate (CR) case is used as the benchmark case where the well is assigned a constant rate of 0.2 Mt/year. The second case simulates a well operating at a constant bottomhole pressure (CP) while the last two cases represent a well operating at variable injection rates (VR) with and without shut-in periods, respectively. Comparison of the diagnostic plots of the CP and the VR cases with the benchmark CR case is used to validate the application of our graphical approach and material balance time analysis discussed earlier. A note that for both of CR and VR cases, CO_2 injection is terminated when the

bottomhole injection pressure reaches the maximum allowable injection pressure of 30.2 MPa (90 % of the formation fracture pressure). For CP case, injection continues until a specified economic injection rate (i.e. injection rate below which injection is not economic) of 27.4 ton/day is reached.

Table 4.1. Input data for simulation

Parameter	Value
Aquifer area (km^2)	100
Thickness (m)	40
Depth to top (m)	2000
Number of grids (radial×vertical)	300×20
Temperature (^oC)	70
Porosity (fraction)	0.25
Horizontal permeability (mD)	100
Vertical permeability (mD)	10
Dip angle (^{o})	0
Rock compressibility (1/kPa)	5.0×10^{-7}
Initial pressure (MPa)	20.1
Fracture pressure (MPa)	33.6
Maximum allowable injection pressure (MPa)	30.2
Brine viscosity (cp)	0.453
CO_2 viscosity (cp)	0.051
Brine compressibility (1/kPa)	4.11×10^{-7}
CO_2 compressibility (1/kPa)	3.08×10^{-5}
CO_2 density (kg/m^3)	644.4
Residual brine saturation (fraction)	0.30
Gas relative permeability in the dry-out zone (-)	0.80
CO_2 endpoint relative permeability (-)	0.33
Gas relative permeability exponent (-)	2.0
Brine relative permeability exponent (-)	2.0

4.3.1. Constant Bottomhole Pressure Case

In this case, the well is assigned a constant bottomhole pressure equal to the maximum allowable injection pressure of 30.2 MPa. All other properties are identical to the base case (Table 4.1). The comparison of the log-log diagnostic plot between CP and CR cases is illustrated by Fig. 4.4 where the rate-normalized pressure change is plotted versus material balance time. Noting that, for the CR case, material balance time is, by definition, the same as the real time of injection. The comparison, shown in Fig. 4.4, illustrates that both CP and CR cases will exhibit a unit-slope line behavior during the BDF period. This means that the injection well operating at CP will behave the same way as that operating at CR during the BDF period when the material balance time is used.

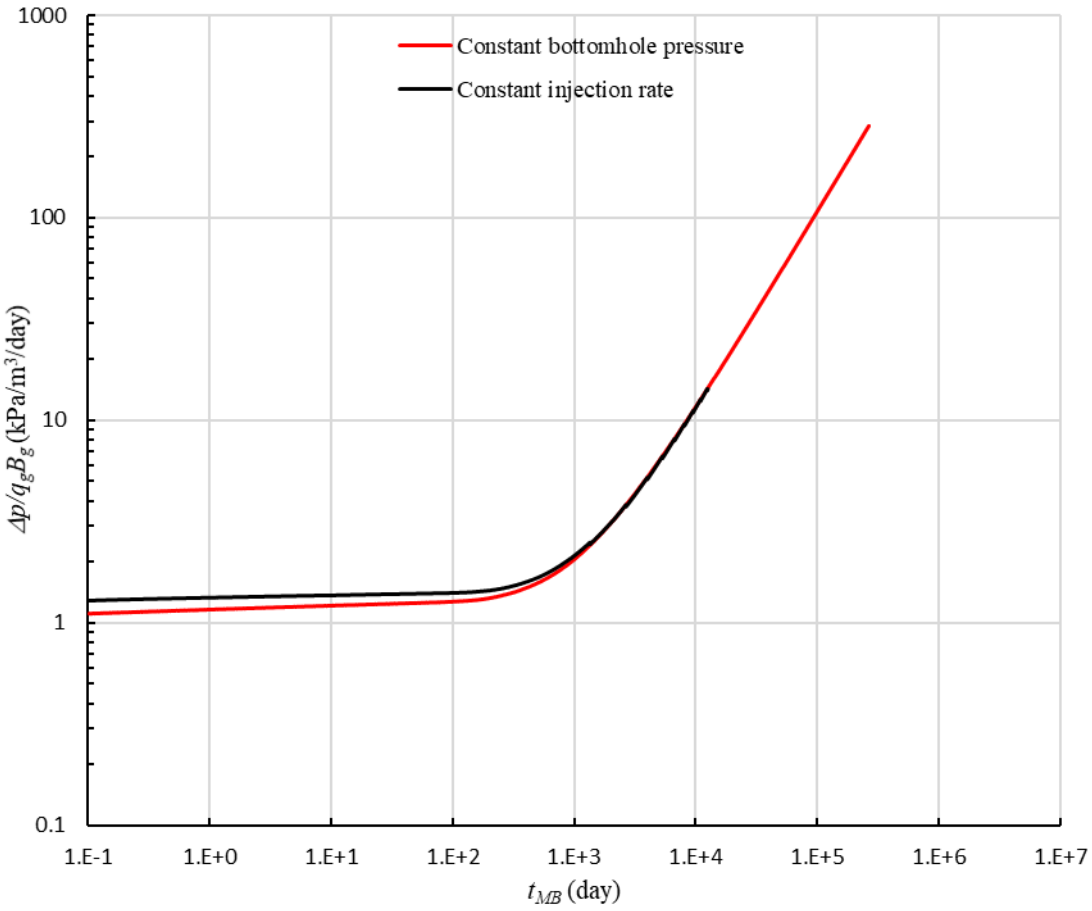

Figure 4.4. Log-log diagnostic plot of rate-normalized pressure buildup versus material balance time for the constant bottomhole pressure and constant injection rate cases

4.3.2. Variable Injection Rate Case

The usefulness of the material balance time is further investigated through application to a variable injection rate case. In this case, the well is assigned a variable injection rate without shut-ins as shown in Fig. 4.5 (a). The injection rates range from 0.05 to 0.5 Mt/year (137 to 1370 ton/day), covering a practical range which can be utilized in storage projects. Rest of the properties are identical to the base case (Table 4.1). A comparison of the log-log diagnostic plot with the CR base case is shown in Fig. 4.6. Again, during the BDF period, the VR case exhibits unit-slope behavior when the material balance time is used. Nevertheless, few data points can deviate a little bit from the unit-slope line behavior due to rate fluctuations and corresponding transient pressure response before BDF is established. Noting that material balance time, by definition, shuffles data points (i.e. some data occurring at late injection times can appear earlier and vice versa).

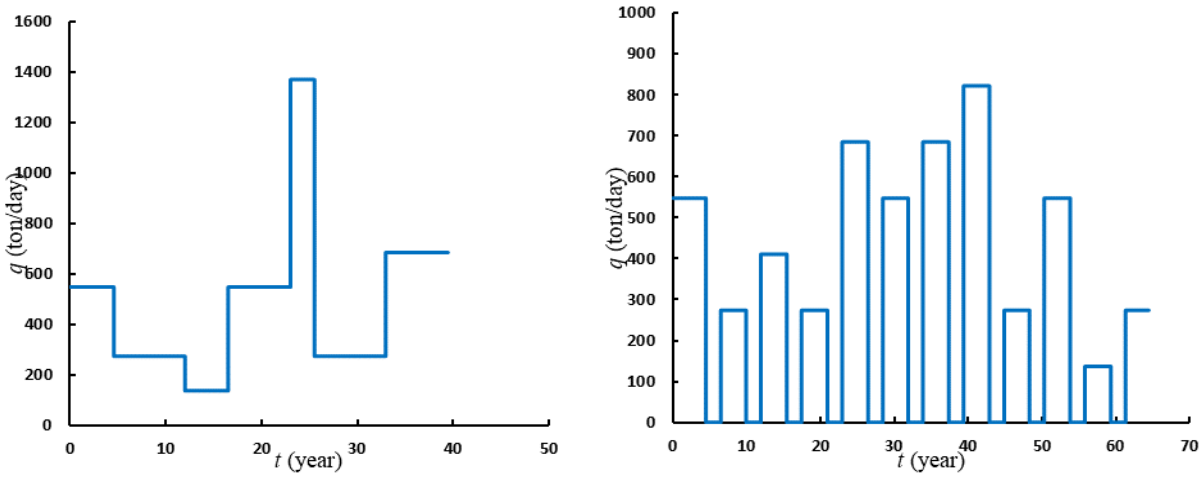

Figure 4.5. Injection rate history for (a) variable rate case without shut-ins (b) variable rate case with shut-ins

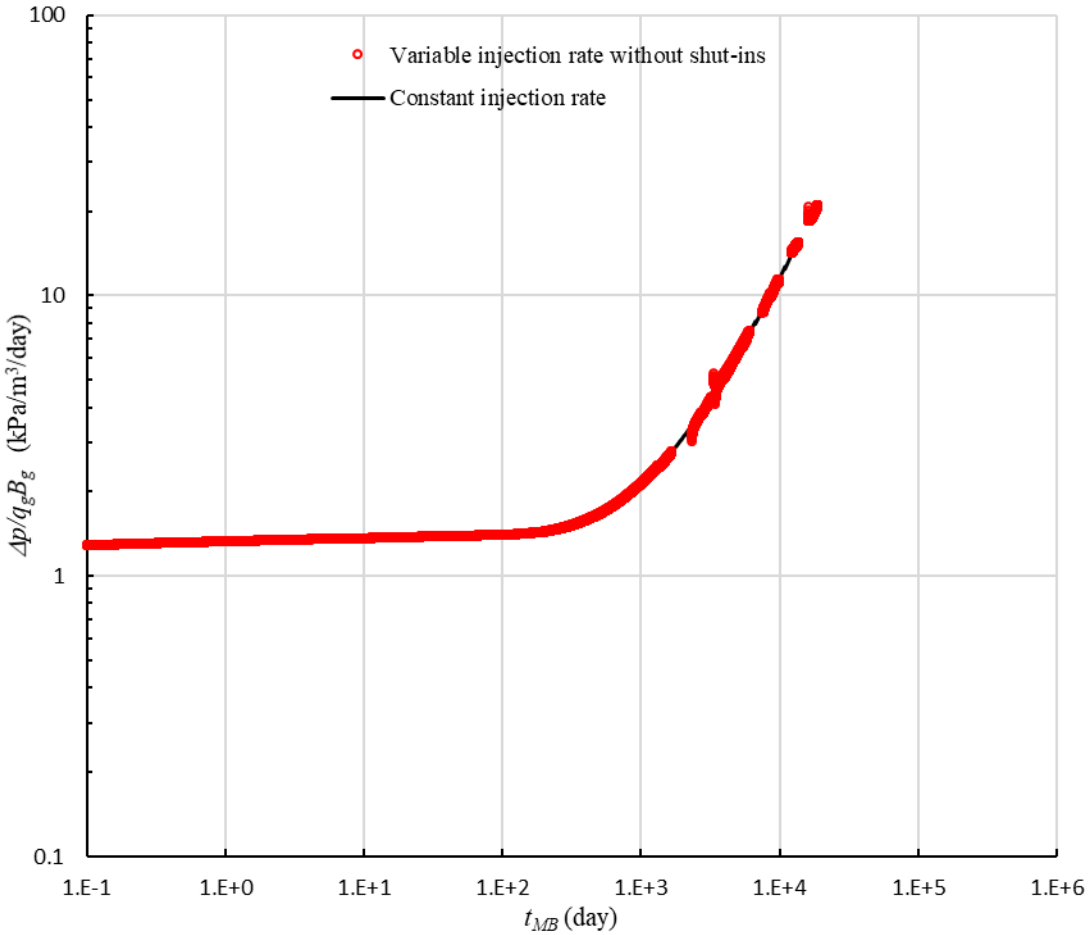

Figure. 4.6. Log-log diagnostic plot of rate-normalized pressure buildup versus material balance time for the variable and constant injection rate cases

4.3.3. Variable Injection Rate Case Including Shut-ins

In reality, the injection operation is controlled by the amount of CO_2 supplied from the CO_2 emission source (e.g. power plants), and temporary shut downs would be inevitable during storage operations. In addition, long shut downs are likely to occur when the point sources experience production problems. In this case, the usefulness of the material balance time is verified through application to a variable injection rate case including shut-in periods. As shown in Fig. 4.5 (b), the well is assigned a variable injection rate – covering the same range as the previous case – including shut-ins. The flow periods – lasting for 5 years each - are separated by shut-in periods each of 2 years duration. The remaining properties are identical to the base case (Table 4.1). As illustrated by the diagnostic plot (Fig. 4.7), few data points slightly deviate from the unit-slope line behavior due to the shut-downs and rate fluctuations. Nevertheless, the majority of the data points follow the unit-slope line behavior. Figs. 4.6 and 4.7 indicate that using the material balance time, wells operating at variable injection rate – with or without shut-ins – will exactly act as if they were operating at constant injection rate. Overall, the diagnostic plots of Figs. 4.4, 4.6 and 4.7 validate the potential application of material balance time to analyze CO_2 injection data for wells operating at different wellbore operating conditions.

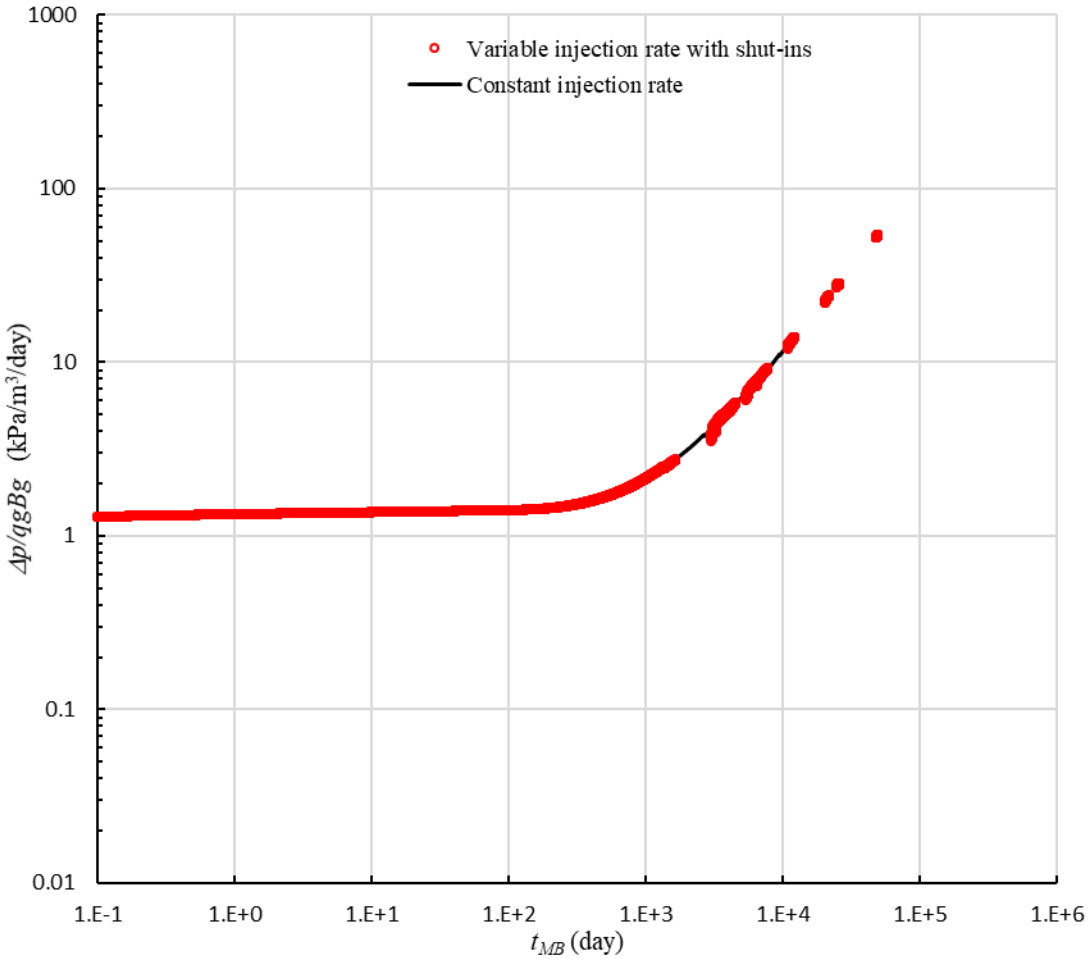

Figure. 4.7. Log-log diagnostic plot of rate-normalized pressure buildup versus material balance time for the variable injection rate case with shut-ins and the constant injection rate case

4.4. Application of the Interpretation Technique

In this section, the interpretation technique is applied to infer the reservoir pore volume, and the storage capacity of a closed saline formation using the abovementioned rigorous and approximate approaches. The graphical technique is applied to the synthetic data of the validation cases.

4.4.1. Constant Bottomhole Pressure Case

The pore volume of the aquifer is inferred through plotting $\Delta p/q_g B_g$ versus t_{MB} on a Cartesian scale. The diagnostic plot shown in Fig. 4.4 indicates that the unit-slope line – which corresponds to the BDF - is observed at 5.55×10^3 day < t_{MB} < 2.65×10^5 day. The data points over this interval are line fitted on a Cartesian scale as illustrated by Fig. 4.8. The fitted line has a slope $m = 1.07\times10^{-3}$ kPa/m^3, and intercept of 0.9556 kPa/m^3/day. Given the rock compressibility ($c_r = 5.0\times10^{-7}$ 1/kPa) and the brine compressibility ($c_w = 4.11\times10^{-7}$ 1/kPa) are known, the reservoir pore volume can be obtained using Eq. 4.5 as follows:

$$V_p = \frac{1}{mc_t} = \frac{1}{m\left(c_r + c_w\right)} = \frac{1}{1.07\times10^{-3}\times\left(5.0\times10^{-7} + 4.11\times10^{-7}\right)} = 1.026\times10^{9}\ \text{m}^3$$

The ultimate storage capacity can be estimated – using the rigorous approach – as follows:

1. Given the formation porosity is 25 %, and thickness is 40 m, calculate the radial extent of the reservoir using Eq. 4.9 as follows:

$$r_e = \sqrt{\frac{V_p}{\pi\phi h}} = \sqrt{\frac{1.026\times10^9}{\pi\times0.25\times40}} = 5714\ \text{m}.$$

2. Given the PVT data, the retardation factors - at the fronts between the two-phase zone and the dry-out and brine zones - are calculated using Eqs. C.5 and C.6 respectively:

$$D_{BL-dry} = \frac{\rho_a\omega_{w,a}}{\rho_a\omega_{w,a} - \rho_g\omega_{w,g}} = \frac{53.86\times0.98}{53.86\times0.98 - 14.65\times0.01} = 1.0029$$

$$D_{brine-BL} = \frac{\rho_a\omega_{CO_2,a}}{\rho_a\omega_{CO_2,a} - \rho_g\omega_{CO_2,g}} = \frac{53.86\times0.017}{53.86\times0.017 - 14.65\times0.99} = -0.067$$

3. With known relative permeability data, calculate the gas fractional flow as function of gas saturation using Eq. C.7.

4. Plot the gas fractional flow curve and estimate the gas saturations and the fractional flow values at the fronts of the dry-out zone and two-phase zone (i.e. S_{gdry}, S_{gBL}, f_{gdry} and f_{gBL}).

5. Calculate the slopes of the fractional flow curve at the fronts using Eqs. C.3 and C.4:

$$\left.\frac{df_g}{dS_g}\right|_{S_{gdry}} = \frac{f_{gdry} - D_{BL-dry}}{S_{gdry} - D_{BL-dry}} = \frac{1-1.0029}{0.693-1.0029} = 0.00934$$

$$\left.\frac{df_g}{dS_g}\right|_{S_{gBL}} = \frac{f_{gBL} - D_{brine-BL}}{S_{gBL} - D_{brine-BL}} = \frac{0.782-(-0.067)}{0.367-(-0.067)} = 1.956$$

6. Corresponding to each data point, calculate the radial extents of the dry-out zone and the two-phase zone using Eqs. 4.10 and 4.11, respectively, as follows:

$$r_{dry} = \sqrt{\frac{Q_g B_g}{\pi\phi h}\left.\frac{df_g}{dS_g}\right|_{S_{gdry}}} = \sqrt{\frac{Q_g B_g}{\pi \times 0.25 \times 40} \times 0.00934} = 0.0172\sqrt{Q_g B_g} \text{ m}$$

$$r_{BL} = \sqrt{\frac{Q_g B_g}{\pi\phi h}\left.\frac{df_g}{dS_g}\right|_{S_{gBL}}} = \sqrt{\frac{Q_g B_g}{\pi \times 0.25 \times 40} \times 1.956} = 0.2495\sqrt{Q_g B_g} \text{ m}$$

7. With known absolute permeability (k = 100 mD), calculate the term b_r – corresponding to each data point - using Eq. 4.8.

8. With b_r, and the injection pressure and rate data, calculate the average reservoir pressure corresponding to each data point using Eq. 4.7.

9. Plot the calculated $\bar{p}$ versus $Q_g B_g$ on a Cartesian scale and extrapolate the straight line to the maximum allowable injection pressure of 30.2 MPa as shown in Fig. 4.9.

10. The corresponding $Q_g B_g$ - which represents the ultimate storage capacity that can be achieved over the project period – is equal to 9.32×10^6 m^3.

11. Calculate the storage efficiency by dividing the ultimate storage capacity by the reservoir pore volume as follow:

$$E = \frac{9.32\times10^6}{1.026\times10^9} = 0.0091$$

The rigorous approach requires a prior knowledge of some reservoir properties such as the relative permeability data, the absolute permeability, formation porosity and thickness which may not be available. Thus, the storage capacity can be estimated using the approximate approach as follows:

1. From the Cartesian plot of Fig. 4.8, the y-intercept – which approximates the quasi-stable value of b_r – reads as 0.9556 kPa/m^3/day.

2. With b_r value, and the pressure and rate data, calculate the average pressure corresponding to each data point using Eq. 4.7.

3. Plot the calculated $\bar{p}$ versus $Q_g B_g$ on a Cartesian scale and extrapolate the straight line to the p_{max} = 30.2 MPa (Fig. 4.10). The corresponding $Q_g B_g$ - which represents the ultimate storage capacity – is equal to 11.12×10^6 m^3.

4. The storage efficiency is given by:

$$E = \frac{11.12\times10^6}{1.026\times10^9} = 0.0108$$

The inferred pore volume is compared with the value that has been used in generating the synthetic data, and the estimated storage capacities are compared with the numerical values. The inferred pore volume has absolute relative error (*ARE*) approximately equals to 2.58 %, and the ultimate storage capacity – estimated using the rigorous and the approximate approaches - has *AREs* ~ 1.29 % and 17.77 % respectively. The comparison is displayed Table 4.2.

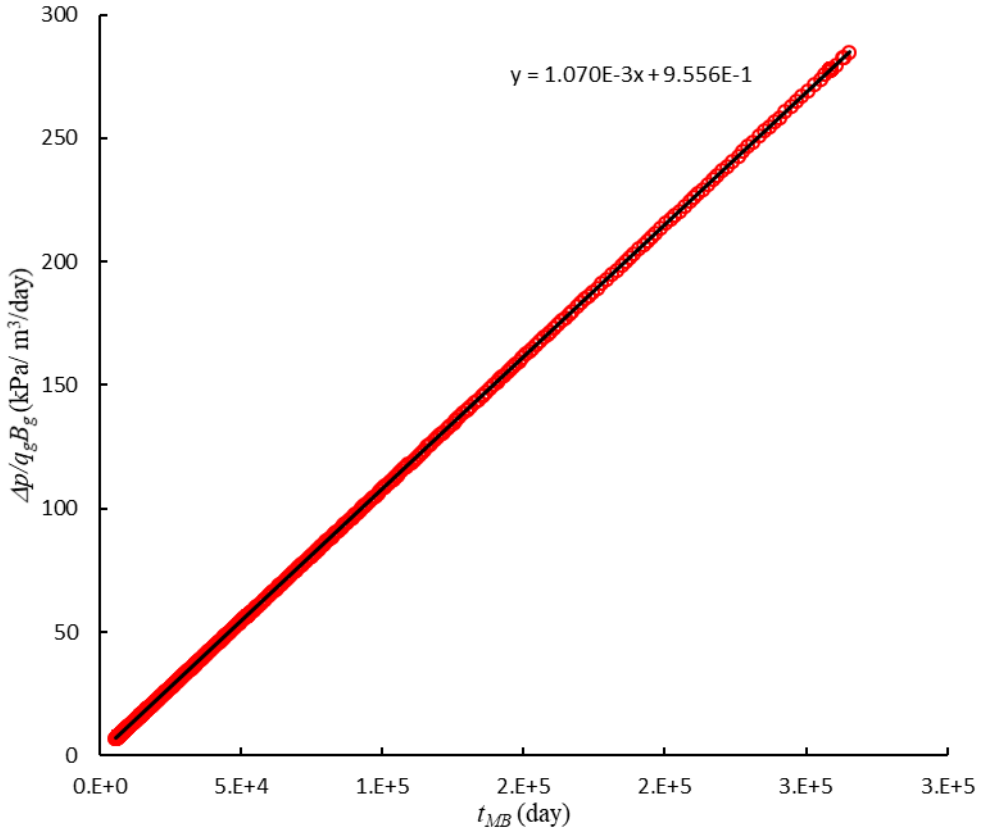

Figure 4.8. Cartesian plot of rate-normalized pressure buildup versus material balance time for the constant bottomhole pressure case

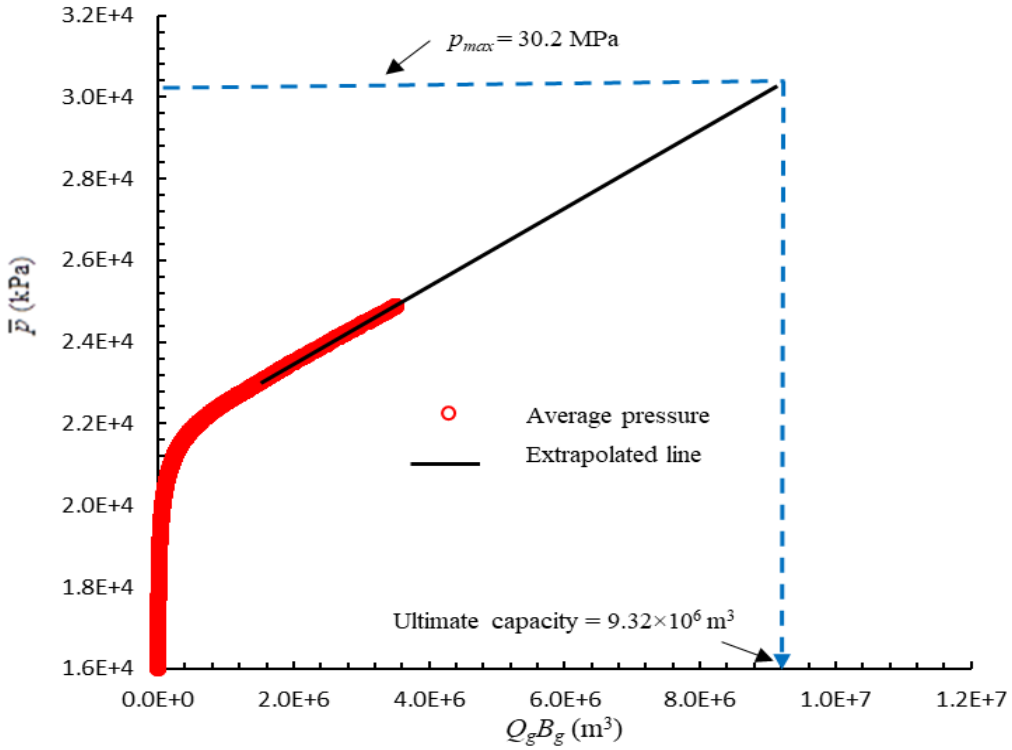

Figure 4.9. Application of the graphical interpretation technique to estimate the ultimate storage capacity for the constant bottomhole injection pressure case using the rigorous approach

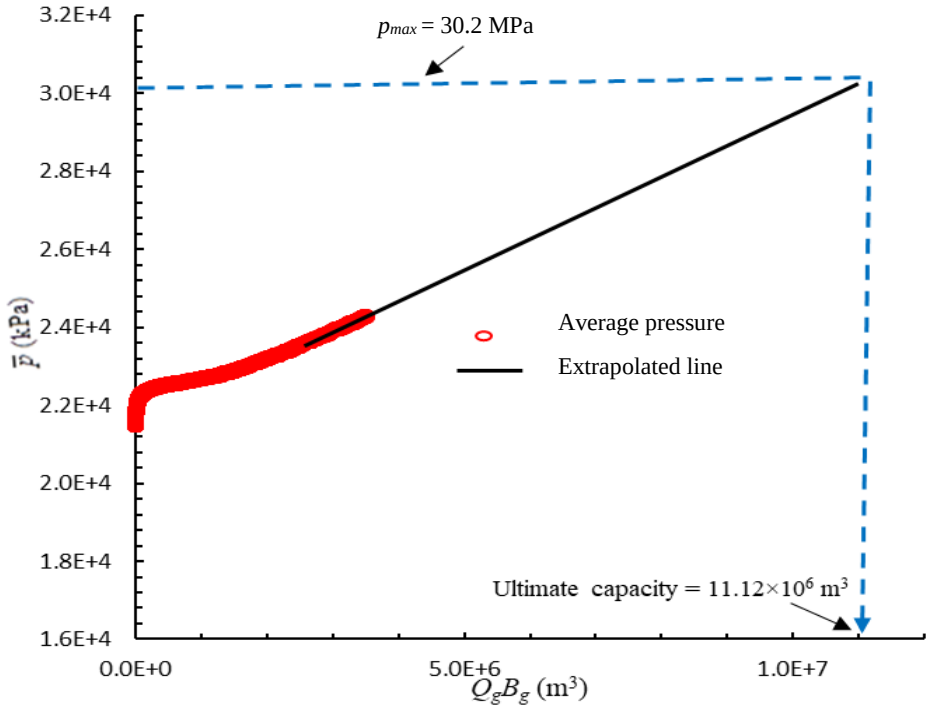

Figure 4.10. Application of the graphical interpretation technique for the constant bottomhole injection pressure case using the approximate approach

4.4.2. Variable Injection Rate Case Without Shut-ins

For this case, the unit-slope line behavior is observed at 5.55×10^3 day < t_{MB} < 1.89×10^4 day (see Fig. 4.6). The corresponding data points are line fitted on a Cartesian scale as shown in Fig. 4.11, and the ultimate storage capacity is estimated using both approaches (Fig. 4.12). The slope and the intercept of the fitted line are 1.067×10^{-3} kPa/m^3 and 0.9140 kPa/m^3/day respectively. Similarly, the reservoir pore volume is obtained using Eq. 4.5. The ultimate storage capacity is estimated using the rigorous and approximate approaches as shown by Figs. 4.12 (a) and (b) respectively. The interpretation results are in good agreement with the simulation values as displayed in Table 4.2. The inferred pore volume has *ARE* ~ 2.87 % and the estimated storage capacity yields *ARE* ~ 1.93 % and 8.72 % for the rigorous and approximate approaches respectively.

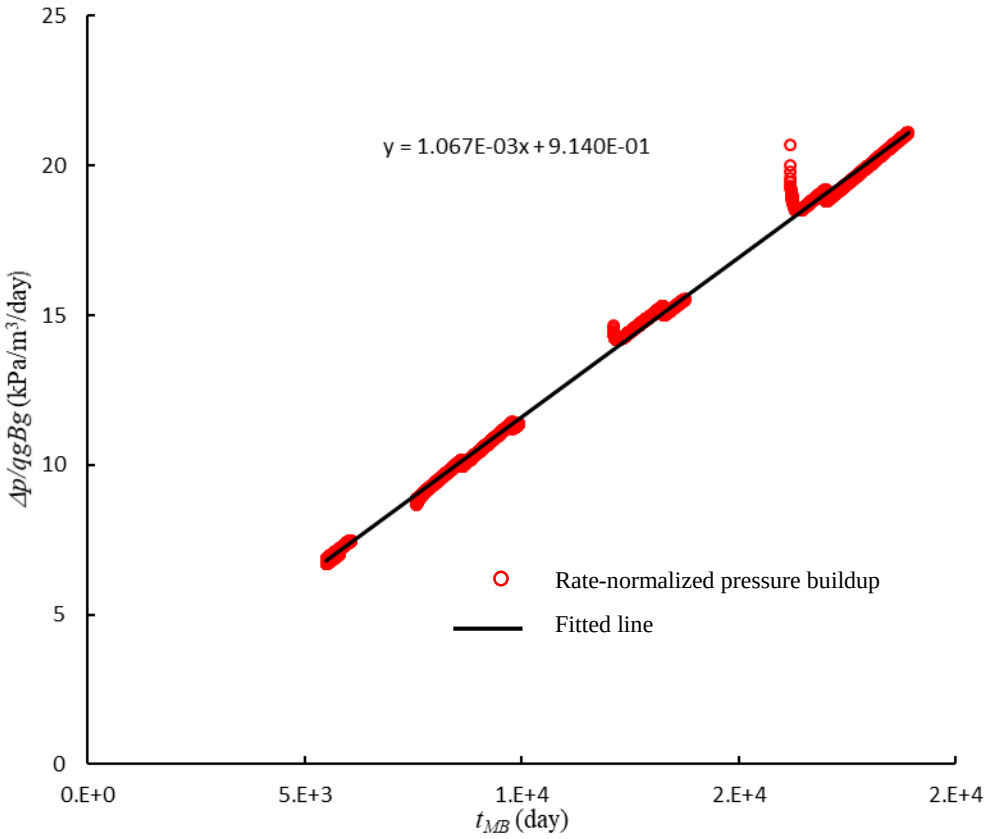

Figure 4.11. Cartesian plot of rate-normalized pressure buildup versus material balance time for the variable injection rate case without shut-ins

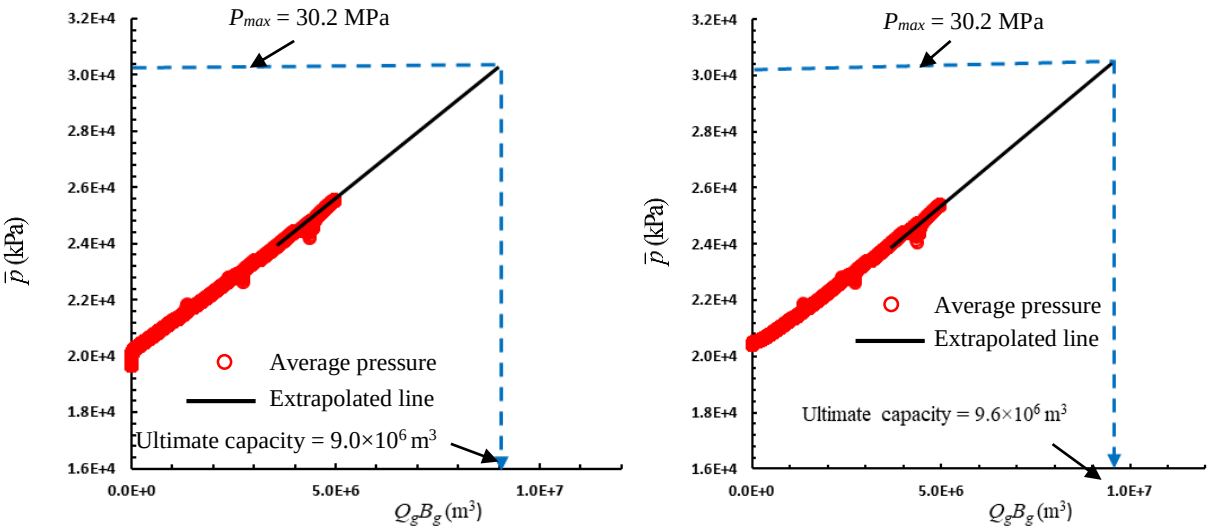

(a) (b)

Figure 4.12. Application of the graphical interpretation technique to estimate the ultimate storage capacity for the variable injection rate case without shut-ins using (a) the rigorous approach (b) the approximate approach

Table 4.2. Comparison of the analytically and the numerically estimated values of the pore volume and the ultimate storage capacity for CP and VR cases

Case	Estimated Pore volume ($\times 10^9 m^3$)	Simulated pore volume ($\times 10^9 m^3$)	Estimated storage capacity ($\times 10^6 m^3$)		Simulated storage capacity ($\times 10^6 m^3$)
			Rigorous	Approx.	
CP	1.026	1.00	9.32	11.12	9.44
VR (no shut-in)	1.029	1.00	9.00	9.60	8.83
VR (with shut-in)	1.027	1.00	9.30	9.80	9.25

Case	Estimated Storage efficiency		Simulated storage efficiency
	Rigorous	Approx.	
CP	0.0091	0.0108	0.0094
VR (no shut-in)	0.0087	0.0093	0.0088
VR (with shut-in)	0.0091	0.0095	0.0093

4.4.3. Variable Injection Rate Case With Shut-ins

For this case, the unit-slope line behavior is observed at 5.55×10^3 day < t_{MB} < 4.98×10^4 day as shown in Fig. 4.7. The corresponding data points are lines fitted on a Cartesian scale (Fig. 4.13). The reservoir pore volume is inferred using Eq. 4.5, and the storage capacity is estimated using

both approaches as shown in Fig. 4.14. The interpretation results are displayed in Table 4.2 along with the simulated values. The inferred pore volume has *ARE* ~ 2.68 %, and the estimated storage capacity has *ARE* ~ 0.49 % for the rigorous approach and 5.90 % for the approximate approach.

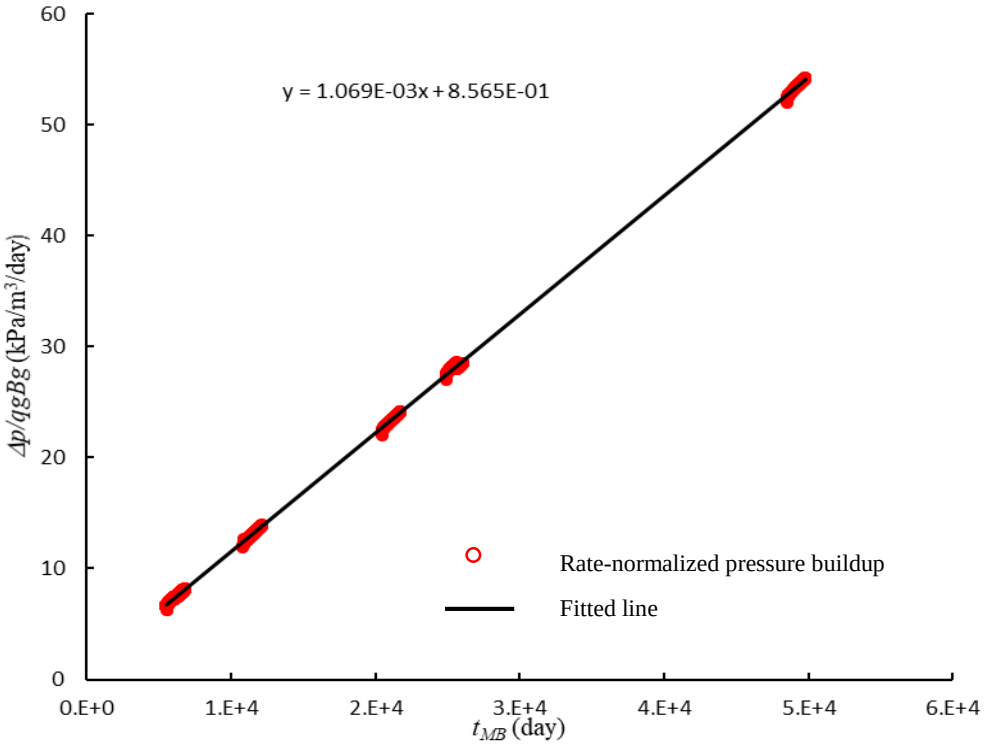

Figure 4.13. Cartesian plot of rate-normalized pressure buildup versus material balance time for the variable injection rate case with shut-ins

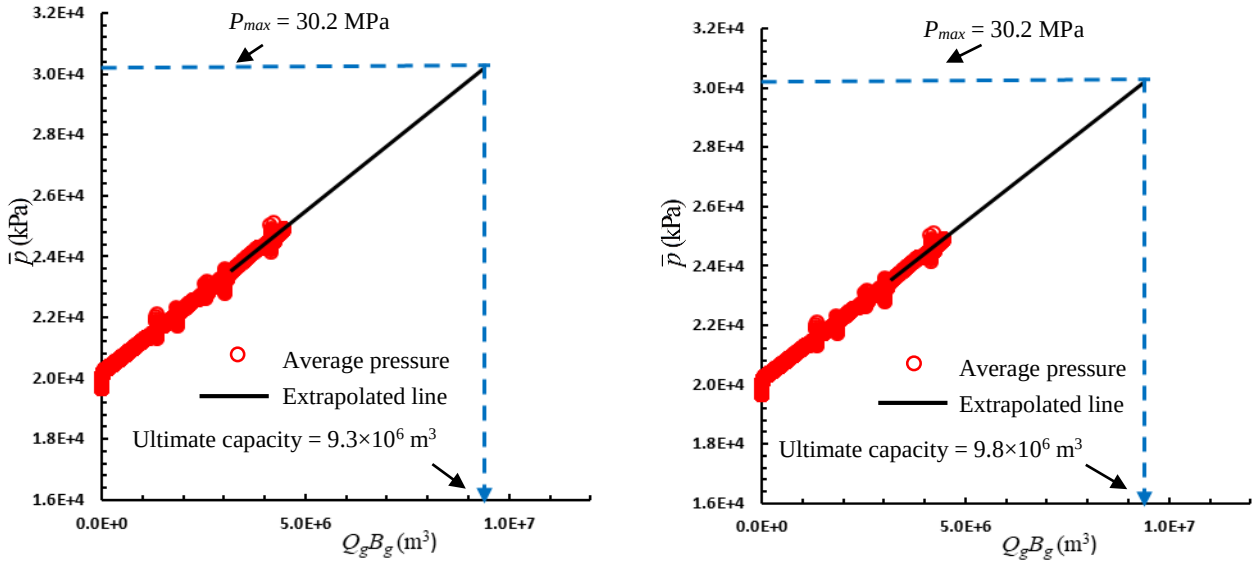

(a) (b)

Figure 4.14. Application of the graphical interpretation technique to estimate the ultimate storage capacity for the variable injection rate case with shut-ins using (a) the rigorous approach (b) the approximate approach

4.5. Field Application

4.5.1. SECARB Denbury's Cranfield Project

The Cranfield CO_2 sequestration project is a part of the Southeast Regional Carbon Sequestration Partnership (SECARB) Phase III demonstration project. For Cranfield project, CO_2 injection was initiated at 1st of December, 2009 in a depleted oil reservoir at Cranfield, Mississippi. The area of study is located within the water leg of the depleted reservoir. The brine-saturated target zone consists of heterogeneous fluvial sandstone of the Cretaceous lower Tuscaloosa formation at ~ 3200 m depth (Hovorka et al., 2013). The storage domain has three wells where CO_2 was injected through an injection well (F1), and observed by two monitoring wells (F2 and F3). The target formation's gross thickness is 25 m, and it is sealed by 33.5 m-thick caprock (Delshad et al., 2013). The initial reservoir pressure and temperature, respectively, equal to 32.06 MPa and 127.6 ^oC. Under these condition, CO_2 is supercritical with a density of 586.04 kg/m^3 and a viscosity of 0.044 cp (Delshad et al., 2013; Zhou et al., 2020). Routine core analysis and logging information showed heterogeneous flow channels interbedded by numerous low quality barriers along the injection interval. This constrained the injected CO_2 within thin high-quality channels/streaks of the target formation. Also, it has been reported that the injection well is located in a relatively low permeability zone as compared to the high core permeabilities at the observation wells. This caused high pressure buildup during CO_2 injection (the bottomhole pressure jumped from 319.8 bar to 410.3 bar during the first 30 minutes of injection before stabilizing at 380 bar after two days). The detailed geology of the target formation, and the injection operations can be accessed at Hovorka et al. (2013); Hovorka et al. (2011). The operational CO_2 injection continued until 7 September 2010, with a total of 126,246 metric tons of CO_2 injected over 281 days (Zhou et al., 2020). The bottomhole injection pressure and rate data are obtained from the US NETL/DOE Energy Data eXchange website (EDX, 2018), and plotted in Figs 4.14 and 4.15. Fig. 4.15 shows the bottomhole injection pressure (in kPa), and the injection rate (in kg/minutes). Fig. 4.16 displays the cumulative injection of CO_2 (in metric tons) as well as the injection rate.

The diagnostic plot of Fig. 4.17 indicates a horizontal-line behavior is observed before t_{MB} ~ 20 day which marks the end of the transient flow period. Beyond the transient period, a clear unit-slope line behavior is not observed (i.e., the slope value is lower than unity). This indicates that the pressure response is somewhat affected by the boundaries although that they are not fully closed. Therefore, the interpretation technique cannot be used to analyze this dataset of the Cranfield project. However, the technique showed its usefulness that the Cranfield GCS injection system is not a fully-closed system, and the external boundaries of the reservoir are likely semi-closed/leaky. This finding is also indicated by Fig. 4.15 which shows an apparent increase in the bottomhole pressure trend. Nevertheless, the increase in not very strong to represent fully-closed outer boundary system. Also, the figure shows that - during shut-in - the bottomhole pressure does not return to the original reservoir pressure, which indicates that the reservoir boundaries are somewhere between closed and open. We run several simulation for closed, open and semi-open systems and plotted the diagnostic plot in Fig. 4.18. We found that for a system to act as a fully open, a slope behavior ~ - 0.01 during the BDF should be observed on the diagnostic plot. Semi-open systems should span between these two extremes (i.e., unit-slope for closed system, and -0.01 for open system) (see Fig. 4.18).

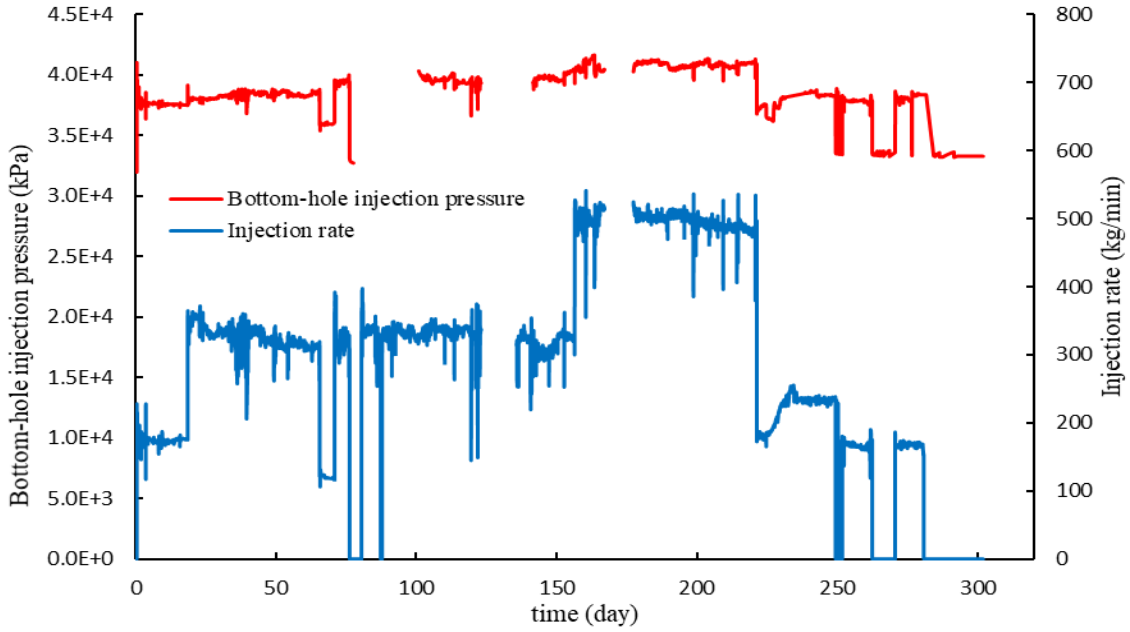

Figure 4.15. Injection history for Cranfield project displayed as bottomhole pressure (primary *y*-axis) and injection rate (secondary *y*-axis)

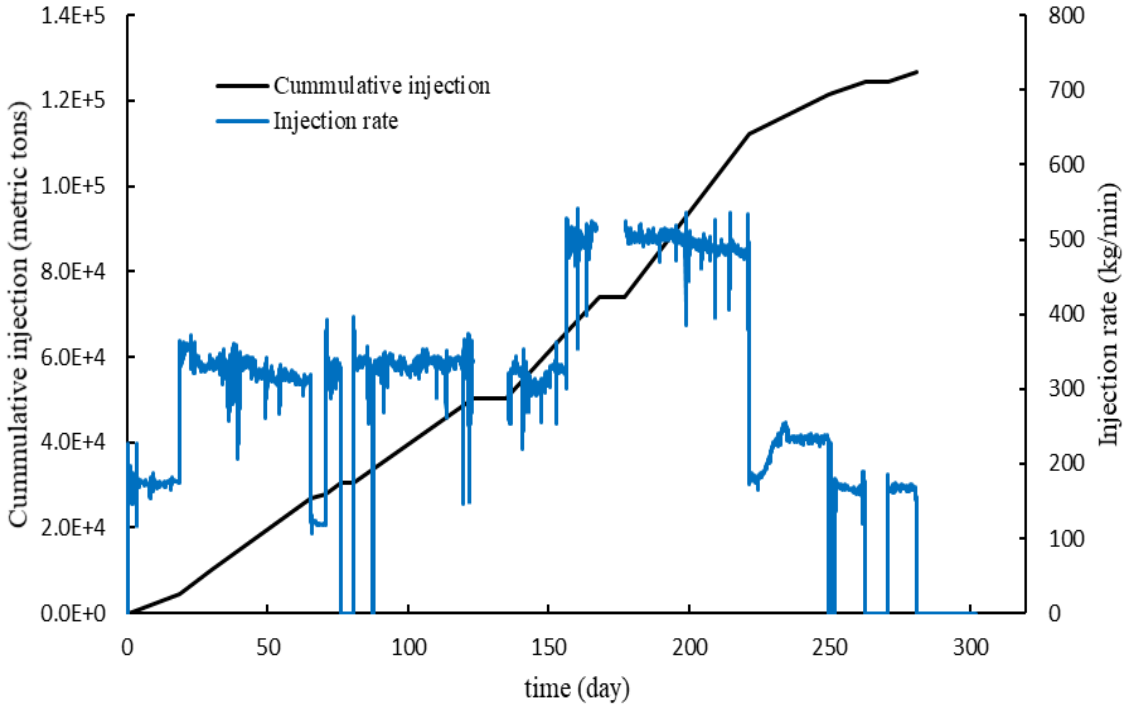

Figure 4.16. Injection history for Cranfield project displayed as cumulative injection (primary *y*-axis) and injection rate (secondary *y*-axis)

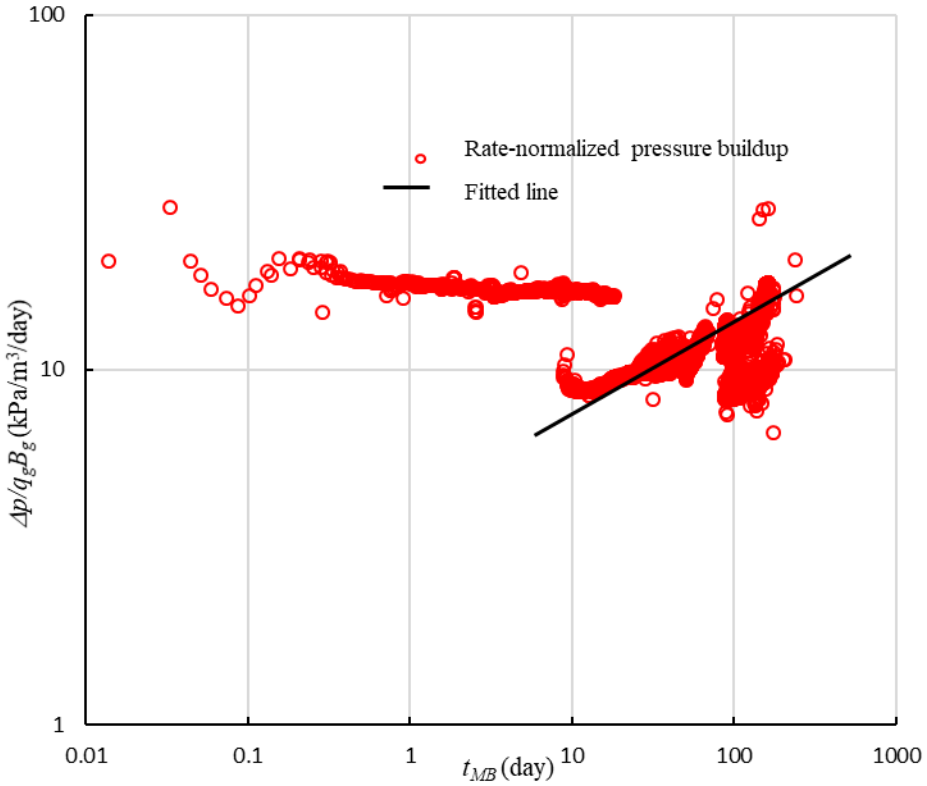

Figure. 4.17. Log-log diagnostic plot of rate-normalized pressure buildup versus material balance time for the field data of Cranfield project

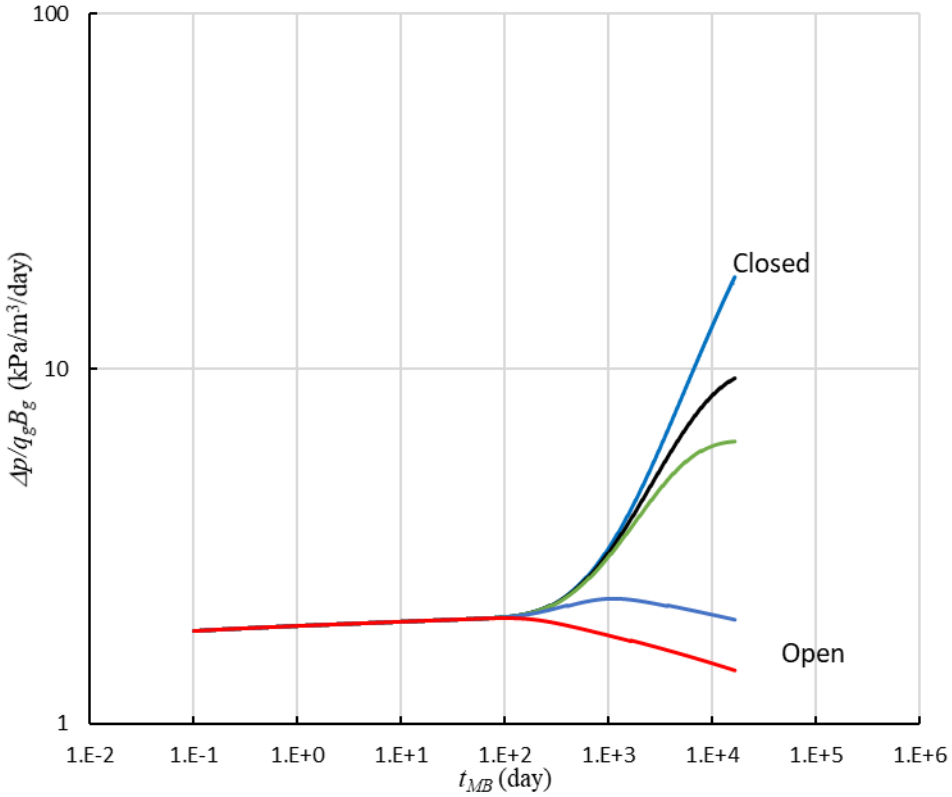

Figure 4.18. Diagnostic plot of the behavior of closed, open, and semi-closed systems

Chapter 5. Effects of Injection Well Operation Conditions on the Injectivity and Subsequent Ultimate Storage Capacity of CO_2 in Deep Saline Aquifers

In previous chapters, we introduced analytical methodologies to characterize CO_2 injectivity and corresponding storage capacity of saline storage aquifers. In this chapter, we investigate the effect of adopting different operation conditions at the injection well on the injectivity variations and the subsequent storage capacity. Practically, the operating condition of the injection well is partly controlled by the amount of CO_2 supplied by the emission source (e.g. power plant) which results in inevitable fluctuations/shut downs during the operation. This can cause dramatic variations in the injectivity behavior, and as a consequence, storage capacity. Therefore, a detailed numerical simulation study is performed using CMG-IMEX (2019) to assess the potential impact of different operating conditions on the volumetric potential of a given fixed pore space. With CO_2 injected continuously or intermittently, constant terminal-rate and constant terminal-pressure CO_2 injection are first studied. The injection scheme that maximizes the volumetric value of a given pore space is accordingly articulated. A simple NPV analysis is conducted afterwards to identify the most economically appealing injection strategy to follow. Next, different injection schemes are applied to a synthetic GCS project with injection history to identify their implications. The study will be concluded by a sensitivity analysis to investigate the impact of varying some reservoir parameters (e.g., the injection rate, vertical permeability, formation dip angle, outer boundary conditions, and well penetration) on the formation storage capacity considering different injection schemes.

5.1. Description of the Simulation Model

We model the radial two-dimensional axially-symmetric closed system shown in Fig. 5.1 using CMG-IMEX (2019) to achieve the goals of this objective. The reservoir and fluid properties (listed in Table 5.1) are representative of a potential CO_2 storage formation in the US Gulf Coast region (Dismukes et al., 2019; Hovorka et al., 2000). To time-step, CMG-IMEX numerically solves the system of governing partial differential equations (PDEs) using the well-known finite-difference discretization scheme. Using finite-difference, the aquifer is discretized into cells/blocks in which the phases' pressures and saturations are numerically solved for after applying the initial and boundary conditions specified to the system. In this study, the aquifer is homogenous and isotropic with uniform thickness and porosity of 75 m and 0.25 respectively. The absolute horizontal and vertical permeabilities are set at 500 mD, and 5 mD, respectively. The areal extent of the aquifer is 93.2 km^2 with closed outer boundaries extending to 5.4 km. The aquifer is considered initially in equilibrium with uniform pressure distribution equal to 20.1 MPa. The aquifer is confined between two impermeable layers at the top and the bottom acting as baffles to prevent CO_2 migration out of the storage formation. The aquifer model is discretized into 300 logarithmically-distributed grids in the radial dimension with the finest grids near the wellbore and the coarsest at the outer boundaries to ensure higher resolution in the vicinity of the injection well. Displacement of CO_2 into aquifers is not controlled only by the viscous forces caused by injection, but it can be affected by the buoyant and capillary forces as well. Therefore, the model is vertically discretized into 30 layers each of 2.5 m to ensure effective buoyancy. The temperature of the injected CO_2 is assumed close enough to the reservoir temperature that the system can be considered isothermal with a temperature of 70 ^oC. Also, as shown by Zeidouni et al. (2014), non-isothermal injection of CO_2 into an aquifer causes only small temperature perturbation limited to the area near the wellbore.

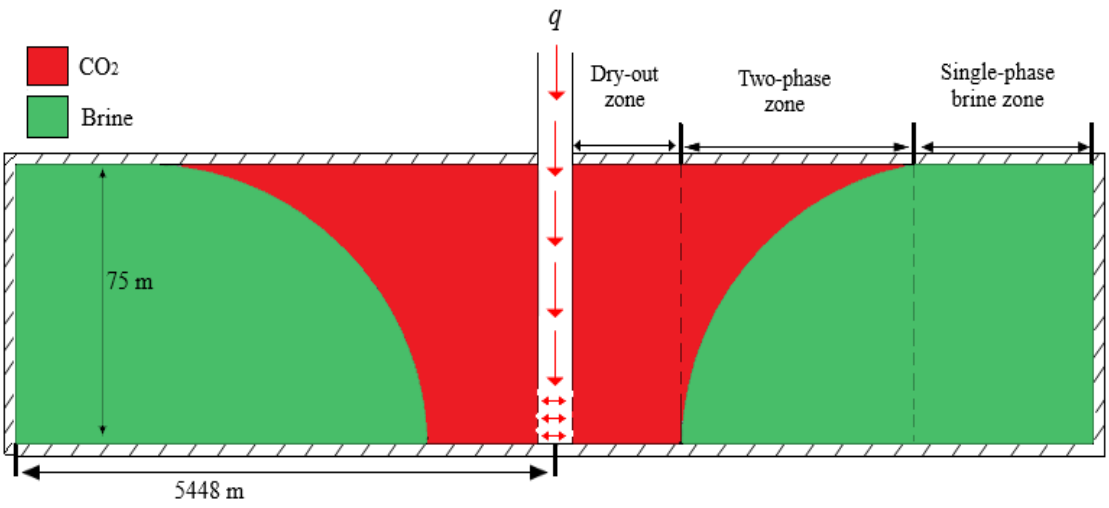

Figure 5.1. Schematic cross-sectional illustration of CO_2 injection through a partially penetrating vertical well into a closed saline aquifer

Table 5.1. Input data for the simulation

Aquifer area (km^2)	93.2
Thickness (m)	75
Depth to top (m)	2000
Number of layers	30
Number of grids (radial × vertical)	300×30
Temperature (^oC)	70
Porosity (fraction)	0.25
Horizontal permeability (mD)	500
Vertical permeability (mD)	5
Dip angle (^{o})	0
Rock compressibility (1/kPa)	5.0×10^{-7}
Initial pressure (MPa)	20.1
Fracture pressure (MPa)	33.6
Maximum allowable injection pressure (MPa)	30.2
Brine viscosity (Pa.sec)	4.53×10^{-4}
CO_2 viscosity (Pa.sec)	5.10×10^{-5}
Brine compressibility (1/kPa)	4.11×10^{-7}
CO_2 compressibility (1/kPa)	3.08×10^{-5}
CO_2 density (kg/m^3)	644.4
Residual brine saturation (fraction)	0.45
Gas relative permeability in the dry-out zone (-)	0.80
CO_2 endpoint relative permeability (-)	0.33
Gas relative permeability exponent (-)	3.0
Brine relative permeability exponent (-)	3.0

The compositional flow of CO_2 and brine can be approximated by the well-known black-oil PVT modeling in which gas represents CO_2 and oil represents brine (Savioli et al., 2012). In this study, the fluid PVT model is generated using Hassanzadeh et al. (2008) procedure which converts the compositional CO_2/brine data from the modified Redlich-Kwong EoS (Spycher et al., 2003) into black-oil PVT data. In the PVT model, the mutual dissolution between CO_2 and brine is honored. The compositional mole fractions of CO_2 and brine – predicted by the modified Redlich-Kwong EoS - are converted to solution gas-oil ratio (R_s) and vaporized oil/gas ratio (R_v). R_s account for CO_2 solubility into the aqueous phase, and R_v accounts for water vaporization into the gaseous phase. The CO_2/brine displacement is governed by PDEs derived by combining the conservation equations of momentum and mass. The PDEs and the black-oil representation of the compositional fluid model can be explained as follows. The conservation equations that govern the compositional two-phase two-component fluid flow in porous media are given by:

For CO_2 component:

$$-\nabla.\left(\rho_g v_g y_g + \rho_o v_o y_o\right) + q_g = \frac{\partial}{\partial t}\left[\phi\left(\rho_g y_g S_g + \rho_o y_o S_o\right)\right] \tag{5.1}$$

For brine component:

$$-\nabla.\left(\rho_g v_g x_g + \rho_o v_o x_o\right) + q_o = \frac{\partial}{\partial t}\left[\phi\left(\rho_g x_g S_g + \rho_o x_o S_o\right)\right] \tag{5.2}$$

where ρ_g, ρ_o are the densities of the gaseous and aqueous phases, respectively, ϕ is the formation porosity, S_g, S_o are the saturations of the gaseous and aqueous phases, respectively, q_g, q_o are the injection rates of CO_2 and brine respectively, y_g, y_o are the mole fractions of CO_2 in the gaseous and aqueous phases respectively, and x_g, x_o are the mole fractions of brine in the gaseous and aqueous phases respectively. The mole fractions are related to the black-oil PVT data (i.e. R_s, R_v, and the phase densities at standard conditions) as follows (Walsh and Lake, 2003):

$$y_g = \frac{\rho_{gsc}}{R_v \rho_{osc} + \rho_{gsc}} \tag{5.3}$$

$$y_o = \frac{R_v \rho_{osc}}{R_v \rho_{osc} + \rho_{gsc}} \tag{5.4}$$

$$x_g = \frac{R_s \rho_{gsc}}{R_s \rho_{gsc} + \rho_{osc}} \tag{5.5}$$

$$x_o = \frac{\rho_{osc}}{R_s \rho_{gsc} + \rho_{osc}} \tag{5.6}$$

With Darcy velocities of the gaseous and aqueous phases are, respectively, defined by:

$$v_g = -\frac{k k_{rg}}{\mu_g}\left(\nabla p_g - \rho_g \nabla z\right) \tag{5.7}$$

$$v_o = -\frac{kk_{ro}}{\mu_o}\left(\nabla p_o - \rho_o \nabla z\right) \tag{5.8}$$

where k is the absolute permeability, μ_g, μ_o are the dynamic viscosities of the gaseous and aqueous phases respectively, p_g, p_o are the pressure of the gaseous and aqueous phases respectively, z is the elevation with respect to the datum level, k_{rg}, k_{ro} are, respectively, the relative permeabilities to the gaseous and aqueous phases generated using Corey (1954b)'s equations given by:

$$k_{rg} = k_{rg}{}^{0}\left[\frac{S_g}{1-S_{or}}\right]^n \tag{5.9}$$

$$k_{ro} = k_{ro}{}^{0}\left[1-\left(\frac{S_g}{1-S_{or}}\right)\right]^m \tag{5.10}$$

In Eqs 5.9 and 5.10, $k_{rg}{}^{o}$ and $k_{ro}{}^{o}$ are the endpoint relative permeabilities to the gaseous and aqueous phases respectively, n and m are the saturation exponents of the gaseous and the aqueous phases respectively, and S_{or} is the residual brine saturation. In this work, the saturation exponents for the gaseous and the aqueous phases are set at 3, and the endpoint relative permeability values are set 0.33 and 1.0 respectively. The residual brine saturation is assigned 0.45, and the relative permeability to gas in the CO_2 dry-out zone is set 0.8 to allow for absolute permeability reduction due to salt precipitation in the vicinity of the wellbore.

Substituting for Eqs. 5.3 through 5.8 into Eqs 5.1 and 5.2, the governing PDEs can be written in terms of the black-oil PVT properties as follows:

For CO_2 component:

$$\nabla.\begin{bmatrix} \rho_g \dfrac{kk_{rg}}{\mu_g}\left(\nabla p_g - \rho_g \nabla z\right)\left(\dfrac{\rho_{gsc}}{R_v\rho_{osc}+\rho_{gsc}}\right)+ \\ \rho_o \dfrac{kk_{ro}}{\mu_o}\left(\nabla p_o - \rho_o \nabla z\right)\left(\dfrac{R_v\rho_{osc}}{R_v\rho_{osc}+\rho_{gsc}}\right) \end{bmatrix} + q_g = \frac{\partial}{\partial t}\begin{bmatrix} \phi\rho_g S_g\left(\dfrac{\rho_{gsc}}{R_v\rho_{osc}+\rho_{gsc}}\right)+ \\ \phi\rho_o S_o\left(\dfrac{R_v\rho_{osc}}{R_v\rho_{osc}+\rho_{gsc}}\right) \end{bmatrix} \tag{5.11}$$

For brine component:

$$\nabla.\begin{bmatrix} \rho_g \dfrac{kk_{rg}}{\mu_g}\left(\nabla p_g - \rho_g \nabla z\right)\left(\dfrac{R_s\rho_{gsc}}{R_s\rho_{gsc}+\rho_{osc}}\right)+ \\ \rho_o \dfrac{kk_{ro}}{\mu_o}\left(\nabla p_o - \rho_o \nabla z\right)\left(\dfrac{\rho_{osc}}{R_s\rho_{gsc}+\rho_{osc}}\right) \end{bmatrix} + q_o = \frac{\partial}{\partial t}\begin{bmatrix} \phi\rho_g S_g\left(\dfrac{R_s\rho_{gsc}}{R_s\rho_{gsc}+\rho_{osc}}\right)+ \\ \phi\rho_o S_o\left(\dfrac{\rho_{osc}}{R_s\rho_{gsc}+\rho_{osc}}\right) \end{bmatrix} \tag{5.12}$$

To solve the system of PDEs for the four primary unknowns (i.e., p_o, p_g, S_o, and S_g), two additional equations/relations are required. The first relation is that the phases' saturations are summed up to unity, and the second is that the phases' pressures are related to each other using the capillary pressure (p_c) as follows:

$$S_g + S_o = 1 \tag{5.13}$$

$$p_g = p_o + p_c(S_o) \tag{5.14}$$

The capillary pressure curve generated using van Genuchten formulation (van Genuchten, 1980). The threshold pressure p_{th} = 20 kPa and pore size distribution parameter m = 0.8 (Zeidouni et al., 2016). The capillary pressure formualtion is given by:

$$p_c(S_o) = -p_{th}\left(\left[S^*\right]^{-1/m} - 1\right)^{1-m} \tag{5.15}$$

where: $S^* = \dfrac{S_o - S_{or}}{1 - S_{or}}$

A total 16 simulations are conducted to achieve the goals of this study. The first four simulations involve injecting CO_2 both continuously and intermittently at constant pressure (CP) and constant rate (CR) schemes in order to articulate the best injection scheme to follow. The remaining 12 runs comprise the sensitivity analysis section where the effect of varying some reservoir parameters (e.g., the injection rate, vertical permeability, formation dip angle, outer boundary conditions, and well penetration) - on the injectivity and the ultimate storage capacity - is investigated. Compared to the continuous CP and CR base cases, injection rates ranging from 0.3 to 1.5 Mt/year, vertical permeabilities of 50 mD, and 250 mD, formation dip angles of 1.5^o and 3^o, open aquifer, and fully penetrating vertical well are tested.

5.2. Continuous Injection

Two endpoint scenarios are considered. First, injection at CR until the maximum allowable bottomhole pressure (p_{max}) is reached. Second, injection at CP of p_{max} until the economic limit rate is reached. For the CR case, CO_2 is injected continuously at 0.5 Mt/year until p_{max} is reached. The p_{max} is calculated to be 30.2 MPa based on 2.0 km depth, 0.3 Poisson ratio for sandstone, and 90 % of the fracture pressure (set as a safety margin). For the CP case, CO_2 is injected at a constant bottomhole pressure set at the p_{max}. The injection continues until the economic limit rate of 27.4 ton/day is reached. Results indicate that the pressure and rate behaviors are controlled by the relative dominance of the dry-out zone expansion versus the effect of the outer boundaries given the injection into a closed system. The dry-out zone expansion is accompanied by average reservoir pressure buildup. At the early time, the dry-out zone expansion is more dominant, improving CO_2 injectivity. Nevertheless, the effect of outer boundaries becomes more dominant over time, causing the injectivity to decline.

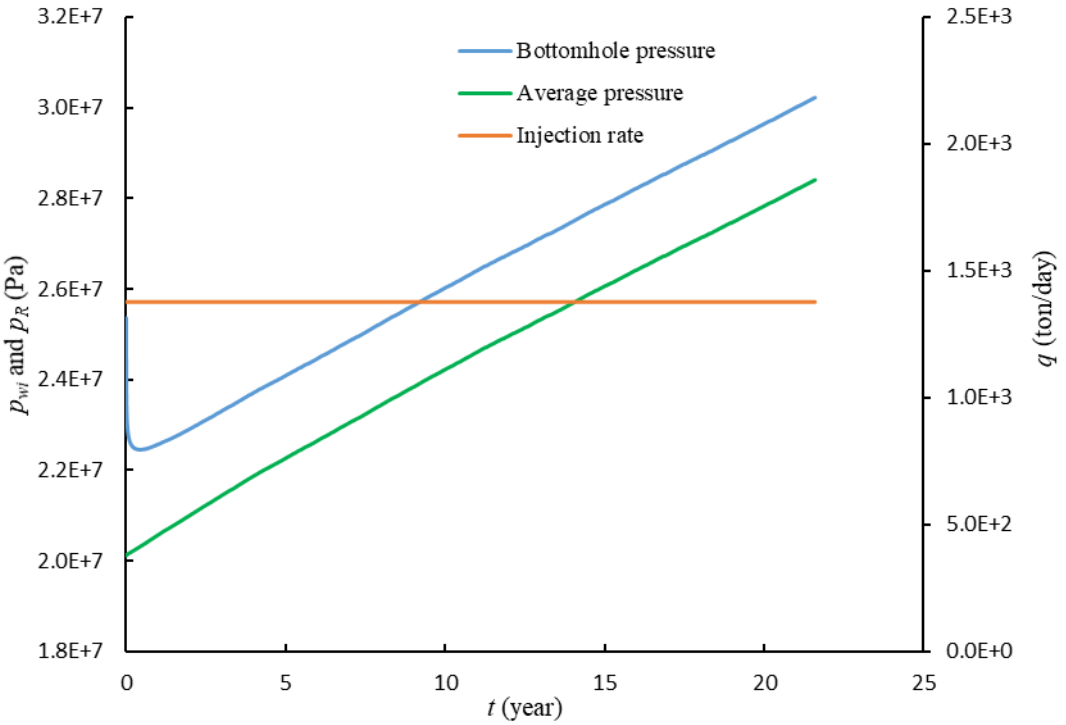

Figure 5.2. Injection bottomhole and average reservoir pressures (on the primary *y*-axis) and injection rates (on the secondary *y*-axis) for continuous injection at constant rate

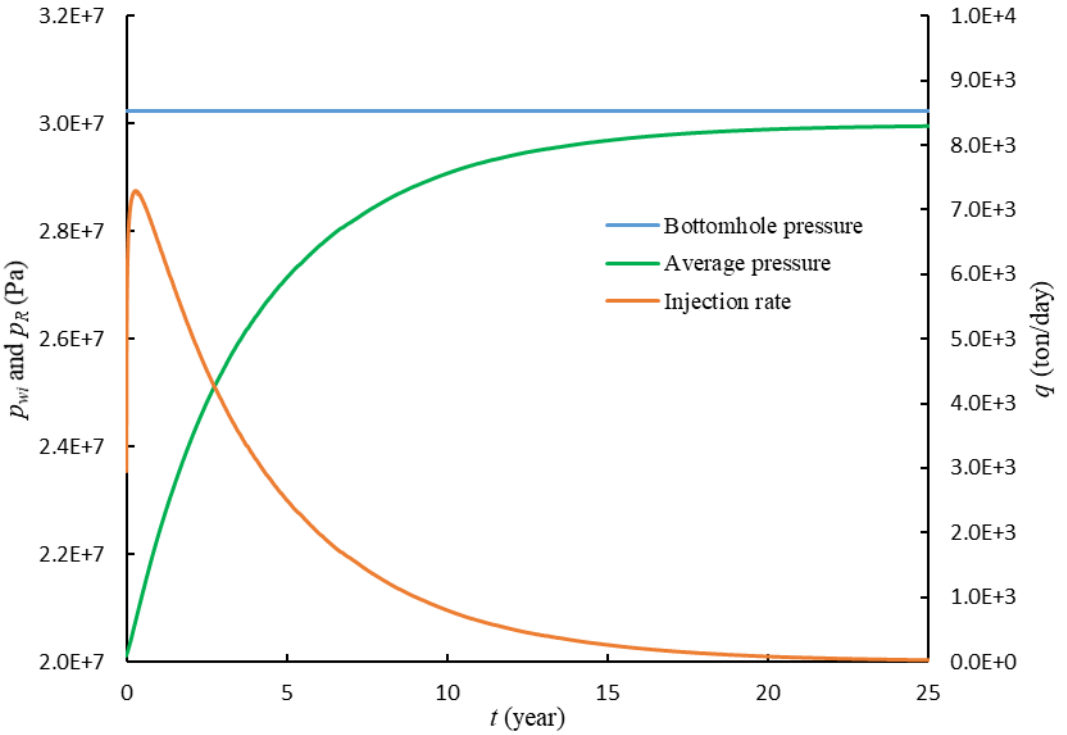

Figure 5.3. Injection bottomhole and average reservoir pressures (on the primary *y*-axis) and injection rates (on the secondary *y*-axis) for continuous injection at constant bottomhole pressure

The injection rates, the bottomhole pressures and the average reservoir pressure for CR and CP cases are shown in Fig. 5.2 and Fig. 5.3 respectively. Injecting at a constant rate of 0.5 Mt/year (1369.9 ton/day) is associated with an initial overpressure of 5.0 MPa at the wellbore. Then, the bottomhole pressure starts to decline (for 6 month) because of the expanding CO_2 dry-out zone. Following this decline, the pressure gradually increases due to the dominance of the boundaries' effects. Similarly, for the CP case, an initial increase in the injection rate – due to the dominating effect of the dry-out zone expansion - is observed for 6 months. This is followed by a decline due to the dominating effect of the closed outer boundaries of the reservoir.

The injectivity index variation for both CR and CP conditions is shown in Fig. 5.4. The injectivity index shows initial increase over time for both injection schemes. This trend is followed by a noticeable decline for CP injection, and a gentle decline for CR injection. The initial increase is related to the expansion of the dry-out zone while the later decline is attributed to the pressure buildup caused by injection into a closed system. The injectivity index for the CP case is initially higher than that for the CR case. This is related to the large high-mobility CO_2 zone created around the wellbore soon after starting injection to satisfy the large overpressure imposed by the CP constraint. This is compared to the relatively smaller CO_2 amount injected over the same period during CR conditions. Rapid decline in the injectivity index for the CP case is observed at late time compared to a very slow decline for the CR case. This is due to injecting large volumes of CO_2 at early time for the CP case which causes the average pressure to build up much faster as compared to the CR case. Also, it should be noted that the injectivity index would decrease monotonically if the system is single-phase (i.e. when brine is injected into the aquifer).

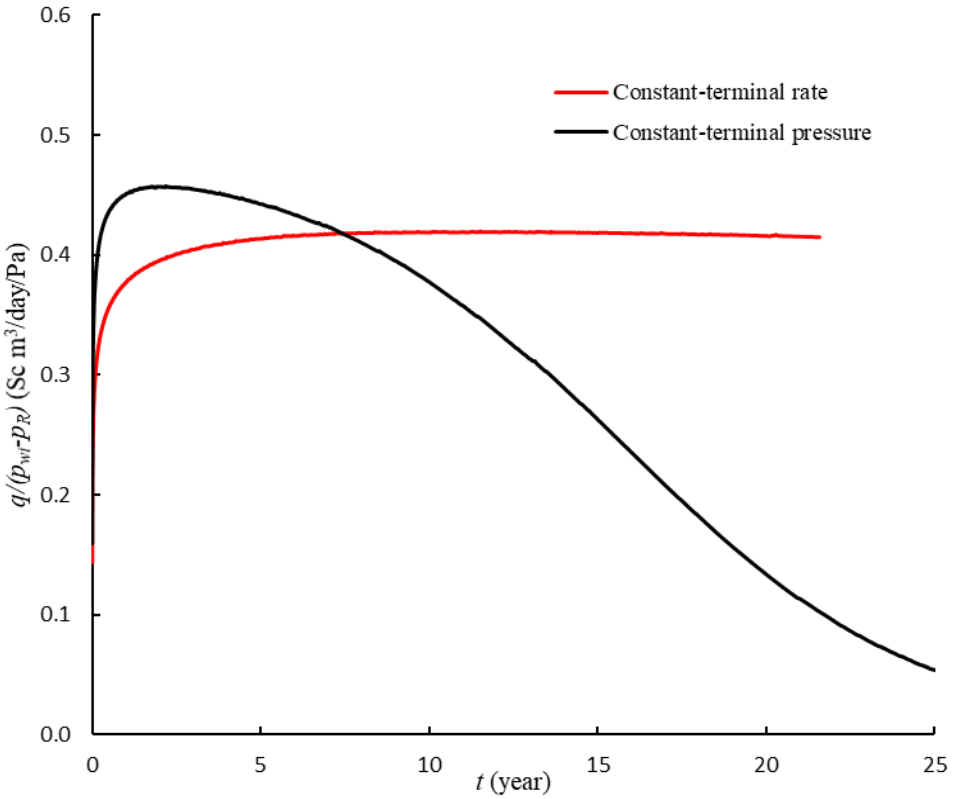

Figure 5.4. Injectivity index variation for continuous injection at constant bottomhole pressure and constant rate conditions

The ultimate storage capacity is the cumulative amount of CO_2 that has been injected when the bottomhole pressure reaches p_{max} - for CR injection - or until the economic limit rate is reached for CP injection. Injection at a constant overpressure of 10.1 MPa at the well results in cumulative storage amount of 12.6 Mt after 25 years of injection when the economic limit has been reached. However, 90 % of this amount has been reached during the first 6.5 years compared to the whole 21.6 years for CR case to inject the same amount. This is due to the high injectivity accommodated during injecting at CP conditions at early times. The cumulative CO_2 injected for both cases is shown in Fig. 5.5. As a whole, the ultimate storage capacity achieved during CP conditions is higher than that achieved during CR conditions by 13.9 %.

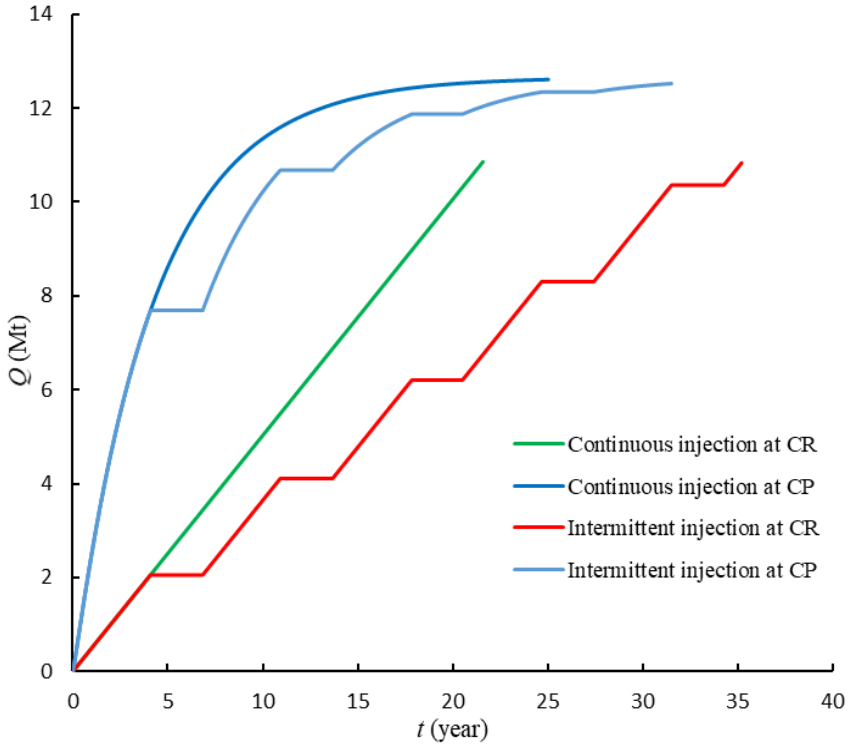

Figure 5.5. Cumulative CO_2 injected for continuous and intermittent injection at constant bottomhole pressure and constant rate conditions

It is unlikely that either of the CP and CR conditions are adopted/encountered in reality since the injection operation is controlled by the CO_2 stream supplied by the emission source. Fluctuations and/or temporary shut downs would be inevitable during the injection operations due to variations in the amounts of supplied CO_2. However, from the above comparison of CP and CR cases, it is clear that the storage capacity can be significantly different depending on the well operating condition. It is also clear that one should adopt injection at CP whenever possible. This would modify the injectivity that follows even though the CP condition cannot be kept permanently.

5.3. Intermittent Injection

Intermittent injection is likely to occur when industrial sources suffer from production problems. Fig. 5.6 illustrates the behavior of bottomhole pressure and the injection rate for intermittent CR

injection. The well is assigned the same injection rate as the continuous CR case (1369.9 ton/day). Each cycle is composed of a flow period of 4.1-year duration followed by a shut-in period of 2.7 years. The injection lasts for a total 35.2 years when the bottomhole pressure reaches the p_{max} (compared to 21.6 years for the continuous CR case). Similar to the continuous CR injection case, at the beginning of injection (i.e. at the first injection period), the bottomhole pressure begins at a higher value that declines rapidly and then increases with injection. The initial high value is attributed to the high-resistivity brine which requires high bottomhole pressure to be displaced by CO_2. The pressure then drops because of forming the dry-out region near the wellbore. However, starting with the second flow period, the injection is initialized with pre-existing CO_2 zone into the aquifer as a result of which the bottomhole pressure no longer decreases.

The injectivity index variation for the intermittent CR case is shown in Fig. 5.7. The first flow period – similar to continuous CR case - shows an increase in the injectivity index as the dry-out zone is expanding. For each of the remaining flow periods, the injectivity index starts at a higher value, followed by a rapid decline and then an increase at later time. The later increase is the result of expanding CO_2 dry-out zone, as expected. However, the early decline – which has not been observed for the first cycle nor the continuous CR injection – appears due to the difference of early-time pressure behavior as explained in the previous paragraph. Next, the index starts to decline slowly when the effect of boundaries becomes dominant. Overall, the injectivity index exhibits an increasing trend over the initial project period followed by a slight decrease when the effect of boundaries becomes dominant.

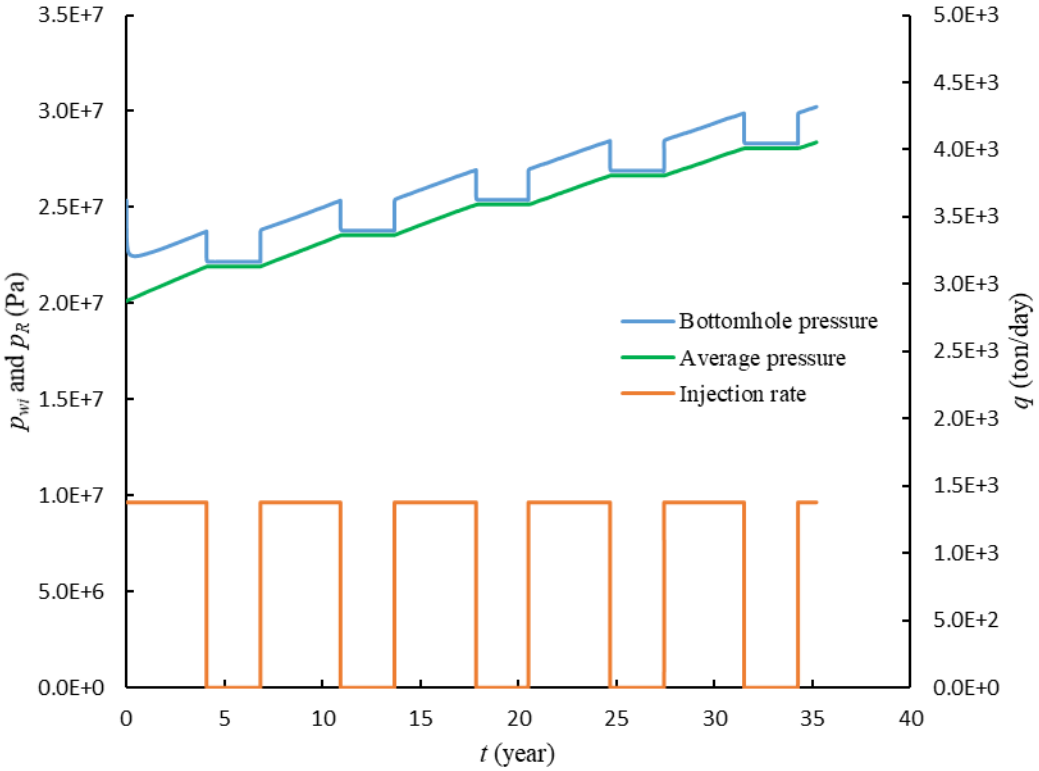

Figure 5.6. Injection bottomhole and average reservoir pressures (on the primary *y*-axis) and injection rates (on the secondary *y*-axis) for intermittent injection at constant rate

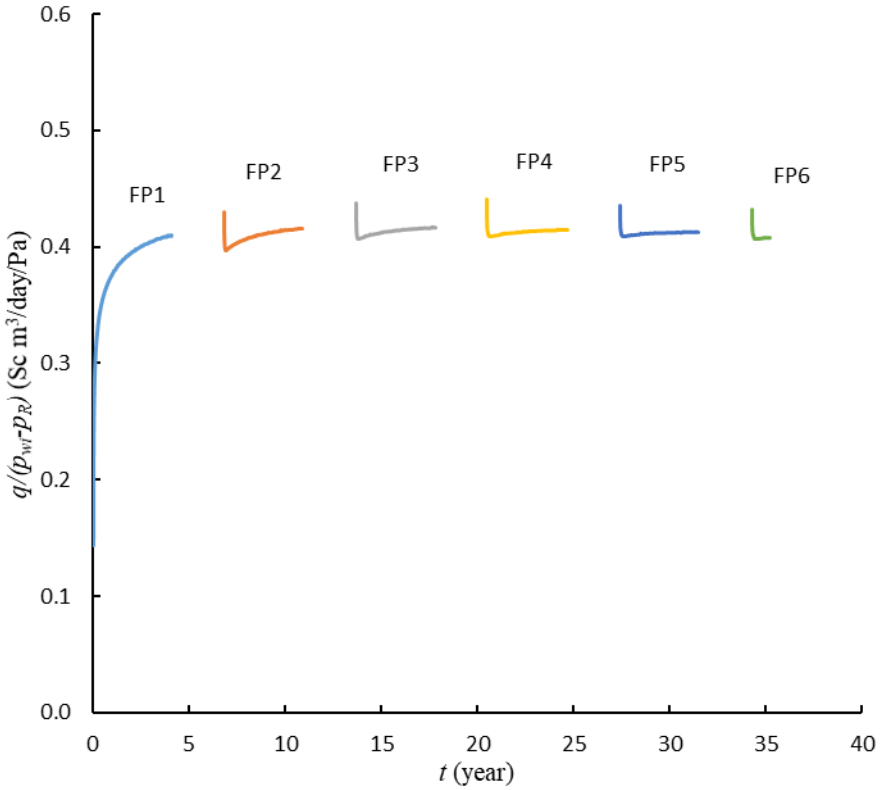

Figure. 5.7. Injectivity index variation for intermittent injection at constant rate

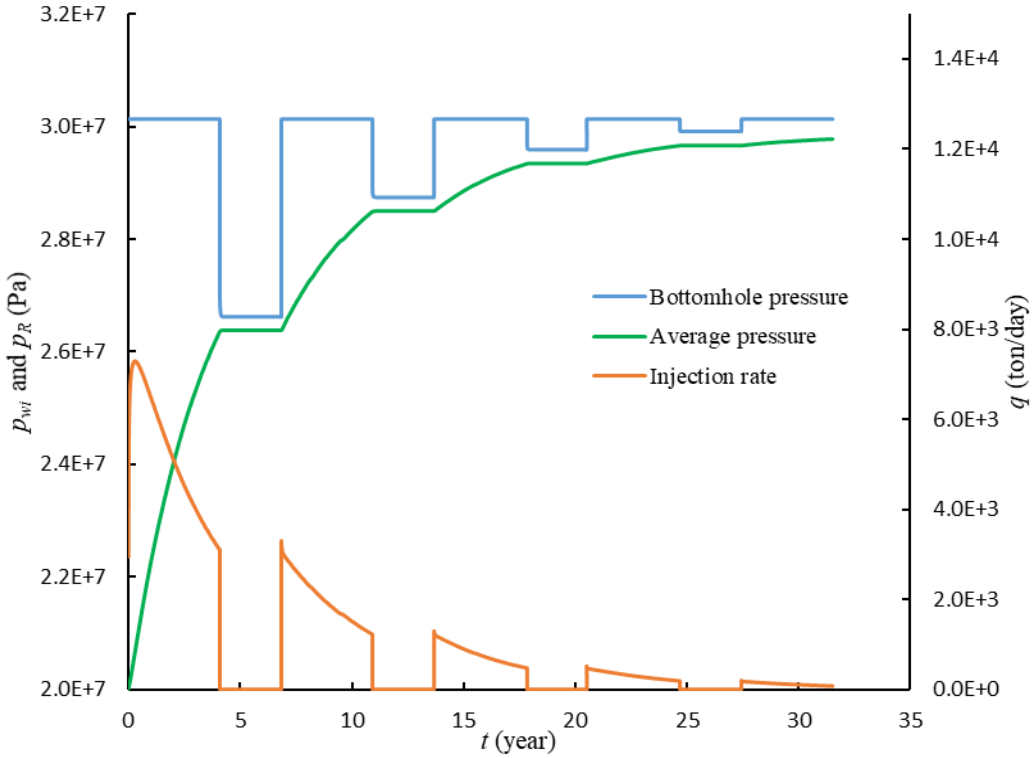

Figure 5.8. Injection bottomhole and average reservoir pressures (on the primary *y*-axis) and injection rates (on the secondary *y*-axis) for intermittent injection at constant pressure

We now investigate, the intermittent injection at CP conditions. The durations of flow and shut-in periods are exactly the same as intermittent CR case (4.1 years for each flow period and 2.7 years for each shut-in period). The bottomhole pressure constraint is set at the p_{max} for each flow period. The economic injection rate of 27.4 ton/day has been reached after 31.5 years of intermittent injection compared to 25 years for the continuous CP injection. The bottomhole injection pressure and the injection rate behavior are shown in Fig. 5.8. Fig. 5.9 shows the injectivity index for this case. The behavior of the rate and the injectivity index can be explained in the same way that the pressure and injectivity index behavior was explained for the intermittent CR case above. Overall, comparison of the injectivity indices of the continuous injection versus the corresponding intermittent injection cases indicates that the injectivity behavior is very similar.

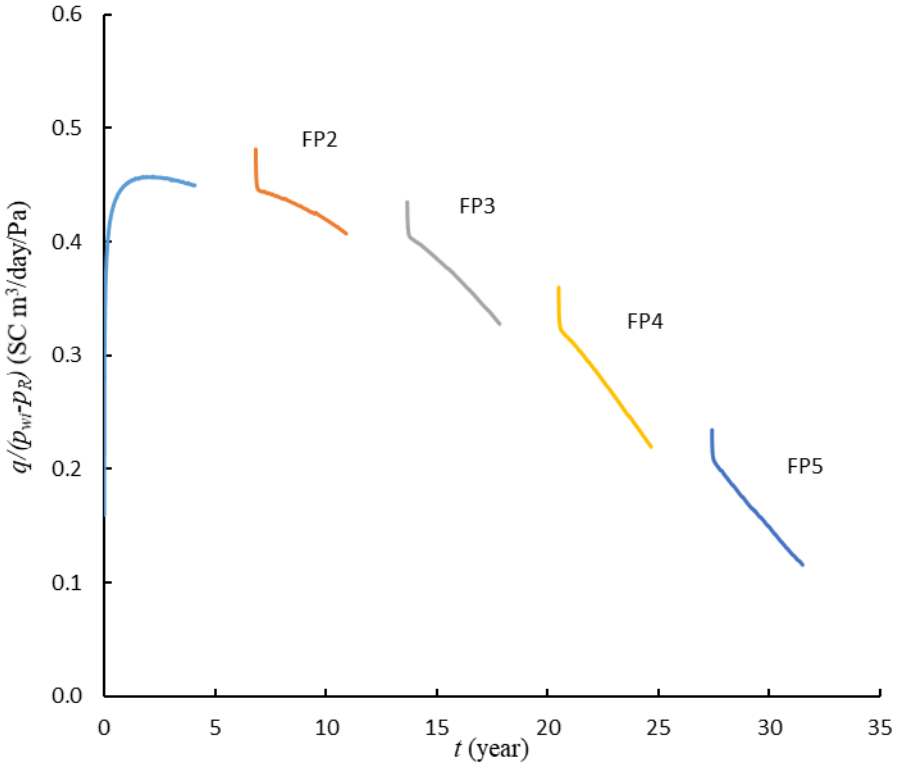

Figure 5.9. Injectivity index variation for intermittent injection at constant bottomhole pressure

5.4. Volumetric and Economic Feasibility of Different Injection Schemes

Based on the comparison shown in Fig. 5.5, different well operating conditions result in different ultimate storage capacity at the end of the injection period. The injection duration is taken as the period at the end of which the economic limit rate is reached for CP injection, and when the bottomhole pressure reaches the p_{max} for CR injection. Due to the discrepancy between the predicted ultimate storage capacity and injection duration for each injection scheme, it is helpful to use a simple NPV analysis as an indicator of economic feasibility of injecting CO_2 under different operating conditions. By comparing the NPVs of different injection scenarios, they can be ranked according to their economic feasibility. The NPV considers the present value of all the project future revenues owing to tax credits granted for storing CO_2, and all the operating and

capital costs associated with CO_2 capture, compression, transport, and storage. NPV is computed as follows (Jahangiri and Zhang, 2011):

$$\mathrm{NPV} = \sum_{i=0}^{N} \frac{\mathrm{NCF}_i}{(1+r)^i} - \mathrm{CAPEX} \tag{5.16}$$

$$\mathrm{NCF}_i = \Delta Q_i \times \left(C_{CO_2} - \mathrm{OPEX}\right) \tag{5.17}$$

Where:

NCF = periodic net cash flow, US$

r = periodic discount rate, fraction

i = periodic increment

N = total number of project periodic increments

CAPEX = initial investment/capital costs, US$

ΔQ_i = cumulative CO_2 injected over i^{th} period, ton

C_{CO2} = tax credit of CO_2 stored per ton, US$

OPEX = total operating cost of CO_2 storage per ton, US$

The total operating cost (OPEX) is calculated by summing the individual costs of CO_2 capture, compression, transport, and storage. However, it is important to note that the main objective of our study is to maximize the value of the injection well by optimization of the injection strategy. Thus, we do not include the cost of capture, compression, and transport in our economic analysis. The cost of storage is the only item to be included as it is part of the injection well optimization. Nguyen and Allinson (2002) pointed out that the operating costs of storing CO_2 is function of the location of the storage site, aquifer/reservoir depth and permeability, rate of throughput and the costs of recompression. All these parameters make the storage OPEX to be variable from case to case. In their paper, Schmelz et al. (2020) presented a comprehensive study on the total OPEX of CO_2 capture, compression, transport and storage implemented from 138 power plants in the US. The authors concluded that 6 US$/ton CO_2 is a reasonable value for storage OPEX. Therefore, 6 US$/ton is used in our NPV analysis as the storage OPEX. The capital expenditure for the storage component includes the cost of drilling a class VI well and the cost of compression at the well site. A total storage CAPEX has been estimated to be 5.0 million US$ (EPA, 2008b). Tax credits are identified by regulatory sectors in order to support large-scale GCS projects (Ghomian et al., 2008) Without these credits, most GCS projects may not be economic especially those not coupled with EOR (e.g. GCS in saline formations) due to the high costs of operation and investment. We assume the tax credit to be US$ 50 per ton based on US Congress's extension of the Section 45Q tax law

in 2018. The selection of discount rate is strongly dependent on several economic parameters including the economic feasibility of alternative options, and consequently rigorous calculation may be needed to estimate the discount rate which is beyond the scope of this work. In this study, the annual discount rate of 10 % is assumed in the calculations of the NPV for different injection schemes (Beck, 2020; Jahangiri and Zhang, 2011) The NPV is calculated using Eq. 5.16 for the following cases: 1) continuous injection at CR, 2) continuous injection at CP, 3) intermittent injection at CR, and 4) intermittent injection at CP. To better compare the feasibility of different injection schemes, we propose determining the *equivalent* ultimate capacity of CO_2 via dividing the NPV by the difference between the tax credits and the operating costs per ton as follows:

$$Q_{equivalent} = \frac{\text{NPV}}{\left(C_{CO_2} - \text{OPEX}\right)} \tag{5.18}$$

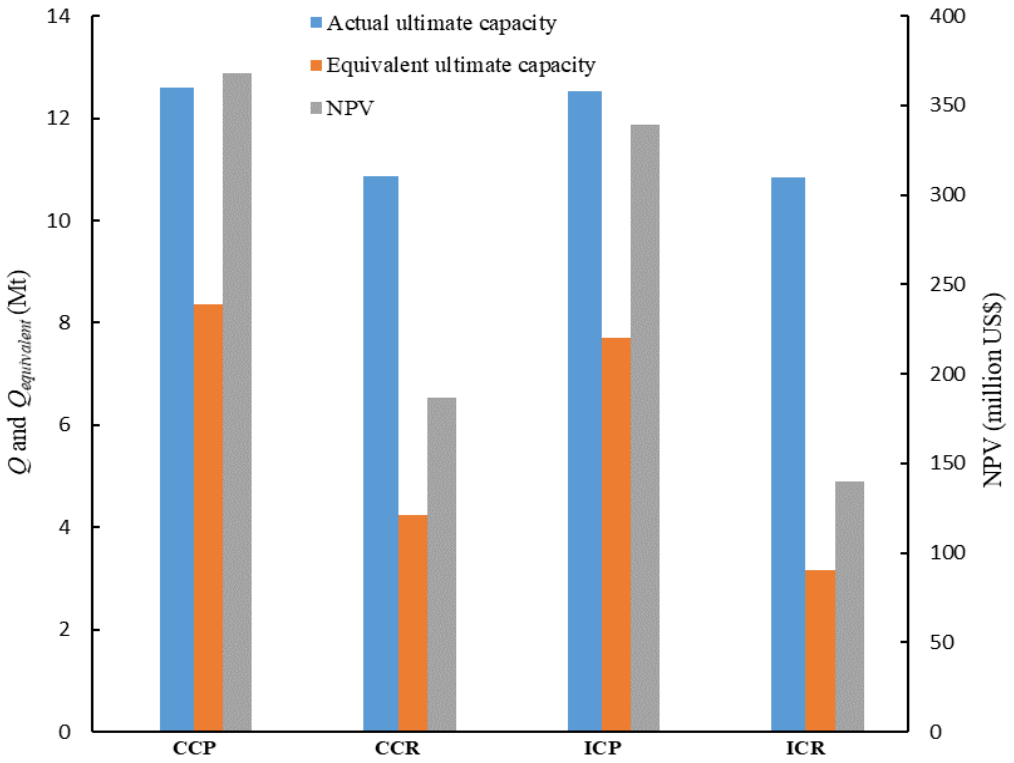

Figure 5.10. Comparison between the NPV, ultimate storage capacity, and equivalent ultimate storage capacity for different injection schemes (CCP and CCR indicate continuous injection at CP and CR respectively – ICP and ICR indicate intermittent injection at CP and CR respectively

$Q_{equivalent}$ is useful in determining the present volumetric value of all CO_2 amounts that can be stored over the whole injection period. Unlike NPV which is a financial concept, $Q_{equivalent}$ is a volumetric concept that honors both the actual ultimate capacity (Q) achieved over the whole project period, and the present economic value of the project. Dividing the NPV (in US$) by the difference between the tax credits and the OPEX (in US$/ton CO_2), the resulting $Q_{equivalent}$ (in ton CO_2) translates the NPV – which considers the cumulative CO_2 injected, the project period, and

the discount rate – into present volumetric value. This is helpful in comparing the volumetric potential of different injection schemes regardless of the injection period or the achieved actual capacity. Similar to the relationship between NPV and the future NCF, $Q_{equivalent}$ is usually less than Q due to the fact that money, and as a consequence the financially-based items, is depreciated over time. Fig. 5.10 illustrates the comparison between NPV, Q, and $Q_{equivalent}$. It is clear that the economic feasibility and the ultimate capacity of a storage formation are dramatically affected by the injection scheme adopted. For the cases presented herein, given a $50 per ton government subsidy, the operator can lose more than 229 million US$ (5.2 equivalent Mt of CO_2) when injecting intermittently at CR rather than continuously at CP. Based on the equivalent storage capacity values, the capacity reduces to 51, 92, and 38 percent of the CP storage capacity for the continuous CR, intermittent CP, and intermittent CR cases, respectively. Based on the comparison shown in Fig. 5.10, the preferred arrangement of the four injection conditions is as follows: 1) injecting continuously at CP, 2) injecting intermittently at CP, 3) injecting continuously at CR, and 4) injecting intermittently at CR. Due to the inevitable fluctuations of CO_2 supply from the emission sources, the operator may gain more than 200 million US$ (4.5 equivalent Mt of CO_2) when injecting intermittently at CP rather than intermittently at CR. Therefore, generally, it is more economic, whenever appropriate, to inject CO_2 as fast as possible (i.e. at CP conditions).

5.5. Application to GCS Project with Injection History

The previous analysis can be helpful in designing the optimum conditions to further proceed with CO_2 injection for storage projects with injection history. To evaluate the effect of the injection well operating condition on the ultimate storage capacity of ongoing projects, the well is assigned an injection rate history lasting for 8 years as shown in Fig. 5.11. Reservoir and fluid properties are identical to those given in Table 5.1. Fig. 5.12 illustrates the effect of adopting the four injection schemes, discussed earlier, on the NPV, the actual and the equivalent capacities achieved beyond the injection history until the end of injection period (i.e., ΔQ, and $\Delta Q_{equivalent}$). Similar to previous simulations, the injection continues until the pressure buildup reaches the p_{max} (for injection at CR) and until the economic rate limit is reached (for injection at CP). By the end of injection, it is clear that injecting CO_2 at CP either continuously or intermittently (i.e. as fast as possible) is much better than injection at CR. The intermittent injection at CP can save 72 million US$ (1.6 equivalent Mt of CO_2) more than intermittent injection at CR. In addition, intermittent injection at CP is profitable more than continuous injection at CR by about 49 million US$ (1.1 equivalent Mt of CO_2). Also, the NPV of continuous injection at CP exceeds that of intermittent CP injection by about 23 million US$ (0.53 equivalent Mt). As expected, this again implies that it is most feasible to inject CO_2 as fast as possible to have a better capacity and return on investment of the considered storage site.

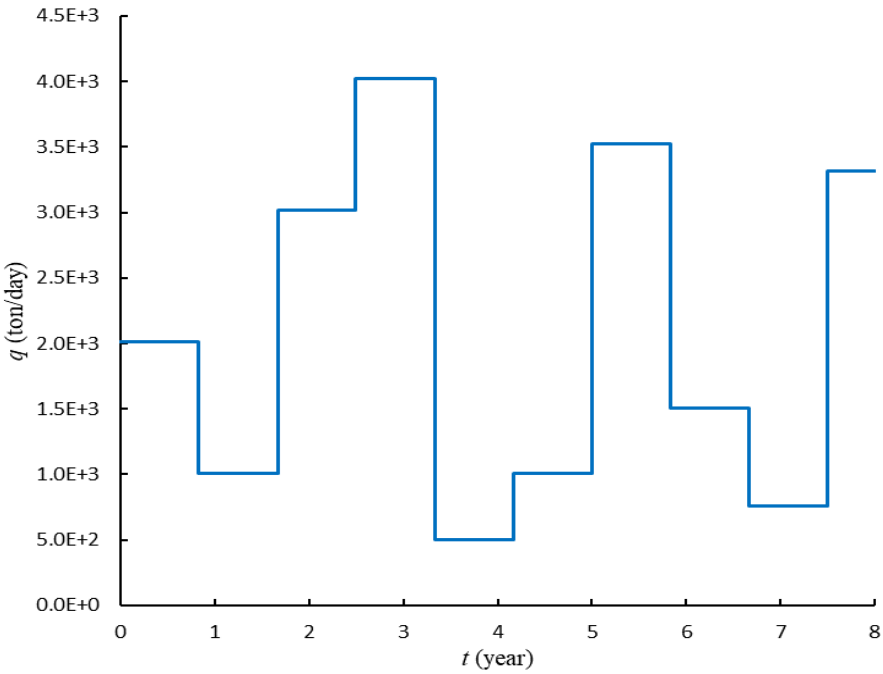

Figure 5.11. Injection rate history for the example application to a GCS project

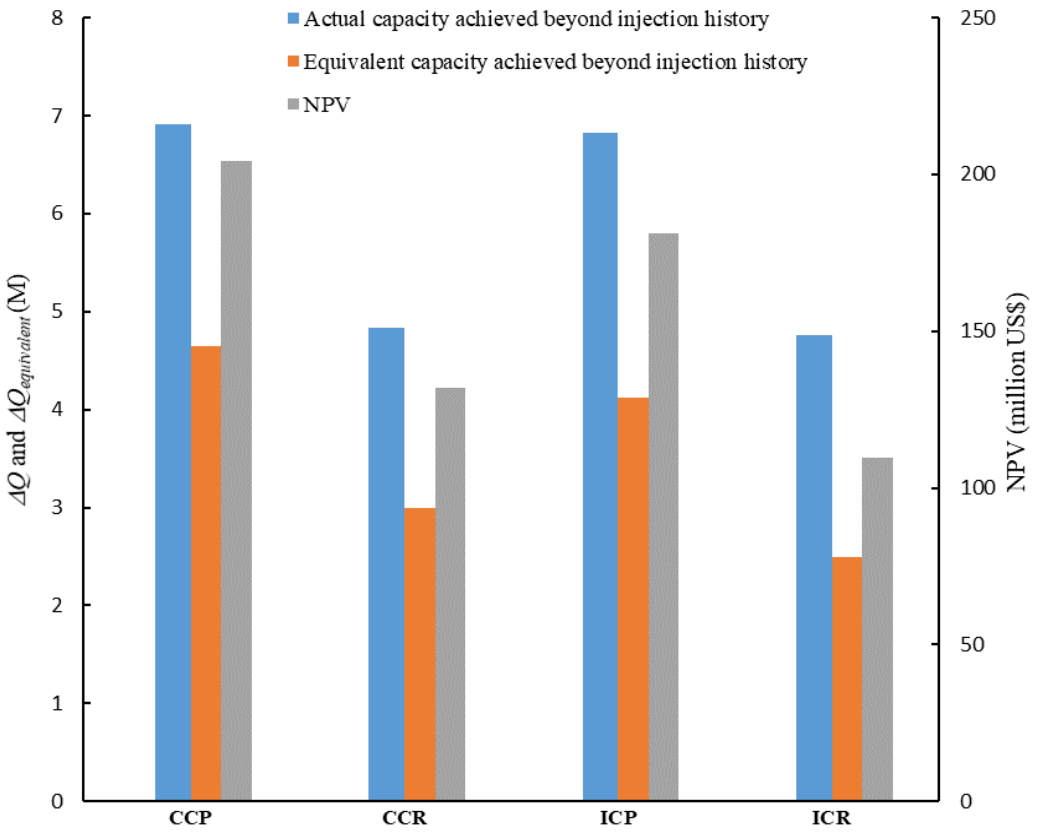

Figure 5.12. Effect of injection schemes on NPV, the ultimate capacity and the equivalent capacity (achieved beyond injection history) for a GCS project with injection history (CCP, CCR, ICP, ICR indicate continuous/intermittent injection at CP and CR, respectively)

5.6. Sensitivity Analysis

CO_2/brine displacement is governed by three forces: the viscous, buoyant, and capillary forces. Capillary forces have smaller effect on the ultimate capacity as compared to the viscous and the buoyant forces (Bachu, 2015; Kopp et al., 2009). The viscous forces are primarily controlled by CO_2 injection rate, the relative and absolute permeabilities. On the other hand, the buoyant forces are mainly affected by the vertical permeability (k_v), formation dip angle, and reservoir thickness. Varying k_v values changes the absolute permeability of the system as well. Also, it has been shown that injectivity, for closed aquifers, is weakly sensitive to the relative permeability (Burton et al., 2008; Mathias et al., 2013). This means that the remaining properties of prime interest are the injection rate, vertical permeability, and formation dip angle. In this section a total of 12 simulation cases are conducted to evaluate the effect of the aforementioned parameters on the ultimate storage capacity, NPV, and equivalent capacity for both CP and CR injection schemes. Additionally, we run additional 4 simulations to investigate the effect of injection through a fully-penetrating well, and into open outer boundary conditions as compared to the base case.

5.6.1. Effect of Injection Rate

In addition to the base case injection rate of 0.5 Mt/year, CO_2 is injected continuously at 0.3, 0.7, 1.0 and 1.5 Mt/year through two simulation runs. These rates cover a practical range which can be encountered in storage projects. Rest of the input parameters are the same as the base case (see Table 5.1).

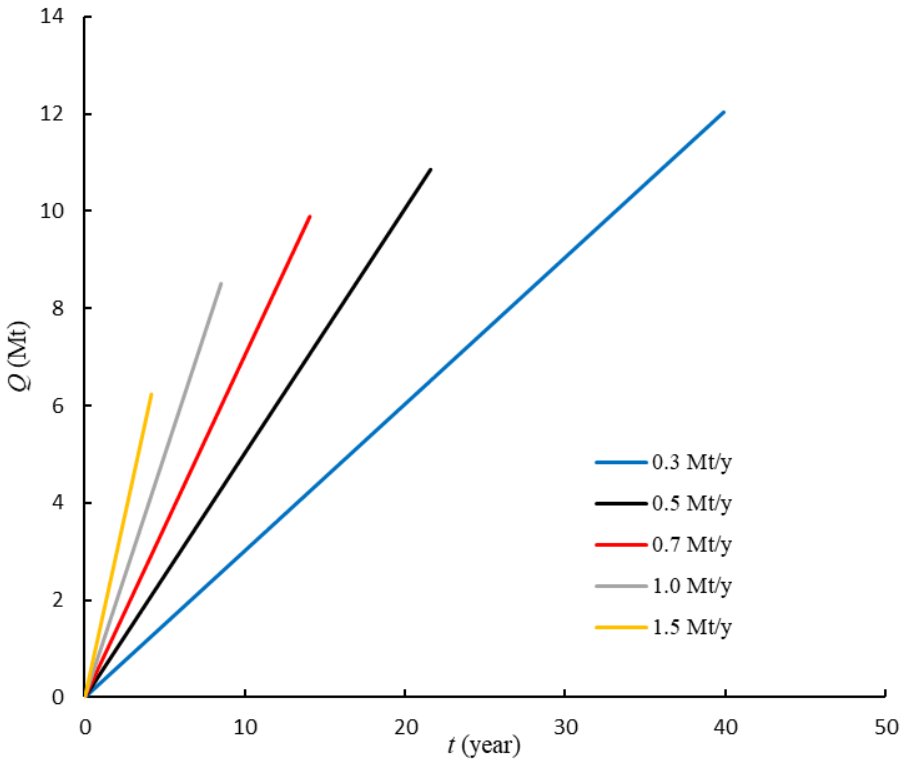

Figure 5.13. Effect of varying the injection rate of CO_2 on the ultimate storage capacity

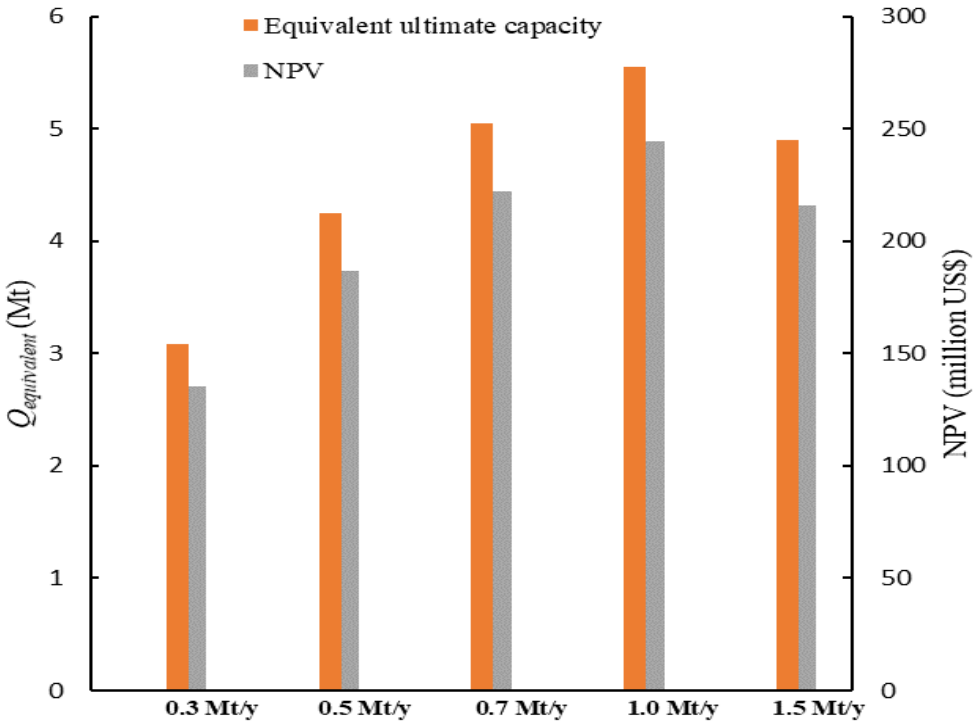

Figure 5.14. Effect of varying the injection rate of CO_2 on NPV and the equivalent storage capacity

As shown in Fig. 5.13, adopting higher injection rates can severely decrease the ultimate storage capacity of a given formation. This is related to the fact that injection at higher rates causes rapid buildup in the bottomhole pressure, which negatively affects the storage capacity. As compared to the base case, the ultimate storage capacity decreases by 8.9 %, 21.6 %, and 42.6 % when injecting, respectively, at 0.7, 1.0 and 1.5 Mt/year. But it improves by 10.9 % for the 0.3 Mt/year injection rate case. However, for the range of the injection rates studied herein, injecting at lower rates may not be economically feasible as it will adversely affect the NPV and the equivalent storage capacity of the formation. This is attributed to the fact that lower injection rates achieve higher storage capacity through elongating the project period which overall negatively impacts the NPV. In other words, higher injection rates shorten the project period, but at the same time achieve higher capacity compared to those achieved during the same period for lower rates (Fig. 5.13). In NPV calculations, the capacity achieved at early times weighs much more than those achieved at late times due to the effect of the discount rate (Eq. 5.18). However, adopting very high injection rates can dramatically shorten the project period, adversely affecting the NPV. Therefore, there should be an economically optimum injection rate that maximizes the NPV and the equivalent capacity. It is noticed that injection rate of 1.0 Mt/year achieves the maximum NPV, therefore, it can be considered as the optimal injection rate that can be practically utilized for the same injection conditions and aquifer parameters. As shown in Fig. 5.14, the operator gains around 35, 57, and 29 million US$ (0.81, 1.30, and 0.66 equivalent Mt of CO_2) when, respectively, injecting at 0.7, 1.0 and 1.5 Mt/year, and loses about 51 million US$ (1.2 equivalent Mt) when injecting at 0.3 Mt/year. It should be noted that very high injection rates are, often, injected through multiple wells to manage overpressure, ensure integrity of the formation rock, and minimizes leakage risks.

5.6.2. Effect of Vertical Permeability

Higher vertical permeability (k_v) improves the system total absolute permeability. But, it causes the buoyancy to be more effective which can negatively affect the sweep efficiency. Generally, k_v is lower than horizontal permeability especially in thin reservoirs and/or due to the presence of interbedding shale laminations. We run four simulations. The base case (k_v = 5 mD) is modified by increasing k_v to 50 mD in the first two runs, and to 250 mD in the other two. The simulation results, shown in Fig. 5.15, indicate that the ultimate storage capacity increases for both CP and CR conditions with higher k_v. As mentioned before, this is related to the fact that higher k_v values, while keeping the horizontal permeability the same, improves the total system permeability. This increases the system flow capacity which causes slower buildup of the average and the bottomhole pressures, and allows for more CO_2 to be injected over the project period. This means that, for the simulations performed herein, the positive effect of improving the system total permeability dominates over the negative effect that can arise due to higher buoyancy. For CR injection, the ultimate capacity improves by 23.7 % and 63.9 % for k_v values of 50 mD and 250 mD respectively. For CP injection, the ultimate capacity increases by 13.2 % and 17.7 % for k_v values of 50 mD and 250 mD respectively. These improvements are also reflected on the NPV and the equivalent capacity as shown in Fig. 5.16. Noting that the increase in NPV and $Q_{equivalent}$, with higher k_v is more sensible for CP injection. This is related to the fact that bulk CO_2 injection occurs at early times for CP scheme which weighs more in the calculations of NPV and $Q_{equivalent}$. However, for CR injection, the cumulative Q is evenly distributed over the injection period.

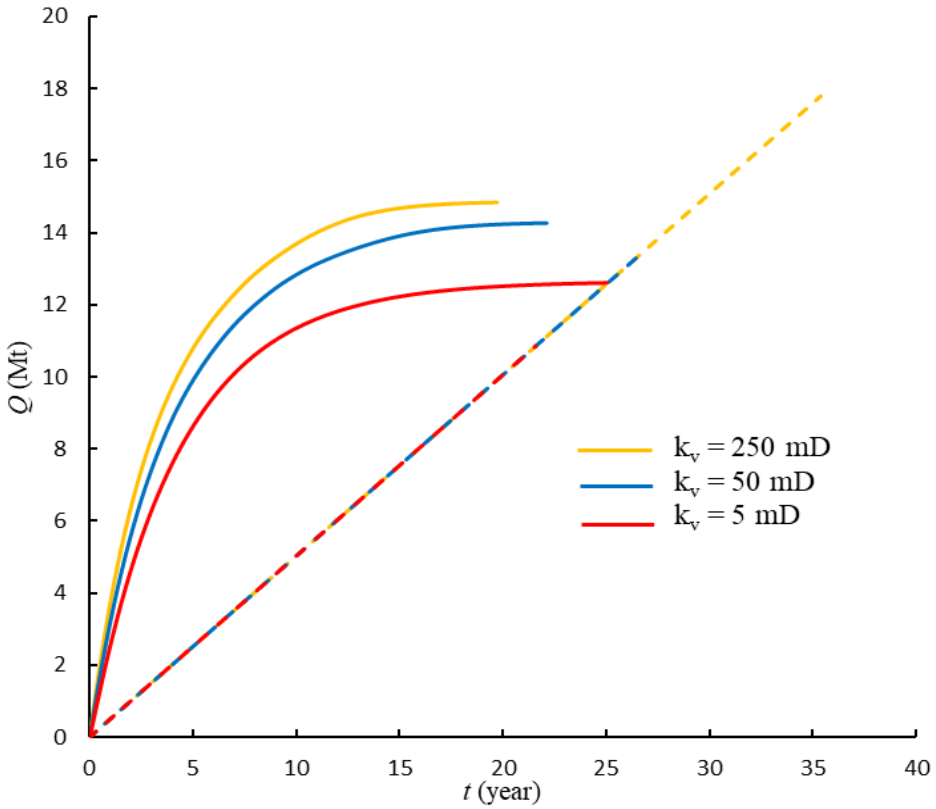

Figure 5.15. Effect of varying the vertical permeability on the ultimate storage capacity - dashed lines show CR and solid lines show CP

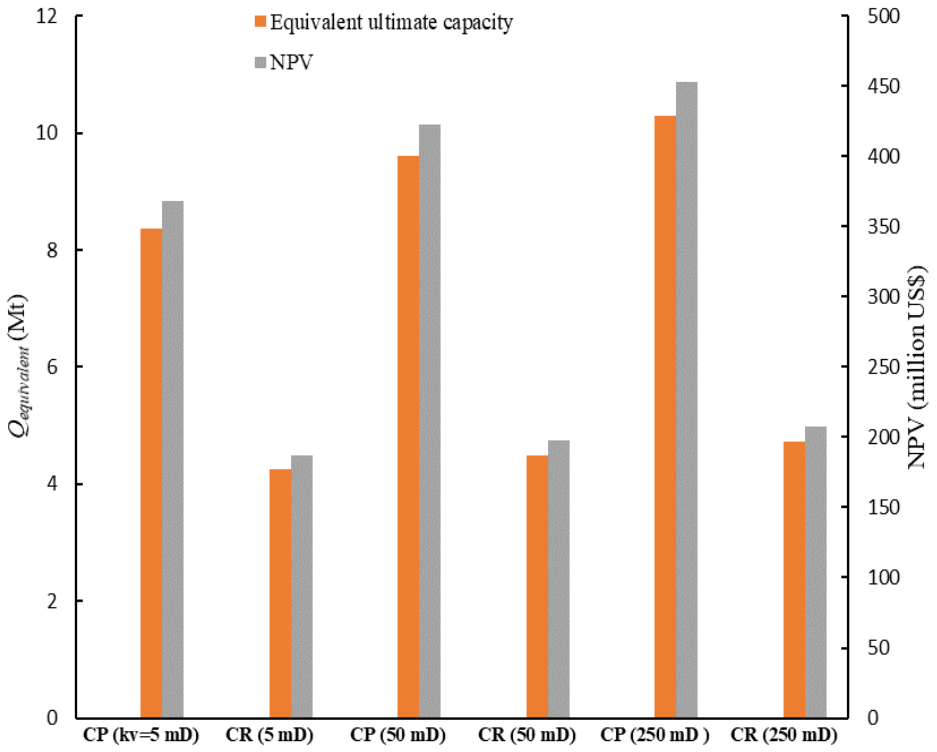

Figure 5.16. Effect of varying the vertical permeability on NPV and the equivalent storage capacity considering CP and CR injection schemes

5.6.3. Effect of Formation Dip Angle

The effect of formation dip angle on the ultimate storage capacity of the aquifer is investigated through four simulation runs considering continuous injection at CP and CR conditions. Compared to the base case, the formation dip angle is set at 1.5° for the first two runs, and at 3° for the other two. The remaining input parameters are identical to the base case shown in Table 5.1. In a way similar to Cartesian grid models, introducing dip angle in the axially-symmetric radial models causes part of the block rings to be elevated and part to be lowered from the un-tilted horizontal plane. Due to dip angle, the extent of the injected CO_2 plume will not be the same in both sides of the injection well. The extent is further updip, but it is limited downdip. As a consequence of this asymmetric distribution of the plume, the storage volume can be underutilized which in turn decreases the ultimate storage capacity of the formation as shown in Fig. 17. When compared to the base case, the ultimate storage capacity for CR operating condition decreases by 5.96 % and 6.68 % for dip angles of 1.5° and 3° respectively, and for CP condition, the capacity decreases by 2.76 % and 3.11 % for dip angles of 1.5° and 3° respectively. Fig. 18 displays the effect of the decreased capacity with increasing dip angle in terms of NPV and $Q_{equivalent}$. Both NPV and $Q_{equivalent}$ decrease with higher dip angles. Similarly, the effect is more noticeable during CP injection as bulk CO_2 injection occurs at early times which weighs higher in the NPV calculations. On the other hand, the cumulative Q is evenly distributed over the project period for CR injection. As a whole, it would be better to store CO_2 as fast as possible (CP scheme) in horizontal or with very small dipping angle formations to utilize the maximum storage volumes.

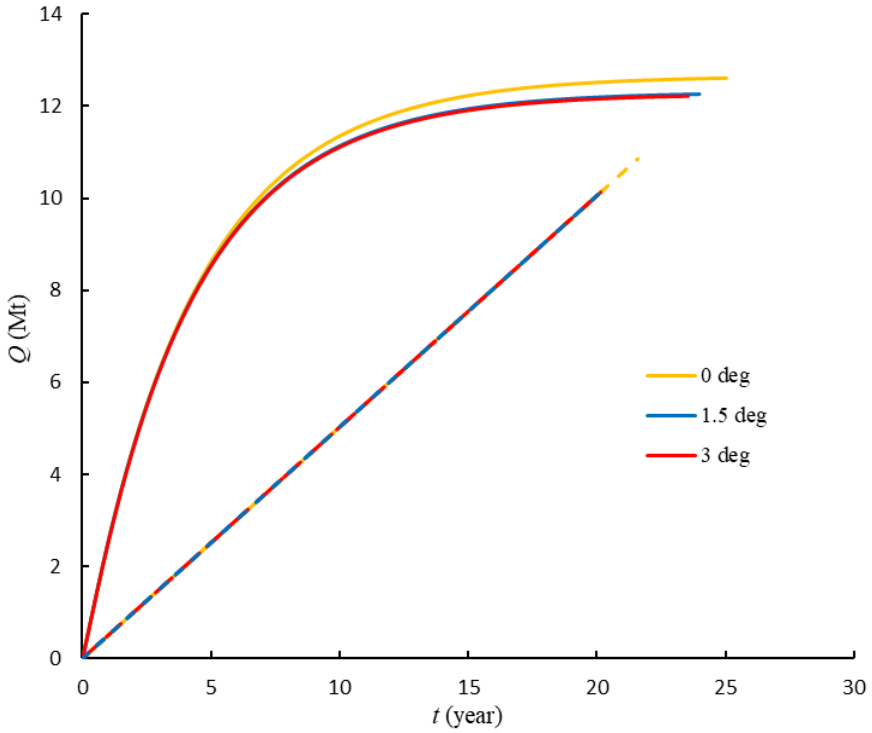

Figure 5.17. Effect of varying the formation dip angle on the ultimate storage capacity - dashed lines show CR and solid lines show CP

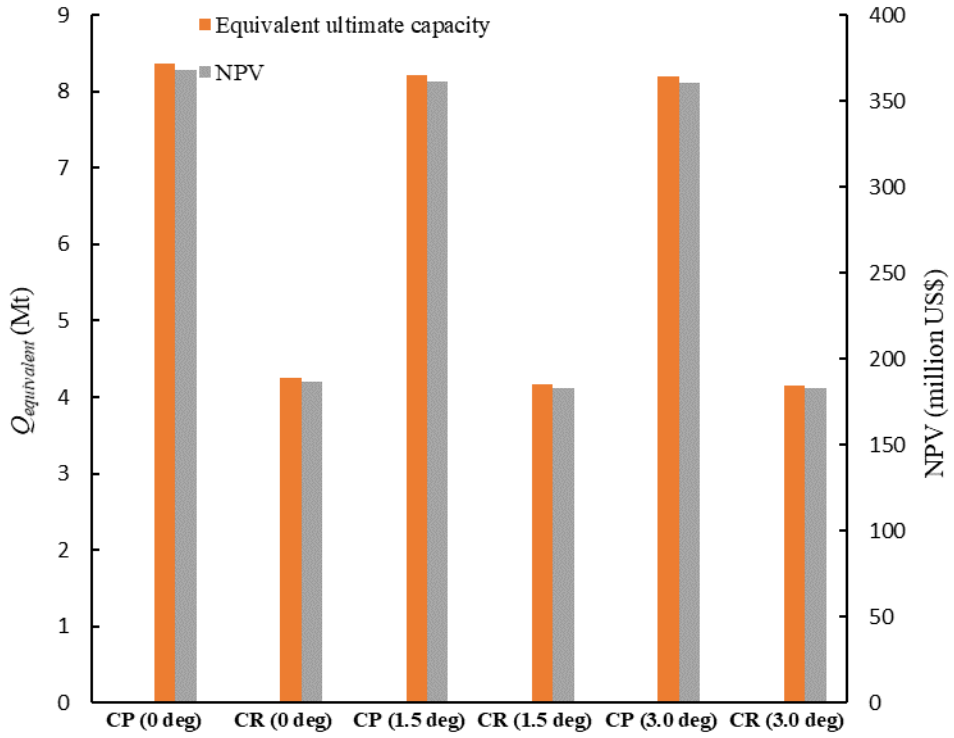

Figure 5.18. Effect of varying the formation dip angle on NPV and the equivalent storage capacity considering CP and CR injection schemes

5.6.4. Effect of Outer Boundary Conditions

The base case, and all the subsequent simulations, assumes that the aquifer is closed with no-flow outer boundaries. Nevertheless, this may not be as common in practice, and open lateral boundaries (referred to as constant-pressure boundaries) could have significant impact on the ultimate storage capacity, NPV, and equivalent storage capacity. The parametric study of Ehlig-Economides and Economides (2010) showed that the ultimate storage capacity of CO_2 in closed aquifers cannot exceed 1.0 % of the formation pore volume. This is because, in bounded aquifers, the injected CO_2 is accommodated by compressing the in-situ brine and the formation rocks. This causes rapid pressure buildup that injection must be stopped before exceeding the maximum allowable pressure (p_{max}). On the other hand, open aquifers can accommodate larger volumes of CO_2 where additional CO_2 expels in-situ brine out of the formation. This allows injection to continue until breakthrough as long as the pressure buildup does not exceed p_{max}. To simulate open aquifer, we modified the base case by introducing a volume modifier of 10^5 km radial extent at the outer gridblocks. The volume modifier imposes almost no change in the primary variables (i.e. pressure and saturation) within the boundary gridblocks during injection. The remaining input parameters are identical to the base case displayed in Table 5.1. We run two simulations considering both injection scenarios (i.e. CP and CR). For both scenarios, injection is stopped when CO_2 plume reaches the external boundaries of the aquifer just prior to the volume modifier. 1.0 % CO_2 saturation is taken as the cutoff value of the plume breakthrough into the external gridblocks. The simulation results, shown in Fig. 5.19, indicate that the ultimate storage capacity is dramatically improved especially for the CP injection scheme for the open system, as expected. When compared to the base case, the ultimate storage capacity for CR operating condition increases from ~ 10 Mt to ~ 37.5 Mt. For CP condition, the ultimate storage capacity increases from ~ 12.6 Mt to ~ 289 Mt.

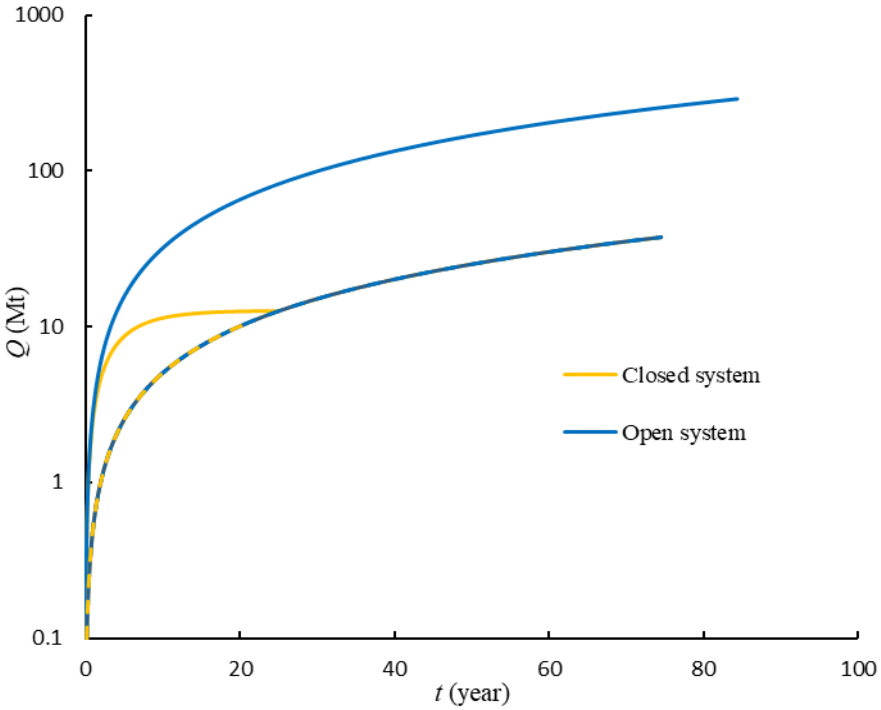

Figure 5.19. Comparison of the ultimate storage capacity for open aquifer versus the base case (closed aquifer) - dashed lines show CR and solid lines show CP

A note that the improved ultimate storage capacities are achieved over much longer periods. For CR conditions, the ~ 37.5 Mt is achieved over ~ 74.5 years as compared to ~ 21.6 years for the base case. Also, for CP conditions, the ~289 Mt is achieved over 84.4 years as compared to ~ 25 years for the base case. This would have an impact on the corresponding NPV *and* $Q_{equivalent}$ which is shown in Fig. 5.20 below. As is indicated, both NPV and $Q_{equivalent}$ are dramatically enhanced for CP condition. Nevertheless, the improvement for the CR condition is hardly observed. As we explained before, this is mainly related to the fact that longer injection period does not necessarily mean higher NPV especially when consistent injection rates are adopted. On the other hand, for CP injection, most of the CO_2 is injected earlier, weighing much more in the NPV calculations.

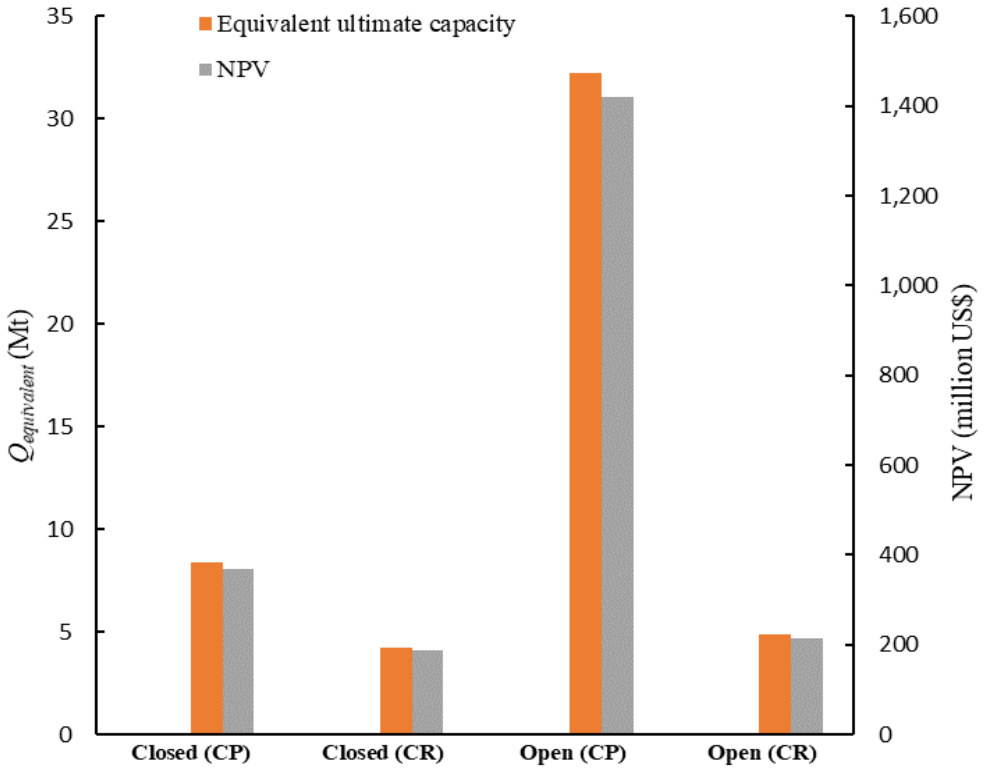

Figure 5.20. The NPV and the equivalent storage capacity for open aquifer versus the base case (closed aquifer) considering CP and CR injection schemes

5.6.5. Fully-Penetrating Injection Well

Due to the buoyancy/gravity override effect, CO_2 tends to migrate upwards below the sealing rocks during and after the injection period. Presence of leaking pathways within the caprock may result in unwanted exposure/leakage of the CO_2 to shallower formations. Therefore, it has been proposed to inject CO_2 through the bottom section of the injection interval when injecting through vertical wells, as indicated in Fig. 5.1. On the other hand, CO_2 injection through fully-penetrating vertical wells completed over the whole thickness of the aquifer could be preferable in situations where leakage risk through the caprock is minimal. The full penetration design would (1) avoid the pressure losses caused by partial penetration, (2) enhance the cylindrical displacement and sweep

efficiency of the injected CO_2, especially at early times of injection, which is preferable for efficient storage, and (3) allow for more volumes of the aquifer brine to come in contact with the injected CO_2 which enhances CO_2 trapping by dissolution. In this case, we modify the base case by injecting CO_2 along the whole thickness of the injection interval. We run two simulations to consider both injection scenarios (i.e., CP and CR). Similar to the base case, injection ceases when the bottomhole pressure reaches the p_{max} for CR scenario, and when the injection rate reaches the economic limit for the CP scenario. Comparison of the ultimate storage capacity achieved during full and partial penetrations for both injection schemes is shown in Fig. 5.21. For injection at CP, the ultimate storage capacity is improved by ~ 28.8 % due to full penetration. Notably, the improved storage capacity is achieved over only ~ 1.9 years as compared to ~ 25 years for the base case. This has been reflected in the NPV and $Q_{equivalent}$ that are dramatically enhanced due to not only the higher cumulative injection, but also, the shorter injection period as shown in Figs. 5.21 and 5.22. For injection at CR, the ultimate storage capacity is improved by about 19.3 %. Unlike injection at CP, there is only marginal improvement in the NPV and $Q_{equivalent}$ for CR. Again, this is because the improved ultimate storage capacity is achieved over a period (~ 25.6 years) slightly longer than that of the base case (~ 21.6 years).

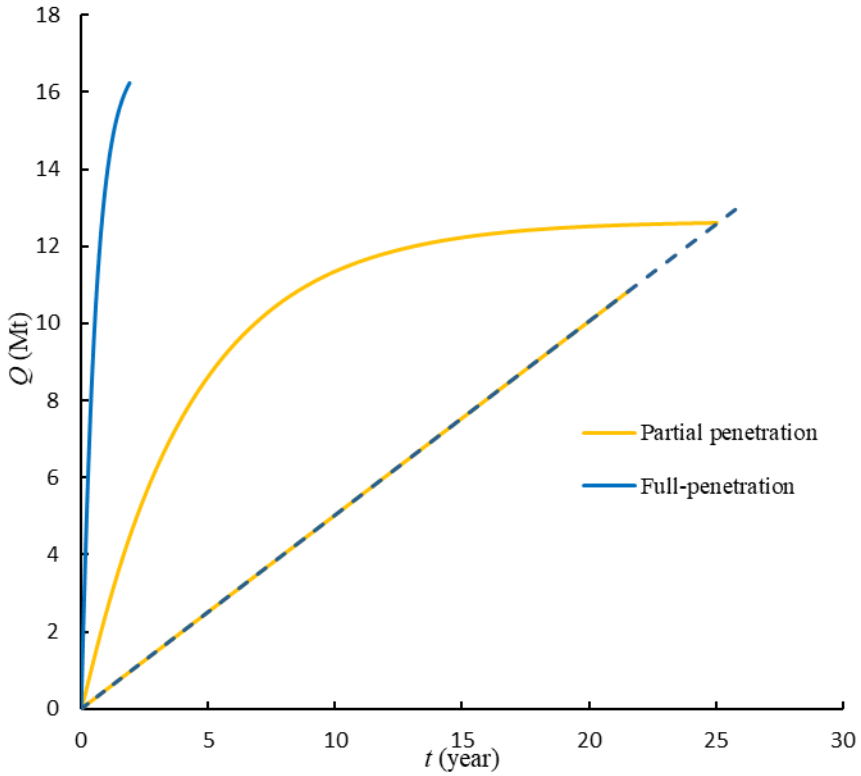

Figure 5.21. Comparison of the ultimate storage capacity for the full-penetration case versus the base case (partial penetration) - dashed lines show CR and solid lines show CP

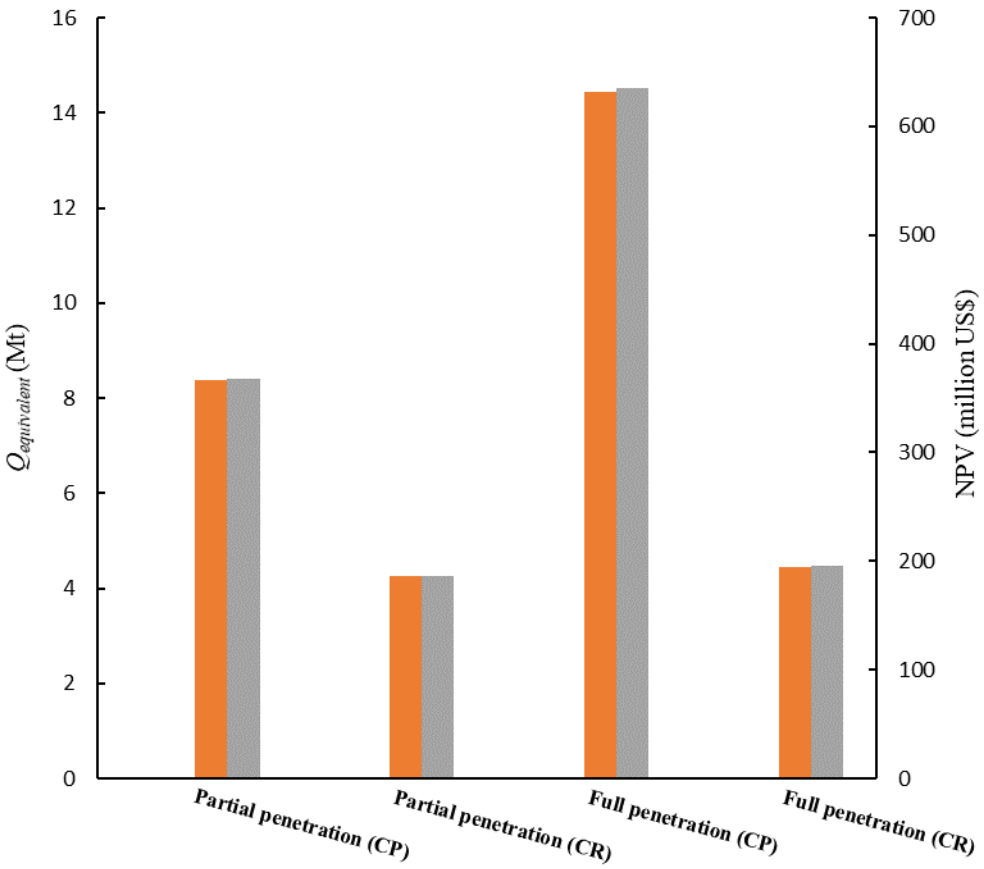

Figure 5.22. The NPV and the equivalent storage capacity for the full-penetration case versus the base case (partial penetration) considering CP and CR injection schemes

Chapter 6. Coupled Wellbore-Reservoir Modeling to Evaluate CO_2 Flow Rate Distribution over Thick Storage Aquifers

Technical and economic feasibility of GCS projects requires maximizing the amount of stored CO_2 per unit pore space of the storage zone per well. Considering injection through a fully penetrating vertical well in a multi-layer thick aquifer, CO_2 would be unevenly distributed over the aquifer thickness, underutilizing the available pore space. In this chapter, we utilize coupled wellbore-reservoir modeling to investigate net effect and the interplay between the reservoir parameters and physical processes that control CO_2 pore-space filling. First, the effects of movement of CO_2/brine interface within the wellbore, individual layer flow capacities, change in the average fluid mobility within layers, and difference in the hydrostatic pressure between the CO_2-filled wellbore and the brine-saturated aquifer are investigated. Then, implications of brine backflow into the wellbore on wellbore refilling with brine, and hence, the rate distribution are addressed. Next, we perform a sensitivity analysis to investigate the impact of varying the injection rate on the flow rate profile. The effects of using a decoupled model, wellbore shut-ins and associated salt dry-out, and presence of permeable formations overlying/underlying the target zone are also studied.

6.1. Description of the Simulation Model

Two-dimensional simulations of CO_2 injection via a fully-penetrating vertical well into an infinite-acting deep saline formation are performed to achieve the goals of this study. The physical system shown in Fig. 6.1 is simulated using a radial axisymmetric model generated using CMG-STARS (CMG-STARS, 2021). The reservoir model is coupled with FlexWell CMG-STARS wellbore model to simulate the complex wellbore physics associated with heat transfer, fluid flow in the wellbore, phase change of CO_2, and interactions with the reservoir rock and fluid. The flexible wellbore option accounts for transient flow behavior within the wellbore. It enables calculations to be made for the axial flow rate and heat transfer in the wellbore, as well as wellbore-reservoir heat transfer. Generally, flexible wellbore modeling can simulate the physical phenomena which cannot be simulated using the commonly-used sink/source well models. This includes simulating (a) multiple tubular strings of the wellbore, and (b) phase segregation, transient flow behavior, and mass accumulation within the wellbore. Flexible wellbore, also, uses more complex calculation approaches for fluid and heat flow within the wellbore. These calculations include (a) pressure losses due to friction within the wellbore, (b) heat losses between the wellbore and surrounding formations, and (c) implicit treatment of fluid head used to calculate the pressure at different layers. This is unlike sink/source well modeling which assumes steady-state flow within the wellbore with no wellbore storativity, transient flow behavior, or heat transfer in the radial/axial directions. The only variable that is evaluated in the sink/source well models is the bottomhole pressure where the hydrostatic head, based on the average fluid density, links all the perforations (Kumar et al., 2010). The FlexWell parameters and the reservoir properties are listed in Table 6.1 below. The well and cement thermal properties are selected based on the typical values used in thermal applications in the petroleum literature (CMG-STARS, 2021; Prats, 1982; Raad et al., 2021). The thermal properties of the formation rock and fluid are adapted from Butler (1991) and Raad et al. (2021). Table 6.2 displays the thermal properties of the formation rock, fluid and wellbore.

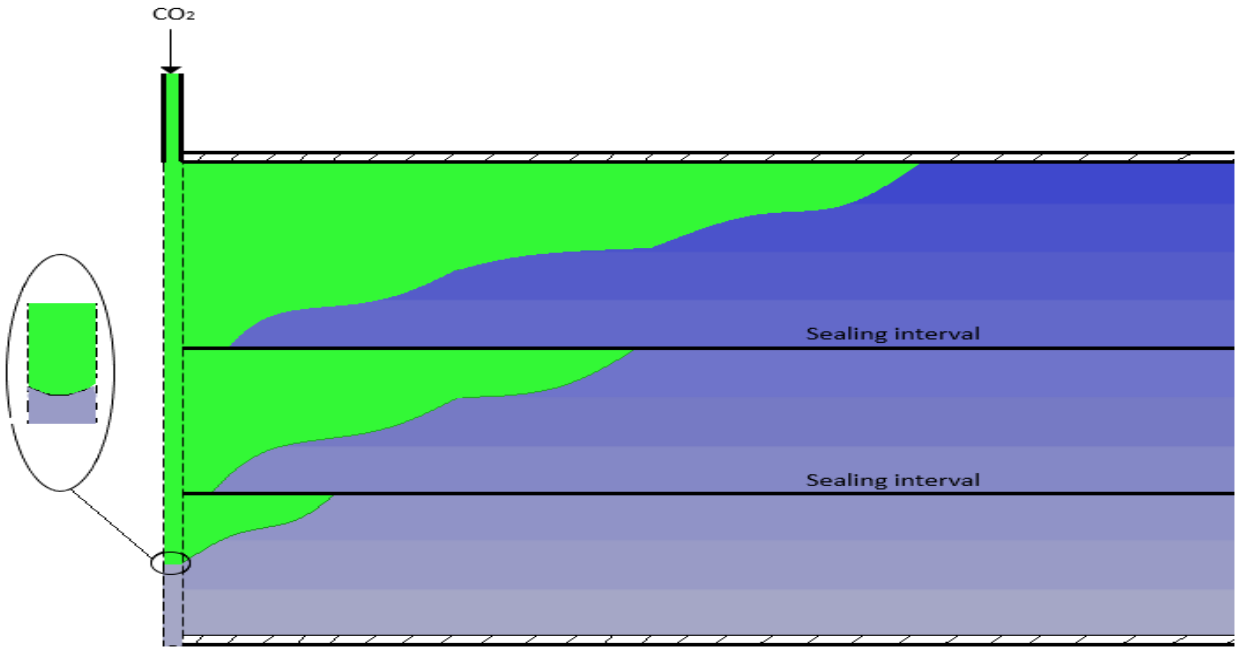

Figure 6.1. A schematic illustration (not to scale) of CO_2 injection via a fully-penetrating vertical well in a multi-layer infinite-acting thick aquifer. The CO_2 plume evolution dependence on CO_2-brine interface, shale laminations, buoyancy, and layer flow capacities is illustrated. Dark to light blue colors respectively indicate higher to lower layer flow capacity

CMG-STARS does not use EoS to achieve phase equilibrium, and modeling the true behavior of CO_2, and the mutual solubility with brine is a little more involved than in CMG-GEM/IMEX. CMG-STARS uses gas-oil *K*-values to model the phase equilibrium of CO_2 at different conditions of pressure and temperature. Gas-oil *K*-values ensures that CO_2 is always in the correct phase in the reservoir as well as within the wellbore. Using gas-oil *K*-values, the gaseous CO_2 is represented by the "gas" phase, and the liquid/supercritical CO_2 is represented by the "oil" phase. In addition, STARS models the mutual solubility between CO_2 and brine (i.e. vaporization of brine into the gaseous CO_2-rich phase, and dissolution of CO_2 into the brine-rich aqueous phase) using oil-water *K*-values. More details on the design of the PVT model, and the procedure of generating the gas-oil and oil-water *K*-values can be accessed at CMG-STARS (2021). As we mentioned before, the CO_2/brine displacement is governed by a system of PDEs that conserve mass, momentum, and Energy. The PDEs that govern conservation of mass of component *i* within a multi-component multi-phase system in porous media is given by (CMG-STARS, 2021):

$$\frac{\partial}{\partial t}\left[V_f\left(\rho_w S_w w_i + \rho_o S_o x_i + \rho_g S_g y_i\right)\right] =$$
$$\sum_{k=1}^{n}\left[T_w \rho_w w_i \Delta\phi_w + T_o \rho_o x_i \Delta\phi_o + T_g \rho_g y_i \Delta\phi_g\right] \qquad (6.1)$$
$$+\sum_{k=1}^{n}\phi\left[D_{wi}\rho_w \Delta w_i + D_{oi}\rho_o \Delta x_i + D_{gi}\rho_g \Delta y_i\right] + \rho_w q_w w_i + \rho_o q_o x_i + \rho_g q_g y_i$$

where V_f is the volume of fluid phases added together, ρ_w, ρ_o and ρ_g are the densities of the water, oil, and gas phases respectively, S_w, S_o, and S_g are the saturations of the water, oil, and gas phases respectively, w_i, x_i, and y_i are the mole fractions of component (i) in the water, oil, and gas phases respectively, T_w, T_o, and T_g are the transmissibility between two grid cells for the water, oil, and gas phases respectively, D_w, D_o, and D_g are the component dispersibility in the water, oil, and gas phases respectively, q_w, q_o, and q_g are the volumetric flow rates of the water, oil, and gas phases respectively, ϕ is the formation porosity, and ϕ_w, ϕ_o, and ϕ_g are the fluid porosities of the water, oil, and gas phases, respectively. This is coupled with the PDE that governs the conservation of energy which is given by:

$$\frac{\partial}{\partial t}\left[V_f\left(\rho_w S_w U_w + \rho_o S_o U_o + \rho_g S_g U_g\right)\right] = \sum_{k=1}^{n}\left[\rho_w H_w \Delta\phi_w + \rho_o H_o \Delta\phi_o + \rho_g H_g \Delta\phi_g\right] + \sum_{k=1}^{n} K\Delta T + \rho_w q_w H_w + \rho_o q_o H_o + \rho_g q_g H_g \tag{6.2}$$

where U_w, U_o, and U_g are the internal energies as a function of temperature and the composition of the water, oil, and gas phases respectively, H_w, H_o, and H_g are the enthalpies of the water, oil, and gas phases respectively, K is the thermal transmissibility at the interface between the two grid cells.

By coupling the abovementioned governing PDEs with the constitutive relations (e.g. Darcy's law, capillary pressure, and relative permeability), the PDEs can be solved for phases' pressures, saturations, and temperatures. The relative permeability data for the gaseous and aqueous phases are generated using Corey's model (Corey, 1954a). The saturation exponents for the gaseous and aqueous phases are set at 2.0 with the residual brine saturation assigned at 0.25. The endpoint relative permeability is set at 1.0 for the aqueous phase and 0.8 for the gaseous phase. The relative permeability to CO_2 in the dry-out zone is set 0.8 to mimic the absolute permeability reduction in the dry-out zone due to salt precipitation that accompany brine vaporization. Significant amounts of CO_2 can be trapped due to relative permeability hysteresis (i.e. by residual trapping) especially at the interface between CO_2 and brine within the aquifer and during shut-in periods when imbibition of the already-drained pores is in effect. Therefore, to enable residual trapping, the maximum trapped gas saturation of the imbibition curve is set at 0.3. The capillary pressure curve is generated using van Genuchten formulation (van Genuchten, 1980) assuming 20 kPa entry pressure, and 0.8 pore size distribution parameter. CO_2 is being injected for a year at a constant mass rate of 0.50 Mt/year via a fully penetrating vertical well located at the center of the aquifer. This rate is equivalent to the standard CO_2 emissions from a medium-sized coal-fired power plant. Physically, a system would behave as infinite-acting when the lateral boundaries are far enough that it requires relatively longer time for the boundaries to feel the pressure perturbations induced at the wellbore. Therefore, we set the outer boundaries at 50 km from the wellbore. The aquifer is infinite-acting with a radial extent of 50 km. The aquifer is homogenous and isotropic with uniform thickness and porosity equal to 100 m and 0.2 respectively. The vertical dimension of the model is divided into 40 layers each with 2.5-m thickness to allow for effective buoyancy. Each layer is

divided into 500 logarithmically-spaced gridblock divisions, making a total of 20000 gridblocks. The logarithmic increment factor is 1.015 with the finest block (0.50 m) near the wellbore and the coarsest (724.50 m) at the edge of the aquifer. This logarithmic discretization ensures higher resolution near the wellbore where most of the changes in the primary variables (i.e. pressure and saturation) take place. The aquifer is underlain by an impermeable layer of 50-m thickness and overlain by 10 layers (each of 200-m thickness) of impermeable overburden. Prior to injection, the aquifer is fully saturated with brine, and the system is in hydrostatic equilibrium with pressure at the top layer equal to 20.1 MPa. CO_2 is injected in supercritical state at the surface generating conditions of 35 ^oC and 9.3 MPa. These values represent the conditions at which CO_2 was injected in the Illinois Basin Decatur Project (Finley et al., 2013). The wellbore and the formation are initialized considering fixed temperature at the surface (20 ^oC) and geothermal gradient of 0.025 $^oC/m$. Other operational conditions and tubular specifications are listed in Table 6.1.

Table 6.1. Fluid and rock properties used for simulation

Property	Value
Reservoir properties	
Aquifer radial extent (km)	50
Thickness (m)	100
Depth to top (km)	2.0
Reference depth (km)	2.0
Pressure at reference depth (MPa)	20.1
Number of layers	40
Number of grids (radial × angular × vertical)	500 × 1 × 40
Formation porosity (fraction)	0.2
Horizontal permeability (m^2)	2.5×10^{-13}
Outer boundary	Infinite-acting
Vertical permeability (m^2)	0
Dip angle (^{o})	0
Rock compressibility (1/kPa)	5.0×10^{-7}
FlexWell properties	
Well head injection temperature (^oC)	35.0
Well head injection pressure (MPa)	9.30
Initial bottomhole pressure (MPa)	20.1
Injection rate (Mt/year)	0.50
Casing internal diameter (m)	0.20
Casing external diameter (m)	0.22
Tubing internal diameter (m)	0.10
Tubing external diameter (m)	0.11

Table 6.2. Formation and well thermal properties used for simulation

Property	Value
Formation properties	
Geothermal gradient ($^oC/m$)	0.025
Ambient temperature (^oC)	20.0
Temperature at top layer (^oC)	70.0
Temperature at bottom layer (^oC)	72.5
Rock thermal conductivity (J/m.day.^oC)	2.47×10^5
Brine thermal conductivity (J/m.day.^oC)	5.35×10^4
Gas thermal conductivity (J/m.day.^oC)	4500
FlexWell properties	
Casing/tubing heat capacity (J/m^3.^oC)	3.63×10^6
Casing/tubing thermal conductivity (J/m.day.^oC)	3.888×10^6
Cement heat capacity (J/m^3.^oC)	1.848×10^6
Cement thermal conductivity (J/m.day.^oC)	118400
Insulation heat capacity (J/m^3.^oC)	3282
Insulation thermal conductivity (J/m.day.^oC)	16800
Well relative roughness (-)	0.0001
Maximum Nusselt number (-)	10000

A total of 14 simulations are conducted to achieve the objectives of this work. Through these simulations, the effects of the aforementioned parameters/processes – both individually and combined - on CO_2 flux distribution between the layers are investigated. Therefore, it is better to start with investigating the effects of the parameters which are active in any modeling setup (i.e. the difference in the pressure gradient between the wellbore and the aquifer, and the effect of the change in the average fluid mobility within layers). Then, the subsequent cases are built-up through incorporating the remaining parameters on one-by-one basis up-to the most mechanistically inclusive case. Here is an overview of the simulations to be presented in the next section. The simulation cases are also summarized in Table 6.3:

i. For the base case, only the effects of the pressure gradient difference and the temporal change in the average fluid mobility within the layers are accounted for. Therefore, the absolute horizontal permeability is assigned 250 mD for all the layers to ensure uniform flow capacity. The vertical-to-horizontal permeability ratio (*kvh*) is assigned 0 to deactivate gravity. The FlexWell is initialized with 100 % CO_2 to eliminate the effect of moving CO_2/brine interface within the wellbore. Moreover, the wellbore is equipped with one-way Venturi valves across all the perforation to prevent backflow of brine (if occurred) into the wellbore. These valves would allow flow of fluids in only one direction (i.e. into the reservoir) without affecting the pressure profile across the perforations or within the wellbore. The discharge coefficient of the Venturi valves is set at 1.0 to allow 100 % of fluids to flow into the reservoir while preventing any unwanted effects on the pressure profile within the wellbore or across the perforations.

ii. The second simulation case accounts for the effect of the wellbore initial conditions. In this case, CO_2 is injected into a well initially filled with brine. This would allow for developing a moving CO_2/brine interface within the wellbore during CO_2 injection. Other rock and fluid properties, and FlexWell parameters are kept identical to the base case.

Table 6.3. Overview of the simulation cases model setups– Green color indicates CO_2, uniform/gradual blue color indicate homogenous/heterogeneous permeability, respectively

Case	Model setup	To investigate the effect of	Schematic illustration of the model
Base	• Homogenous reservoir • Well initially filled with CO_2 • *kvh* = 0.0	• Pressure gradient difference between wellbore and aquifer • Change in average fluid mobility within layers	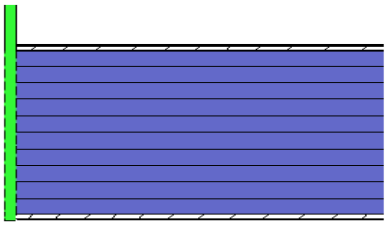
Case 2	Base case modified by: • Considering well initially filled with brine	Base case objectives and: • Movement of CO_2/brine interface	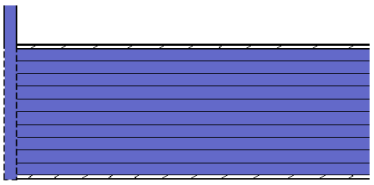
Case 3	Case 2 modified by: • Setting *kvh*=1.0	Case 2 objectives and: • Gravity override	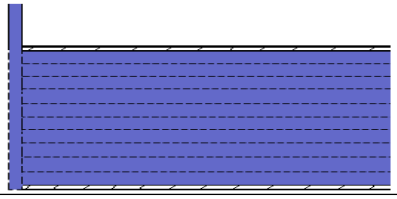
Case 4	Case 3 modified by: • Allowing for backflow of brine	Case 3 objectives and: • Brine backflow	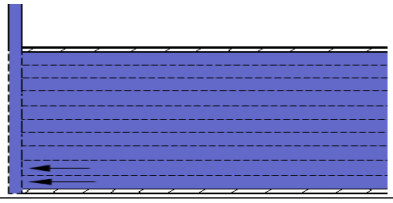
Case 5	Case 3 modified by: • Considering vertically heterogeneities Scenario (a): ascending order permeability (top/bottom layer = 160/340 mD with 4.5 mD increment). Scenario (b): same as scenario (a), but with reversed order of permeabilities.	Case 3 objectives and: • Individual layer flow capacities	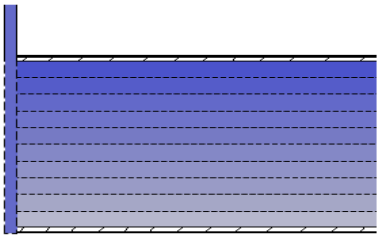

Table 6.4. Overview of the simulation cases to be investigated as additional investigations

Case	Model setup	To investigate the effect of	Schematic illustration of the model
Additional Investigations	(1) Case 4 modified by: • Considering sink/source well injection.		To investigate the effect of ignored wellbore-reservoir coupling.
	(2) Case 4 modified by: • Intermittent injection (2 month shut-in following an initial 2-month flow period).		To investigate the effect of wellbore shut-in and associated salt dry-out.
	(3) Case 4 modified by reducing the injection rate by half (i.e., to 0.25 Mt/year)		To investigate the effect of injection rate on wellbore filling.
	(4) Case 4 modified by introducing semi-permeable underlying/overlying rocks.		To investigate the effect of leaking trough upper/lower formations

iii. The third simulation case incorporates the effect of gravity override on CO_2 flux distribution. This is achieved by modifying *kvh* to 1.0. The remaining rock and fluid properties, and FlexWell parameters are kept the same as the base case except that the FlexWell is initialized with brine to assimilate the reality.

iv. The impact of brine backflow to the wellbore, and thus, on the flux distribution, is next studied. Brine backflow may occur only if the gravity is effective. To achieve this, the third simulation case is re-run such that brine backflow to the wellbore is allowed. This is achieved by removing the one-way Venturi valves along the perforations so that fluids can flow in both directions (i.e. from and into the wellbore).

v. The effect of varying the individual layer flow capacities on the CO_2 flux distribution is next investigated. The individual layer flow capacities are changed through varying the absolute horizontal permeability of the corresponding layer. We re-run the third simulation case while varying the permeability in a systematic increasing/decreasing order, but keeping the average value identical to the base case. Other rock and fluid properties, and FlexWell parameters are kept identical to the base case except that the FlexWell is initially filled with brine.

vi. Finally, we perform additional investigations to study the effect of implementing a decoupled reservoir model, and the effect of intermittent CO_2 injection and associated salt-dry out. The model setup for these cases is illustrated in Table 6.4. In addition, the effect of varying some other parameters are addressed. The parameters include CO_2 injection rate, and the presence of semi-pervious formations overlying/underlying the aquifer.

6.2. Results

6.2.1. Base Case

For the base case, we investigate the effect of the difference in the pressure gradient between the wellbore and the aquifer, and the effect of the change in the average fluid mobility (see Table 6.3).

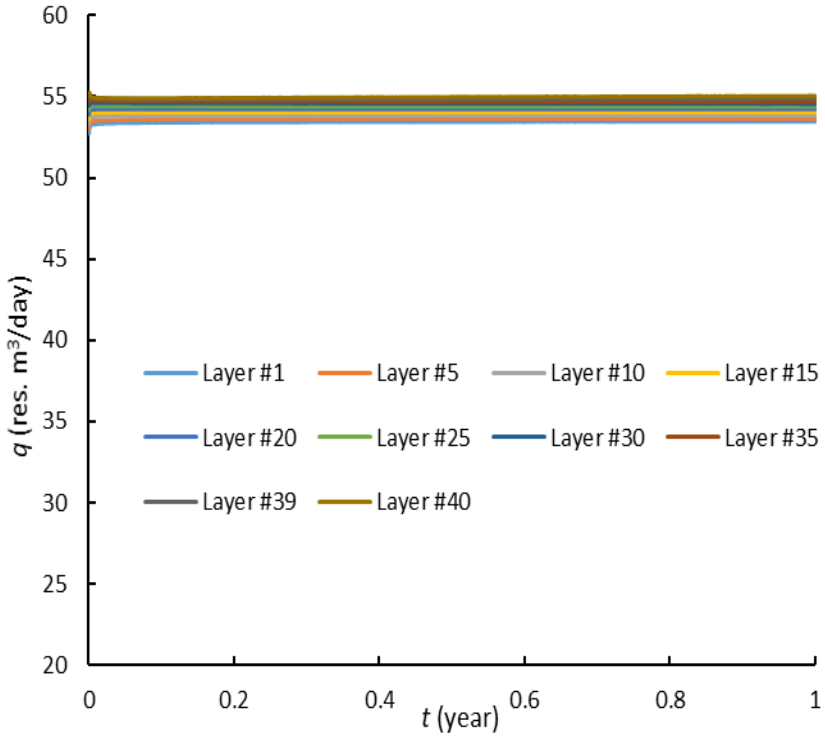

Figure 6.2. The flow rate distribution profile between layers for the base case

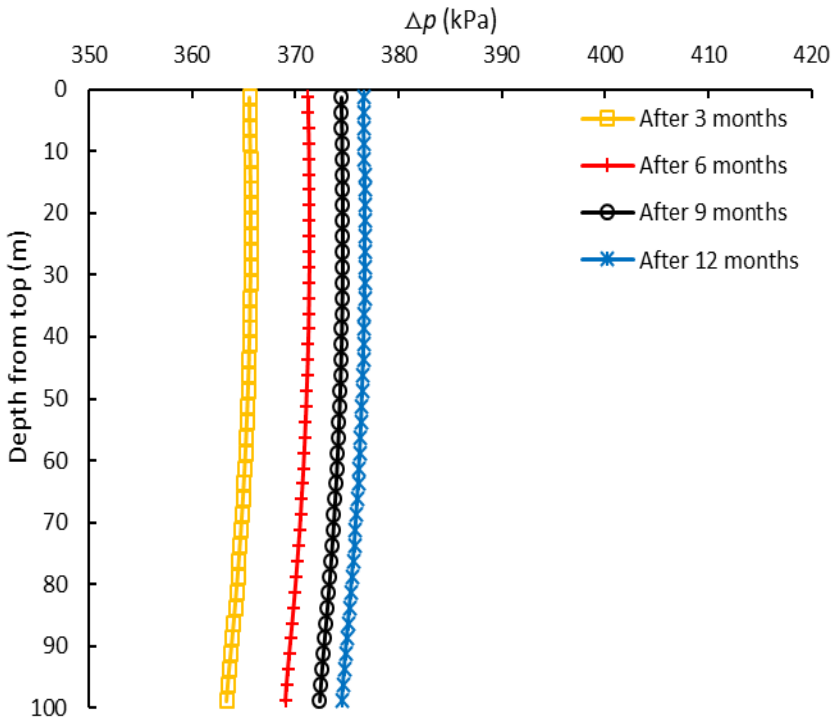

Figure 6.3. The profile of pressure difference between the wellbore and the aquifer at different times for the base case

Fig. 6.2 displays the flow rate (q) distribution over the 1-year injection period into selected 10 layers to better visualize the results. The layers are layers #1 (top-most layer), #5, #10, #15, #20,

#25, #30, #35, #39, and #40 (bottom-most layer). A note that the flow rates correspond to the first radial cell that connect the wellbore to the aquifer, and they are evaluated in-situ at the wellbore downhole conditions. Fig. 6.2 shows that the flow rates are almost identical among all the layers. This behavior is attributed to the identical layers' flow capacities as well as the pressure difference behavior between the wellbore and the aquifer. Fig. 6.3 shows the profile of the pressure difference ($\triangle p$) in kPa after 3, 6, 9 and 12 months of injection. The pressure difference is almost identical along the injection interval, and it slightly increases over time. A note that the pressure difference represents the difference - at any depth along the injection interval - in the pressure between the wellbore and the aquifer where the aquifer pressure means the average value over the entire radial extent.

6.2.2. Effect of Moving CO_2-Brine Interface within the Wellbore (Case 2)

For this case, we investigate the effect of the CO_2/brine interface movement within the wellbore (see Table 6.3). Fig. 6.4 shows the saturation profile of CO_2 within the wellbore at different times. CO_2 reaches the bottommost perforation within 35 minutes of injection. Nevertheless, the wellbore is not instantaneously filled with CO_2. It takes 1.75 hr for the well to be fully filled with CO_2. The rapid movement of the interface, and brine flushing out of the wellbore, causes insignificant effect on the corresponding pressure difference and rate profiles as compared to the base case. Similarly, the flow rates into layers are almost identical.

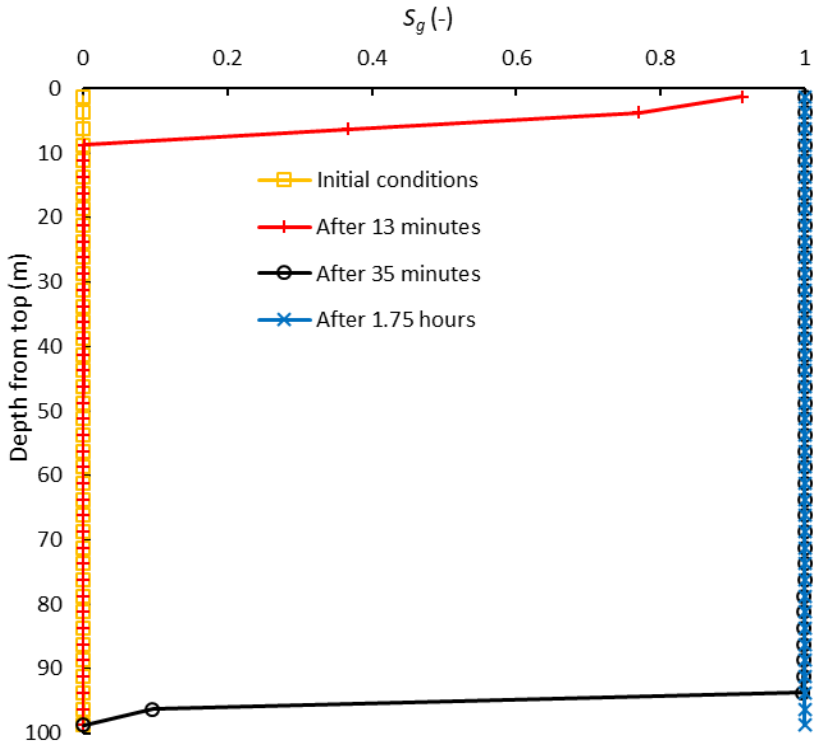

Figure 6.4. The saturation profile of CO_2 at different times within the wellbore for case 2

6.2.3. Effect of Buoyancy/Gravity Override (Case 3)

In this case, we investigate the effect of gravity (see Table 6.3). The flow rate distribution and pressure difference between the wellbore and the aquifer, and are shown in Figs. 6.5 and 6.6 respectively. Unlike the previous two cases, the flow rates are noticeably different among layers (i.e., the highest flow rate within layer #1 and lowest within layer #40). Intermediate layers span between these two extremes with rates eventually decline to 0 for layers #39 and #40. This behavior is due to the gravity-driven displacement which follows the initial viscous-driven period controlled by pressure difference.

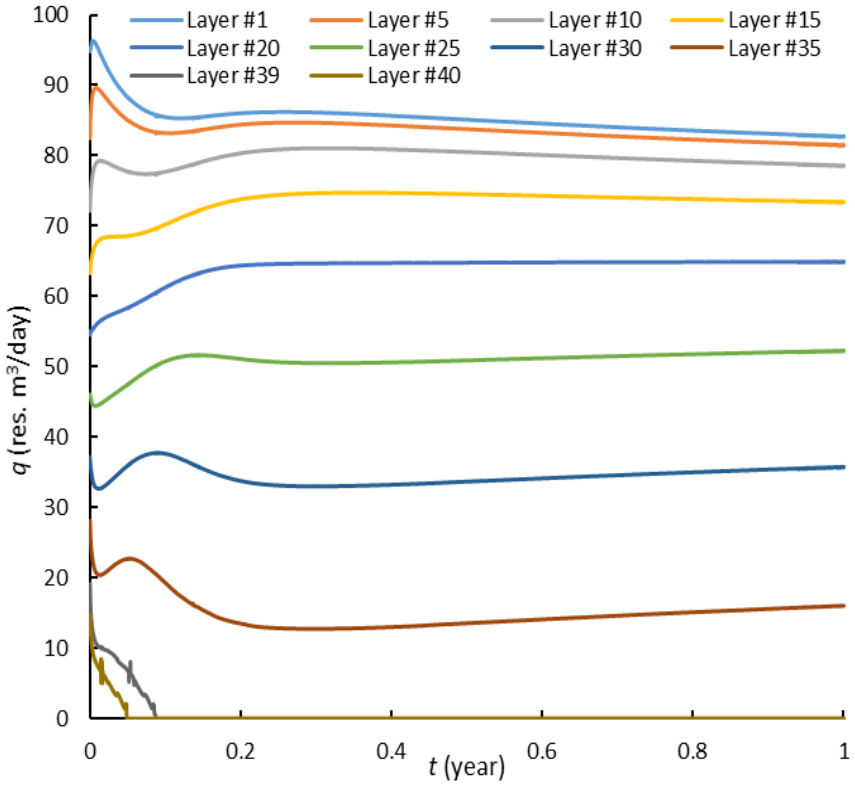

Figure 6.5. The flow rate distribution profile between layers for case 3

This is unlike the previous cases where the flow was viscous-driven over the whole injection period. As a consequence, the flow rate into layers #39 and #40 successively declines to 0 within 17 and 32 days from the start of injection. Specifically, the shut-in is attributed to the down-flow of brine within the aquifer. This is illustrated by Fig. 6.7 which visualizes the vertical component of brine velocity. As shown, brine is allowed to flow vertically due to gravity which is not the case for previous cases. A note that this downward velocity is the vertical velocity (in z-direction) averaged over the radial distance. In addition, buoyancy amplifies the change in the average fluid mobility within the layers. That is why the transient variation in the flow rates within the layers is more visible for this case. However, there are upright/inverted humps observed in the flow rates at the early time of injection especially through the upper layers. This can be attributed to the fact that CO_2 cannot override brine, at beginning of injection, where it should first displace the in-situ brine which completely saturates the near wellbore region. The least resistant path for CO_2 flow

occurs at the upper layers where less overburden of brine is met. Therefore, humps in flow rates are more severe/sensible in the upper layers as compared to the bottom ones during this "transient period" to honor the constraint of constant rate of injection imposed at the wellbore. Then, "a stabilized" flow period is established through all layers once the dry-out zone is formed in the vicinity of the wellbore. The dry-out zone decreases the resistance to CO_2 flow along the injection interval. The duration and the severity of the flow rate humps during the transient period varies from layer to layer depending on the average mobility of the fluids within the layers which is a function of the extent of the dry-out zone within the layer. This means that the severity of the humps should be normally less as we go deeper given the expansion of the dry-out zone in the upper formation which creates a path for CO_2 to flow upwards.

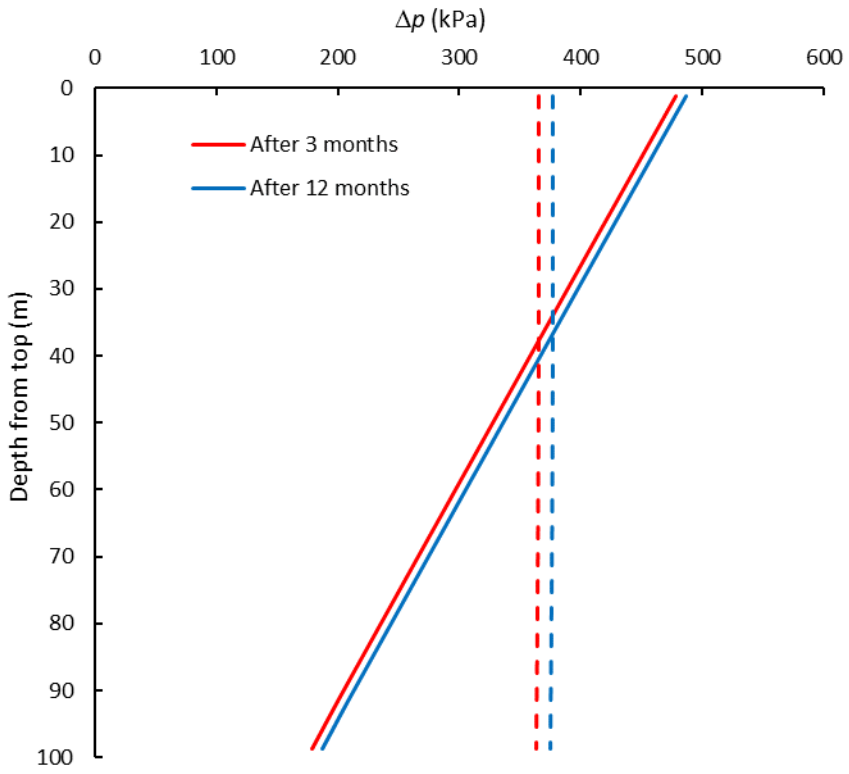

Figure 6.6. The profile of the pressure difference between wellbore and aquifer at different times - solid lines refer to case 3 and dashed lines refer to base case

Additionally, the CO_2/brine interface rapidly reaches the bottom of the wellbore (in less than 37 minutes), but complete flushing of the brine from the wellbore is not instantaneous. The wellbore gets fully saturated with CO_2 within 7.7 hr of injection (see Fig. 6.8) as compared to 1.75 hr for case 2. This discrepancy in flushing time is because CO_2 is allowed to migrate upwards when gravity effects are strong which causes relatively slower fill-up of the wellbore with CO_2.

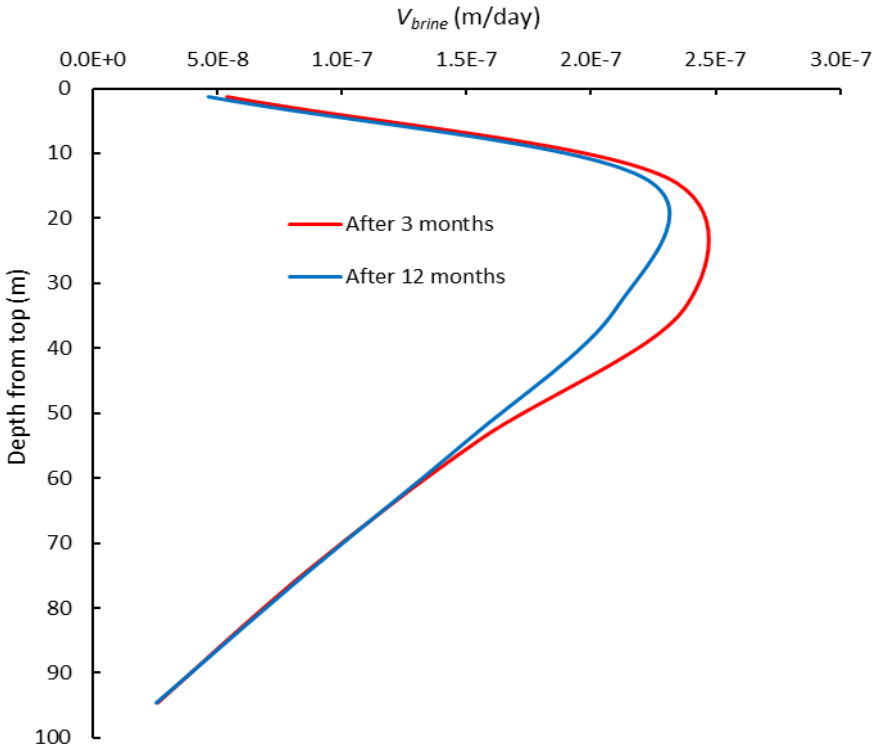

Figure 6.7. The profile of downward velocity of brine over the entire field at different times for case 3

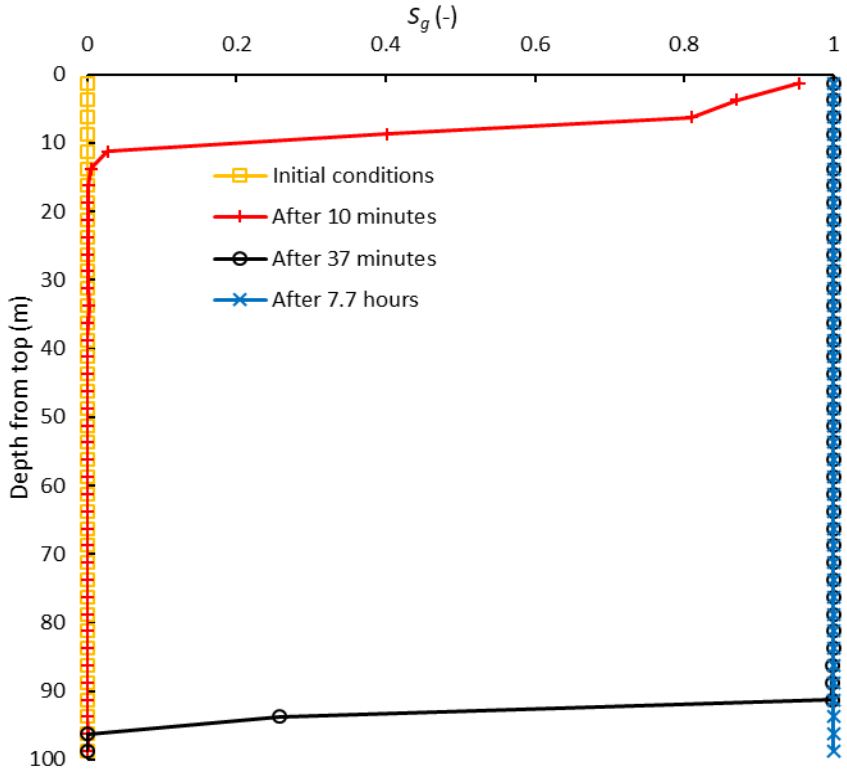

Figure 6.8. The profile of CO_2 saturation at different times within the wellbore for case 3

6.2.4. Effect of Brine Backflow into the Wellbore (Case 4)

Backflow of the aquifer brine to the wellbore can be initiated when one (or more) of the bottom perforations no longer contribute to injection. Therefore, in this case, we include the effect of brine backflow to the wellbore (see Table 6.3). The flow distribution into the layers is similar to case 3. Also, the flow rate into layers #39 and #40 successively declines to 0 within approximately 20 and 34 days of injection, indicating the start of brine backflow. Fig. 6.9 shows the temporal behavior of CO_2 saturation profile in the wellbore. Within 4.5 hr from start of injection, the wellbore gets fully saturated with CO_2. Nevertheless, and unlike case 3, brine appears at the bottom of the wellbore with further injection. Within 3 months, CO_2/brine interface rises up to the 95-m depth-from-top level. This interface level, which covers the two bottommost perforations, stabilizes for the rest of the injection period. Backflow of brine into the wellbore can be explained in terms of the velocity profile of brine. In other words, brine - which flows back into the wellbore - is being pushed by the advancing CO_2 at the top layers of the aquifer. This can be illustrated by the vertical component of CO_2 and brine velocities.

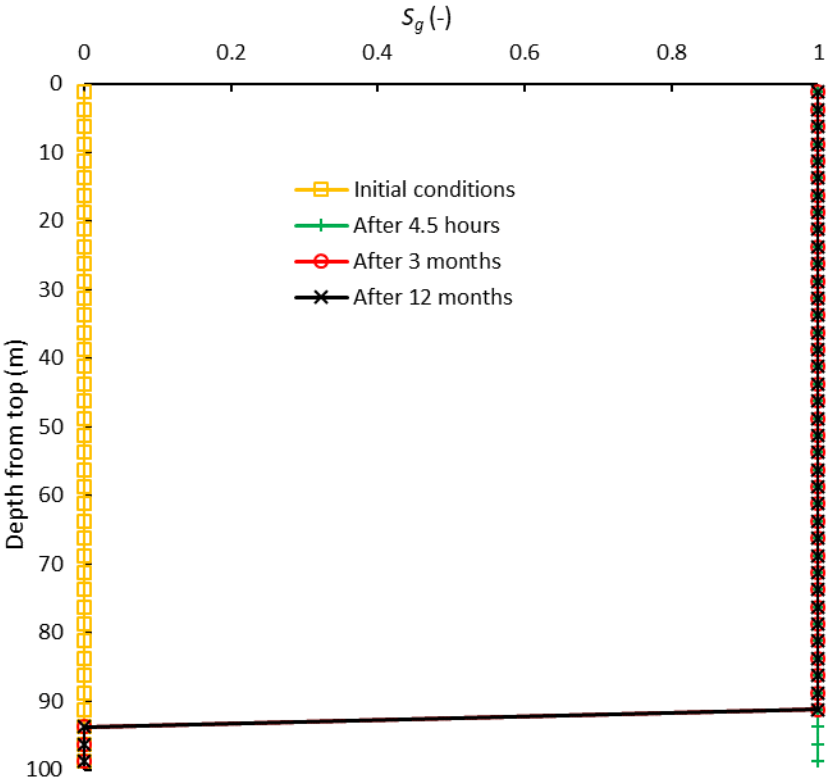

Figure 6.9. The profile of CO_2 saturation at different times within the wellbore for case 4

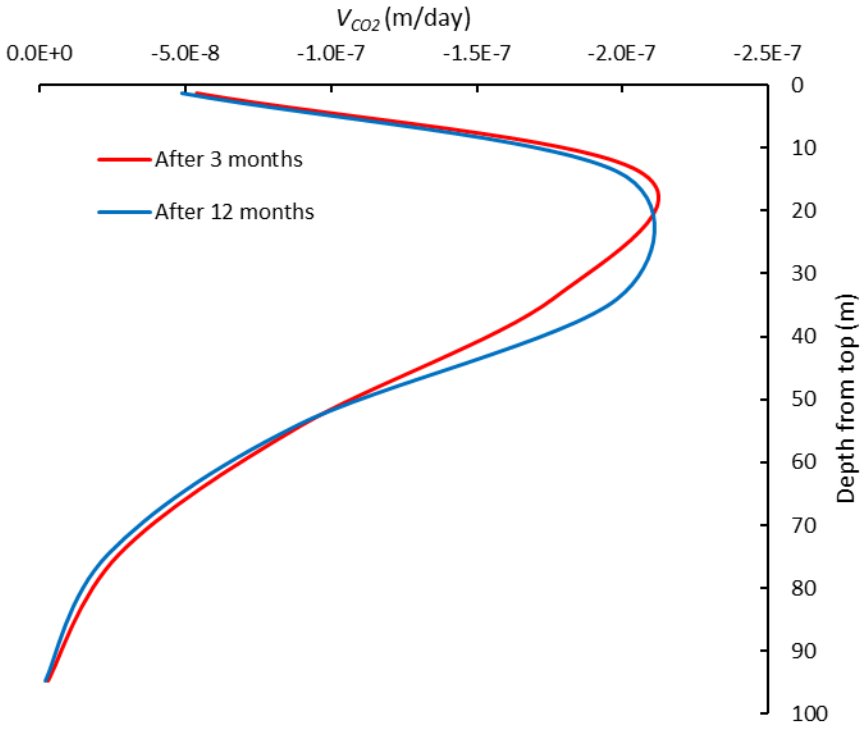

Figure 6.10. The average upflow vertical velocity of CO_2 at different times over the entire field for case 4

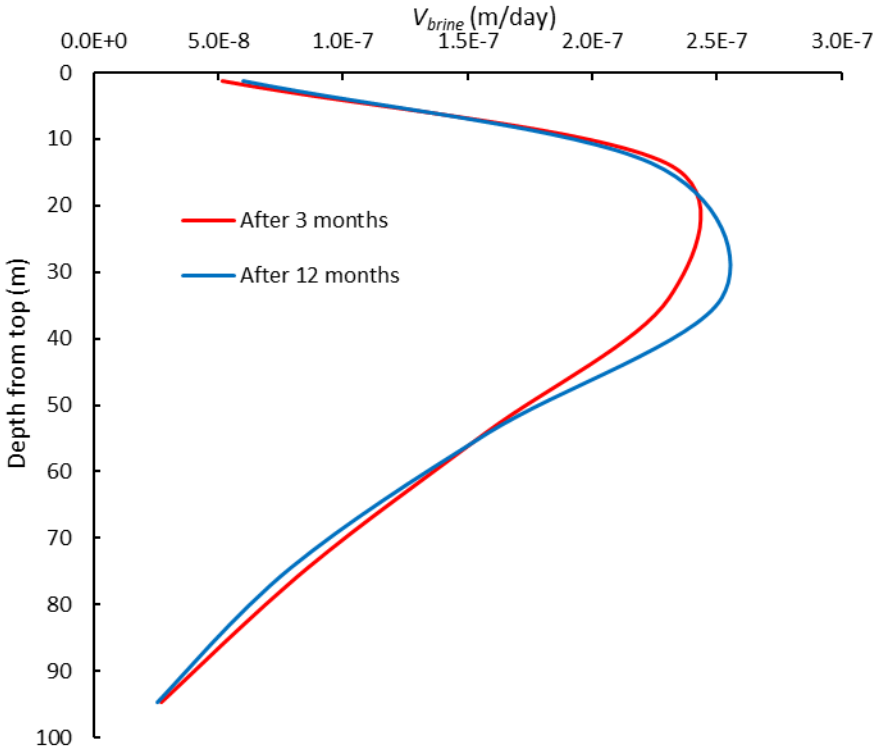

Figure 6.11. The average downflow vertical velocity of brine at different times over the entire field for case 4

Figs. 6.10 and 6.11 respectively show the average velocity of CO_2 and brine in *z*-direction averaged over the entire field with the positive direction pointing downwards. The behavior of the vertical velocity indicates that brine advances deeper (positive) while CO_2 advances toward the top seal (negative). CO_2 moves faster upward with highest vertical velocity near the aquifer's top, pushing brine down towards the bottom of the injection interval. Getting deeper, CO_2 velocity, and accordingly brine velocity, reduces and eventually reaches a minimum. The brine pushed downwards by CO_2 finds its way into the wellbore through one (or more) of the underutilized perforations, if backflow is allowed. Temporally, the steady-state behavior of the velocity can be explained as follows. At the beginning of CO_2 injection, CO_2 cannot override brine, and it should first displace the brine radially. This means that during this "transient" period, CO_2, and brine as a result, moves outwards mostly in the radial direction and less likely in the vertical direction. Later, when the dry-out zone is formed, buoyancy becomes more effective and CO_2 tends to override brine, migrating upwards while pushing brine downwards in a steady-state manner. This behavior is more similar to the behavior of the flow rates along the penetration layers where a stabilized flow period follows the initial transient flow period.

By comparison with the results of case 3, it is evident that backflow of brine has insignificant effect on the flow rate distribution although it affects the behavior of pressure difference. Fig. 6.12 shows that the maximum pressure difference is at the top layers, and the minimum is at the bottom ones. However, it is approximately constant below the 95-m depth-from-top level where brine 100 % saturates the wellbore. This is where the hydrostatic gradient in the wellbore is the same as in the aquifer due to backflow.

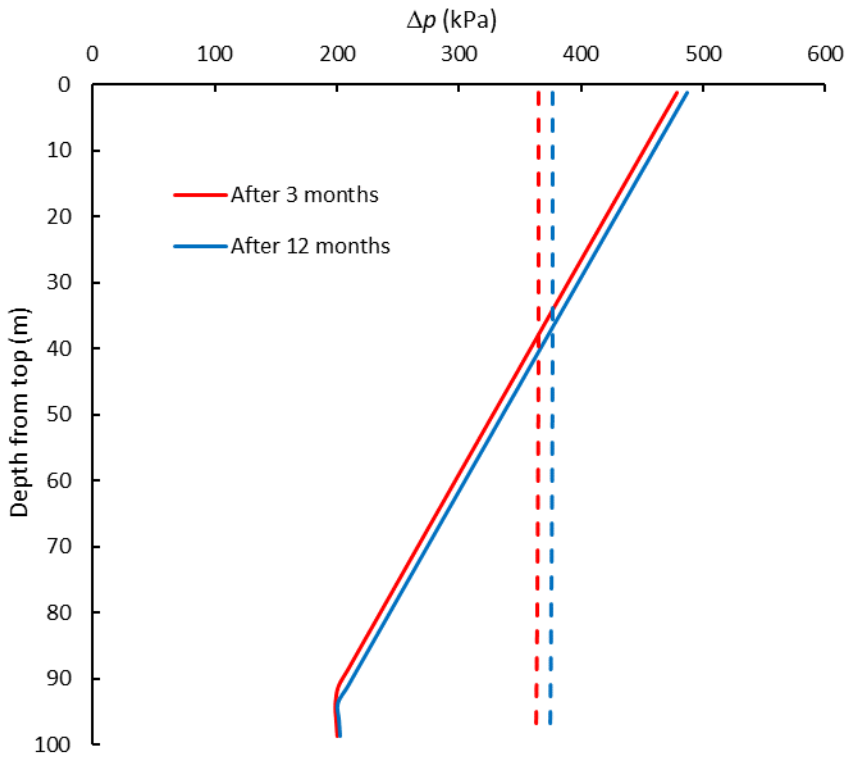

Figure 6.12. The profile of the pressure difference between wellbore and aquifer at different times – solid lines refer to case 4 and dashed lines refer to base case

6.2.5. Effect of Vertical Heterogeneity in Layers' Flow Capacities (Case 5)

In this case, we investigate the effect of layers' flow capacities on flow rate profile through layers. We re-run case 3 while varying the layers' flow capacities (see Table 6.3). The flow rate profiles, for scenarios (a) and (b), are displayed in Figs. 6.13 and 6.14, respectively. The corresponding pressure difference profiles are shown in Figs. 6.15 and 6.16. Similarly, the pressure difference is highest within layer #1 and lowest within layer #40. Results of both scenarios indicate that the flow rate distribution is viscous-dominant at the beginning of injection and before the buoyancy dominates. Specifically, for scenario (a), the flow rates, at the very early time, are generally higher at the bottom layers and lower at the upper ones. Soon when gravity dominates, this behavior is suppressed as CO_2 tends to flow upwards. Conversely, for scenario (b), the highest proportion of CO_2 flows into layer #1 and lowest flows into layer #40 since the beginning. The rate behavior for scenario (b) is similar to that of case 3 except that the span of flow rates is higher for scenario (b). This is because of the descending order flow capacities which amplifies the gravity effect. More importantly, the flow rate through the bottommost two perforations successively declines to 0 depending on the layer flow capacity (i.e. the lower the flow capacity, the faster the decline). This behavior is slower for scenario (a) due to the ascending order of flow capacities which makes all perforations, except the bottommost one, contribute to injection over the whole period. This means that the duration of the period of transition from viscous to buoyant-dominant flow depends on the flow capacity profile. The transition period is short when the flow capacities are higher at the upper layers (scenario-b), and longer when they are higher the bottom layers (scenario-a).

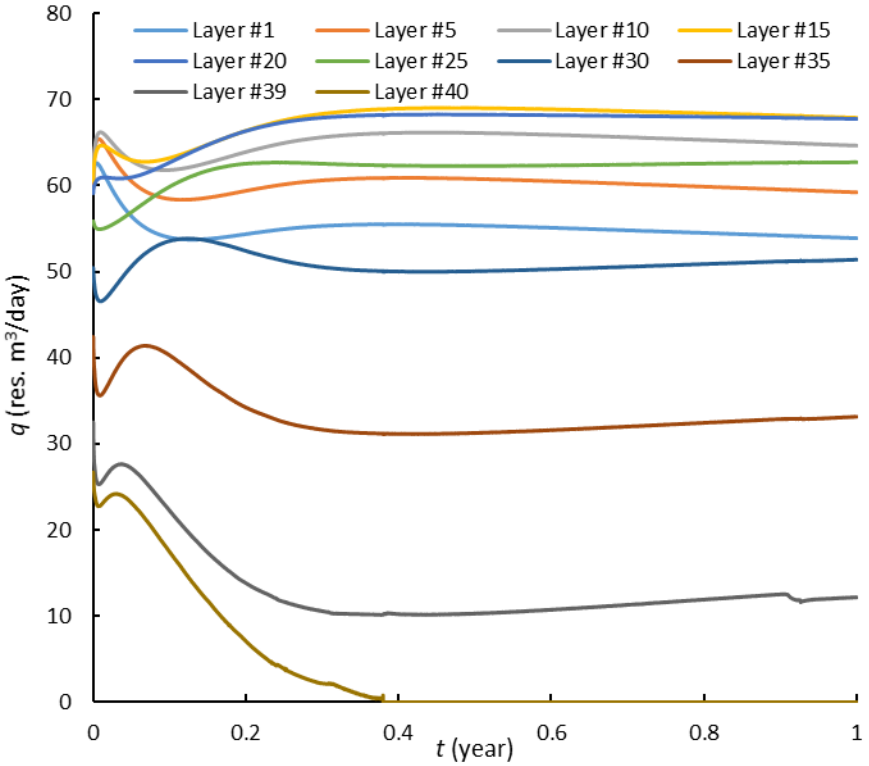

Figure 6.13. The flow rate distribution profile between layers for case 5 for ascending order flow capacities scenario

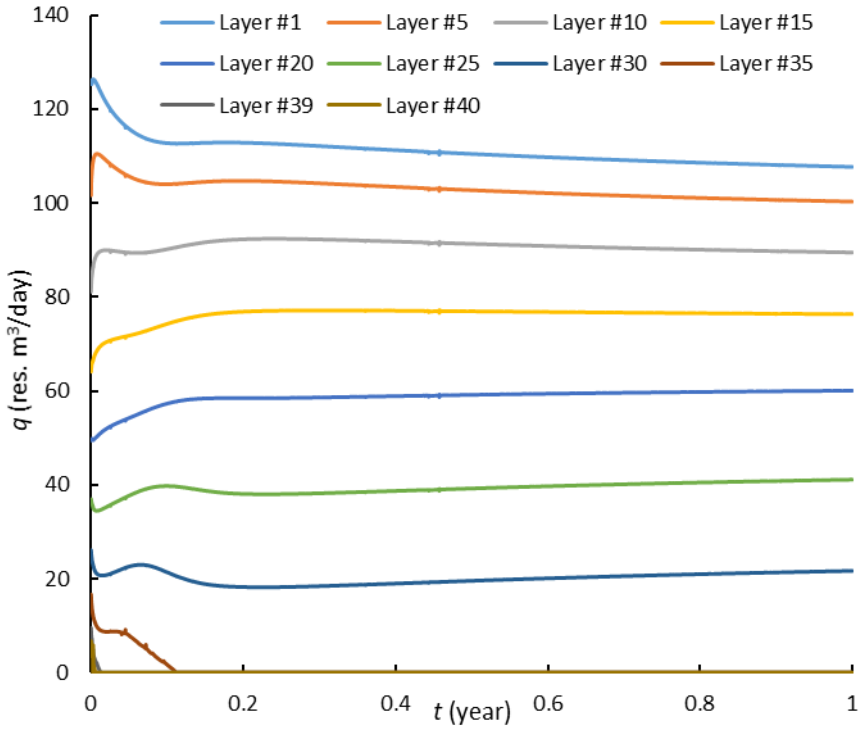

Figure 6.14. The flow rate distribution profile between layers for case 5 for descending order flow capacities scenario

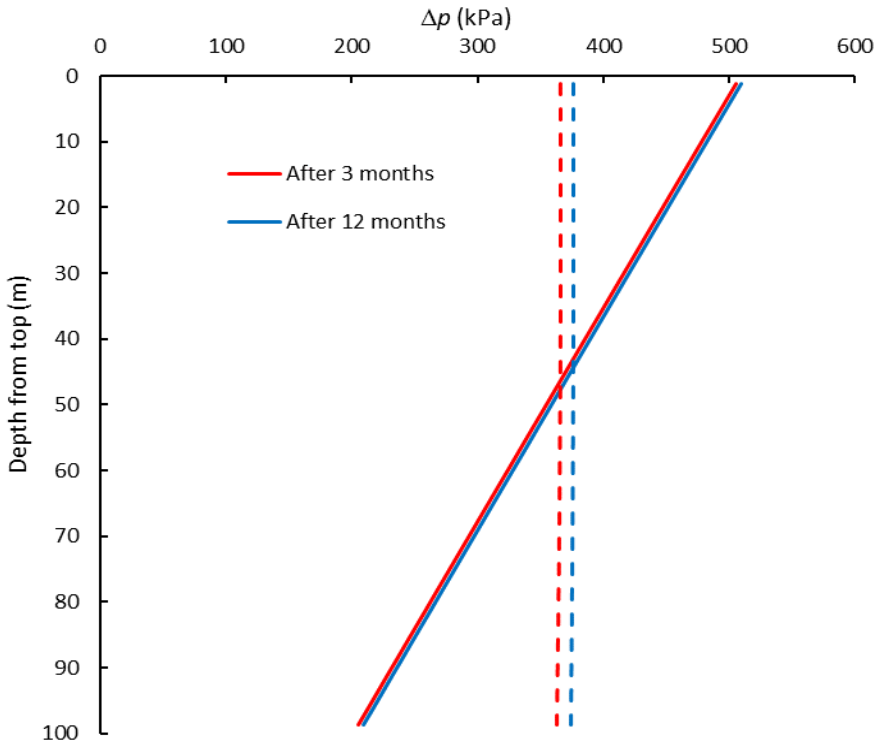

Figure 6.15. The profile of pressure difference between the wellbore and the aquifer at different times - solid lines refer to case 5 with ascending order flow capacities scenario and dashed lines refer to base case

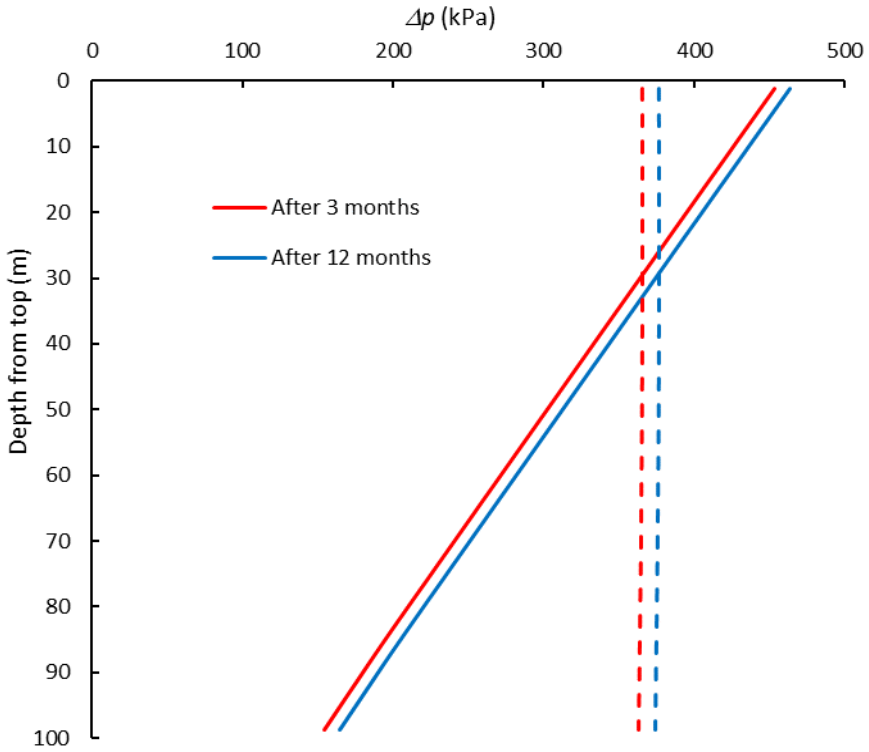

Figure 6.16. The profile of pressure difference between the wellbore and the aquifer at different times – solid lines refer to case 5 with descending order flow capacities scenario and dashed lines refer to base case

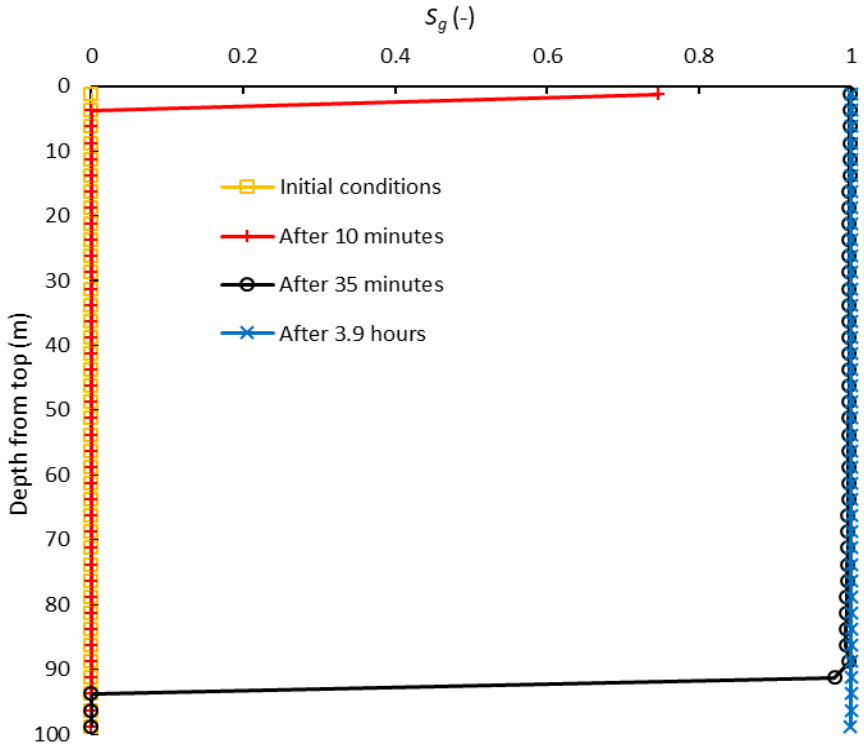

Figure 6.17. The saturation profile of CO_2 at different times within the wellbore for case 5 for ascending order flow capacities scenario

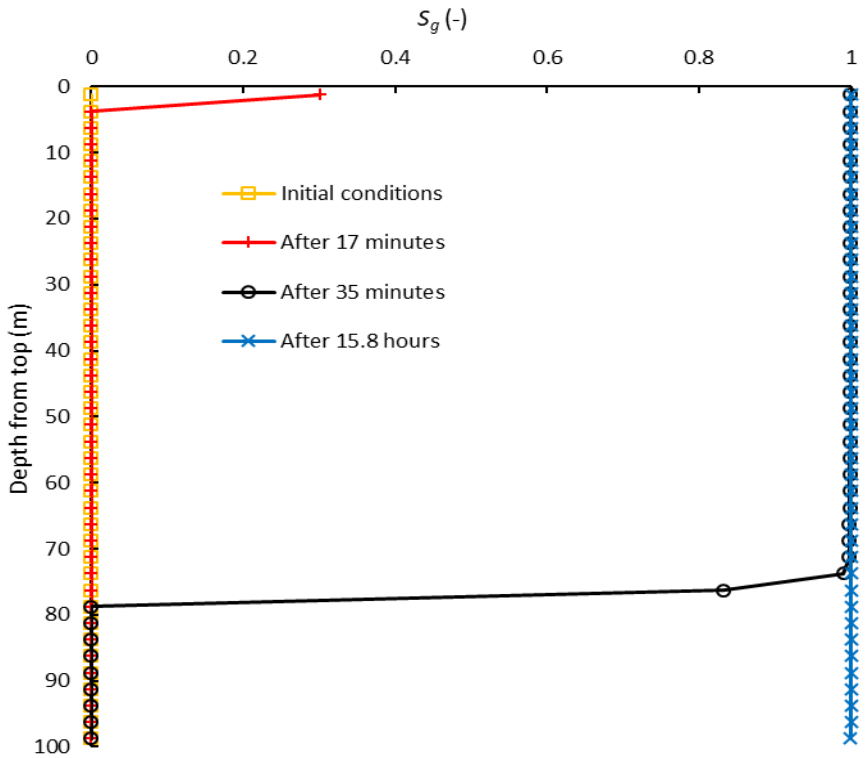

Figure 6.18. The saturation profile of CO_2 at different times within the wellbore for case 5 for descending order flow capacities scenario

Fig. 6.17 and 6.18 show CO_2 saturation profile within the wellbore for scenarios (a) and (b) respectively. Complete brine flushing took only 3.9 hr for scenario (a) as compared to 15.8 hr for scenario (b). This relatively high discrepancy in the flushing time is related to the order of flow capacities. For scenario (b), the upper layers have higher flow capacities, taking higher proportions of CO_2 allowing for slower fill-up of the wellbore as compared to scenario (a).

In addition, we investigated the effect of flow capacity heterogeneity when gravity is deactivated. In this case (case 5*), we repeated case 2 considering both scenarios of flow capacity profile. The flow rate profile for scenarios (a) and (b) is shown in Figs. 6.19 and 6.20, respectively. Figs. 6.21 and 6.22 report the corresponding profiles of the pressure difference between the wellbore and the aquifer after 3, 6, 9, and 12 months. Results of both scenarios show that the flow rate distribution between layers is viscous-driven. Figs. 6.21 and 6.22 indicate that the pressure difference is almost identical along the injection interval. This means that, solely following the pressure difference profile, the upper layers should take higher proportions of the injected CO_2 as compared to the lower ones. However, this behavior is suppressed when layers' flow capacities follow ascending order, and amplified when they follow descending order. Overall, the flow rate profile follows the flow capacity profile. For scenario (a), the effect of pressure difference opposes the effect of flow capacity profile. Consequently, the flow rate distribution is highest at the lower layers and lowest at the upper ones. For scenario (b), both parameters (i.e. pressure difference and flow capacity) act in the same direction. As shown in Fig. 6.20, the flow rates follow the same trend as the base case except that the discrepancies between the flow rates are amplified due to the descending order flow capacities.

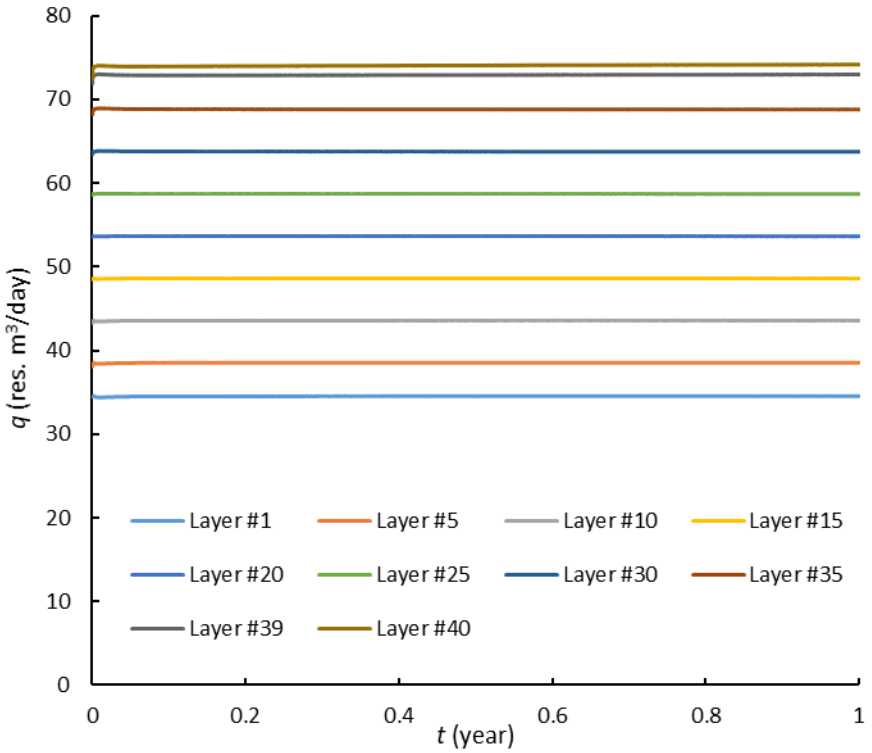

Figure 6.19. The flow rate distribution profile between layers for case 5* for ascending order flow capacities scenario

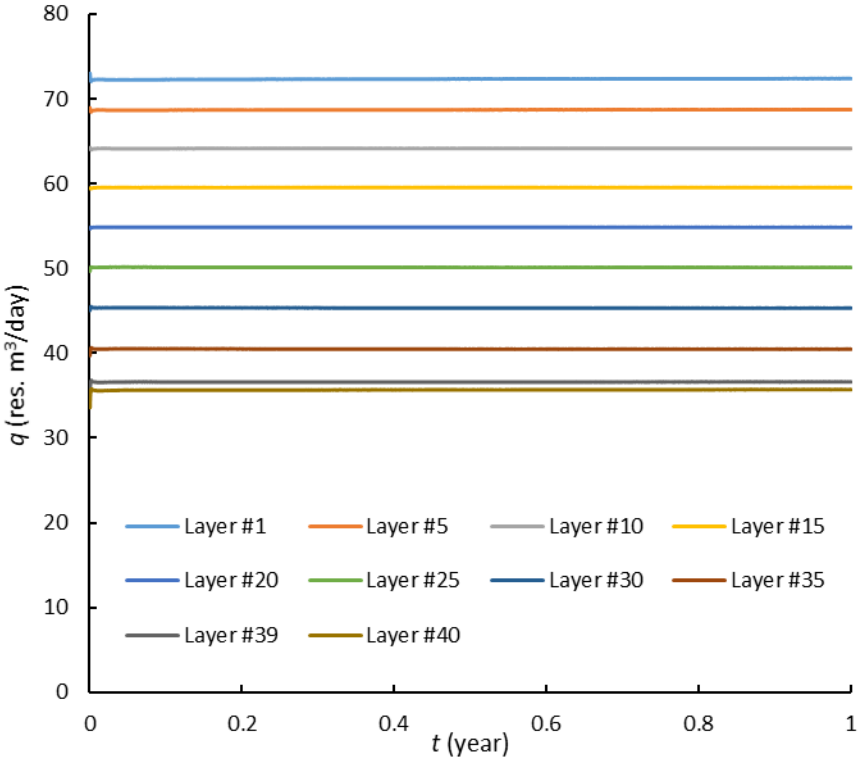

Figure 6.20. The flow rate distribution profile between layers for case 5* for descending order flow capacities scenario

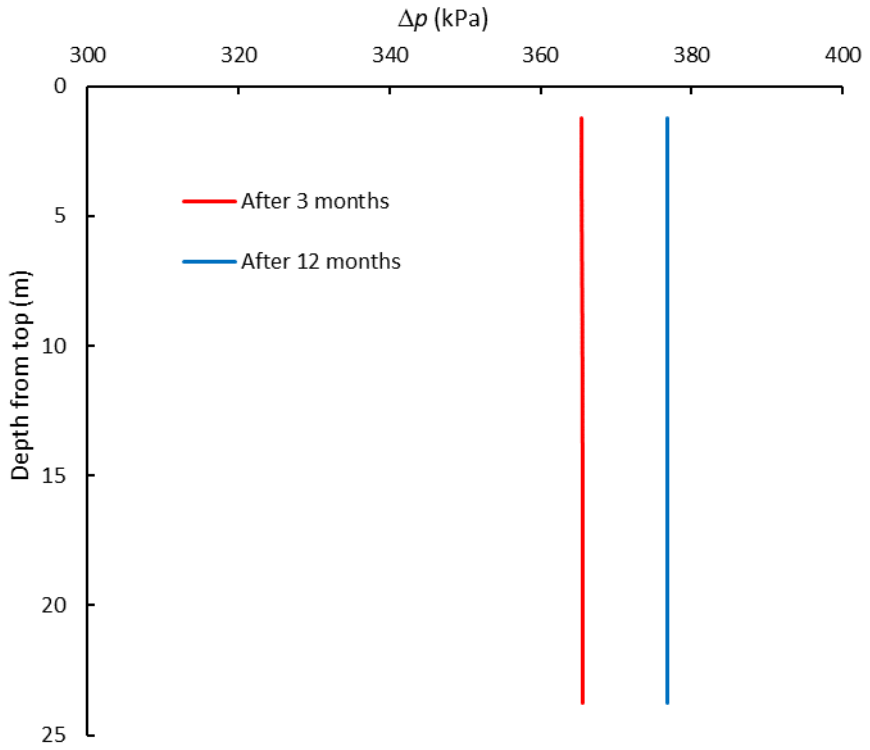

Figure 6.21. The evolution of pressure difference profile between the wellbore and the aquifer for case 5* for ascending order flow capacities scenario

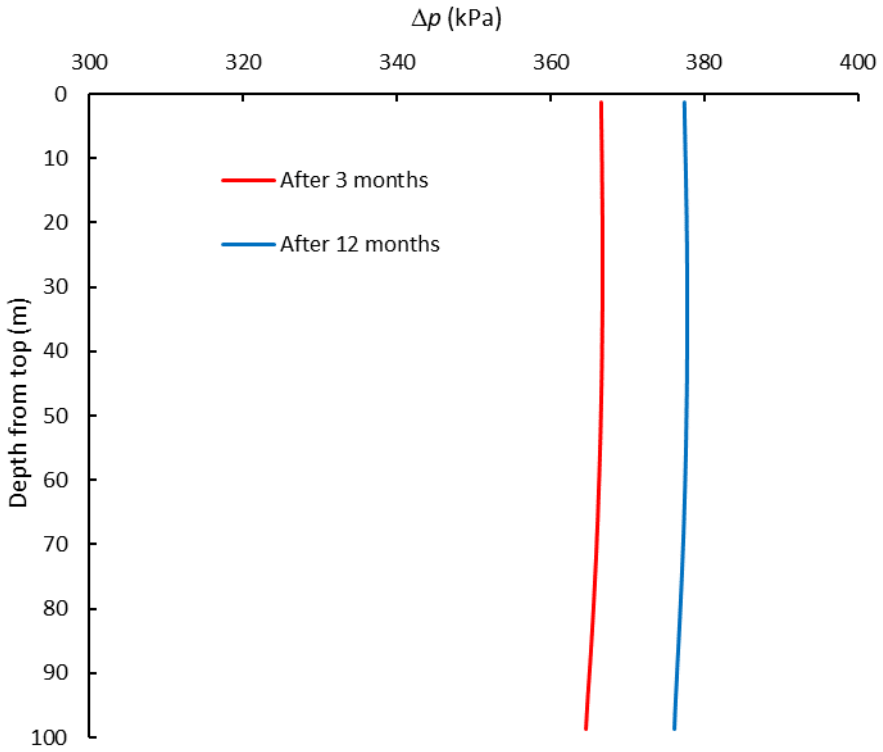

Figure 6.22. The evolution of pressure difference profile between the wellbore and the aquifer for case 5* for descending order flow capacities scenario

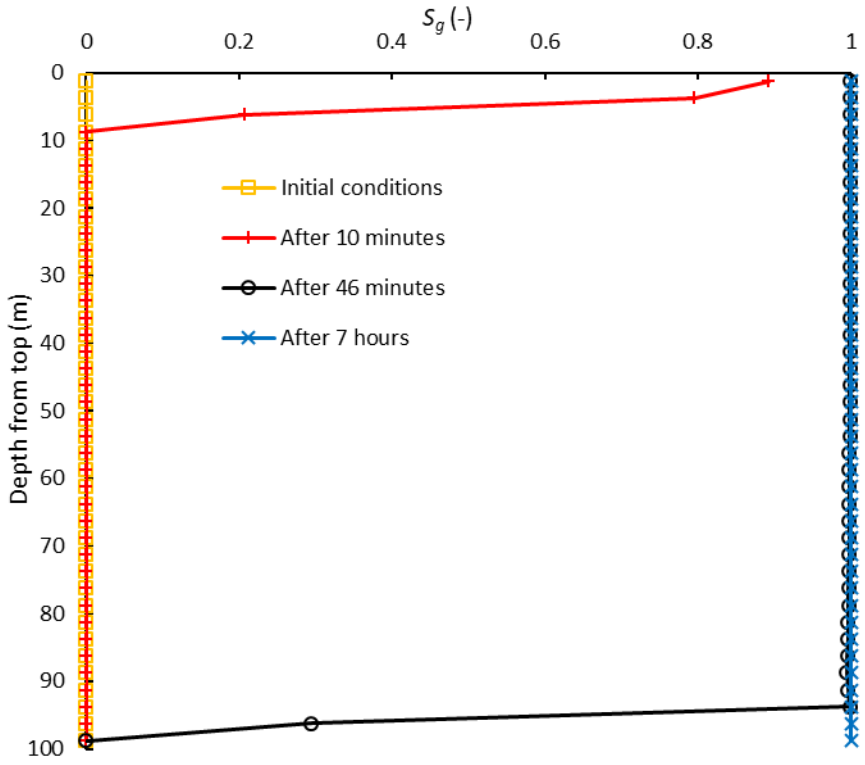

Figure 6.23. The saturation profile of CO_2 at different times within the wellbore for case 5* for ascending order flow capacities scenario

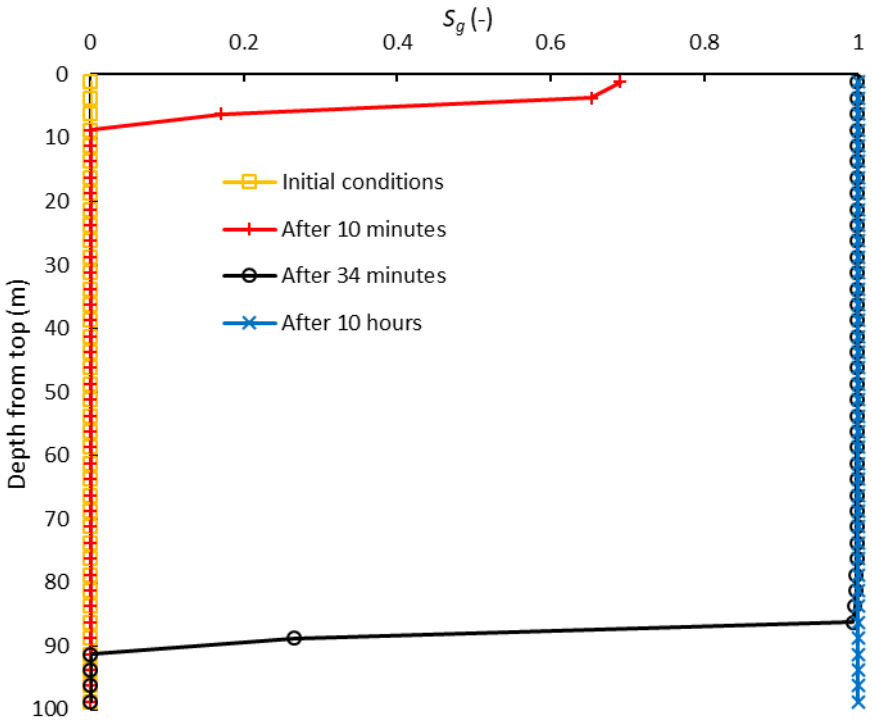

Figure 6.24. The saturation profile of CO_2 at different times within the wellbore for case 5* for descending order flow capacities scenario

Figs. 6.23 and 6.24 show CO_2 saturation profile within the wellbore for scenarios (a) and (b), respectively. Similar to case 5, complete flushing of brine for descending order flow capacities (10 hr) is slower than that for ascending order flow capacities (7 hr). As we explained before, this is attributed to the higher flow capacities in the upper layers, which take higher proportions of CO_2 which and allow for slower fill-up of the wellbore. However, it is noticed that the discrepancy in the flushing time is not high for case 5* as compared to case 5. This is attributed to the gravity effects which, if active and dominant, slows down the CO_2 flow down the wellbore, and as a result, the flushing time of brine.

6.3. Additional Investigations

The parameters that control CO_2 distribution along the injection interval have been investigated in the previous section. However, these parameters can be affected by several factors related to the characteristics of the injection domain, adopted injection rate/scheme, and the modeling approach. Therefore, in this section, we investigate how the flow rate distribution along the injection interval would be affected by the following factors: (a) the adopted injection scheme (i.e. continuous versus intermittent) and associated salt dry-out, (b) the decoupled (i.e. sink/source well injection) versus the coupled modeling approaches, (c) varying CO_2 injection rate, and (d) the presence of semi-pervious cap/baserock.

6.3.1. Effect of Intermittent CO_2 Injection and the Associated Salt Dry-Out

In practice, there would be inevitable shutdowns and rate fluctuations during injection operations. Therefore, we repeat case 4 except that the wellbore is shut-in for 2 months following an initial flow period of the same duration. The shut-in period is followed by a latter flow period lasting for the remaining 8 months as shown in Fig. 6.25. Fig. 6.26 shows CO_2 saturation profile within the wellbore at different times. Similar to case 4, CO_2 completely saturates the wellbore within 4.5 hr of injection. Then, due to backflow, CO_2/brine interface rises up to the 95-m level by end of the initial flow period. Unlike case 4, the interface continuously rises due to shut-in until it reaches the 5-m level by end of the shut-in period. Then, it declines and stabilizes again at the 95-m level with continuous injection during the latter flow period. The interface stabilization during the latter flow period occurs within few hours. This means that despite the noticeable effect of intermittent injection on wellbore filling with brine during shut-in, it should have insignificant effect on the flow rate distribution. Fig. 6.27 shows a comparison of the flow rate profile with case 4. Beyond the transient period, which last for few days, both profiles overlap each other during the flowing periods. Nevertheless, these results do not tell the whole story. In other words, we accounted for salt dry-out effect in our modeling through reducing the relative permeability to gas by 20 % to mimic the absolute permeability reduction in the dry-out zone. However, the intermittent injection does not affect the amount of salt dry-out in the model. In reality, brine backflow during shut-in increases the salinity around the wellbore because it redissolves the already precipitated salt next to the wellbore. Also, brine backflow exposes more well perforations to salt dry-out which would not have been exposed if there was no backflow. Consequently, the drying out process following well shut-in will cause an increased amount of precipitated salt which translates to further lowering the permeability in the near wellbore region. Proper modeling of this process requires further investigation of how salinity varies around the wellbore and warrants a separate study. With the

current model, this process could have been modelled if we change the end point relative permeability to a lower number after shut-in for the layers that experience brine backflow. This would affect the rate distribution over the layers especially if the formation permeability is highly sensitive to salt precipitation. Accordingly, brine backflow can affect the amount of salt dry out both in (1) the layers that were open during injection but are now exposed to brine due to brine backflow during shut-in, and (2) the layers that stopped contributing to injection during injection period (e.g., layers #39 and #40). Fig. 6.28 shows a simulator-generated CO_2 saturation profile at end of the initial injection period (top), and by end of the shut-in period (bottom). As shown, at end of the shut-in period, brine relatively re-saturates the near wellbore region along the injection interval due to brine backflow. This should re-dissolve the already precipitated salt which would, increase the overall salinity in the vicinity of the wellbore. Then, with further CO_2 injection, more salt should precipitate with drying-out which, as a result, would lower the absolute permeability and injectivity.

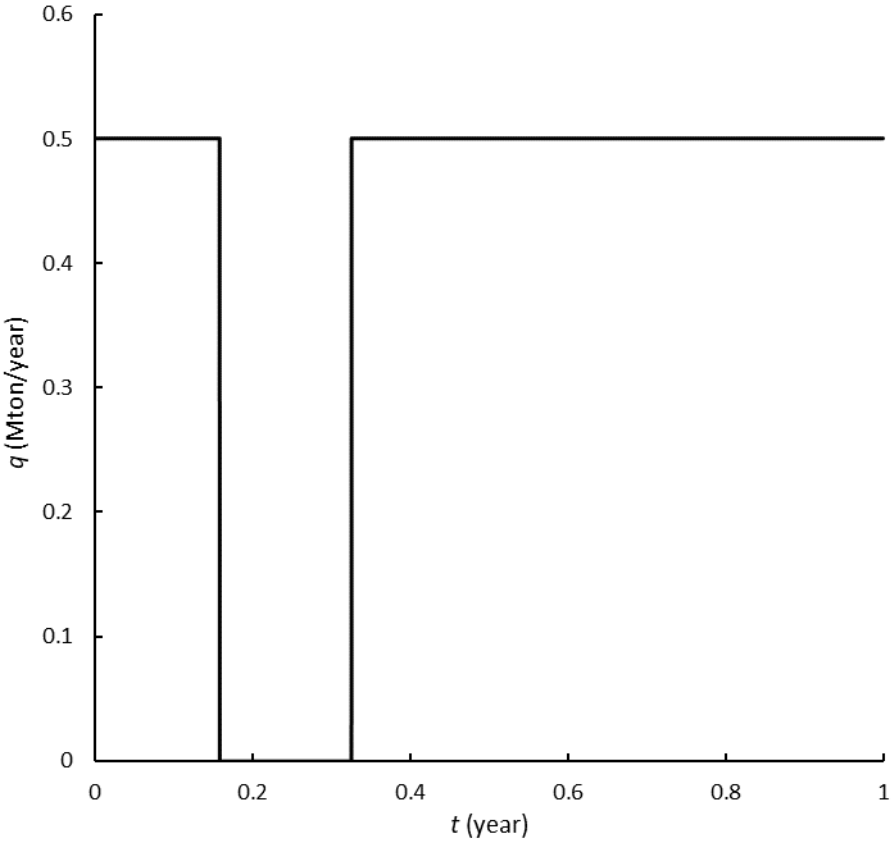

Figure 6.25. The injection rate history for case 4 with shut-in

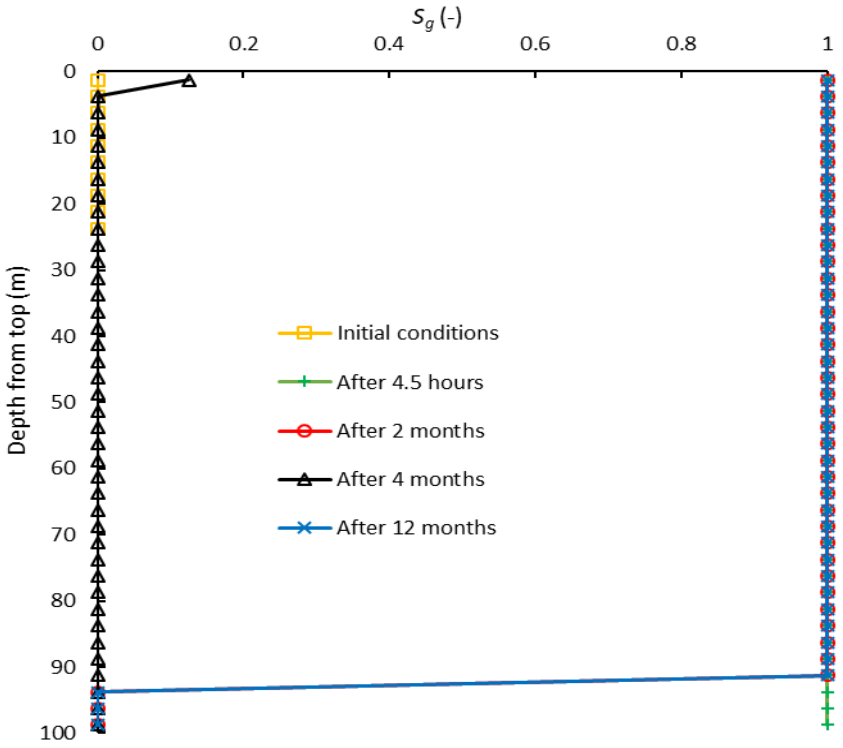

Figure 6.26. The saturation profile of CO_2 at different times within the wellbore for case 4 with shut-in

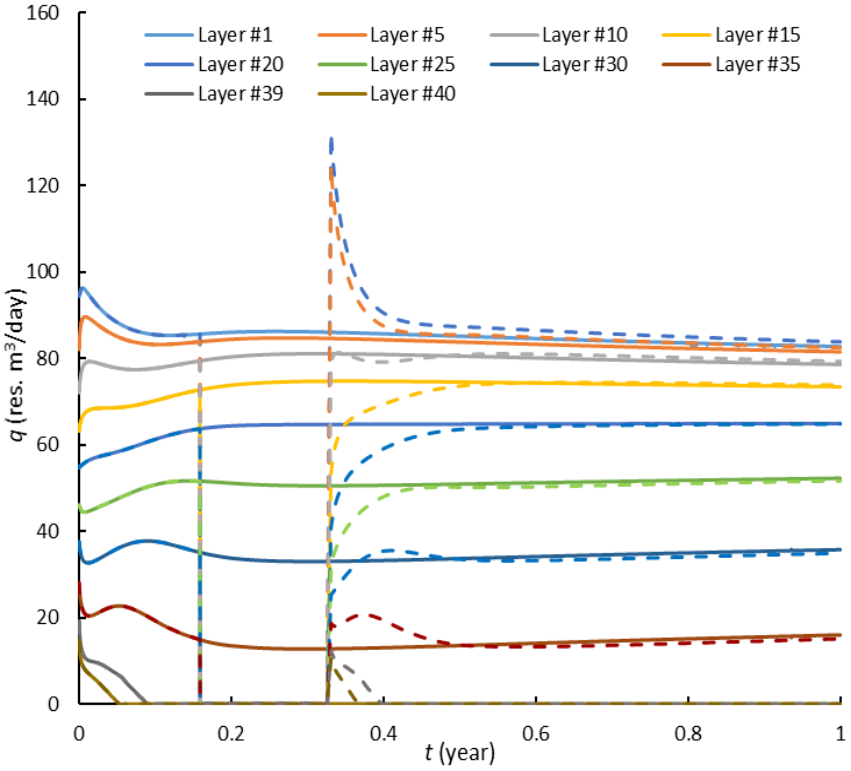

Figure 6.27. Comparison of the flow rate distribution between layers for case 4 without and with shut-in

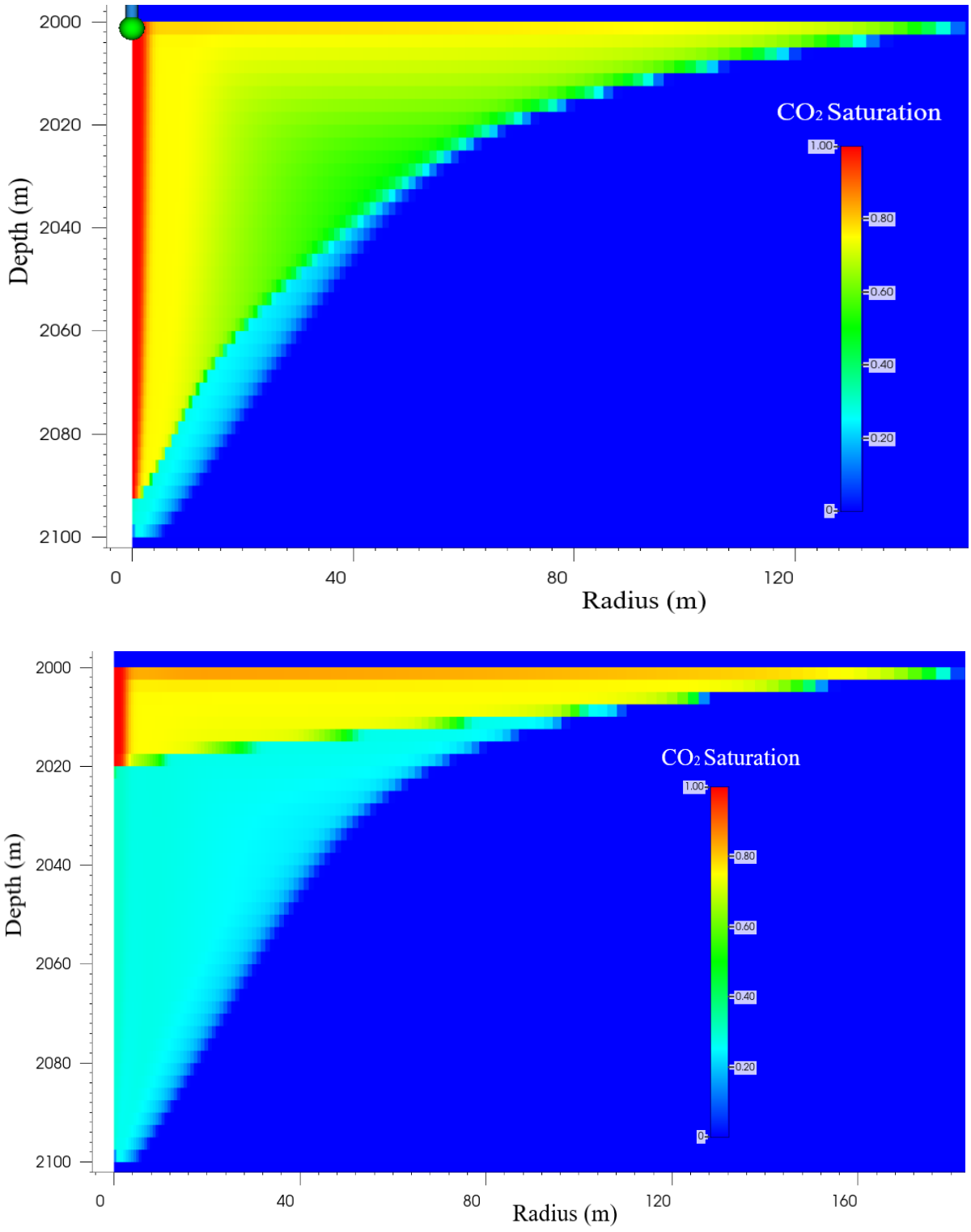

Figure 6.28. CO_2 saturation profile at end of the initial injection period (top), and by end of the shut-in period (bottom)

6.3.2. Effect of Decoupled Wellbore-Reservoir Modeling (Sink Well Injection)

Investigation of the parameters that affect CO_2 flux distribution, requires accurate modeling of the injection process using a fully coupled wellbore-reservoir model. This would allow for simulating complex wellbore physics that could not be modelled using simple sink/source wells. Ennis-King et al. (2018) suggested that reasonable prediction of plume evolution is possible without the need to fully coupled models through (1) representing the wellbore by assigning high permeability to the innermost column of gridblocks, and (2) optimizing/tuning the proportion of CO_2 flowing into the topmost gridblocks to match field observations of plume. Our goal in this work is to analyze all the factors that affect flow rate distribution along the injection interval. Thus, we investigate how the flow rate distribution would be affected when decoupled modeling approach (i.e. sink well injection) is adopted. We created the decoupled model by modifying the "Well and Recurrent Date" section of the coupled model as follows: (1) removing the FlexWell (both annulus and tubing sections of the flexible wellbore), and (2) adding a single well – implemented in CMG-STARS - with the same trajectory instead. The remaining sections of the model are kept exactly the same as the coupled model. To ensure that the decoupled model is comparable to the coupled model, the following has been accounted for using keywords suitable for sink/source well models: (a) the pressure losses and heat exchange calculations along the injection interval, and (b) the pressure and heat losses from surface down to the first perforation. Fig. 6.29 compares the results of the coupled and decoupled models for the base case. The figure shows the flow rate profile only for layers #1, 10, 20, 30, 39 and 40 to better visualize the results. The comparison indicates that results of sink-well injection follow the same trends as those of the coupled model with very insensible differences in magnitudes.

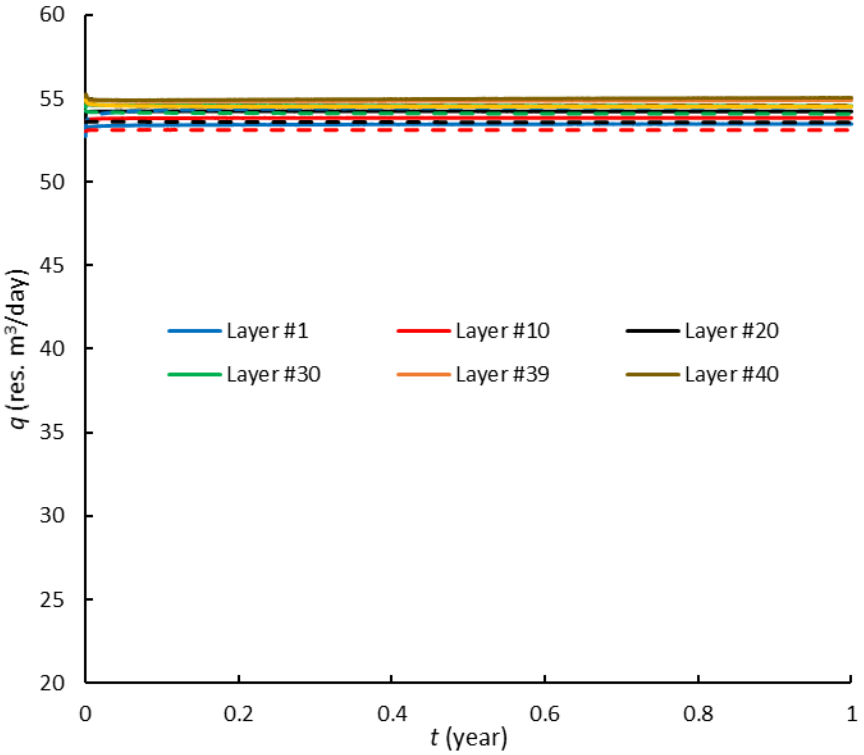

Figure 6.29. The flow rate distribution profile for the base case - Solid lines refer to the coupled wellbore-reservoir model, and dashed lines refer to the sink well injection

We, also, applied the decoupled modeling approach to case 4 to address the effect of decoupling on the more complex cases. The comparison of the flow rate distribution displayed in Fig. 6.30 indicates that both models follow the same trends, but with a more sensible deviations in magnitudes, as expected. This is related to the dominant gravity forces which cause the exaggerations – arising from neglecting some of the wellbore physics (e.g. wellbore storativity, mass accumulation, transient flow behavior, and phase segregation) - to play a more important role. For instance, when gravity force is dominant, ignoring phase segregation has significant impact on CO_2 saturation profile within the wellbore. This, in turn, should affect the flow rate distribution along the injection interval.

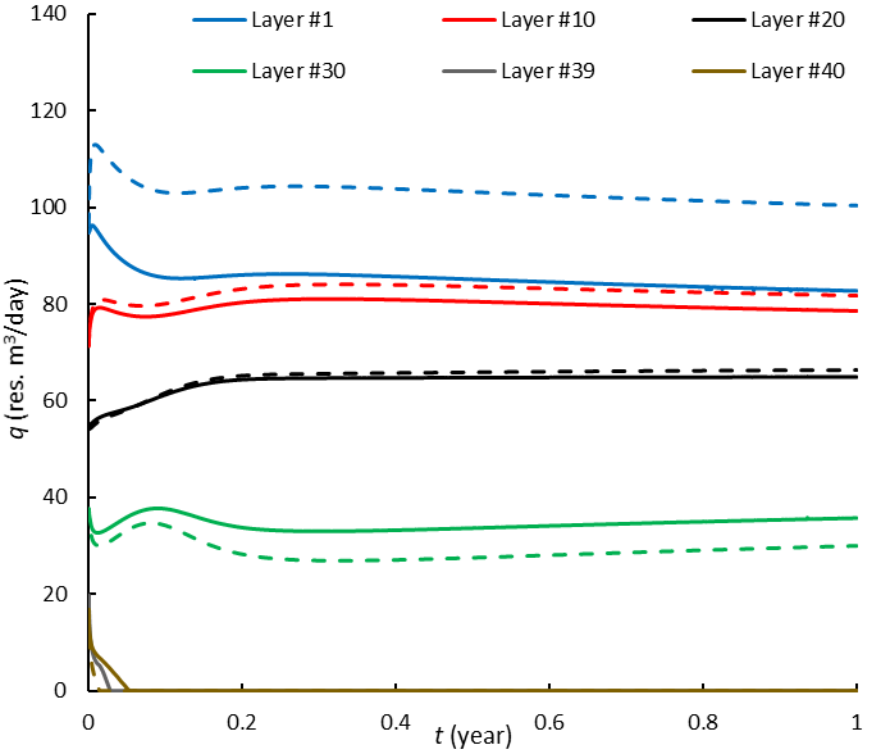

Figure 6.30. The flow rate distribution profile for case 4 - Solid lines refer to the coupled wellbore-reservoir model, and dashed lines refer to the sink well injection

Fig. 6.31 shows mismatch of CO_2 saturation profile within the wellbore for the coupled model versus the sandface saturation profile for the decoupled model. As is shown, for the coupled model, CO_2 saturation sharply declines from 100 % to 0 % corresponding to the two bottommost layers. However, for the decoupled model, CO_2 saturation declines from 100 % to 22 % corresponding to layers # 33 through 35. Meanwhile, CO_2 saturation holds constant around 22 % corresponding to the five bottommost layers, indicating that no phase segregation is happening therein. This is not the situation for the base case where the steady-state conditions are achieved faster due to the dominating viscous forces. As is shown in Fig. 6.32, CO_2 saturation is 100 % along the total length of the wellbore/sandface for the coupled/decoupled models which also justifies the relatively close match between the rate profiles for the base case. This means that disregarding the wellbore-reservoir coupling can cause deviations in the estimated rate profile. The deviation is slight in situations where gravity force is negligible (e.g. due to very low *kvh*) and viscous force is very

strong (e.g. due to very high injection rate). Such conditions would allow for the rate distributions, obtained using coupled and decoupled models, to agree or slightly deviate due to (a) the faster establishment of the steady-state flow behavior within the wellbore, and (b) the minimal effect of phase segregation. On the other hand, the deviations could be higher if more complex cases - that involve more physical processes - are modeled using sink/source wells. For instance, deviations that arise from neglecting some wellbore physics (e.g. wellbore storativity, mass accumulation, and phase segregation) can be exaggerated in conditions where gravity force dominates the transient flow behavior within the wellbore and phase segregation play a more important role. Therefore, it would be more accurate when coupled wellbore-reservoir modeling is adopted, whenever possible, to simulate CO_2 injection.

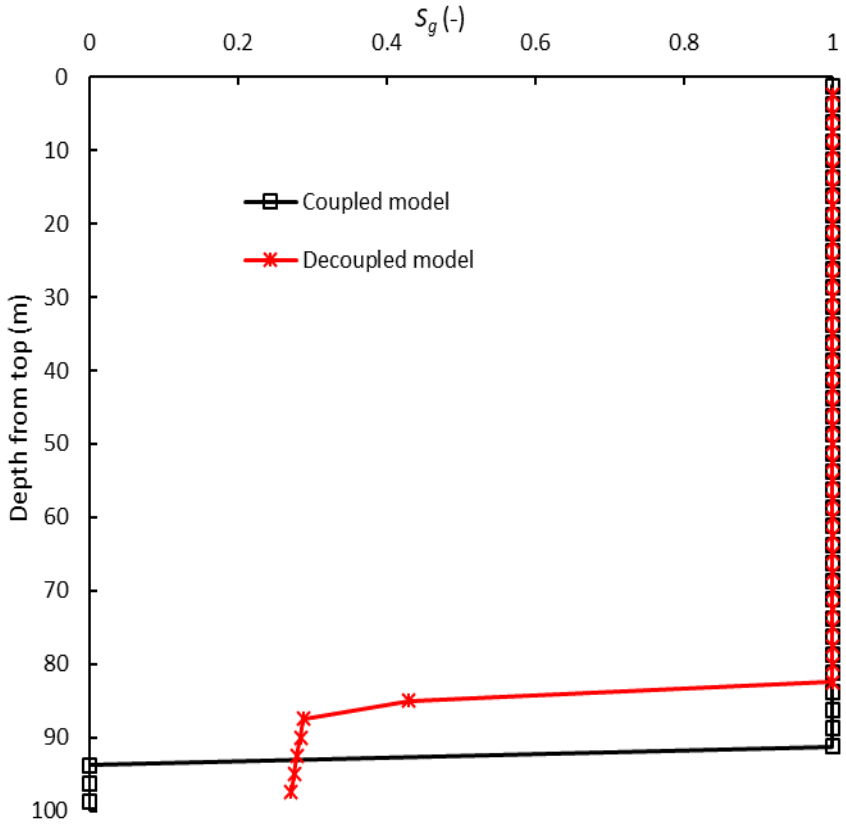

Figure 6.31. Comparison of CO_2 saturation profiles within the wellbore (for coupled model) vs at the sandface (for the decoupled model) for case 4

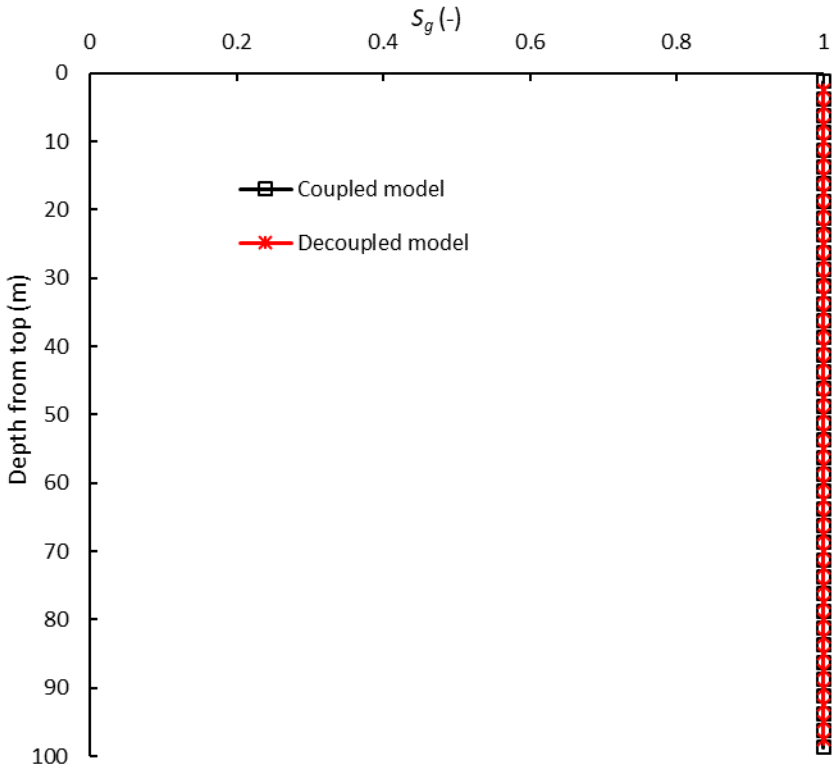

Figure 6.32. Comparison of CO_2 saturation profiles within the wellbore (for coupled model) vs at the sandface (for the decoupled model) for the base case

6.3.3. Effect of CO_2 Injection Rate

The results presented in the results section indicate that the injected CO_2 reaches the bottom of the wellbore within short time, and complete flushing of brine from the wellbore can take few hours/days. This is related to several factors including, but not limited to, the high injection rate adopted in the simulations (0.50 Mt/year). As stated by Ennis-King et al. (2018), CO_2 may not reach the bottom of the injection interval even after the whole period of injection if the injection rate is below a threshold value. This implies that the adopted injection rate can have a signficant effect on the timing/efficiency of brine diplacement by CO_2 within the wellbore which would evidently affect the flow rate profile. Therefore, we re-run case 4 while decreasing the rate of injection by a factor of two (i.e. to 0.25 Mt/year). Fig. 6.33 shows CO_2 saturation profile within the wellbore at different times. Due to the reduced injection rate, CO_2/brine interface stabilizes at 65-m level within the wellbore as compared to the 95-m level for case 4. Consequently, only the upper 26 perforations contribute to injection over the whole injection period. Nevertheless, the flow rate profile is similar to that achieved by the high injection rate scenario (Fig. 6.34). This concludes that adopting higher injection rates, whenever possible, is advantageous in maximizing injectivity through better utilization of the perforations.

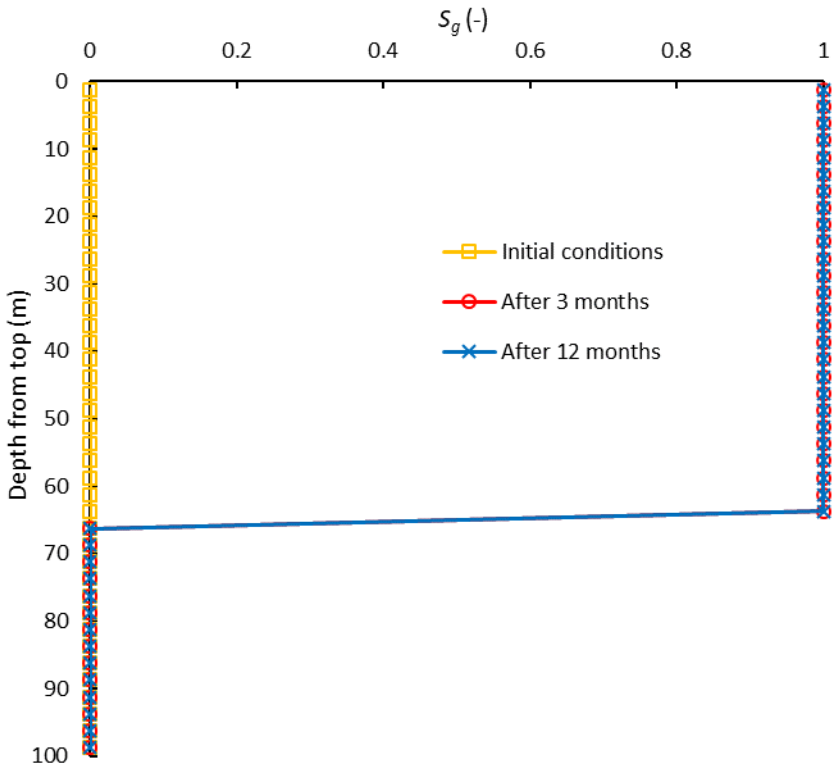

Figure 6.33. The profiles of CO_2 saturation at different times within the wellbore applied to case 4 with reduced injection rate of 0.25 Mt/year rate

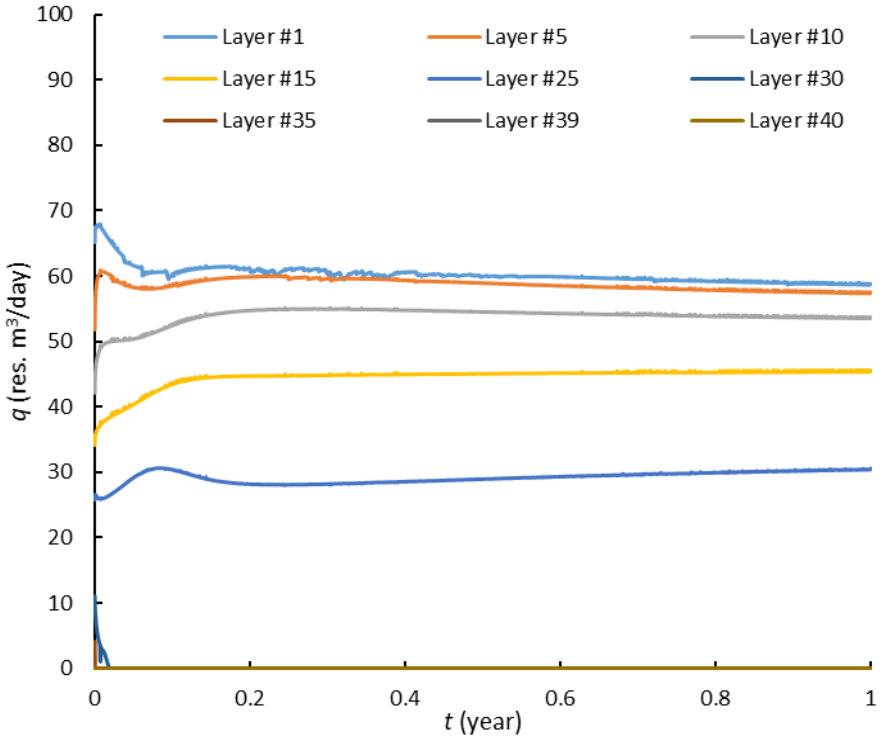

Figure 6.34. The profiles of flow rate distribution between layers applied to case 4 with reduced injection rate of 0.25 Mt/year rate

6.3.4. Effect of the Presence of Semi-Pervious Cap/Base-rock

In practice, the wellbore and target formation are not completely isolated from shallower/deeper intervals. Thus, extending the geological model to include permeable overlying/underlying layers is important. We repeat case 4 while modifying the permeability of the confining impermeable layers to be one hundredth of the injection interval (2.5 mD). To visualize the effect of the presence of slightly permeable confining boundaries on the rate distribution, we compared the rate profile of this case with that of case 4. Comparison shows that the presence of semi-pervious cap/baserock does not affect the profile trends nor the preference of flow into the layers (see Fig. 6.35 below). This is expected because the presence of the semi-pervious cap/baserock does not affect the viscous/gravity forces which control the flow rate distribution along the injection interval (as we explained in the results section). However, the magnitude of flow rates should be different because we are comparing two "different" models (i.e. with/without semi-pervious cap/baserock).

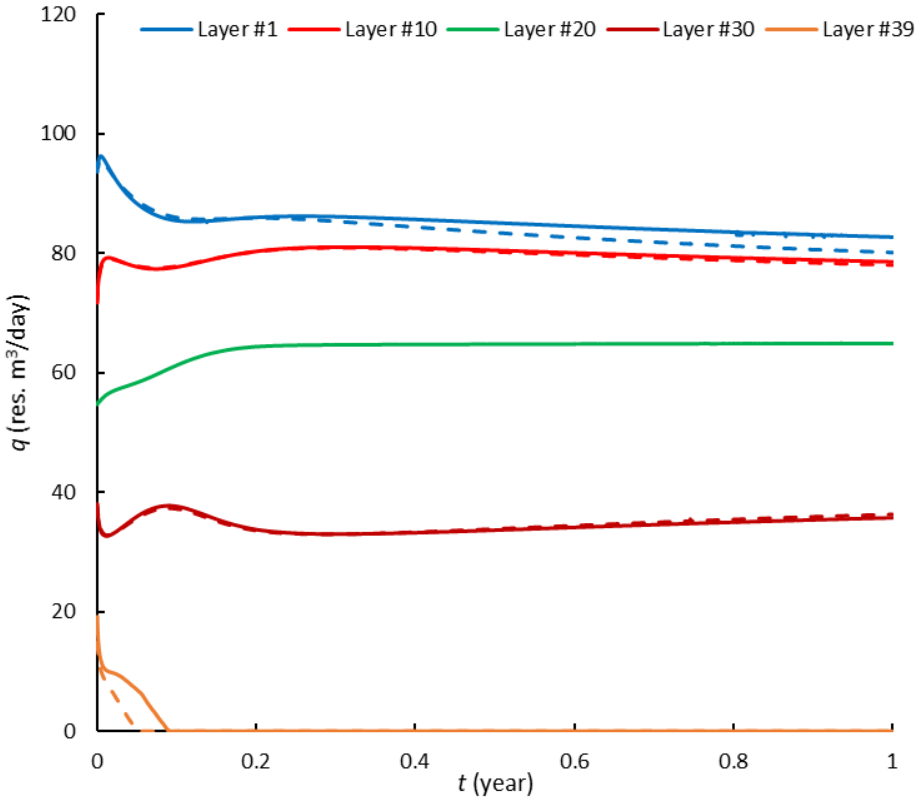

Figure 6.35. Comparison between the flow rate distribution profiles for case 4 (solid lines) and case 4 with semi-pervious confining layers (dashed lines)

Chapter 7. Evolution of Overpressure in High-Gravity Storage Saline Formations

The bottomhole overpressure which accompanies the injection of CO_2 is considered one of the main limiting factors to inject CO_2 at the desired high rates and volumes. Therefore, to optimize the storage potential of the formation, it is required to reliably predict the overpressure which is the goal of this chapter. In this chapter, we develop a closed-form analytical solution to predict the bottomhole pressure response during CO_2 injection in infinite-acting deep saline formations. While accounting for strong gravity forces, the solution is developed considering vertical equilibrium of pressure with a sharp interface separating CO_2 and brine. First, a closed-form analytical solution is developed to estimate the temporal-spatial evolution of the CO_2/brine interface. The solution extends the semi-analytical/iterative solutions presented in the literature to predict the evolution of the plume. Then, the closed-form pressure solution is obtained by coupling the interface solution with the previously-developed semi-analytical solutions that determine the pressure distribution. The pressure solution at the wellbore is validated against synthetic data generated using numerical simulation. Finally, the robustness of the developed pressure solution will be substantiated through validation against real field bottomhole pressure data obtained from a GCS pilot project.

7.1. Development of the Analytical Model

7.1.1. Evolution of the CO_2 Plume

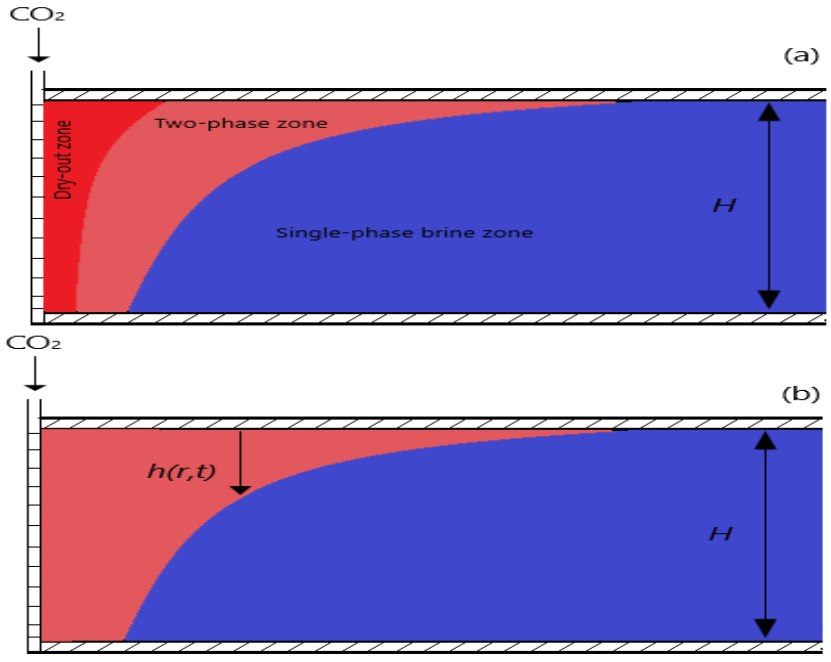

Figure 7.1. Schematic illustration (not to scale) of (a) the physical CO_2/brine system, and (b) the sharp interface approximation of the physical system

Consider the physical system shown in Fig. 7.1 (a), CO_2 is injected at a constant rate through a fully-penetrating vertical well centered in the middle of a homogenous and isotropic reservoir with uniform thickness and porosity. As we explained in the previous chapters, a saturation profile is

formed in the near wellbore region soon after the start of injection. However, with the assumptions of negligible local capillary pressure and fully immiscible fluids, the transitional "two-phase" zone between CO_2 and brine can be approximated by a sharp interface Fig. 7.1 (b).

With these assumptions along with considering constant fluid properties, Nordbotten et al. (2005a) developed a semi-analytical model to predict the evolution of CO_2/brine interface. In developing the model, the authors utilized the principle of energy minimization where the pressure buildup at the injection well should be minimized due to gravity. For a given a value of gravity number and mobility ratio, the model can be solved numerically for the evolution of the interface as a function of the similarity variable. According to their solution, the plume is constrained by the solution of a third order polynomial equation given by (Nordbotten et al., 2005a):

$$-\frac{(M-1)}{\chi\left[(M-1)h_{gD}+1\right]^2}+\Gamma h_{gD}+\Lambda=0 \tag{7.1}$$

where the Lagrangian multiplier Λ is the solution of the transcendental equation given by:

$$\Lambda(M-1)^2-\Gamma(M-1)+\Gamma M\ln\left(\frac{\Gamma+\Lambda}{\Lambda M}\right)=\frac{2M\left[\Lambda(M-1)-\Gamma\right]^2}{M-1} \tag{7.2}$$

where the dimensionless groups of the gravity number, similarity variable, height of the interface, and mobility ratio are respectively given by Celia et al. (2011); (Nordbotten and Celia, 2006; Nordbotten et al., 2005a):

$$\Gamma=\frac{2\pi(\rho_w-\rho_w)gkH^2}{q\mu_w} \tag{7.3}$$

$$\chi=\frac{r_D^2}{t_D}\quad\text{where:}\quad r_D=\frac{r}{r_w}\quad\text{and}\quad t_D=\frac{qt}{2\pi H\phi(1-S_{wr})r_w^2} \tag{7.4}$$

$$h_{gD}(\chi)=\frac{h(r,t)}{H} \tag{7.5}$$

$$M=\frac{\lambda_c}{\lambda_w}\quad\text{where:}\quad \lambda_c=\frac{k_{rc}}{\mu w}\quad\text{and}\quad \lambda_w=\frac{k_{rw}}{\mu_w} \tag{7.6}$$

where χ is the similarity variable, h_{gD} is the dimensionless height of the interface, Γ is the gravity number, ρ_c and ρ_w are the densities of CO_2 and brine respectively, g is the acceleration of gravity, k is the absolute permeability of the formation, H is the thickness of the aquifer, q is the volumetric injection rate of CO_2 at downhole conditions, μ_c and μ_w are the viscosities of CO_2 and brine respectively, S_{wr} is the residual brine saturation behind the interface, r_D is the dimensionless radius from the injection well, t_D is the dimensionless injection time, r is the radial extent of the interface from the injection well, r_w is the wellbore radius of the injection well, t is the injection time, M is

the mobility ratio, λ_c and λ_w are the mobilities of CO_2 and brine respectively, k_{rc} and k_{rw} are the relative permeabilities to CO_2 and brine respectively, and ϕ is the formation porosity.

Two big limitations of the abovementioned model are (1) the need of numerical/iterative solution, and (2) the underestimation of the interface extension at high gravity numbers, yielding its results unreliable when gravity forces are effective and strong. In 2006, the authors extended their work where they presented similarity solutions for the evolution of the interface and the corresponding pressure field (Nordbotten and Celia, 2006). The similarity solutions are represented by coupled second order Ordinary Differential Equations (ODEs). For a given mobility ratio and gravity number, the ODE for the interface can be solved numerically as a function of the similarity variable. Nevertheless, their model still requires numerical solution. We overcome this drawback through providing a closed-form solution able to predict the evolution of the plume over a wider range of mobility ratios and gravity numbers. The closed-form model extends the Nordbotten et al. (2005a)'s semi-analytical model. Utilizing the fact that there is a finite outermost location (denoted as χ_{max}) where the dimensionless height of the interface is zero (Nordbotten and Celia, 2006), i.e.:

$$h_{gD}\Big|_{\chi_{\max}} = 0 \tag{7.7}$$

Substituting for the boundary condition of Eq. 7.7 into Eq. 7.1 and rearranging, then the Lagrangian multiplier can be expressed as:

$$\Lambda = \frac{(M-1)}{\chi_{\max}} \tag{7.8}$$

When Γ is sufficiently small (i.e. < 0.5), then $\chi_{\max} = 2M$ (Okwen et al., 2010). However, for the ranges $5.0 \le M \le 20.0$ and $0.5 \le \Gamma \le 50$, Okwen et al. (2010) introduced an approximation for $\chi_{\max}$ by solving (Nordbotten and Celia, 2006)'s ODE (Eq. 13 in their work). The approximation for $\chi_{\max}$ is given by:

$$\chi_{\max} \simeq (0.0324M - 0.0952)\Gamma + (0.1778M + 5.9682)\Gamma^{0.5} + 1.6962M - 3.0472 \tag{7.9}$$

Substituting from Eq. 7.9 into Eq. 7.8 then Eq. 7.1, the semi-analytical solution for the evolution of the interface can now be written in the form of a 3rd order polynomial equation given by:

$$\frac{1}{\chi\left[(M-1)h_{gD}+1\right]^2} - \frac{\Gamma h_{gD}}{(M-1)} = \frac{1}{\chi_{\max}} \tag{7.10}$$

Then, a closed-form analytical expression for the interface can be obtained by solving Eq. 7.10. The solution has the following form:

$$h_{gD}=\begin{cases}0 & \chi>\chi_{\max}\\ \dfrac{1}{(M-1)}\left\{\begin{aligned}&\left[\frac{b}{\chi}-\frac{a^3}{27}+\left[-\frac{2a^3b}{27\chi}+\frac{b^2}{\chi^2}\right]^{\frac{1}{2}}\right]^{\frac{1}{3}}\\ &+\left[\frac{b}{\chi}-\frac{a^3}{27}-\left[-\frac{2a^3b}{27\chi}+\frac{b^2}{\chi^2}\right]^{\frac{1}{2}}\right]^{\frac{1}{3}}-\frac{1}{3}a-1\end{aligned}\right\} & \chi_{\min}<\chi<\chi_{\max}\\ 1 & \chi<\chi_{\min}\end{cases} \tag{7.11}$$

where:

$$\chi_{\max}=2M \qquad \text{for } \Gamma<0.5$$

$$\chi_{\max}\simeq(0.0324M-0.0952)\Gamma+(0.1778M+5.9682)\Gamma^{0.5}+1.6962M-3.0472 \text{ for } 0.5\le\Gamma\le 50$$

$$\chi_{\min}=\frac{\chi_{\max}(M-1)}{M^2(\Gamma\chi_{\max}+M-1)}$$

$$a=\frac{(M-1)^2}{\chi_{\max}\Gamma}-1$$

$$b=\frac{1}{2}\frac{(M-1)^2}{\Gamma}$$

A note that the expressions in the square-root brackets of Eq. 7.11 must be positive for the solution to be mathematically valid. Consequently, χ is constrained by the following expression:

$$\chi<\frac{27(M-1)^2}{4\Gamma\left[\dfrac{(M-1)^2}{\chi_{\max}\Gamma}-1\right]^3} \tag{7.12}$$

As will be shown later in the validation section, this constraint is not restrictive for the practical ranges of mobility ratios and gravity numbers studied herein.

7.1.2. Evolution of the Overpressure

As mentioned above, Nordbotten and Celia (2006) developed similarity solutions, represented by ODEs for the evolution of the interface and the corresponding pressure field. Once the evolution of the interface is solved for, the corresponding pressure can be obtained by numerically solving the coupled ODE for the pressure field given by:

$$-\frac{dp_D}{d\chi}=\frac{1}{(M-1)h_{gD}+1}\left[Mh_{gD}\frac{dh_{gD}}{d\chi}+\frac{1}{2\Gamma\chi}\right] \tag{7.13}$$

where:

$$p_D=\frac{p(r,t)-p_i}{(\rho_w-\rho_c)gH}$$

For an infinite-acting system, Eq. 7.13 has the following solution for the behavior of pressure field, in dimensionless form, during CO_2 injection (Nordbotten et al., 2009):

$$\Delta p_D=\frac{1}{2\Gamma}\int_{\chi}^{\psi}\frac{d\chi}{\left[(M-1)h_{gD}+1\right]\chi}-\frac{M}{M-1}\left\{h_{gD}-\frac{\ln\left[(M-1)h_{gD}+1\right]}{(M-1)}\right\} \tag{7.14}$$

where:

$$p_D=\frac{p(r,t)-p_i}{(\rho_w-\rho_c)gH}\ \text{ and }\ \psi=\frac{4.5\pi Hk(1-S_{wr})}{q\mu_w(c_r+c_w)}$$

In Eqs. 7.13 and 7.14, p_D is the dimensionless pressure, *p(r,t)* is the pressure as a function of position and time, p_i is the initial pressure of the aquifer, ψ is the similarity variable corresponding to the outer location at which the pressure has not changed relative to the initial pressure, and c_r and c_w are the compressibilities of the formation rock and brine respectively.

Substitution of Eq. 7.11 into Eq. 7.14 would result in the following semi-analytical formulation for the overpressure during injection. The details of the derivation of the semi-analytical solution are given in Appendix D.

$$\Delta p_{wD}=\frac{1}{2M\Gamma}\ln\left(\frac{\chi_{\min}}{\chi}\right)+\frac{1}{2\Gamma}\ln\left(\frac{\psi}{\chi_{\max}}\right)-\frac{M}{M-1}\left\{1-\frac{\ln(M)}{(M-1)}\right\}$$
$$+\frac{1}{2\Gamma}\int_{\chi_{\min}}^{\chi_{\max}}\frac{d\chi}{\chi\left(\left[\frac{b}{\chi}-\frac{a^3}{27}+\left[-\frac{2a^3b}{27\chi}+\frac{b^2}{\chi^2}\right]^{\frac{1}{2}}\right]^{\frac{1}{3}}+\left[\frac{b}{\chi}-\frac{a^3}{27}-\left[-\frac{2a^3b}{27\chi}+\frac{b^2}{\chi^2}\right]^{\frac{1}{2}}\right]^{\frac{1}{3}}-\frac{a}{3}\right)} \tag{7.15}$$

As will be shown later in the validation section, a better match with the simulated bottomhole results is achieved by introducing the coefficient (ß) to the definition of $\chi_{\min}$ as follows:

$$\chi_{\min} = \frac{\beta\chi_{\max}\left(M-1\right)}{M^2\left(\Gamma\chi_{\max}+M-1\right)} \tag{7.16}$$

Using non-linear regression analysis, the coefficient (ß) is given as a function of the mobility ratio and gravity number as follows:

$$\beta = \exp\left[4.0165M^{0.25} - 4.9974\Gamma^{0.25} - 12.279\right]$$

Then, to obtain a fully-analytical (closed-form) solution, the integral term of Eq. 7.15 can be simplified by dropping some factors which were found to have little effect on the pressure response. As a result, the solution would reduce to:

$$\Delta p_{wD} = \frac{1}{2M\Gamma}\ln\left(\frac{\chi_{\min}}{\chi}\right) + \frac{1}{2\Gamma}\ln\left(\frac{\psi}{\chi_{\max}}\right) - \frac{M}{M-1}\left\{1-\frac{\ln\left(M\right)}{\left(M-1\right)}\right\} + \frac{1}{2\Gamma}\int_{\chi_{\min}}^{\chi_{\max}} \frac{d\chi}{\chi\left(\left[\frac{2b}{\chi}\right]^{\frac{1}{3}} - \frac{a}{3}\right)} \tag{7.17}$$

Integrating Eq. 7.17, the following solution for the bottomhole pressure behavior during CO_2 injection, in dimensionless form, is obtained:

$$\Delta p_{wD} = \frac{1}{2M\Gamma}\ln\left(\frac{\chi_{\min}}{\chi}\right) + \frac{1}{2\Gamma}\ln\left(\frac{\psi}{\chi_{\max}}\right) - \frac{9}{2a\Gamma}\ln\left[\frac{3\sqrt[3]{2b} - a\sqrt[3]{\chi_{\max}}}{3\sqrt[3]{2b} - a\sqrt[3]{\chi_{\min}}}\right] - \frac{M}{M-1}\left\{1-\frac{\ln\left(M\right)}{\left(M-1\right)}\right\} \tag{7.18}$$

where χ_{min} is defined by Eq. 7.16. Using non-linear regression analysis, the coefficient (ß) is given as a function of the mobility ratio and gravity number as follows:

$$\beta = \exp\left[4.8731\left(M^{0.25}-3\right)\Gamma^{0.5} + 10.5863\Gamma^{0.25} - 14.7132\right] \tag{7.19}$$

An important note that, in reality, no geologic formation would follow all the aforementioned assumptions. However, most of the assumptions are not restrictive that the developed analytical model would be valid at a relatively large number of CO_2 repositories. Nevertheless, as any other analytical model, we should expect to see good match with field data or numerical solutions that adopt the same assumptions (or close to). On the other hand, we expect to see noticeable deviations in cases that violate the adopted assumptions. At least, the analytical model can be used as a quick (not alternative) tool compared to the expensive numerical simulators that may not be available in

practice or need detailed geologic model to represent the subsurface. As will be shown in the validation section, the developed solutions approximately match the stabilized trend of the bottomhole pressure for simulated/field data, validating its practical application.

7.2. Validation of the Analytical Model

Table 7.1. Input data for validation cases (empty cells indicate same as left column)

	Case 1 (M = 2.3)	Case 1 (M = 3.3)	Case 3 (M = 4.4)	Case 4 (M = 6.0)
Residual saturation of brine	0.3			
Endpoint relative permeability for gas	0.25	0.37	0.49	0.67
Injection rate (Mt/year)	0.5-1.0			
Gravity number	1.0 to 3.00			
Number of layers	30			
Number of grids (radial × angular)	1000 × 1			
Initial reservoir pressure (MPa)	20.1			
Total injection time (years)	10			
Depth to top (km)	2.0			
Porosity (fraction)	0.25			
Reservoir temperature (^{o}C)	70			
Injection well radius (m)	0.1			
Horizontal permeability (mD)	300			
Vertical permeability (mD)	300			
Dip angle (^{o})	0			
Rock compressibility (1/kPa)	5e-7			
Reservoir extent (km)	100			
Reservoir thickness (m)	40-60-68			
Density of CO_2 (kg/m^3)	638.1			
Viscosity of CO_2 (cp)	0.051			
Density of brine (kg/m^3)	1027.5			
Viscosity of brine (cp)	0.453			
Gas relative permeability exponent	3.0			
Brine relative permeability exponent	3.0			

The semi-analytical and analytical models represented by Eqs. 7.15 and 7.18 are validated against numerical simulation results. In addition, the models are compared with the previous analytical models presented in the literature to predict the behavior of the bottomhole pressure in response to CO_2 injection at a constant rate. The synthetic data is generated using CMG-IMEX (2021). The PVT model is generated using Hassanzadeh et al. (2008) algorithm, and the relative permeability data is obtained using Corey's model (Corey, 1954b). The saturation exponents for CO_2 and brine

are set at 3.0 with endpoint relative permeability of 1.0 for brine. To simulate different mobility ratios, the endpoint relative permeability to CO_2 is assigned values ranging from 0.25 to 0.67 with residual brine saturation of 0.3. Also, to ensure covering a wide and practical range of gravity numbers, injection rates of 0.5 and 1.0 Mt/year, and reservoir thicknesses ranging from 40 to 68 m are adopted. A summary of the input data used in the validation is shown in Table 7.1.

7.2.1. Case 1: Low Mobility Ratio

For this case, a low mobility ratio of 2.3 is simulated through assigning values of 0.25 and 0.30, respectively, for CO_2 end-point relative permeability, and residual saturation of brine. Gravity numbers of 0.51 and 1.02 are modelled by injecting at constant rates of 1.0 Mt/year and 0.5 Mt/year, respectively, into a 40 m-thick aquifer. Higher gravity numbers of 2.30 and 2.95 are simulated through increasing the thickness of the aquifer from 40 m to 60 and 68 m, respectively.

We validate the developed semi-analytical and analytical solutions against the analytical solution of Celia et al. (2011) as well as the numerical simulation results. To emphasize the effect of gravity, we, also, compare the developed solutions with analytical solutions presented in the literature to predict the evolution of bottomhole pressure during CO_2 injection without accounting for gravity effects (Azizi and Cinar, 2013a; Mathias et al., 2009). For this case, the comparisons between the analytical and numerical bottomhole pressures for different gravity numbers is shown in Fig. 7.2. The comparisons indicate a good match between the developed solutions and the numerical results. On the other hand, solutions of Mathias et al. (2009), Azizi and Cinar (2013a), and Celia et al. (2011) experience significant deviations from the numerical results. As shown, the deviation gets bigger with higher gravity numbers, as expected. It is also noticed that, at low gravity numbers, the analytical solution of Azizi and Cinar (2013a) yields less deviation against the numerical results and the developed analytical solutions. However, as gravity number increases, the deviation gets bigger (see Figs. 7.2 through 7.5). This is expected given that Azizi and Cinar (2013a)'s solution is viscous-driven solution. Among all other solutions, Mathias et al. (2009)'s solution shows the biggest deviation from the numerical results and the developed analytical solutions as well. This is due to the fact that the solution neglects the effects of gravity both in the evolution of the interface and the corresponding pressure field. On the other hand, Celia et al. (2011)'s solution shows less deviation as compared to the solutions of Azizi and Cinar (2013a) and Mathias et al. (2009) especially at high gravity numbers. This is because Celia et al. (2011)'s solution accounts for the effects of gravity on the evolution of pressure, but not on the evolution of the interface. Also, it is worth to note that all the analytical solutions mismatch the early-time bottomhole pressure behavior. As shown by the simulated results, the pressure reaches a maximum at the early period of injection. Then, it sharply declines before reaching stabilization at late times. This discrepancy can be explained as follows. The "hump" observed in the simulation during this "transient flow" period is attributed to the fact that, at the beginning of injection, CO_2 cannot override brine, and it should first displace the in-situ brine that completely saturates the near wellbore region. This requires a certain threshold pressure to displace brine by CO_2, causing the observed increase in the bottomhole pressure trend. During this period, the flow is viscous-dominant such that there is no room for the upward migration of CO_2. Once the dry-out zone is formed in the vicinity of the wellbore, the gravity becomes effective, and the axial/radial resistance to CO_2 flow decreases, causing the bottomhole pressure to decrease. This marks the establishment of the "stabilized flow" period where the bottomhole pressure starts to plateau. On the other hand, the analytical model is initialized considering vertical equilibrium of pressure with a sharp

interface between CO_2 and brine. This means that the transient flow behavior is not accounted for, and the solutions are developed considering an "already-existing" CO_2 region behind CO_2-brine interface. That is why a discrepancy between the analytical and numerical solutions should be observed during the early-time of injection, as expected.

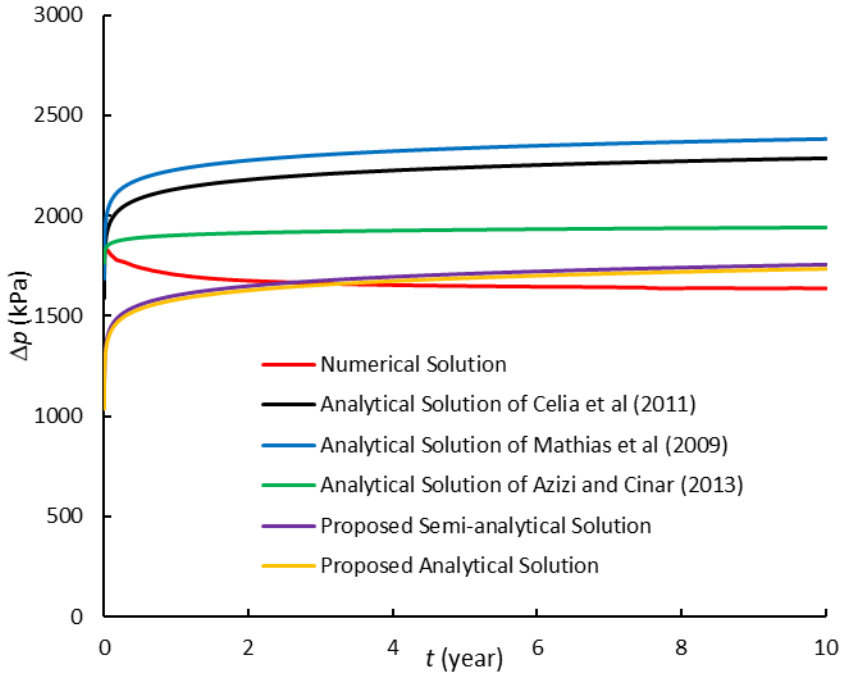

Figure 7.2. Comparison of the analytical and numerical bottomhole pressures for case 1 (M = 2.3) for gravity number of 0.51

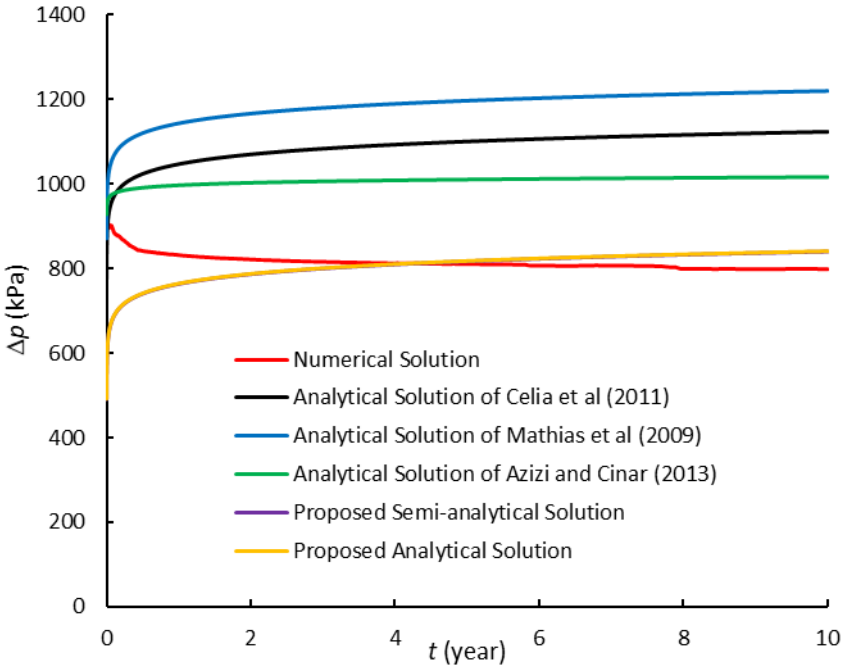

Figure 7.3. Comparison of the analytical and numerical bottomhole pressures for case 1 (M = 2.3) for gravity number of 1.02

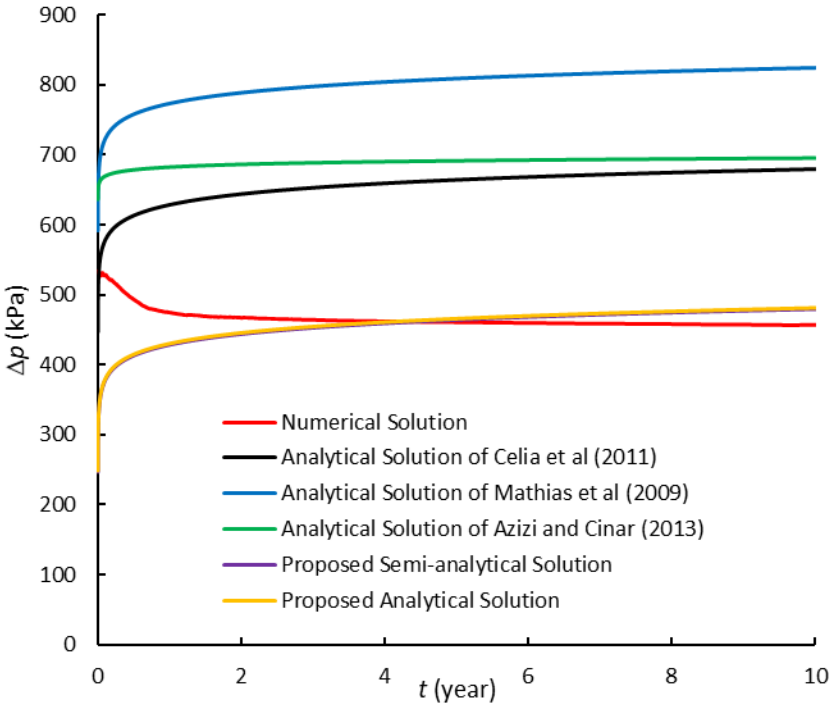

Figure 7.4. Comparison of the analytical and numerical bottomhole pressures for case 1 (M = 2.3) for gravity number of 2.30

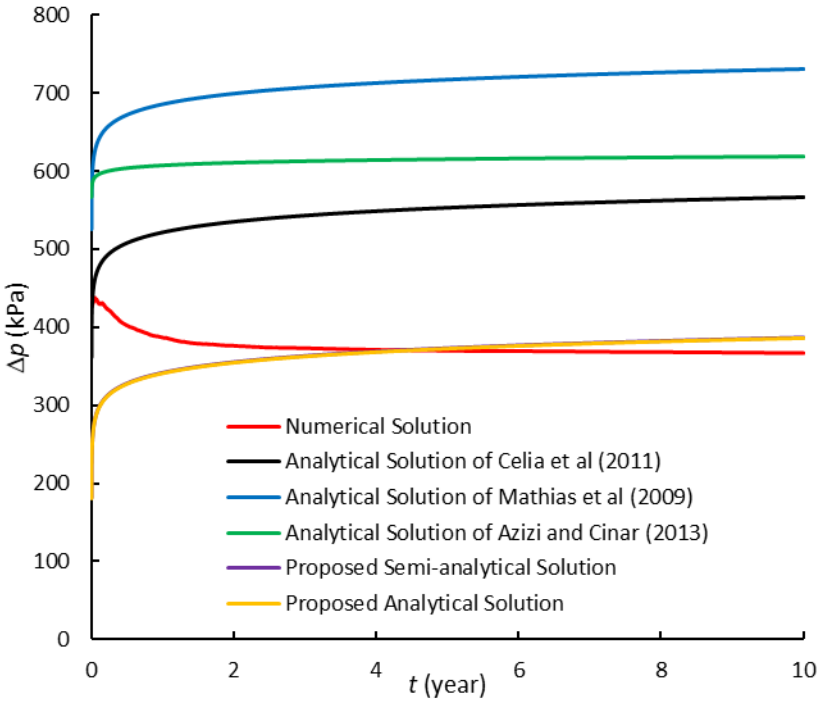

Figure 7.5. Comparison of the analytical and numerical bottomhole pressures for case 1 (M = 2.3) for gravity number of 2.95

7.2.2. Cases 2 and 3: Low Mobility Ratios

In cases 2 and 3, intermediate mobility ratios of 3.3 and 4.4 are simulated. This is achieved through increasing the end-point relative permeability to CO_2 to 0.37 and 0.49, respectively for cases 2 and 3. Similar to case 1, gravity numbers of 0.51 and 1.02 are simulated by injecting at constant rates of 1.0 Mt/year and 0.5 Mt/year respectively into a 40-m thick aquifer. Higher gravity numbers of 2.30 and 2.95 are modelled by setting the aquifer thickness at 60 and 68 m respectively while injecting at 0.5 Mt/year. The remaining rock and fluid properties are kept identical to case 1 given in Table 7.1.

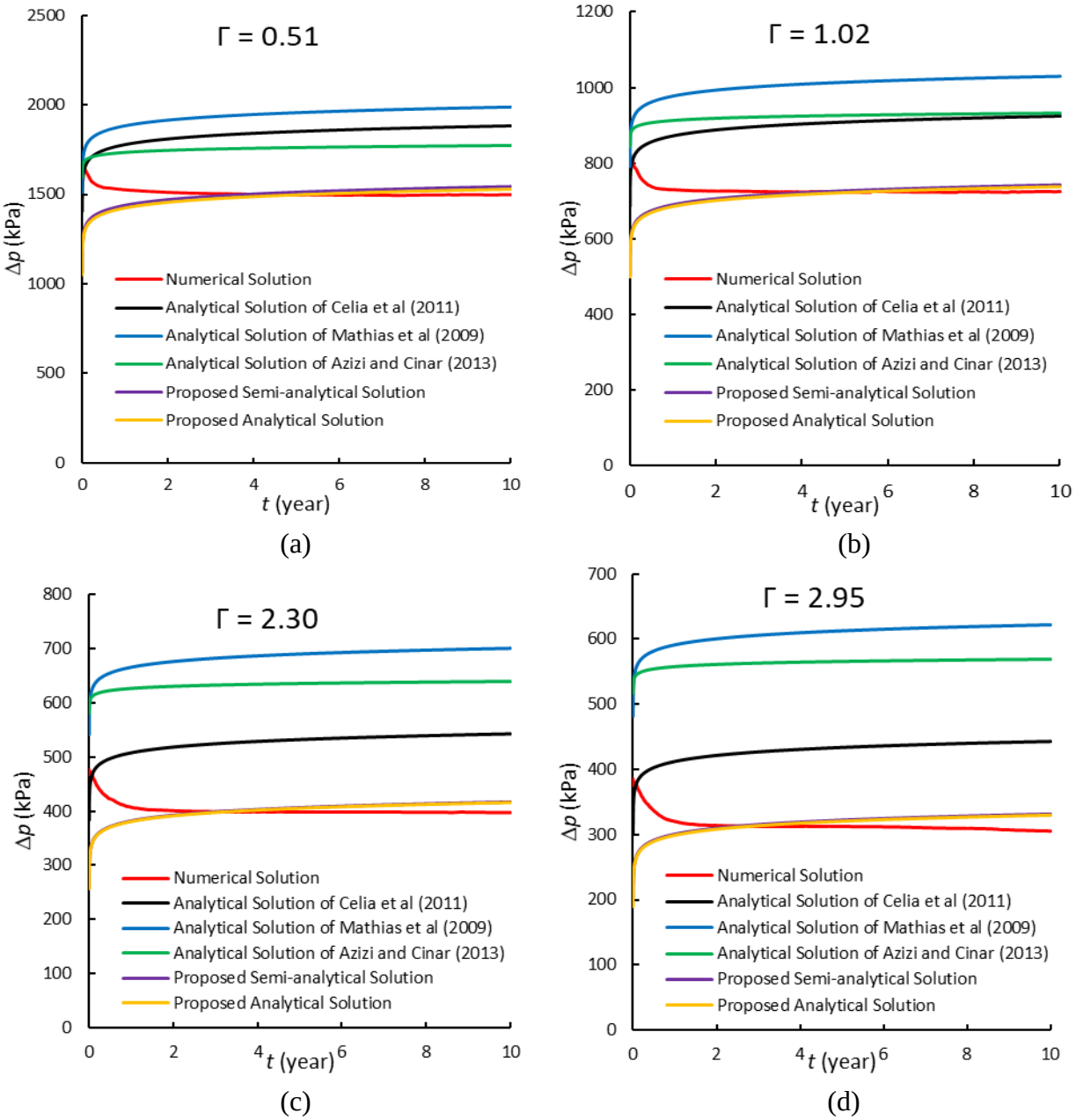

Figure 7.6. Comparison of the analytical and numerical bottomhole pressures for case 2 (M = 3.3) for gravity numbers of (a) 0.51, (b) 1.02, and (c) 2.30, and (d) 2.95

Similar to case 1, we compared the bottomhole pressures, predicted by the developed analytical solutions, against the numerical simulation results for different gravity numbers. The comparison results are displayed in Figs. 7.6 and 7.7 for case 2 and 3, respectively. Similarly, the comparison results indicate that the developed semi-analytical and analytical solutions yield good match with the numerical results. Also, the solution of Azizi and Cinar (2013a) yields less deviation as compared to Mathias et al. (2009) and Celia et al. (2011)'s solution at low gravity number. On the other hand, at higher gravity numbers, Celia et al. (2011)'s solution shows the least deviation among them. Over the whole range of gravity numbers, the solution of Mathias et al. (2009) shows the highest deviation among other analytical solutions as noted.

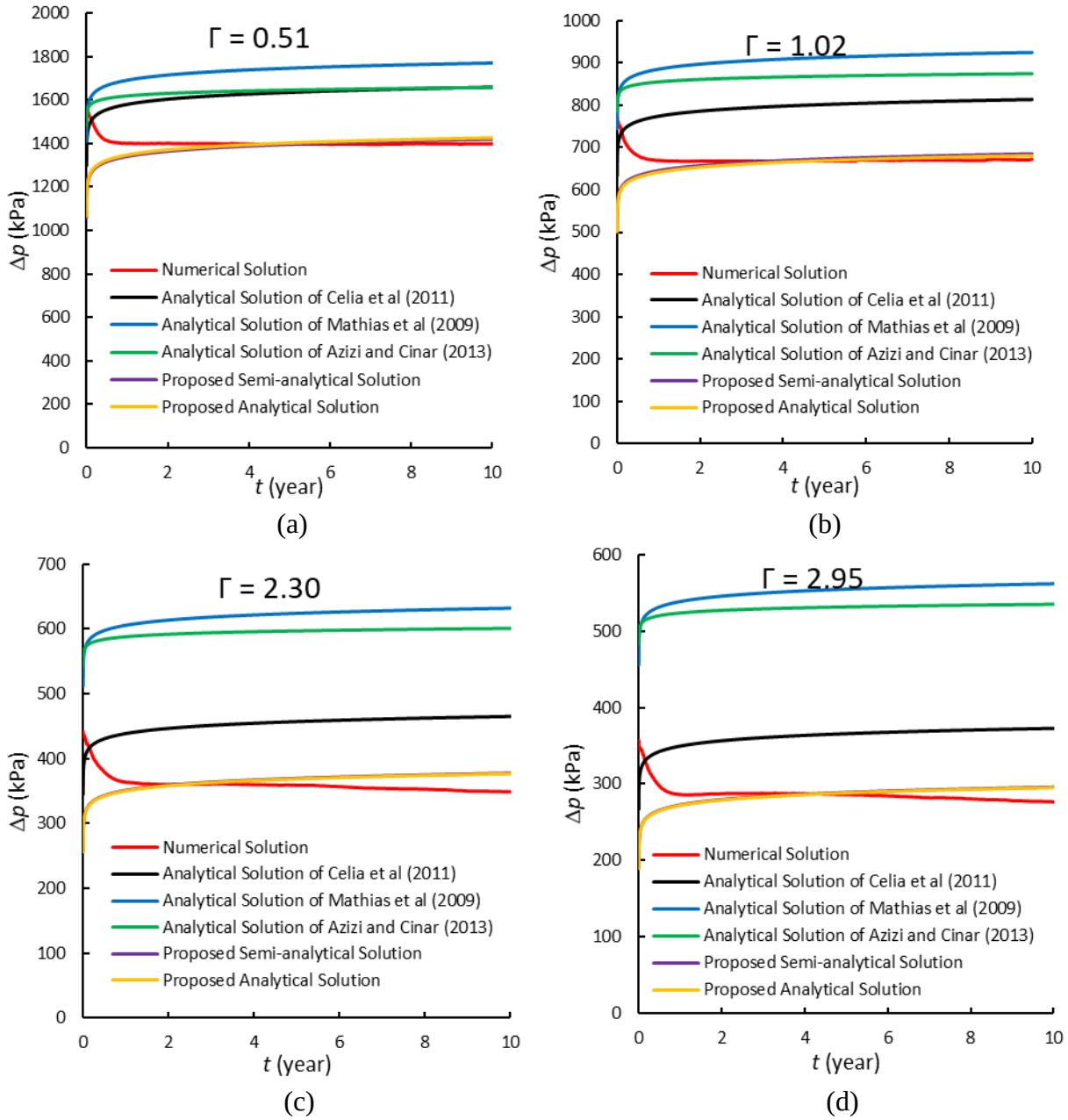

Figure 7.7. Comparison of the analytical and numerical bottomhole pressures for case 3 (M = 4.4) for gravity numbers of (a) 0.51, (b) 1.02, (c) 2.30 and (d) 2.95

7.2.3. Case 4: High Mobility Ratios

In case 4, the effect of increasing the mobility ratio is further investigated. A higher mobility ratio of 6.0 is adopted by setting the CO_2 end-point relative permeability at 0.67. All other rock and fluid properties are kept identical to case 1 given in Table 7.1. A note that, for this case, simulating gravity numbers higher than 2.30 shows numerical instability for the model setup presented herein. Therefore, for this case, we compared the analytically-estimated bottomhole pressures against the numerical simulation results for gravity numbers of 0.5, 1.0, and 2.30.

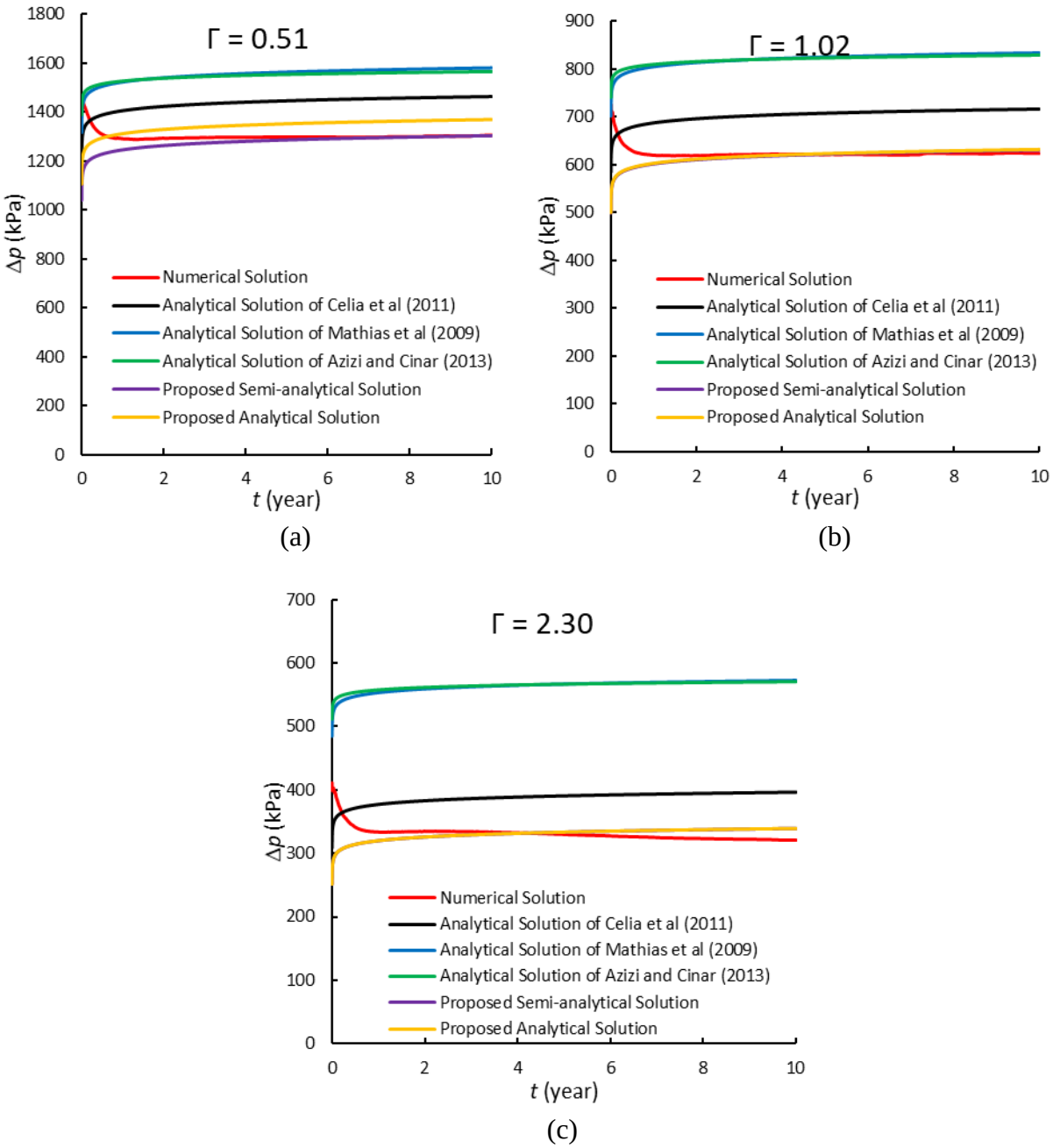

Figure 7.8. Comparison of the analytical and numerical bottomhole pressures for case 4 (M = 6.0) for gravity numbers of (a) 0.51, (b) 1.02, and (c) 2.30

The comparisons are shown in Fig. 7.8. Similar to the previous cases, the bottomhole pressures predicted by the developed analytical and semi-analytical solutions are in reasonable agreement with the numerical results. Also, for all gravity numbers, Mathias et al. (2009)'s solution exhibits the highest deviation among other solutions. Unlike the previous cases, the solution of Celia et al. (2011) shows the least deviation against the numerical results and the developed solutions over the whole range of gravity numbers. This is unlike the previous cases where the solution of Azizi and Cinar (2013a) yields better match at low gravity numbers. This behavior is expected given that higher mobility ratios compensate for low gravity numbers which causes the displacement to be more gravity-driven even at low gravity numbers.

7.3. Field Application

We validate the developed analytical and semi-analytical models against bottomhole pressure data obtained from Frio-I pilot project (Hovorka et al., 2006). Frio-I is a pilot research project conducted at the South Liberty oil field in Dayton, Texas (Doughty et al., 2007). The test was performed in September 2004, and it lasted for about 10 days over which 1600 metric tons of CO_2 were injected into 1500-m deep brine-saturated sandstone formation. CO_2 was injected into 23-m thick sand layer referred to as "C Sandstone" at an average injection rate of about 40 US gallons per minute. During the test, 4 short shut-in periods were observed, of which one was performed to conduct a falloff test. The top of the perforated interval occurs at a depth of 1540 m, and pre-CO_2 injection testing indicated high quality sandstone with an average permeability and porosity of 2100 mD and 0.34, repevtively (see Fig. 7.9). The histroy of injection rate and the bottomhole pressure is plotted in Fig. 7.10 below. The injection bottomhole pressure and rate data were obtained from the DOE/NETL Energy Data eXchange website (EDX, 2018).

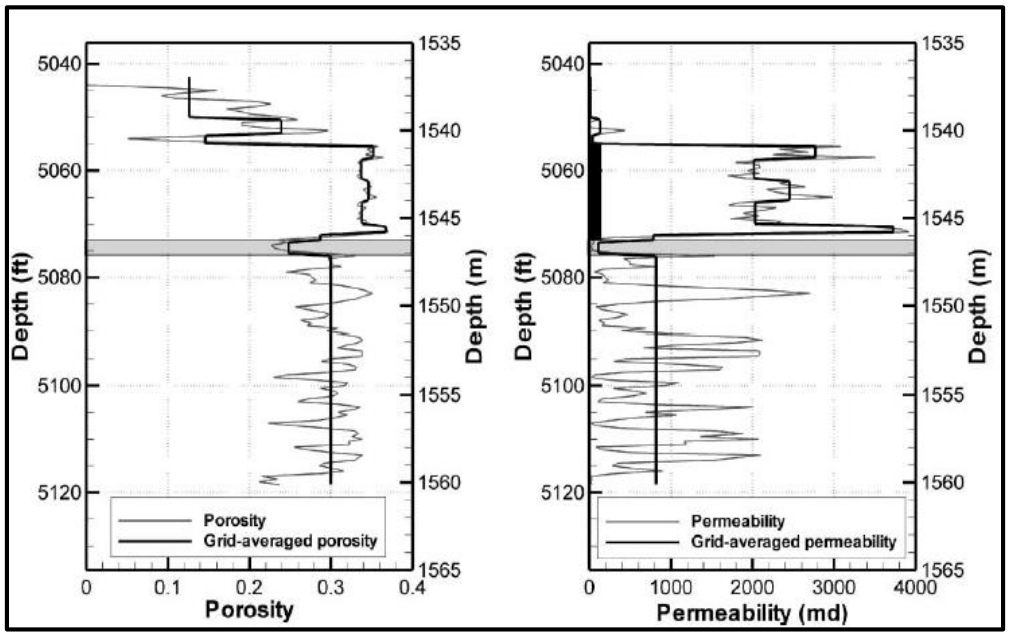

Figure 7.9. Porosity and permeability of the Frio C sandstone (Hovorka et al., 2006)

In addition to the above injection history, some other reservoir parameters (e.g., fluid viscosities and densities) are required to validate the developed analytical models. The initial pressure and temperature of the storage formation are 14.8 MPa and 57 ^{o}C respectively (Doughty et al., 2007). At these reservoir conditions, CO_2 exists in supercritical state with 629 kg/m^3 density and 0.04832 cp viscosity. The density and viscoisty of brine - evaluated at the reservoir conditions - are 991 kg/m^3 and 0.4902 cp resepectively The relative permeability data – required to calculate the mobility ratio, and to solve Azizi and Cinar (2013a)'s model for validation - is generated using Corey's model. The residual brine saturation is set at 0.25, Corey's expenents at 2.0 for CO_2 and 4.0 for brine, and the end-point relative permeabilities are 1.0 for brine and 0.25 for CO_2. The same properties were used by Zeidouni (2023) in analyzing Frio-I pressure interference data. With this, the gravity number is calculated to be 2.0 and the mobility ratio is 2.5. This indicates the less-dominant gravity flow due to the relatively thin target formation (i.e. 23 m).

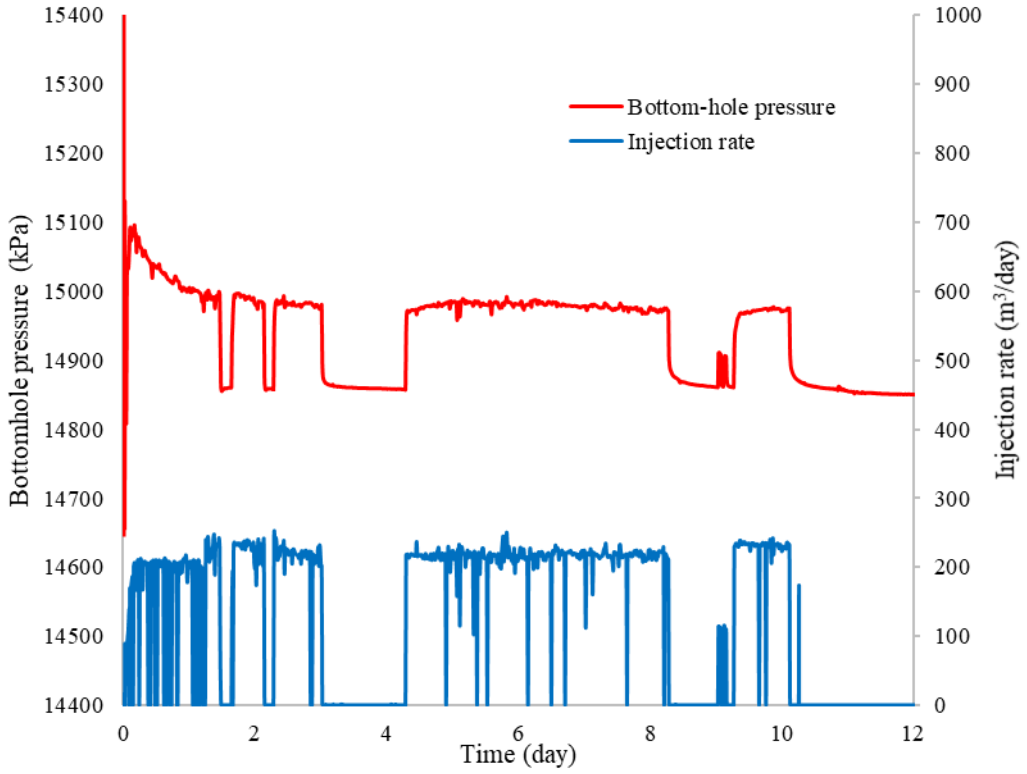

Figure 7.10. Bottomhole injection pressure and rate data for the Frio pilot test

The validation results - shown in Fig. 7.11 - indicate that the proposed analytical/semi-analytical solutions approximately match the trend of the bottomhole pressure of Frio-I pilot test. Literature models overstimate the stabilized bottomhole pressure, as expected. A note that the early-time transient flow period is clearly observed in the field data. This confirms the discrepancy between analytical solutions and the simulation/field data at early-time. However, our proposed analytical model matches the stabilized behavior. This substantiates the validity to predict the time-evolution of the bottomhole injection pressure over practical gravity numbers and mobility ratios.

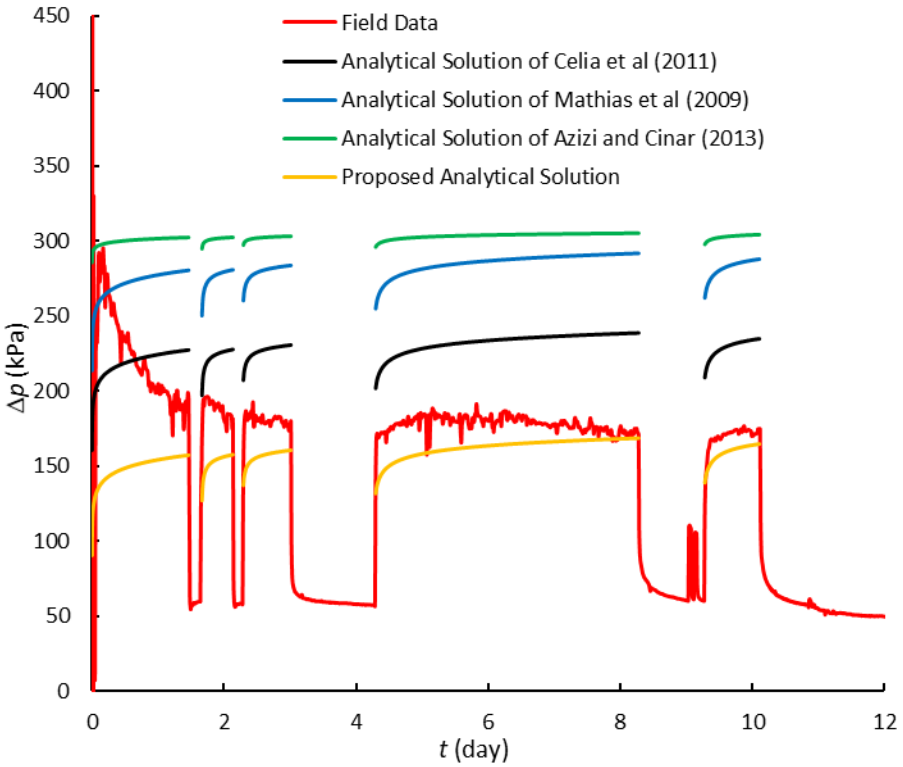

Figure 7.11. Comparison of the analytical/semi-analytical models with the bottomhole pressures obtained from Frio-I pilot test

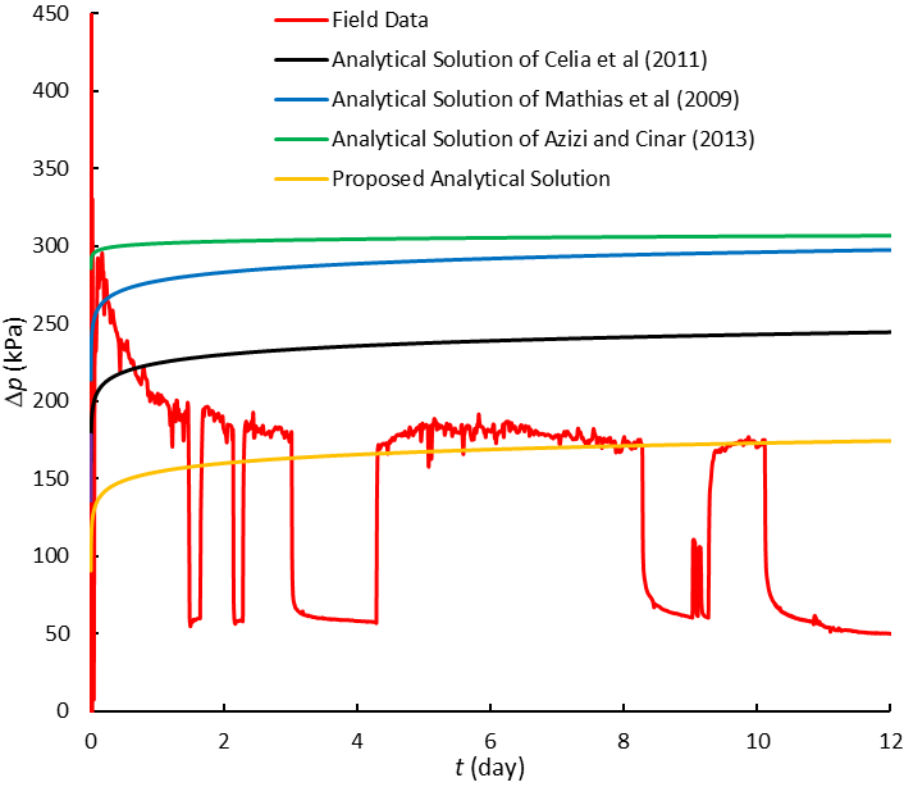

Figure 7.12. Comparison of the analytical/semi-analytical models – while neglecting the shut-in periods - with the bottomhole pressures obtained from Frio-I pilot test

As we mentioned before, four short shut-ins were observed during the Frio-I pilot operations. The first two were due to occasional shut-downs, and they lasted for less than two hours. The other two were performed to conduct pressure transient tests (e.g., falloff testing). Application of the analytical solutions while negelcting the shut-in periods is shown in Fig. 7.12. Similarly, the comparison with the field data shows that the proposed model yields the best match with the recorded bottomhole pressures as compared to the analytical models reported in the literature. Neverthless, in cases with extended shut-in periods, this may not work, and the shut-in periods should be eliminated as indicated in Fig. 7.11.

Chapter 8. Conclusions and Recommendations

The main scope of this research study is to use pressure and rate transient analyses techniques to (1) characterize the dry-out zone and CO_2 plume for the purpose of assessing CO_2 injectivity, and constraining the injected CO_2 within the designated storage formation through analyzing the falloff pressure data, and (2) infer the pore volume and the ultimate storage capacity of a closed storage formation through interpreting the available injection pressure and rate data history. Additionally, this work is aimed at investigating the different parameters that affect the injectivity behavior, and subsequent storage capacity of a target saline formation. This is achieved through (1) investigating the operating conditions of the injection well for the purpose of articulating the best strategy that maximizes the volumetric and economic value of a fixed pore space devoted for CO_2, (2) studying the net effect and the interplay between the physical processes that control the distribution of CO_2 along the injection interval of a high-gravity storage complex, and (3) developing an analytical model to predict the overpressure, and accounts for strong gravity effects. The goal is to optimize CO_2 injectivity while protecting the geomechanical integrity of the formation rock. An overview of the latest studies relevant to the objectives of our study are introduced. Then, research objectives are set to fill the research gaps drawn from the literature, and the following conclusions are drawn from the results:

8.1. Pressure Falloff Testing to Characterize CO_2 Plume and Dry-Out Zone during CO_2 Injection in Deep Saline Formations

A graphical interpretation technique is developed to infer the fluids' mobilities and radial extents of the dry-out zone and CO_2 plume. The methodology is based on a three-region analytical solution developed to represent the pressure behavior during a pause during CO_2 injection through a fully-penetrating vertical well into a single-layer infinite-acting aquifer. The unknowns are inferred via analyzing the transient pressure and time responses recorded/measured during a falloff test. The interpretation technique involves plotting the shut-in pressure versus the corresponding shut-in time on a semi-log scale. Straight line behaviors should be observed corresponding to the three zones of saturation within the aquifer. Based on the approximate solutions of the analytical model, mobilities of the fluids within the dry-out and two-phase zones are obtained from the slope of the straight line. The radial extents of the dry-out zone and the plume are obtained via manipulating the *y*-intercepts and the approximate solutions of the analytical model. The potential application of the interpretation technique is tested against synthetic data conducted considering a single-layer infinite-acting aquifer. Limitations of the analytical solution are addressed through testing the effects of gravity override, closed aquifer's outer boundaries, formation dip angle, anisotropy of horizontal permeability, variable injection rate during the period that precedes the falloff test, linear/channeled reservoirs, and long/short injection periods. Moreover, the robustness of the interpretation technique is substantiated through application to real field datasets obtained from commercial-scale GCS projects. Additionally, this work provides practical implications needed to design falloff tests in CO_2/brine systems. The design guidelines are (1) the effects of wellbore storage, (2) movement of CO_2/brine interface during shut-in, (3) rate fluctuations and/or shut-downs. Violation of these guidelines can lead to inability to apply the interpretation technique in interpreting falloff tests. For example, the WBS effect should be eliminated while conducting the test, or it could otherwise mask the early-time pressure responses required for the interpretation.

8.2. Injection Data Analysis to Estimate the Ultimate Storage Capacity of Deep Closed Saline Formations

A two-step analytical graphical interpretation technique is developed to (1) infer the pore volume of closed aquifers, and (2) estimate the ultimate storage capacity. These unknowns are obtained through analyzing the injection pressure, rate, and cumulative volume data routinely measured as part of storage projects' surveillance. On a log-log diagnostic plot of the rate-normalized pressure buildup versus material balance time, wells operating at any pressure/rate schedule should show a unit-slope line behavior during the BDF period. The corresponding data points show a straight line behavior on Cartesian scale. The pore volume is obtained from the slope of the straight line. Then, the ultimate storage capacity is estimated by extrapolating the aquifer average pressure ($\bar{p}$) to the maximum allowable injection pressure. The average pressure is not available in practice, but it can be calculated from the injection rate and pressure data using material balance techniques. Two approaches have been presented to calculate $\bar{p}$; namely the rigorous and approximate approaches. The potential application of the graphical interpretation technique is tested against four synthetic cases representing injection wells operating at different conditions. The first case is a benchmark case where the well is assigned a constant rate of injection. The remaining three cases simulate wells operating at a constant bottomhole pressure, variable injection rate with and without shut-ins. On a log-log diagnostic plot of the rate-normalized pressure buildup versus material balance time, all the cases show a unit-slope line behavior during the BDF period. This observation validates the usefulness of material balance time to interpret pressure and rate data of variable schedules. The interpretation results show that the reservoir pore volume can be accurately inferred by fitting the data points, which correspond to the BDF period, on a Cartesian scale. The ultimate storage capacity can be estimated through extrapolating the calculated average pressure to the maximum allowable injection pressure. Results show that the estimated storage capacities, using both the rigorous and the approximate approaches, are in good match with the numerically estimated values. Nevertheless, the approximate approach consistently overestimates the predicted storage capacity as compared to the rigorous approach and the simulated values. This is attributed to the assumption that the time-dependent term (b_r) is kept fixed in calculating the average pressure. However, b_r continues to decrease, although at very slow rate, before reaching the quasi-steady state (stabilization) during the BDF period. Application of the graphical technique to a field dataset - obtained from GCS projects – shows a semi-unit slope line behavior on the diagnostic plot. This indicates that not all storage systems would behave as purely closed systems.

8.3. Effects of Injection Well Operation Conditions on the Injectivity and Subsequent Ultimate Storage Capacity of CO_2 in Deep Saline Aquifers

In practice, the operating condition of the injection well is controlled by the rate fluctuations of the CO_2 stream. Therefore, the effect of continuous and intermittent CO_2 injection is evaluated in terms of the injectivity index and its potential impact on the ultimate capacity. For injection at a constant terminal rate (CR), we assigned a constant rate of injection equal to 0.5 Mt/year. Injection ceases when the bottomhole pressure buildup reaches the maximum allowable pressure the formation can withstand. For injection at a constant terminal pressure (CP), we assigned a constant bottomhole injection pressure equal to the maximum allowable pressure. Injection ceases when the injection rate reaches its economic limit. The ultimate capacity is found to be improved for the

CP case for both continuous and intermittent injections compared to the CR case. This can be attributed to the higher mobility CO_2 dry-out zone that has been created soon after staring injection during CP injection compared to the relatively small zone formed over the same period during CR injection. The economic feasibility of different injection schemes is also investigated through a simple NPV analysis. Results show that injecting CO_2 as fast as possible either continuously (or intermittently) is preferred over continuously (or intermittently) injecting at a constant rate. For the cases presented herein, more than 229 million US$ (5.2 equivalent Mt of CO_2) can be saved when injecting continuously at CP rather than intermittently at CR. The same analysis is applied to an example GCS project with injection rate history. The effect of well operating condition, on the ultimate storage capacity and NPV of ongoing GCS projects, is significant. Specifically, injecting CO_2 as fast as possible can increase the ultimate storage capacity more than CR injection. For the case studied herein, the intermittent injection at CP can save 72 million US$ (1.6 equivalent Mt of CO_2) more than intermittent injection at CR. Overall, analysis show that the preferentiality of CO_2 injection can be arranged as: 1) continuous injection at a constant-terminal pressure, 2) intermittent injection at a constant-terminal pressure, 3) continuous injection at a constant-terminal rate, and 4) intermittent injection at a constant-terminal rate. In addition, a sensitivity analysis was performed to test the effect of varying the injection rate, the vertical permeability, the formation dip angle, outer boundary condition, and well penetration on the storage capacity for both injection schemes. Results show that there should be an economically optimum injection rate which maximizes the NPV and the equivalent ultimate storage capacity of the formation. Also, injection in dipping formations causes asymmetric distribution of CO_2 plume which decreases the ultimate storage capacity. In addition, we found when the vertical permeability is higher, the positive effect of improving the system permeability dominates over the negative effect that can arise due to higher buoyancy. Injection in open systems was found to have a significant impact on the storage potential and NPV analysis. Also, injection in a fully-penetrating well was found desirable in terms of the storage capacity, and it should be adopted whenever leakage risk is minimal. In all the simulation cases, injecting CO_2 as fast as possible (i.e. at CP conditions) improves the equivalent ultimate capacity of the formation, and increases the NPV of the project.

8.4. Coupled Wellbore-Reservoir Modeling to Evaluate CO_2 Flow Rate Distribution over Thick Storage Saline Aquifers

Maximizing the amount of stored CO_2 per unit pore space of the storage zone per well is required. Considering injection through a fully penetrating vertical well in a multi-layer thick aquifer, CO_2 would be unevenly distributed over the aquifer thickness, underutilizing the available pore space. Therefore, in this work, we investigate the net effect and the interplay between different physical processes/parameters that control the CO_2 flux distribution in high-gravity thick aquifers. This includes: (1) movement of CO_2/brine interface within the wellbore, (2) buoyancy/gravity override, (3) difference in the hydrostatic pressure gradient between the CO_2-filled wellbore and the brine-saturated aquifer, (4) individual layer flow capacities, (5) temporal change in the effective/average mobility of fluids within the layers, and (6) backflow of brine into the wellbore. To account for the wellbore physics, heat exchange, and wellbore-reservoir interactions, we coupled the reservoir model with a wellbore model introduced using STARS-FlexWell. Results show that movement of the CO_2/brine interface has insignificant effect on the CO_2 flow rate distribution. This is because complete flushing of brine from the wellbore takes place within very short time after the start of

injection. For the cases studied in this work, the flushing time ranges from 1.75 hr to 15.8 hr depending on model setup. Flushing is slower when buoyancy is strong and/or higher flow capacity at the upper layers which promote higher flow rates through them, and as a result, slower wellbore fill-up. In addition, results show that when buoyancy is insignificant, the flow rate distribution is viscous-driven, and primarily controlled by (1) pressure difference between the wellbore and the aquifer and (2) layers' flow capacities. The pressure difference generally permits higher rates into the shallower layers as compared to the deeper ones. Nevertheless, its effect can be muted if higher flow capacity layers are at shallower depths, and amplified if the higher capacity layers are at the bottom of perforated interval. When buoyancy is significant, the early-time viscous-dominant flow quickly turns into gravity-dominant flow making preferential CO_2 flow into the upper layers. Therefore, strong buoyancy can underutilize the bottom layers while possibly completely shutting off some bottom perforations. In this case, CO_2 that advances at the top layers pushes brine back into the wellbore through the shut-off perforations, triggering brine backflow. Also, brine backflow is found to have insignificant impact on flow rate profile for continuous injection. However, for elongated shut-in periods, brine backflow can introduce higher salinities around the wellbore, and therefore, cause higher permeability reductions due to additional salt dry-out.

In addition, we investigated the effect of the injection rate on brine displacement by CO_2 in the wellbore. Our analysis shows that CO_2/brine interface would stabilize at shallower depths and may not reach the bottom of the injection interval over the whole injection period when the injection rate is low. This could result in further underutilization of the bottom perforations. As a result, injection at higher rates, whenever possible, is preferable for maximizing injectivity. In addition, we showed that decoupled wellbore-reservoir modeling can cause slight deviations in reproducing the results of the coupled model. This is mainly attributed to the physical processes which cannot be simulated using sink/source wells. The deviation is insensible when steady-state flow conditions are achieved faster within the wellbore (e.g. due to strong viscous forces). On the other hand, the deviation is more observed when the transient flow behavior within the wellbore plays a more important role such that the deviations arising from neglecting some wellbore physics can be exaggerated (e.g. due to strong viscous forces).Therefore, wellbore-reservoir coupling is strongly recommended when modeling CO_2 injection. Results also show that the presence of semi-pervious overlying/underlying formations has no/slight effect on the flow rate distribution. However, it can affect the magnitudes of the flow rate because of the different modeling setup, as expected.

8.5. Evolution of Overpressure in High-Gravity Storage Saline Formations

While accounting for the effects of strong gravity forces, an analytical solution is developed to predict the bottomhole pressure during CO_2 injection through a fully penetrating vertical well centered in the middle of a high-gravity infinite-acting saline aquifer. The solution is developed by analytically solving ODEs introduced by other works in the literature. In these works, the following assumptions were introduced to linearize the governing equations: (1) the system is homogeneous, (2) the system is isotropic, and (3) the fluid properties are constant temporally and spatially which requires isothermal flow conditions. Then, the linearized governing equation is approximated by an ODE through considering (5) vertical equilibrium of pressure, (6) negligible capillary pressure that the transition between CO_2 and brine can be approximated by a sharp interface, (7) no mutual dissolution between CO_2 and brine, (8) only residual brine saturation exists

in the CO_2-rich phase region behind the interface, and (9) the reservoir is saturated with brine ahead of the interface. A note that the assumption of negligible mutual dissolution means that the densities of CO_2 and brine in the analytical model, respectively, represent the densities of the single-phase CO_2 and brine evaluated at reservoir conditions. In other words, behind the interface, the gaseous phase is 100 % CO_2 and, ahead of the interface, the aqueous phase is 100 % brine. In addition, the assumption of negligible capillary pressure is generally acceptable over large spatial scales especially in high quality reservoirs where the viscous and gravity forces play a more important role. With these aforementioned assumptions, the ODE can be solved analytically via specifying two boundary conditions and one initial condition. The boundary conditions are: (1) infinite outer boundary of the reservoir, and (2) constant rate of injection at the inner boundary (i.e., the wellbore). Uniform distribution of pressure across the reservoir is considered the initial condition. The analytical pressure solution is validated against synthetic data generated using a black-oil numerical reservoir simulator through four cases covering a wide and practical range of mobility ratios and gravity numbers. For all cases, results indicate that the developed solution is in good match with the simulated pressures. The solution is also validated against real field dataset obtained from a pilot/research GCS project to determine its robustness and practical utility. Predictions of the overpressure from our analytical solution indicate a reasonable agreement with the field data and the simulations performed using a more complicated multi-phase flow simulator. In addition, results show that the developed solution improves the available models by taking into account the effects of gravity both on the evolution of the interface and the overpressure. This would allow for more accurate estimations for CO_2 injectivity, and as a result, the subsequent storage capacity for the formation. One limitation is that the proposed solution, along with the literature models, is unable to capture the early-time transient behavior of pressure. Nevertheless, for all the cases, it matches well the stabilized behavior of pressure achieved beyond the transient-flow behavior. This is because, at the beginning of injection, CO_2 cannot override brine, and it should first displace the in-situ brine that completely saturates the near wellbore region. This requires a certain threshold pressure to displace brine by CO_2 which causes the observed pressure hump. Once the dry-out zone is formed, gravity gets effective, decreasing resistance to CO_2 flow, and hence, the pressure trend. This establishes the steady-state flow where the bottomhole pressure starts to plateau. On the other hand, the analytical models are developed assuming an already-existing CO_2 region behind the interface. That is why a discrepancy between the analytical and numerical solutions should be observed during the early-time of injection.

8.6. Recommendations for Future Work

According to the abovementioned conclusions and objectives, additional work is needed to reveal the importance of utilizing PTA and RTA in characterizing CO_2/brine systems. This is in addition to performing more investigations on the parameters that affect CO_2 injectivity. Therefore, the following is recommended as future work:

1. Inference of the gravity number using PTA/RTA techniques: storing the maximum possible amounts of CO_2 within a given storage domain is desirable. During CO_2 injection, the pore space available to accommodate CO_2 can be underutilized because of gravity override. A lower gravity number is preferred because it expresses a more uniform/cylindrical displacement of CO_2. On the other hand, biasness of CO_2 flow towards the top of the injection zone - which

translates to a larger gravity number – negatively impacts storage capacity. This means that practical estimation of the gravity number is required to measure the storage potential of a given storage zone through offering more reliable estimates of storage capacity. Moreover, the practically-inferred gravity numbers can be used as one of the selection criteria of potential storage zones. Therefore, developing an analytical procedure to infer the gravity number through analyzing the bottomhole pressure behavior during injection/falloff tests is required. Our proposed analytical model to predict the overpressure - which accounts for gravity forces - can be utilized for this purpose.

2. Revisiting the falloff interpretation technique to account for the effects of gravity override. Results of the falloff interpretation technique showed that gravity override negatively effects the estimated plume extent. This is due to the fact that the developed interpretation technique is derived considering negligible gravity forces. This situation may not be common in practice especially in thick aquifers where the gravity override – driven by the density difference between CO_2 and brine – can be amplified. Therefore, revisiting the falloff solution to account for the effect of gravity override is required.

3. Revisiting the falloff interpretation technique for well-established linear flow behavior. We applied the falloff interpretation technique to channeled reservoirs where the plume is affected by the limited extent of the reservoir in one direction. This caused the linear flow behavior to establish and slightly distort the IARF behavior required to apply the developed interpretation technique. Results showed that the IARF behavior can be still observed although for a short time and the interpretation technique can be still applied. Nevertheless, in situations where the linear flow behavior is well established and dominating (e.g., in fractured wells), the analytical solution should be revisited using the linear flow diffusivity equations. Then, an interpretation methodology can be derived accordingly.

4. Investigating the effect of injection well operating conditions on the injectivity variations and subsequent ultimate storage capacity to injection via multi-well systems. In our investigation performed as part of this work, we considered injection through a single well. Most of the time, CO_2 is injected through multiple wells to reduce the overpressure within the storage reservoir. Therefore, it could be feasible to extend our work to multi-well systems.

5. Investigating how backflow of brine would affect the salinity of around the wellbore, and hence, injectivity and storage capacity. Although we have accounted for salt dry-out around the wellbore in our modeling approaches, we did not consider how the salinity around the wellbore can be affected when backflow of brine occurs especially during elongated shut-in periods. Proper modeling of this process requires investigating how salinity around the wellbore is changed with backflow of brine which redissolves the already precipitated salt in the dry-out zone. The subsequent effect on the absolute permeability and injectivity can be then identified.

Appendix A. Derivation of the Analytical Solution to Predict the Bottomhole Pressure Behavior during Falloff

Applying Laplace transformation to Eqs. 3.1, 3.2, and 3.3 yields:

$$\frac{1}{r_D}\frac{d}{dr_D}\left(r_D\frac{d\overline{p_{D1}}}{dr_D}\right)=z\overline{p_{D1}}-g_1(r_D) \tag{A.1}$$

$$\frac{1}{r_D}\frac{d}{dr_D}\left(r_D\frac{d\overline{p_{D2}}}{dr_D}\right)=\frac{1}{F_{\lambda g}\eta_{D2}}\left(z\overline{p_{D2}}-g_2(r_D)\right) \tag{A.2}$$

$$\frac{1}{r_D}\frac{d}{dr_D}\left(r_D\frac{d\overline{p_{D3}}}{dr_D}\right)=\frac{1}{\eta_{D3}}\left(z\overline{p_{D3}}-g_3(r_D)\right) \tag{A.3}$$

Applying Laplace transformation to the boundary conditions (Eqs. 3.14 through 3.19) yields:

$$r_D\frac{d\overline{p_{D1}}}{dr_D}=0,\quad r_D\to 0 \tag{A.4}$$

$$\overline{p_{D1}}=\overline{p_{D2}},\quad r_D=r_{Ddry} \tag{A.5}$$

$$\frac{d\overline{p_{D1}}}{dr_D}=F_{\lambda g}\frac{d\overline{p_{D2}}}{dr_D},\quad r_D=r_{Ddry} \tag{A.6}$$

$$\overline{p_{D2}}=\overline{p_{D3}},\quad r_D=r_{DBL} \tag{A.7}$$

$$\frac{d\overline{p_{D3}}}{dr_D}=F_{\lambda w}\frac{d\overline{p_{D2}}}{dr_D},\quad r_D=r_{DBL} \tag{A.8}$$

$$\overline{p_{D3}}=0,\quad r_D\to\infty \tag{A.9}$$

Eqs. A.1 through A.3 are non-homogeneous ordinary differential equations which can be solved using the variation of parameters method (King et al., 2003). The solutions of Eqs. A.1 through A.3 can be written as:

$$\overline{p_{D1}} = AI_o\left(r_D\sqrt{z}\right) + BK_o\left(r_D\sqrt{z}\right) + K_o\left(r_D\sqrt{z}\right)\int_0^{rD} xg_1(x)\,I_o\left(x\sqrt{z}\right)dx + I_o\left(r_D\sqrt{z}\right)\int_{rD}^{rDdry} xg_1(x)\,K_o\left(x\sqrt{z}\right)dx \tag{A.10}$$

$$\overline{p_{D2}} = CI_o\left(r_D\sqrt{\frac{z}{F_{\lambda g}\eta_{D2}}}\right) + DK_o\left(r_D\sqrt{\frac{z}{F_{\lambda g}\eta_{D2}}}\right) + \frac{1}{F_{\lambda g}\eta_{D2}}K_o\left(r_D\sqrt{\frac{z}{F_{\lambda g}\eta_{D2}}}\right) \times \int_{rDdry}^{rD} xg_2(x)\,I_o\left(x\sqrt{\frac{z}{F_{\lambda g}\eta_{D2}}}\right)dx + \frac{1}{F_{\lambda g}\eta_{D2}}I_o\left(r_D\sqrt{\frac{z}{F_{\lambda g}\eta_{D2}}}\right)\int_{rD}^{rDBL} xg_2(x)\,K_o\left(x\sqrt{\frac{z}{F_{\lambda g}\eta_{D2}}}\right)dx \tag{A.11}$$

$$\overline{p_{D3}} = EI_o\left(r_D\sqrt{\frac{z}{\eta_{D3}}}\right) + FK_o\left(r_D\sqrt{\frac{z}{\eta_{D3}}}\right) + \frac{1}{\eta_{D3}}K_o\left(r_D\sqrt{\frac{z}{\eta_{D3}}}\right) \times \int_{rDBL}^{rD} xg_3(x)\,I_o\left(x\sqrt{\frac{z}{\eta_{D3}}}\right)dx + \frac{1}{\eta_{D3}}I_o\left(r_D\sqrt{\frac{z}{\eta_{D3}}}\right)\int_{rD}^{\infty} xg_3(x)\,K_o\left(x\sqrt{\frac{z}{\eta_{D3}}}\right)dx \tag{A.12}$$

where x is an arbitrary variable of integration and z is the time variable in Laplace domain. After applying the boundary conditions of Eqs. A.4 through A.9 to obtain the values of the coefficients A, B, C, D, E, and F, the solutions of Eqs. A.1 through A.3 in Laplace domain are given by:

$$\overline{p_{D1}} = AI_o\left(r_D\sqrt{z}\right) + K_o\left(r_D\sqrt{z}\right)\int_0^{rD} xg_1(x)\,I_o\left(x\sqrt{z}\right)dx + I_o\left(r_D\sqrt{z}\right)\int_{rD}^{rDdry} xg_1(x)\,K_o\left(x\sqrt{z}\right)dx \tag{A.13}$$

$$\overline{p_{D2}} = CI_o\left(r_D\sqrt{\frac{z}{F_{\lambda g}\eta_{D2}}}\right) + DK_o\left(r_D\sqrt{\frac{z}{F_{\lambda g}\eta_{D2}}}\right) + \frac{1}{F_{\lambda g}\eta_{D2}}\int_{rDdry}^{rD} xg_2(x)\,K_o\left(r_D\sqrt{\frac{z}{F_{\lambda g}\eta_{D2}}}\right) \times I_o\left(x\sqrt{\frac{z}{F_{\lambda g}\eta_{D2}}}\right)dx + \frac{1}{F_{\lambda g}\eta_{D2}}\int_{rD}^{rDBL} xg_2(x)\,K_o\left(x\sqrt{\frac{z}{F_{\lambda g}\eta_{D2}}}\right)I_o\left(r_D\sqrt{\frac{z}{F_{\lambda g}\eta_{D2}}}\right)dx \tag{A.14}$$

$$\overline{p_{D3}} = FK_o\left(r_D\sqrt{\frac{z}{\eta_{D3}}}\right) + \frac{1}{\eta_{D3}}\int_{rDBL}^{rD} xg_3(x)\,K_o\left(r_D\sqrt{\frac{z}{\eta_{D3}}}\right)I_o\left(x\sqrt{\frac{z}{\eta_{D3}}}\right)dx + \frac{1}{\eta_{D3}}\int_{rD}^{\infty} xg_3(x)\,K_o\left(x\sqrt{\frac{z}{\eta_{D3}}}\right)I_o\left(r_D\sqrt{\frac{z}{\eta_{D3}}}\right)dx \tag{A.15}$$

where:

$$A=\frac{1}{I_o\left(r_{Ddry}\sqrt{z}\right)}\left[l_1+\frac{I_o\left(r_{Ddry}\sqrt{\frac{z}{F_{\lambda g}\eta_{D2}}}\right)M+K_o\left(r_{Ddry}\sqrt{\frac{z}{F_{\lambda g}\eta_{D2}}}\right)L}{W}\right] \tag{A.16}$$

$$F=\frac{1}{K_o\left(r_{DBL}\sqrt{\frac{z}{\eta_{D3}}}\right)}\left[-l_2+\frac{I_o\left(r_{DBL}\sqrt{\frac{z}{F_{\lambda g}\eta_{D2}}}\right)M+K_o\left(r_{DBL}\sqrt{\frac{z}{F_{\lambda g}\eta_{D2}}}\right)L}{W}\right] \tag{A.17}$$

$$C=\frac{M}{W} \tag{A.18}$$

$$D=\frac{L}{W} \tag{A.19}$$

$$\begin{aligned}W=&\left[-\sqrt{\frac{F_{\lambda g}}{\eta_{D2}}}I_1\left(r_{Ddry}\sqrt{\frac{z}{F_{\lambda g}\eta_{D2}}}\right)+\frac{I_1\left(r_{Ddry}\sqrt{z}\right)}{I_o\left(r_{Ddry}\sqrt{z}\right)}I_o\left(r_{Ddry}\sqrt{\frac{z}{F_{\lambda g}\eta_{D2}}}\right)\right]\\&\times\left[-F_{\lambda w}\sqrt{\frac{1}{F_{\lambda g}\eta_{D2}}}K_1\left(r_{DBL}\sqrt{\frac{z}{F_{\lambda g}\eta_{D2}}}\right)+\frac{\sqrt{\frac{1}{\eta_{D3}}}K_1\left(r_{DBL}\sqrt{\frac{z}{\eta_{D3}}}\right)}{K_o\left(r_{DBL}\sqrt{\frac{z}{\eta_{D3}}}\right)}K_o\left(r_{DBL}\sqrt{\frac{z}{F_{\lambda g}\eta_{D2}}}\right)\right]\\&-\left[\frac{\sqrt{\frac{1}{\eta_{D3}}}K_1\left(r_{DBL}\sqrt{\frac{z}{\eta_{D3}}}\right)}{K_o\left(r_{DBL}\sqrt{\frac{z}{\eta_{D3}}}\right)}I_o\left(r_{DBL}\sqrt{\frac{z}{F_{\lambda g}\eta_{D2}}}\right)+F_{\lambda w}\sqrt{\frac{1}{F_{\lambda g}\eta_{D2}}}I_1\left(r_{DBL}\sqrt{\frac{z}{F_{\lambda g}\eta_{D2}}}\right)\right]\\&\times\left[\sqrt{\frac{F_{\lambda g}}{\eta_{D2}}}K_1\left(r_{Ddry}\sqrt{\frac{z}{F_{\lambda g}\eta_{D2}}}\right)+\frac{I_1\left(r_{Ddry}\sqrt{z}\right)}{I_o\left(r_{Ddry}\sqrt{z}\right)}K_o\left(r_{Ddry}\sqrt{\frac{z}{F_{\lambda g}\eta_{D2}}}\right)\right]\end{aligned} \tag{A.20}$$

$$
\begin{aligned}
M = & \left[-F_{\lambda w}\sqrt{\frac{1}{F_{\lambda g}\eta_{D2}}}K_1\left(r_{DBL}\sqrt{\frac{z}{F_{\lambda g}\eta_{D2}}}\right)+\frac{\sqrt{\frac{1}{\eta_{D3}}}K_1\left(r_{DBL}\sqrt{\frac{z}{\eta_{D3}}}\right)}{K_o\left(r_{DBL}\sqrt{\frac{z}{\eta_{D3}}}\right)}K_o\left(r_{DBL}\sqrt{\frac{z}{F_{\lambda g}\eta_{D2}}}\right)\right] \\
& \times\left[l_3-\frac{I_1\left(r_{Ddry}\sqrt{z}\right)}{I_o\left(r_{Ddry}\sqrt{z}\right)}l_1\right] \\
& +\left[-\frac{I_1\left(r_{Ddry}\sqrt{z}\right)}{I_o\left(r_{Ddry}\sqrt{z}\right)}K_o\left(r_{Ddry}\sqrt{\frac{z}{F_{\lambda g}\eta_{D2}}}\right)-\sqrt{\frac{F_{\lambda g}}{\eta_{D2}}}K_1\left(r_{Ddry}\sqrt{\frac{z}{F_{\lambda g}\eta_{D2}}}\right)\right] \\
& \times\left[l_4+\frac{\sqrt{\frac{1}{\eta_{D3}}}K_1\left(r_{DBL}\sqrt{\frac{z}{\eta_{D3}}}\right)}{K_o\left(r_{DBL}\sqrt{\frac{z}{\eta_{D3}}}\right)}l_2\right]
\end{aligned}
\tag{A.21}
$$

$$
\begin{aligned}
L = & \left[-\sqrt{\frac{F_{\lambda g}}{\eta_{D2}}}I_1\left(r_{Ddry}\sqrt{\frac{z}{F_{\lambda g}\eta_{D2}}}\right)+\frac{I_1\left(r_{Ddry}\sqrt{z}\right)}{I_o\left(r_{Ddry}\sqrt{z}\right)}I_o\left(r_{Ddry}\sqrt{\frac{z}{F_{\lambda g}\eta_{D2}}}\right)\right] \\
& \times\left[l_4+\frac{\sqrt{\frac{1}{\eta_{D3}}}K_1\left(r_{DBL}\sqrt{\frac{z}{\eta_{D3}}}\right)}{K_o\left(r_{DBL}\sqrt{\frac{z}{\eta_{D3}}}\right)}l_2\right]-\left[l_3-\frac{I_1\left(r_{Ddry}\sqrt{z}\right)}{I_o\left(r_{Ddry}\sqrt{z}\right)}l_1\right] \\
& \times\left[\frac{\sqrt{\frac{1}{\eta_{D3}}}K_1\left(r_{DBL}\sqrt{\frac{z}{\eta_{D3}}}\right)}{K_o\left(r_{DBL}\sqrt{\frac{z}{\eta_{D3}}}\right)}I_o\left(r_{DBL}\sqrt{\frac{z}{F_{\lambda g}\eta_{D2}}}\right)+F_{\lambda w}\sqrt{\frac{1}{F_{\lambda g}\eta_{D2}}}I_1\left(r_{DBL}\sqrt{\frac{z}{F_{\lambda g}\eta_{D2}}}\right)\right]
\end{aligned}
\tag{A.22}
$$

$$
\begin{aligned}
l_1 = & -K_o\left(r_{Ddry}\sqrt{z}\right)\int_0^{rDdry} xg_1(x)I_o\left(x\sqrt{z}\right)dx \\
& +\frac{1}{F_{\lambda g}\eta_{D2}}I_o\left(r_{Ddry}\sqrt{\frac{z}{F_{\lambda g}\eta_{D2}}}\right)\int_{rDdry}^{rDBL} xg_2(x)K_o\left(x\sqrt{\frac{z}{F_{\lambda g}\eta_{D2}}}\right)dx
\end{aligned}
\tag{A.23}
$$

$$l_2 = -\frac{1}{F_{\lambda g}\eta_{D2}} K_o\left(r_{DBL}\sqrt{\frac{z}{F_{\lambda g}\eta_{D2}}}\right)\int_{rDdry}^{rDBL} xg_2(x) I_o\left(x\sqrt{\frac{z}{F_{\lambda g}\eta_{D2}}}\right)dx + \frac{1}{\eta_{D3}} I_o\left(r_{DBL}\sqrt{\frac{z}{\eta_{D3}}}\right)\int_{rDBL}^{\infty} xg_3(x) K_o\left(x\sqrt{\frac{z}{\eta_{D3}}}\right)dx \quad \text{(A.24)}$$

$$l_3 = K_1\left(r_{Ddry}\sqrt{z}\right)\int_0^{rDdry} xg_1(x) I_o\left(x\sqrt{z}\right)dx + \sqrt{\frac{1}{F_{\lambda g}\eta_{D2}{}^3}} I_1\left(r_{Ddry}\sqrt{\frac{z}{F_{\lambda g}\eta_{D2}}}\right)\int_{rDdry}^{rDBL} xg_2(x) K_o\left(x\sqrt{\frac{z}{F_{\lambda g}\eta_{D2}}}\right)dx \quad \text{(A.25)}$$

$$l_4 = \frac{F_{\lambda w}}{F_{\lambda g}\eta_{D2}}\sqrt{\frac{1}{F_{\lambda g}\eta_{D2}}} K_1\left(r_{DBL}\sqrt{\frac{z}{F_{\lambda g}\eta_{D2}}}\right)\int_{rDdry}^{rDBL} xg_2(x) I_o\left(x\sqrt{\frac{z}{F_{\lambda g}\eta_{D2}}}\right)dx + \frac{1}{\eta_{D3}}\sqrt{\frac{1}{\eta_{D3}}} I_1\left(r_{DBL}\sqrt{\frac{z}{\eta_{D3}}}\right)\int_{rDBL}^{\infty} xg_3(x) K_o\left(x\sqrt{\frac{z}{\eta_{D3}}}\right)dx \quad \text{(A.26)}$$

where I_o, K_o, I_1, and K_1 are the zero-order and the first-order modified Bessel function of the first and the second kinds respectively. The inverse Laplace of Eqs. A.13 through A.15 can be written in the following form respectively:

$$p_{D1} = \frac{1}{2\Delta t_D}\int_0^{rDdry} xg_1(x)\exp\left(-\frac{r_D^2 + x^2}{4\Delta t_D}\right) I_o\left(\frac{xr_D}{2\Delta t_D}\right)dx + \mathcal{L}^{-1}\left[AI_o\left(r_D\sqrt{z}\right)\right] \quad \text{(A.27)}$$

$$p_{D2} = \frac{1}{2F_{\lambda g}\eta_{D2}\Delta t_D}\int_{rDdry}^{rDBL} xg_2(x)\exp\left(-\frac{x^2 + r_D{}^2}{4F_{\lambda g}\eta_{D2}\Delta t_D}\right) I_o\left(\frac{xr_D}{2F_{\lambda g}\eta_{D2}\Delta t_D}\right)dx + \mathcal{L}^{-1}\left[CI_o\left(r_D\sqrt{\frac{z}{F_{\lambda g}\eta_{D2}}}\right)\right] + \mathcal{L}^{-1}\left[DK_o\left(r_D\sqrt{\frac{z}{F_{\lambda g}\eta_{D2}}}\right)\right] \quad \text{(A.28)}$$

$$p_{D3} = \frac{1}{2\eta_{D3}\Delta t_D}\int_{rDBL}^{\infty} xg_3(x)\exp\left(-\frac{r_D{}^2 + x^2}{4\eta_{D3}\Delta t_D}\right) I_o\left(\frac{xr_D}{2\eta_{D3}\Delta t_D}\right)dx + \mathcal{L}^{-1}\left[FK_o\left(r_D\sqrt{\frac{z}{\eta_{D3}}}\right)\right] \quad \text{(A.29)}$$

The dimensionless falloff pressure at the wellbore is obtained by setting $r_D = 1$ in Eq. A.27 as:

$$p_{wD}(\Delta t_D) = \frac{1}{2\Delta t_D}\int_0^{rDdry} xg_1(x)\exp\left(-\frac{x^2 + 1}{4\Delta t_D}\right) I_o\left(\frac{x}{2\Delta t_D}\right)dx + \mathcal{L}^{-1}\left[AI_o\left(\sqrt{z}\right)\right] \quad \text{(A.30)}$$

Appendix B. Derivation of the Late-Time Asymptotic Approximation of the Analytical Falloff Solution

For long time behavior, the modified Bessel functions assume the following forms (Abramowitz and Stegun, 1965):

$$I_0(z) = 1$$
$$K_0(z) = -\ln(0.8907z)$$
$$I_1(z) = 0$$
$$K_1(z) = \frac{1}{z}$$

Applying to Eqs. A.16 through A.26, the coefficient *A* reduces to the following form:

$$A = l_1 + \frac{M}{W} + \frac{K_o\left(r_{Ddry}\sqrt{\frac{z}{F_{\lambda g}\eta_{D2}}}\right)L}{W} \tag{B.1}$$

Expanding Eq. B.1 and simplifying yields:

$$\begin{aligned} A = &-K_o\left(r_{Ddry}\sqrt{z}\right)\int_0^{rDdry} xg_1(x)\,dx + \frac{1}{F_{\lambda g}\eta_{D2}}\int_{rDdry}^{rDBL} xg_2(x)K_o\left(x\sqrt{\frac{z}{F_{\lambda g}\eta_{D2}}}\right)dx \\ &-\frac{1}{F_{\lambda g}\eta_{D2}}K_o\left(r_{DBL}\sqrt{\frac{z}{F_{\lambda g}\eta_{D2}}}\right)\int_{rDdry}^{rDBL} xg_2(x)\,dx + \frac{1}{\eta_{D3}}\int_{rDBL}^{\infty} xg_3(x)K_o\left(x\sqrt{\frac{z}{\eta_{D3}}}\right)dx \\ &+\left[\frac{F_{\lambda w}}{F_{\lambda g}}K_o\left(r_{DBL}\sqrt{\frac{z}{\eta_{D3}}}\right) - \frac{1}{F_{\lambda g}}K_o\left(r_{DBL}\sqrt{\frac{z}{F_{\lambda g}\eta_{D2}}}\right)\right]\int_0^{rDdry} xg_1(x)\,dx \\ &+\frac{F_{\lambda w}}{F_{\lambda g}\eta_{D2}}K_o\left(r_{DBL}\sqrt{\frac{z}{\eta_{D3}}}\right)\int_{rDdry}^{rDBL} xg_2(x)\,dx + \frac{1}{F_{\lambda g}}K_o\left(r_{Ddry}\sqrt{\frac{z}{F_{\lambda g}\eta_{D2}}}\right)\int_0^{rDdry} xg_1(x)\,dx \end{aligned} \tag{B.2}$$

Then, the dimensionless bottomhole falloff pressure reduces to:

$$p_{wD}(\Delta t_D) = \frac{1}{2\Delta t_D}\int_0^{rDdry} xg_1(x)\exp\left(-\frac{x^2+1}{4\Delta t_D}\right)dx + \mathcal{L}^{-1}[A] \tag{B.3}$$

The inverse Laplace transform of Eq. B.2 is given by:

$$\mathcal{L}^{-1}[A] = -\frac{1}{2\Delta t_D}\int_0^{rDdry} x g_1(x)\,dx + \frac{1}{F_{\lambda g}\eta_{D2}}\frac{1}{2\Delta t_D}\int_{rDdry}^{rDBL} x g_2(x)\exp\left(-\frac{x^2}{4\Delta t_D F_{\lambda g}\eta_{D2}}\right)dx$$
$$-\frac{1}{F_{\lambda g}\eta_{D2}}\frac{1}{2\Delta t_D}\int_{rDdry}^{rDBL} x g_2(x)\,dx + \frac{1}{\eta_{D3}}\int_{rDBL}^{\infty} x g_3(x)\frac{1}{2\Delta t_D}\exp\left(-\frac{x^2}{4\Delta t_D \eta_{D3}}\right)dx \qquad \text{(B.5)}$$
$$+\frac{F_{\lambda w}}{F_{\lambda g}}\frac{1}{2\Delta t_D}\int_0^{rDdry} x g_1(x)\,dx + \frac{F_{\lambda w}}{F_{\lambda g}\eta_{D2}}\frac{1}{2\Delta t_D}\int_{rDdry}^{rDBL} x g_2(x)\,dx$$

Then, Eq. A.30 reduces to:

$$p_{wD}(\Delta t_D) = \frac{1}{2\Delta t_D}\int_0^{rDdry} x g_1(x)\exp\left(-\frac{x^2+1}{4\Delta t_D}\right)dx + \mathcal{L}^{-1}[A] \qquad \text{(B.6)}$$

Substituting for g_1, g_2, and g_3 into Eqs. B.5 and B.6 and performing the integrations, the late time asymptotic solution is given by:

$$p_{wD}(\Delta t_D) = \frac{1}{2}\frac{\overline{\lambda_g}}{\overline{\lambda_w}}\ln\left(\frac{\Delta t_D + t_{iD}}{\Delta t_D}\right) \qquad \text{(B.7)}$$

Appendix C. The Fractional Flow Curve of the Modified Buckley-Leverett Displacement Theory

The radial extents of the dry-out and the two-phase zones can be estimated based on the fractional flow equation of the modified Buckley-Leverett displacement theory as follows (Burton et al., 2008; Noh et al., 2007; Zeidouni et al., 2009):

$$r_{dry} = \sqrt{\frac{Q_g B_g}{\pi \phi h} v_{Ddry}} \tag{C.1}$$

$$r_{BL} = \sqrt{\frac{Q_g B_g}{\pi \phi h} v_{DBL}} \tag{C.2}$$

where v_{Ddry} and v_{DBL} are the dimensionless velocities of the fronts of the dry-out zone and the two-phase zone respectively, and can be determined by constructing two tangents to the gas fractional flow curve (Fig. C.1) as follows:

$$v_{Ddry} = \frac{f_{gdry} - D_{BL-dry}}{S_{gdry} - D_{BL-dry}} = \left.\frac{df_g}{dS_g}\right|_{S_{gdry}} \tag{C.3}$$

$$v_{DBL} = \frac{f_{gBL} - D_{brine-BL}}{S_{gBL} - D_{brine-BL}} = \left.\frac{df_g}{dS_g}\right|_{S_{gBL}} \tag{C.4}$$

where f_{gdry} and f_{gBL} are the values of the gas fractional flow at r_{dry} and r_{BL} respectively. $D_{brine\text{-}BL}$ and $D_{BL\text{-}dry}$ are the retardation factors of the fronts between the two-phase zone and the single-phase brine and dry-out zones respectively. The retardation factors are defined by the phase concentration in different zones (Noh et al., 2007; Zeidouni et al., 2009):

$$D_{BL-dry} = \frac{\rho_a \omega_{w,a}}{\rho_a \omega_{w,a} - \rho_g \omega_{w,g}} \tag{C.5}$$

$$D_{brine-BL} = \frac{\rho_a \omega_{CO_2,a}}{\rho_a \omega_{CO_2,a} - \rho_g \omega_{CO_2,g}} \tag{C.6}$$

where ρ_a and ρ_g are the molar densities (in kmole/m^3) of the aqueous and the gaseous phases respectively, $\omega_{w,a}$ and $\omega_{w,g}$ are the mole fractions of water in the aqueous and the gaseous phases respectively, $\omega_{CO2,a}$ and $\omega_{CO2,g}$ are the mole fractions of CO_2 in the aqueous and gaseous phases respectively. Neglecting capillary and gravity forces, the gas fractional flow – as a function of gas

saturation – is given by (Noh et al., 2007; Zeidouni et al., 2009):

$$f_g\left(S_g\right)=\frac{1}{1+\left(\mu_g/\mu_a\right)\left(k_{ra}/k_{rg}\right)} \tag{C.7}$$

where μ_a and μ_g are the viscosities of the aqueous and gaseous phases respectively, k_{ra} and k_{rg} are the relative permeabilities to the aqueous and gaseous phases respectively.

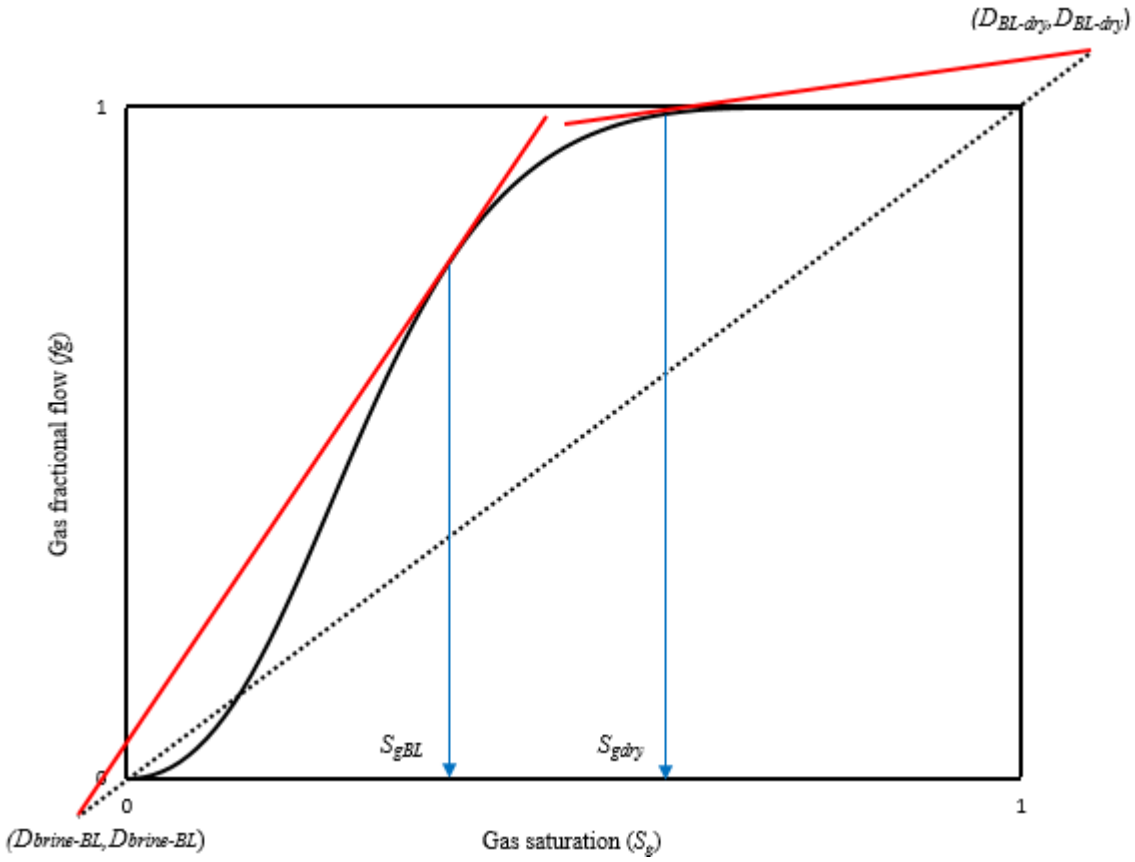

Figure C.1. Fractional flow curve of the gaseous phase in CO_2/brine displacement

Appendix D. Derivation of the Semi-Analytical Solution to Predict the Bottomhole Pressure Behavior during CO_2 Injection

Recalling the integral solution introduced by Nordbotten et al. (2009) for the ODE of Eq. 7.13:

$$\Delta p_D = \frac{1}{2\Gamma}\int_{\chi}^{\psi} \frac{d\chi}{\left[(M-1)h_{gD}+1\right]\chi} - \frac{M}{M-1}\left\{h_{gD} - \frac{\ln\left[(M-1)h_{gD}+1\right]}{(M-1)}\right\} \tag{D.1}$$

Substituting for h_{gD} from Eq. 7.11 into Eq. D.1, we get:

For $\chi \geq \psi$, Eq. (D.1) reduces to:

$$\Delta p_D = \frac{1}{2\Gamma}\int_{\psi}^{\psi} \frac{d\chi}{\left[(M-1)(0)+1\right]\chi} - \frac{M}{M-1}\left\{0 - \frac{\ln\left[(M-1)(0)+1\right]}{(M-1)}\right\} = 0 \tag{D.2}$$

For $\chi_{min} \leq \chi \leq \psi$, Eq. D.1 expands to:

$$\Delta p_D = \frac{1}{2\Gamma}\int_{\chi}^{\psi} \frac{d\chi}{\left[(M-1)(0)+1\right]\chi} - \frac{M}{M-1}\left\{0 - \frac{\ln\left[(M-1)(0)+1\right]}{(M-1)}\right\} \tag{D.3}$$

Simplifying and integrating, we get:

$$\Delta p_D = \frac{1}{2\Gamma}\ln\left(\frac{\psi}{\chi}\right) \tag{D.4}$$

For $\chi_{min} \leq \chi \leq \chi_{max}$, Eq. D.1 expands to:

$$\Delta p_D = \frac{1}{2\Gamma}\int_{\chi}^{\chi_{\max}} \frac{d\chi}{\left[(M-1)h_{gD}+1\right]\chi} + \frac{1}{2\Gamma}\int_{\chi_{\max}}^{\psi} \frac{d\chi}{\left[(M-1)h_{gD}+1\right]\chi} - \frac{M}{M-1}\left\{h_{gD} - \frac{\ln\left[(M-1)h_{gD}+1\right]}{(M-1)}\right\} \tag{D.5}$$

Substituting for h_{gD} into Eq. D.5, we get:

$$\Delta p_D = \frac{1}{2\Gamma}\ln\left(\frac{\psi}{\chi_{\max}}\right) + \frac{1}{2\Gamma}\int_{\chi}^{\chi_{\max}} \frac{d\chi}{\left[\left[\frac{b}{\chi}-\frac{a^3}{27}+\left[-\frac{2a^3b}{27\chi}+\frac{b^2}{\chi^2}\right]^{\frac{1}{2}}\right]^{\frac{1}{3}}+\left[\frac{b}{\chi}-\frac{a^3}{27}-\left[-\frac{2a^3b}{27\chi}+\frac{b^2}{\chi^2}\right]^{\frac{1}{2}}\right]^{\frac{1}{3}}-\frac{1}{3}a\right]\chi}$$
$$-\frac{M}{(M-1)^2}\left\{\begin{array}{l}\left[\left[\frac{b}{\chi}-\frac{a^3}{27}+\left[-\frac{2a^3b}{27\chi}+\frac{b^2}{\chi^2}\right]^{\frac{1}{2}}\right]^{\frac{1}{3}}+\left[\frac{b}{\chi}-\frac{a^3}{27}-\left[-\frac{2a^3b}{27\chi}+\frac{b^2}{\chi^2}\right]^{\frac{1}{2}}\right]^{\frac{1}{3}}-\frac{1}{3}a-1\right. \\ \left.-\ln\left[\left[\frac{b}{\chi}-\frac{a^3}{27}+\left[-\frac{2a^3b}{27\chi}+\frac{b^2}{\chi^2}\right]^{\frac{1}{2}}\right]^{\frac{1}{3}}+\left[\frac{b}{\chi}-\frac{a^3}{27}-\left[-\frac{2a^3b}{27\chi}+\frac{b^2}{\chi^2}\right]^{\frac{1}{2}}\right]^{\frac{1}{3}}-\frac{1}{3}a\right]\right\} \quad \text{(D.6)}$$

For $\chi \le \chi_{min}$, Eq. D.1 expands to:

$$\Delta p_D = \frac{1}{2\Gamma}\int_{\chi}^{\chi_{\min}} \frac{d\chi}{\left[(M-1)(1)+1\right]\chi} + \frac{1}{2\Gamma}\int_{\chi_{\max}}^{\psi} \frac{d\chi}{\left[(M-1)(0)+1\right]\chi}$$
$$-\frac{M}{M-1}\left\{1-\frac{\ln\left[(M-1)(1)+1\right]}{(M-1)}\right\}$$
$$+\frac{1}{2\Gamma}\int_{\chi_{\min}}^{\chi_{\max}} \frac{d\chi}{\left[(M-1)\left[\frac{1}{(M-1)}\left\{\begin{array}{l}\left[\frac{b}{\chi}-\frac{a^3}{27}+\left[-\frac{2a^3b}{27\chi}+\frac{b^2}{\chi^2}\right]^{\frac{1}{2}}\right]^{\frac{1}{3}} \\ +\left[\frac{b}{\chi}-\frac{a^3}{27}-\left[-\frac{2a^3b}{27\chi}+\frac{b^2}{\chi^2}\right]^{\frac{1}{2}}\right]^{\frac{1}{3}}-\frac{1}{3}a-1\end{array}\right\}+1\right]\chi\right]} \quad \text{(D.7)}$$

Which simplifies to:

$$\Delta p_D = \frac{1}{2M\Gamma}\ln\left(\frac{\chi_{\min}}{\chi}\right)+\frac{1}{2\Gamma}\ln\left(\frac{\psi}{\chi_{\max}}\right)-\frac{M}{M-1}\left\{1-\frac{\ln(M)}{(M-1)}\right\}$$
$$+\frac{1}{2\Gamma}\int_{\chi_{\min}}^{\chi_{\max}}\frac{d\chi}{\left[\left[\frac{b}{\chi}-\frac{a^3}{27}+\left[-\frac{2a^3b}{27\chi}+\frac{b^2}{\chi^2}\right]^{\frac{1}{2}}\right]^{\frac{1}{3}}+\left[\frac{b}{\chi}-\frac{a^3}{27}-\left[-\frac{2a^3b}{27\chi}+\frac{b^2}{\chi^2}\right]^{\frac{1}{2}}\right]^{\frac{1}{3}}-\frac{a}{3}\right]\chi} \quad \text{(D.8)}$$

The integral term of Eq. D.8 cannot be solved analytically. Therefore, the above model represents a semi-analytical solution that accounts for strong gravity effects and can be utilized to estimate the pressure field during CO_2 injection.

References

Abramowitz, M., Stegun, I.A., 1965. Handbook of mathematical functions with formulas, graphs, and mathematical table, US Department of Commerce. National Bureau of Standards Applied Mathematics series 55.

Agarwal, R.G., Gardner, D.C., Kleinsteiber, S.W., Fussell, D.D., 1999. Analyzing well production data using combined-type-curve and decline-curve analysis concepts. SPE Reservoir Evaluation & Engineering 2, 478-486.

Alfi, M., Hosseini, S., Alfi, M., Shakiba, M., 2015. Effectiveness of 4D Seismic Data to Monitor CO_2 Plume in Cranfield CO_2-EOR Project, Carbon Management Technology Conference, Sugarland, Texas, USA. CMTC-439559-MS.

Alkan, H., Cinar, Y., Ülker, E., 2010. Impact of capillary pressure, salinity and in situ conditions on CO_2 injection into saline aquifers. Transport in porous media 84, 799-819.

Ambastha, A.K., 1989. Pressure transient analysis for composite systems. Stanford Univ., CA (USA). Petroleum Research Inst.

Aminu, M.D., Nabavi, S.A., Rochelle, C.A., Manovic, V., 2017. A review of developments in carbon dioxide storage. Applied Energy 208, 1389-1419.

Arts, R., Eiken, O., Chadwick, A., Zweigel, P., van der Meer, B., Kirby, G., 2004. Seismic monitoring at the Sleipner underground CO_2 storage site (North Sea). Geological Society, London, Special Publications 233, 181-191.

Arts, R., Eiken, O., Chadwick, A., Zweigel, P., Van der Meer, L., Zinszner, B., 2003. Monitoring of CO_2 injected at Sleipner using time lapse seismic data, Greenhouse Gas Control Technologies-6th International Conference. Elsevier, pp. 347-352.

Azizi, E., Cinar, Y., 2013a. Approximate analytical solutions for CO_2 injectivity into saline formations. SPE Reservoir Evaluation & Engineering 16, 123-133.

Azizi, E., Cinar, Y., 2013b. A new mathematical model for predicting CO_2 injectivity. Energy Procedia 37, 3250-3258.

Bachu, S., 2015. Review of CO_2 storage efficiency in deep saline aquifers. International Journal of Greenhouse Gas Control 40, 188-202.

Bachu, S., Bonijoly, D., Bradshaw, J., Burruss, R., Holloway, S., Christensen, N.P., Mathiassen, O.M., 2007. CO_2 storage capacity estimation: Methodology and gaps. International journal of greenhouse gas control 1, 430-443.

Beck, L., 2020. Carbon capture and storage in the USA: the role of US innovation leadership in climate-technology commercialization. Clean Energy 4, 2-11.

Blasingame, T., Lee, W., 1986. Variable-rate reservoir limits testing, Permian Basin Oil and Gas Recovery Conference. Society of Petroleum Engineers.

Blasingame, T., Lee, W., 1988. The variable-rate reservoir limits testing of gas wells, SPE Gas Technology Symposium.

Bradshaw, J., Bachu, S., Bonijoly, D., Burruss, R., Holloway, S., Christensen, N.P., Mathiassen, O.M., 2007. CO_2 storage capacity estimation: issues and development of standards. International journal of greenhouse gas control 1, 62-68.

Buckley, S.E., Leverett, M., 1942. Mechanism of fluid displacement in sands. Transactions of the AIME 146, 107-116.

Burton, M., Kumar, N., Bryant, S.L., 2008. Time-dependent injectivity during CO_2 storage in aquifers, SPE Symposium on Improved Oil Recovery. Society of Petroleum Engineers.

Burton, M., Kumar, N., Bryant, S.L., 2009. CO_2 injectivity into brine aquifers: Why relative permeability matters as much as absolute permeability. Energy Procedia 1, 3091-3098.

Butler, R.M., 1991. Thermal recovery of oil and bitumen.

Cantucci, B., Buttinelli, M., Procesi, M., Sciarra, A., Anselmi, M., 2016. Algorithms for CO_2 Storage Capacity Estimation: Review and Case Study, in: Vishal, V., Singh, T.N. (Eds.), Geologic Carbon Sequestration: Understanding Reservoir Behavior. Springer International Publishing, Cham, pp. 21-44.

Celia, M.A., Nordbotten, J.M., Court, B., Dobossy, M., Bachu, S., 2011. Field-scale application of a semi-analytical model for estimation of CO_2 and brine leakage along old wells. International Journal of Greenhouse Gas Control 5, 257-269.

Chadwick, A., Arts, R., Eiken, O., Williamson, P., Williams, G., 2006a. Geophysical monitoring of the CO 2 plume at Sleipner, North Sea, Advances in the geological storage of carbon dioxide. Springer, pp. 303-314.

Chadwick, A., Noy, D., Lindeberg, E., Arts, R., Eiken, O., Williams, G., 2006b. Calibrating reservoir performance with time-lapse seismic monitoring and flow simulations of the Sleipner CO_2 plume.

Chadwick, A., Williams, G., Delepine, N., Clochard, V., Labat, K., Sturton, S., Buddensiek, M.-L., Dillen, M., Nickel, M., Lima, A.L., 2010. Quantitative analysis of time-lapse seismic monitoring data at the Sleipner CO_2 storage operation. The Leading Edge 29, 170-177.

Chadwick, R., Arts, R., Eiken, O., 2005. 4D seismic quantification of a growing CO_2 plume at Sleipner, North Sea, Geological Society, London, Petroleum Geology Conference series. Geological Society of London, pp. 1385-1399.

Chadwick, R., Noy, D., 2010. History-matching flow simulations and time-lapse seismic data from the Sleipner CO_2 plume, Geological Society, London, petroleum geology conference series. Geological Society of London, pp. 1171-1182.

Chadwick, R., Noy, D., Arts, R., Eiken, O., 2009. Latest time-lapse seismic data from Sleipner yield new insights into CO_2 plume development. Energy Procedia 1, 2103-2110.

Chadwick, R.A., Noy, D.J., 2015. Underground CO_2 storage: demonstrating regulatory conformance by convergence of history- matched modeled and observed CO_2 plume behavior using Sleipner time- lapse seismics. Greenhouse Gases: Science and Technology 5, 305-322.

Chen, H.-K., Brigham, W., 1978. Pressure buildup for a well with storage and skin in a closed square. Journal of Petroleum Technology 30, 141-146.

Chen, Z., Liao, X., Zhao, X., Feng, X., Zang, J., He, L., 2015. A new analytical method based on pressure transient analysis to estimate carbon storage capacity of depleted shales: A case study. International Journal of Greenhouse Gas Control 42, 46-58.

CMG-IMEX, 2019. Computer Modeling Group Ltd, Calgary.

CMG-IMEX, 2020. Computer Modeling Group Ltd, Calgary.

CMG-IMEX, 2021. Computer Modeling Group Ltd, Calgary.

CMG-STARS, 2021. Advanced Process and Thermal Reservoir Simulator. Version 2021.10. CMG STARS.

Connaughton, C.R., Crawford, P.B., 1975. Factors affecting solution gas drive recovery, Annual Technical Meeting. Petroleum Society of Canada.

Corey, A.T., 1954a. The interrelation between gas and oil relative permeabilities. Producers monthly, 38-41.

Corey, A.T., 1954b. The interrelation between gas and oil relative permeabilities. Producers monthly 19, 38-41.

Couëslan, M.L., Butsch, R., Will, R., Locke II, R.A., 2014. Integrated reservoir monitoring at the Illinois Basin–Decatur Project. Energy Procedia 63, 2836-2847.

De Simone, S., Krevor, S., 2021. A tool for first order estimates and optimisation of dynamic storage resource capacity in saline aquifers. International Journal of Greenhouse Gas Control 106, 103258.

Delshad, M., Kong, X., Tavakoli, R., Hosseini, S.A., Wheeler, M.F., 2013. Modeling and simulation of carbon sequestration at Cranfield incorporating new physical models.

International Journal of Greenhouse Gas Control 18, 463-473.

Dismukes, D.E., Zeidouni, M., Zulqarnain, M., Hughes, R., Hall, K., Snyder, B., Layne, M., Lorenzo, J.M., John, C., Harder, B., 2019. Integrated Carbon Capture and Storage in the Louisiana Chemical Corridor. Louisiana State Univ., Baton Rouge, LA (United States).

Doughty, C., Freifeld, B., Trautz, R., 2007. Site Characterization for CO2 Geologic Storage and Vice Versa: The Frio Brine Pilot. Yrcsd. ziDS as a Case Study.

Doughty, C., Pruess, K., Benson, S.M., Hovorka, S.D., Knox, P.R., Green, C.T., 2001. Capacity investigation of brine-bearing sands of the Frio Formation for geologic sequestration of CO_2. GCCC Texts and Reports.

Edwards, R.W., Celia, M.A., Bandilla, K.W., Doster, F., Kanno, C.M., 2015. A model to estimate carbon dioxide injectivity and storage capacity for geological sequestration in shale gas wells. Environmental science & technology 49, 9222-9229.

EDX, 2018. Frio Brine Pilot Study, Gulf Coast Carbon Center, Bureau of Economic Geology, Jackson School of Geosciences, The University of Texas at Austin, Regional Carbon Sequestration Partnership, Frio Brine Project Data, 2018-05-30.

Ehlig-Economides, C., Anchliya, A., Song, B., 2010. Pressure falloff test interpretation for leakage detection during CO_2 injection in a deep saline aquifer, SPE Europec featured at EAGE Conference and Exhibition? SPE, pp. SPE-131675-MS.

Ehlig-Economides, C., Economides, M.J., 2010. Sequestering carbon dioxide in a closed underground volume. Journal of Petroleum Science and Engineering 70, 123-130.

Ennis-King, J., Paterson, L., Michael, K., 2018. Evolution of the Vertical Distribution of CO_2 Over the Wellbore Completion Interval During Injection: Comparison of Theory, Simulations and Field Data, 14th Greenhouse Gas Control Technologies Conference Melbourne, pp. 21-26.

EPA, 2008a. Federal requirements under the underground injection control (UIC) program for carbon dioxide (CO_2) geological sequestration (GS) wells, Report, Environmental Protection Agency.

EPA, 2008b. Geologic CO_2 Sequestration Technology and Cost Analysis.

Finley, R.J., Frailey, S.M., Leetaru, H.E., Senel, O., Couëslan, M.L., Scott, M., 2013. Early operational experience at a one-million tonne CCS demonstration project, Decatur, Illinois, USA. Energy Procedia 37, 6149-6155.

Fraim, M., 1987. Gas reservoir decline-curve analysis using type curves with real gas pseudopressure and normalized time. SPE Formation Evaluation 2, 671-682.

Ganjdanesh, R., Hosseini, S.A., 2018. Development of an analytical simulation tool for storage capacity estimation of saline aquifers. International Journal of Greenhouse Gas Control 74, 142-154.

Gershenzon, N.I., Ritzi Jr, R.W., Dominic, D.F., Mehnert, E., Okwen, R.T., 2017a. Capillary trapping of CO_2 in heterogeneous reservoirs during the injection period. International Journal of greenhouse gas control 59, 13-23.

Gershenzon, N.I., Ritzi Jr, R.W., Dominic, D.F., Mehnert, E., Okwen, R.T., Patterson, C., 2017b. CO_2 trapping in reservoirs with fluvial architecture: Sensitivity to heterogeneity in permeability and constitutive relationship parameters for different rock types. Journal of Petroleum Science and Engineering 155, 89-99.

Gershenzon, N.I., Soltanian, M., Ritzi Jr, R.W., Dominic, D.F., 2014. Influence of small scale heterogeneity on CO_2 trapping processes in deep saline aquifers. Energy Procedia 59, 166-173.

Ghaderi, S.M., Keith, D.W., Leonenko, Y., 2009. Feasibility of injecting large volumes of CO_2 into aquifers. Energy Procedia 1, 3113-3120.

Ghomian, Y., Urun, M.B., Pope, G.A., Sepehrnoori, K., 2008. Investigation of economic incentives for CO_2 sequestration, SPE Annual Technical Conference and Exhibition. Society of Petroleum Engineers.

Giorgis, T., Carpita, M., Battistelli, A., 2007. 2D modeling of salt precipitation during the injection of dry CO_2 in a depleted gas reservoir. Energy Conversion and Management 48, 1816-1826.

Han, W.S., Lee, S.Y., Lu, C., McPherson, B.J., 2010. Effects of permeability on CO_2 trapping mechanisms and buoyancy- driven CO_2 migration in saline formations. Water Resources Research 46.

Hassanzadeh, H., Pooladi-Darvish, M., Elsharkawy, A.M., Keith, D.W., Leonenko, Y., 2008. Predicting PVT data for CO_2–brine mixtures for black-oil simulation of CO_2 geological storage. international journal of greenhouse gas control 2, 65-77.

Horner, D., 1951. Pressure build-up in wells, 3rd world petroleum congress. world petroleum congress.

Hosseini, S.A., Kim, S., Zeidouni, M., 2014. Application of multi-well analytical models to maximize geological CO_2 storage in brine formations. Energy Procedia 63, 3563-3567.

Hovorka, S., Romero, M., Treviño, R., Warne, A., Ambrose, W., Knox, P., Tremblay, T., 2000. Project evaluation: phase II: optimal geological environments for carbon dioxide disposal in brine-bearing formations (aquifers) in the United States: The University of Texas at Austin, Bureau of Economic Geology, final report prepared for US Department of Energy,

National Energy Technology Laboratory, under contract no. DEAC26-98FT40417.

Hovorka, S.D., Benson, S.M., Doughty, C., Freifeld, B.M., Sakurai, S., Daley, T.M., Kharaka, Y.K., Holtz, M.H., Trautz, R.C., Nance, H.S., 2006. Measuring permanence of CO_2 storage in saline formations: the Frio experiment. Environmental Geosciences 13, 105-121.

Hovorka, S.D., Meckel, T.A., Trevino, R.H., 2013. Monitoring a large-volume injection at Cranfield, Mississippi—Project design and recommendations. International Journal of Greenhouse Gas Control 18, 345-360.

Hovorka, S.D., Meckel, T.A., Trevino, R.H., Lu, J., Nicot, J.-P., Choi, J.-W., Freeman, D., Cook, P., Daley, T.M., Ajo-Franklin, J.B., 2011. Monitoring a large volume CO_2 injection: Year two results from SECARB project at Denbury's Cranfield, Mississippi, USA. Energy Procedia 4, 3478-3485.

Hu, L., Bayer, P., Alt-Epping, P., Tatomir, A., Sauter, M., Brauchler, R., 2015. Time-lapse pressure tomography for characterizing CO_2 plume evolution in a deep saline aquifer. International Journal of Greenhouse Gas Control 39, 91-106.

Huerta, N.J., Cantrell, K.J., White, S.K., Brown, C.F., 2020. Hydraulic fracturing to enhance injectivity and storage capacity of CO_2 storage reservoirs: Benefits and risks. International Journal of Greenhouse Gas Control 100, 103105.

IEAGHG, 2010. Injection strategies for CO_2 storage sites. Report No. 2010/4.

Jahangiri, H.R., Zhang, D., 2011. Optimization of the net present value of carbon dioxide sequestration and enhanced oil recovery, Offshore Technology Conference. Offshore Technology Conference.

Jikich, S.A., Sams, W.N., Bromhal, G., Pope, G., Gupta, N., Smith, D.H., 2003. Carbon dioxide injectivity in brine reservoirs using horizontal wells, National Energy Technology Laboratory, United States Department of Energy (eds) Proceedings for the 2nd national conference on carbon sequestration, May, pp. 5-8.

Kamal, M.M., 2009. Transient Well Testing. Society of Petroleum Engineers.

King, A.C., Billingham, J., Otto, S.R., 2003. Differential equations: linear, nonlinear, ordinary, partial. Cambridge University Press.

Kopp, A., Class, H., Helmig, R., 2009. Investigations on CO_2 storage capacity in saline aquifers: Part 1. Dimensional analysis of flow processes and reservoir characteristics. International Journal of Greenhouse Gas Control 3, 263-276.

Kumar, A., Oballa, V., Card, C., 2010. Fully-coupled wellbore design and optimization for thermal operations, Canadian unconventional resources and international petroleum conference. OnePetro.

Kumar, N., Bryant, S.L., 2009. Semi-analytical model to determine perforation interval for secure CO_2 storage in saline aquifers. Energy Procedia 1, 3071-3078.

Mathias, S.A., de Miguel, G.J.G.M., Thatcher, K.E., Zimmerman, R.W., 2011a. Pressure buildup during CO 2 injection into a closed brine aquifer. Transport in porous media 89, 383-397.

Mathias, S.A., Gluyas, J.G., de Miguel, G.J.G.M., Bryant, S.L., Wilson, D., 2013. On relative permeability data uncertainty and CO_2 injectivity estimation for brine aquifers. International Journal of Greenhouse Gas Control 12, 200-212.

Mathias, S.A., Gluyas, J.G., González Martínez de Miguel, G.J., Hosseini, S.A., 2011b. Role of partial miscibility on pressure buildup due to constant rate injection of CO_2 into closed and open brine aquifers. Water Resources Research 47.

Mathias, S.A., González Martínez de Miguel, G.J., Thatcher, K.E., Zimmerman, R.W., 2011c. Pressure buildup during CO 2 injection into a closed brine aquifer. Transport in porous media 89, 383-397.

Mathias, S.A., Hardisty, P.E., Trudell, M.R., Zimmerman, R.W., 2009. Approximate solutions for pressure buildup during CO 2 injection in brine aquifers. Transport in Porous Media 79, 265-284.

Mattar, L., Anderson, D., 2005. Dynamic Material Balance (Oil or Gas-in-place without shut-ins), Canadian International Petroleum Conference. OnePetro.

Miller, C., Dyes, A., Hutchinson Jr, C., 1950. The estimation of permeability and reservoir pressure from bottom hole pressure build-up characteristics. Journal of Petroleum Technology 2, 91-104.

Miri, R., Hellevang, H., 2016. Salt precipitation during CO_2 storage—A review. International Journal of Greenhouse Gas Control 51, 136-147.

Mishra, S., Kelley, M., Raziperchikolaee, S., Ganesh, P.R., Valluri, M., Keister, L., Burchwell, A., Mawalkar, S., Place, M., Gupta, N., 2021. A comprehensive analysis of transient pressure and rate data from CO_2 storage projects in a depleted pinnacle reef oil field complex, Michigan, USA. International Journal of Greenhouse Gas Control 107, 103294.

Mishra, S., Kelley, M., Zeller, E., Slee, N., Gupta, N., Bhattacharya, I., Hammond, M., 2013. Maximizing the value of pressure monitoring data from CO_2 sequestration projects. Energy Procedia 37, 4155-4165.

NETL, 2007. Carbon Sequestration Atlas of the United States and Canada. US Department of Energy, Office of Fossil Energy, National Energy Technology Laboratory.

Nguyen, D., Allinson, W., 2002. The economics of CO_2 capture and geological storage, SPE Asia Pacific Oil and Gas Conference and Exhibition. Society of Petroleum Engineers.

Noh, M.H., Lake, L.W., Bryant, S.L., Araque-Martinez, A.N., 2007. Implications of Coupling Fractional Flow and Geochemistry for CO_2 Injection in Aquifers. SPE Reservoir Evaluation and Engineering 10, 406-414.

Nordbotten, J.M., Celia, M.A., 2006. Similarity solutions for fluid injection into confined aquifers. Journal of Fluid Mechanics 561, 307-327.

Nordbotten, J.M., Celia, M.A., Bachu, S., 2005a. Injection and storage of CO 2 in deep saline aquifers: analytical solution for CO 2 plume evolution during injection. Transport in Porous media 58, 339-360.

Nordbotten, J.M., Celia, M.A., Bachu, S., Dahle, H.K., 2005b. Semianalytical solution for CO_2 leakage through an abandoned well. Environmental science & technology 39, 602-611.

Nordbotten, J.M., Kavetski, D., Celia, M.A., Bachu, S., 2009. Model for CO_2 leakage including multiple geological layers and multiple leaky wells. Environmental science & technology 43, 743-749.

Norouzi, A.M., Babaei, M., Han, W.S., Kim, K.-Y., Niasar, V., 2021. CO_2-plume geothermal processes: A parametric study of salt precipitation influenced by capillary-driven backflow. Chemical Engineering Journal 425, 130031.

Okwen, R., Stewart, M., Cunningham, J., 2011a. Effect of well orientation (vertical vs. horizontal) and well length on the injection of CO 2 in deep saline aquifers. Transport in porous media 90, 219-232.

Okwen, R.T., Stewart, M.T., Cunningham, J.A., 2010. Analytical solution for estimating storage efficiency of geologic sequestration of CO_2. International Journal of Greenhouse Gas Control 4, 102-107.

Okwen, R.T., Stewart, M.T., Cunningham, J.A., 2011b. Temporal variations in near-wellbore pressures during CO_2 injection in saline aquifers. International Journal of Greenhouse Gas Control 5, 1140-1148.

Oruganti, Y.D., Mishra, S., 2013. An improved simplified analytical model for CO_2 plume movement and pressure buildup in deep saline formations. International Journal of Greenhouse Gas Control 14, 49-59.

Ott, H., de Kloe, K., Marcelis, F., Makurat, A., 2011. Injection of supercritical CO_2 in brine saturated sandstone: pattern formation during salt precipitation. Energy Procedia 4, 4425-4432.

Ozah, R.C., Lakshminarasimhan, S., Pope, G.A., Sepehrnoori, K., Bryant, S.L., 2005. Numerical simulation of the storage of pure CO_2 and CO_2-H2S gas mixtures in deep saline aquifers, SPE Annual Technical Conference and Exhibition. Society of Petroleum Engineers.

Palacio, J., Blasingame, T., 1993. Decline curve analysis using type curves: Analysis of gas well production data. paper SPE 25909, 12-14.

Pooladi-Darvish, M., Moghdam, S., Xu, D., 2011. Multiwell injectivity for storage of CO_2 in aquifers. Energy Procedia 4, 4252-4259.

Prats, M., 1982. Thermal recovery.

Pruess, K., Müller, N., 2009. Formation dry- out from CO_2 injection into saline aquifers: 1. Effects of solids precipitation and their mitigation. Water Resources Research 45.

Raad, S.M.J., Lawton, D., Maidment, G., Hassanzadeh, H., 2021. Transient non-isothermal coupled wellbore-reservoir modeling of CO_2 injection—Application to CO_2 injection tests at the CaMI FRS site, Alberta, Canada. International Journal of Greenhouse Gas Control 111, 103462.

Ramey, H., 1970. Approximate solutions for unsteady liquidflow in composite reservoirs. Journal of Canadian Petroleum Technology 9.

Raza, A., Gholami, R., Wheaton, R., Rabiei, M., Rasouli, V., Rezaee, R., 2019. Primary recovery factor as a function of production rate: implications for conventional reservoirs with different drive mechanisms. Energy Sources, Part A: Recovery, Utilization, and Environmental Effects 41, 2778-2785.

Savioli, G., Santos, J., Carcione, J., Gei, D., 2012. Numerical modeling of fluid flow and time-lapse seismograms applied to CO_2 storage and monitoring, 10th World Congress on Computational Mechanics, pp. 8-13.

Schmelz, W.J., Hochman, G., Miller, K.G., 2020. Total cost of carbon capture and storage implemented at a regional scale: northeastern and midwestern United States. Interface focus 10, 20190065.

Shchipanov, A., Kollbotn, L., Berenblyum, R., 2019. Characterization and monitoring of reservoir flow barriers from pressure transient analysis for CO_2 injection in saline aquifers. International Journal of Greenhouse Gas Control 91, 102842.

Singh, H., Bromhal, G.S., 2019. Two risk metrics for CO_2 storage reservoirs with varying domain size, heterogeneity, and injection rate. Greenhouse Gases: Science and Technology 9, 754-769.

Spivey, J.P., Lee, W.J., 2013. Applied well test interpretation. Society of Petroleum Engineers Richardson, TX.

Spycher, N., Pruess, K., Ennis-King, J., 2003. CO_2-H2O mixtures in the geological sequestration of CO_2. I. Assessment and calculation of mutual solubilities from 12 to 100 C and up to 600 bar. Geochimica et cosmochimica acta 67, 3015-3031.

Stehfest, H., 1970. Remark on algorithm 368: Numerical inversion of Laplace transforms. Communications of the ACM 13, 624.

Streibel, M., Finley, R.J., Martens, S., Greenberg, S., Möller, F., Liebscher, A., 2014. From pilot to demo scale–Comparing Ketzin results with the Illinois Basin-Decatur project. Energy Procedia 63, 6323-6334.

Torp, T.A., Dale, J., 2003. Demonstrating storage of CO_2 in geological reservoirs: the Sleipner and SACS projects, Greenhouse Gas Control Technologies-6th International Conference. Elsevier, pp. 311-316.

Tran, N., Zeidouni, M., 2018. Pressure transient technique to constrain CO 2 plume boundaries. Environmental earth sciences 77, 1-12.

Tran, N.H., Zeidouni, M., 2017. CO_2 plume characterization using pressure arrival time, SPE Health, Safety, Security, Environment, & Social Responsibility Conference-North America. Society of Petroleum Engineers.

van Genuchten, M.T., 1980. A closed- form equation for predicting the hydraulic conductivity of unsaturated soils. Soil science society of America journal 44, 892-898.

Walsh, M., Lake, L.W., 2003. A generalized approach to primary hydrocarbon recovery.

Wen, G., Benson, S.M., 2019. CO_2 plume migration and dissolution in layered reservoirs. International Journal of Greenhouse Gas Control 87, 66-79.

Xiao, C., Tian, L., Yang, Y., Zhang, Y., Gu, D., Chen, S., 2016. Comprehensive application of semi-analytical PTA and RTA to quantitatively determine abandonment pressure for CO_2 storage in depleted shale gas reservoirs. Journal of Petroleum Science and Engineering 146, 813-831.

Zeidouni, M., 2023. Transient Pressure Interference During CO_2 Injection in Saline Aquifers, SPE EuropEC-Europe Energy Conference featured at the 84th EAGE Annual Conference & Exhibition. OnePetro.

Zeidouni, M., Hovorka, S.D., Shi, K., 2016. Tracer test to constrain CO 2 residual trapping and plume evolution. Environmental Earth Sciences 75, 1451.

Zeidouni, M., Nicot, J.-P., Hovorka, S.D., 2014. Monitoring above-zone temperature variations associated with CO 2 and brine leakage from a storage aquifer. Environmental earth sciences 72, 1733-1747.

Zeidouni, M., Pooladi-Darvish, M., Keith, D., 2009. Analytical solution to evaluate salt precipitation during CO_2 injection in saline aquifers. International Journal of Greenhouse Gas Control 3, 600-611.

Zhou, Q., Yang, X., Zhang, R., Hosseini, S.A., Ajo- Franklin, J.B., Freifeld, B.M., Daley, T.M., Hovorka, S.D., 2020. Dynamic processes of CO_2 storage in the field: 1. Multiscale and multipath channeling of CO_2 flow in the hierarchical fluvial reservoir at Cranfield, Mississippi. Water Resources Research 56, e2019EF001360.

Zuluaga, E., 2005. Geochemical effects in two-phase flow. PhD Dissertation, U. of Texas at Austin. Austin, Texas.

Publications

Peer-Reviewed Journal Papers

Abdelaal, Mohamed, Mehdi Zeidouni, and Ian J. Duncan. "Effects of injection well operation conditions on CO_2 storage capacity in deep saline aquifers." *Greenhouse Gases: Science and Technology* 11.4 (2021): 734-749.

Abdelaal, Mohamed, and Mehdi Zeidouni. "Pressure falloff testing to characterize CO_2 plume and dry-out zone during CO_2 injection in saline aquifers." *International Journal of Greenhouse Gas Control* 103 (2020): 103160.

Abdelaal, Mohamed, and Mehdi Zeidouni. "Injection data analysis using material balance time for CO_2 storage capacity estimation in deep closed saline aquifers." *Journal of Petroleum Science and Engineering* 208 (2022): 109385.

Abdelaal, Mohamed, and Mehdi Zeidouni. "Coupled Wellbore-Reservoir Modeling to Evaluate CO_2 Injection Rate Distribution over Multi-Layer Thick Storage Complex." *International Journal of Greenhouse Gas Control*, 129 (2023): 103987.

Abdelaal, Mohamed, and Mehdi Zeidouni. "CO_2-Brine Interface Evolution and Corresponding Overpressure in High-Gravity CO_2 Storage Complex." *Journal of Geoenergy Science and Engineering*, 234 (2024): 212592.

Conference Proceedings and Posters

Abdelaal, Mohamed, and Mehdi Zeidouni. "Using Injection Pressure and Rate Data Analysis to Estimate CO_2 Storage Capacity of Closed Saline Aquifers." *AGU Fall Meeting Abstracts*. Vol. 2021.

Abdelaal, Mohamed, and Mehdi Zeidouni. "Field Application of Rate-Transient Analysis to Determine the Closed versus Open Outer Boundary Condition of Active CO_2 Storage Saline Systems." *17th International Conference on Greenhouse Gas Control Technologies, accepted.*

Meetings and Talks

Abdelaal, Mohamed "Rate-Transient Analysis for CO_2 Storage Capacity Estimation" *Gulf-of Mexico (GoM) SECARB Offshore* Annual *Joint Meeting*. May 15-17, 2022.

Abdelaal, Mohamed "Coupled Wellbore-Reservoir Modeling to Evaluate CO_2 Injection Rate Distribution over Multi-Layer Thick Storage Complex." *Gulf-of Mexico (GoM) SECARB Offshore Annual Joint Meeting*. April 5-7, 2023.

Vita

Mohamed Abdelaal is a Graduate Research Assistant at Craft & Hawkins Department of Petroleum Engineering at Louisiana State University. Mohamed started his PhD study in Spring 2020, and is expected to graduate in August 2024. Mohamed obtained B.Sc. in 2014 and M. Sc. in 2018 both in Petroleum Engineering from Suez University in Egypt. From 2016 to 2020, Mohamed was working as a teaching and research assistant at the Department of Petroleum Engineering at Suez University. With a solid background in Petroleum Reservoir Engineering, Mohamed's research at LSU is focused on pressure/rate transient analysis with application to unconventional shale/tight reservoirs and geological CO_2 storage (GCS). Mohamed's work includes analytical and numerical modeling of fluid flow in porous media to investigate and assess the utility and potential of target storage formations for CO_2 storage. Mohamed performs geological reservoir characterization using various forms of data integration to gain a deeper understanding of both conceptual and practical issues related to GCS projects.